Trinity College Dublin
Coláiste na Tríonóide, Baile Átha Cliath
The University of Dublin

Investigating the Feasibility of Photostimulation for the Development of a Low Energy-Spread Electron Microscope Source.

A PhD thesis by:

Frances Quigley

Supervisor
Dr Lewys Jones

Co-Supervisor
Dr Cormac McGuinness

Submitted to Trinity College Dublin
for the degree of:
Doctor of Philosophy

School of Physics

January 3, 2024

Declarations

I have read and I understand the plagiarism provisions in the General Regulations of the University Calendar for the current year, found at: http://www.tcd.ie/calendar.

I have also completed the Online Tutorial on avoiding plagiarism 'Ready, Steady, Write', located at http://tcd-ie.libguides.com/plagiarism/ready-steady-write.

I declare that this thesis has not been submitted as an exercise for a degree at this or any other university, and it is entirely my own work.

I agree to deposit this thesis in the University's open access institutional repository or allow the Library to do so on my behalf, subject to Irish Copyright Legislation and Trinity College Library conditions of use and acknowledgement.

I consent to the examiner retaining a copy of the thesis beyond the examining period, should they so wish (EU GDPR May 2018).

This project resulted in a number of manuscripts and abstracts published by the author. Where this work has been incorporated into this thesis, it has been appropriately cited. For any figures reproduced from other publications, permission to reproduce them was obtained, and they are cited as specified by the license agreement. Any assistance received during experiments or experimental analysis is clearly stated at the beginning of each chapter, and all other work is by the author.

Frances Quigley

October 2023

Abstract

Electron microscopes use fast-moving electrons as illumination to generate high resolution images down to the atomic scale. They are a valuable tool in various research fields, from palaeontology to material science. Low voltage imaging in particular is becoming an increasingly popular technique due to its many applications. These include imaging materials sensitive to knock-on damage, decreasing charging effects on insulating samples and improving surface sensitive imaging. However, the illumination of the beam during low voltage imaging is limited by chromatic aberration, the premature focus of lower energy electrons on the optic axis compared to higher energy electrons.

Decreasing the electron's energy-spread (ΔE) is one route to reducing the chromatic defocus blur. This can be achieved by installing an electron monochromator or upgrading to a lower energy-spread electron source, such as a cold field emission gun (FEG) ($\Delta E \approx 0.3eV$). These however can be expensive options, out of the reach of less funded laboratories.

This thesis presents an alternative solution, exploiting the photoelectric effect where photons are used to stimulate the direct release of low energy-spread electrons from the low workfunction material Lanthanum Hexaboride (LaB_6). Using fibre optics and a UV laser diode, a prototype has been retrofitted onto the existing thermionic LaB_6 electron gun in a ZEISS EVO SEM, and results from this will be presented. Based on previous literature, the photoelectrons produced from this retrofitted emitter are predicted to have an energy-spread as low as ΔE_e=0.37±0.04 eV.

Images generated from this photoelectron emitter will be shown, and the optimisation of the developed apparatus to increase its photoelectron current will be outlined. Finally, the semi-permanent installation of this novel photoelectron emitter will be characterised with its resolution and brightness compared to other thermionic electron sources evaluated.

While SEM images were successfully captured with this photoemitter, some further performance improvements would be needed before it is practically useful in low voltage imaging. Therefore, solutions to upgrade the emitter will also be outlined alongside some alternative uses for the source, including beam modulation and time-resolved SEM imaging. This prototype will hopefully lay the foundation for increasing the sustainability of existing microscopes, extending their lifetime by potentially increasing their functionality and performance.

Acknowledgments

This journey to completing my PhD was made possible through the invaluable support of many individuals, and I'd like to extend a sincere thank you to everyone involved.

First and foremost, I'd like to thank my supervisor, Lewys Jones. I have thoroughly enjoyed my PhD experience, and having a supportive supervisor was a significant factor in this. So thank you for your help, guidance, and encouragement throughout the last four years.

To my co-supervisor, Cormac McGuinness, thank you for your invaluable input over the course of my PhD and for sharing your experience and knowledge during the construction of various experiments.

I would also like to thank Clive Downing for offering endless advice and answering my many questions on adapting the EVO and all things microscopy related. Many of my experiments would not have been achieved without your troubleshooting and technical expertise, so thank you.

Jonathan Peters was extremely helpful in assisting in the automation and set up of the electronic components in my experiments, as well as offering general advice throughout the whole PhD process. So I would like to extend a big thank you to him as well.

Armin Hayn was a prominent person in designing the experiment to characterise the photoemitter. I'd like to thank him for very kindly processing images captured in the EVO to determine our photoemitter's brightness and generously providing results from two standard tungsten and LaB_6 ZEISS EVO SEMs for comparison.

I'd also like to thank the Advanced Microscopy Laboratory staff for the training I have received. A particular mention to Dermot Daly and Megan Canavan for providing different equipment for my experiments and their valuable expertise.

I of course would also like to mention everyone in the Ultramicroscopy group and the AML office. While it may be too long to list everyone individually, I would like to thank them all for their support and for making the office such a nice place to work in over the last four years. I would also like to especially thank Patrick McBean for his tech advice over the years.

Last, and by no means least, this PhD was only achieved with the support of my friends and family, and I would like to extend my heartfelt gratitude to you all. While I unfortunately cannot list everyone, there are a few people I'd like to mention especially. To my brothers, Ben and Shane, thank you for offering

never-ending support over the last four years. To Paul, I couldn't have asked for a more supportive partner. Whether it be the highs or lows of the PhD, you were always there without fail. I cannot stress how amazing you've been throughout this whole process, so I'd like to express my sincere thanks. I'd also like to share my genuine thanks to my sister Margaret; right from the beginning, you were offering words of encouragement and advice. I could not have asked for a more fantastic cheerleader or a more fantastic sister. And finally, I'm very fortunate to have incredibly encouraging parents, John and Josephine. This would not have been possible without their invaluable and unwavering support, so I'd like to offer my final and wholehearted thanks to them.

Acknowledgement of Funding Bodies

This project was funded by Trinity College Dublin through the Provost Project Award, Science Foundation Ireland, and the Royal Society, grant number: URF/RI/191637. I would like to thank these organisations for their support.

During my PhD, I had the privilege of attending several conferences. I'd like to express my gratitude to the following organisations for the awards and scholarships I received from them, which made my attendance at these events possible:

- The European Microscopy Society for awarding me a scholarship to present at the virtual Joint Meeting of Dreiländertagung and Multinational Congress on Microscopy 2020.
- The Royal Microscopical Society for their travel bursaries to attend Microscopy and Microanalysis 2022 and Microscience Microscopy Conference 2023.
- The Trinity Trust and the Microscopy Society of America for their travel grants to attend Microscopy and Microanalysis 2022.
- The Institute of Physics for awarding me the CR Barber Trust Travel Grant to present a poster at the Quantitative Electron Microscopy School 2022 and for partially funding my attendance at the Institute of Physics Spring Meeting 2023.

Statement of Impact of the Covid-19 Pandemic

Due to the COVID-19 lockdown, my research was interrupted due to campus closures, inability to access the facilities in the Advanced Microscopy Laboratory (AML), and inability to complete training in the AML and on campus. I was also impacted by the travel restrictions and delays in shipping essential equipment due to the pandemic. All of these issues meant the subsequent delay in building my photoelectron emitter prototype. While this emitter was fully constructed by the end of my research, some improvements to its design and experiments in relation to characterising its properties were unfortunately not completed due to the aforementioned impact of the pandemic.

Outcomes of Research

Publications

- **Quigley, F.**, Downing, C., McGuinness, C., and Jones, L. (2023). *A Retrofittable Photoelectron Gun for Low Voltage Imaging Applications in the Scanning Electron Microscope.* Microscopy and Microanalysis **29**(5), 1610-1617.
- **Quigley, F.**, McBean, P., O'Donovan, P., Peters, J.P., and Jones, L. (2022). *Cost and Capability Compromises in STEM Instrumentation for Low-Voltage Imaging.* Microscopy and Microanalysis **28**(4), 1437-1443.

Conference Oral Presentations

- **Quigley, F.**, Downing, C., McGuinness, C., and Jones, L. *The Retrofittable Photoelectron Source: Increasing the Functionality of Electron Microscopes.* Institute of Physics Spring Meeting , 11th March 2023.
- **Quigley, F.**, Downing, C., McGuinness, C., and Jones, L. *The Retrofittable Photoelectron Source: A Potential Improvement to Low Voltage SEM Imaging.* 16th Multinational Congress on Microscopy, 8th September 2022.
- **Quigley, F.**, Downing, C., McGuinness, C., and Jones, L. *Retrofitting a Photoelectron Source: Improving Resolution and Functionality.* Microscopy and Microanalysis conference, 4th August 2022.
- **Quigley, F.**, Downing, C., McGuinness, C., and Jones, L. *Building a Sub €2,000 Photoelectron Emitter.* 2nd Joint Symposium MSI and SMS, 7th April 2022.
- **Quigley, F.**, McGuinness, C., and Jones, L. (2021). *The Development of a Low Energy Spread Electron Gun Based on the Photoelectric Effect.* The Society of Electron Microscope Technology Meeting, 8th December 2021.
- **Quigley, F.**, McBean, P., O'Donovan, P. and Jones L. (2021) *The Resolvability of Features at Low Voltage and Low Dose Imaging.* The Joint Meeting of Dreiländertagung and Multinational Congress on Microscopy, 23rd August 2021.
- **Quigley, F.**, McBean, P., O'Donovan, P. and Jones, L. *To Monochromate or not to Monochromate: Balancing Electron Dose and Energy Spread Requirements.* Microscience Microscopy Congress, 7th July 2021.
- **Quigley, F.**, McBean, P., O'Donovan, P. and Jones, L. *Cost and Capability Compromises in (S)TEM Instrumentation for Low-Voltage Imaging.* Atom Workshop XVI, 5th May 2021.

Conference Poster Presentations

- **Quigley, F.**, Downing, C., McGuinness, C., and Jones, L. *Developments in Designing a Retrofittable Photoelectron Source for Low Voltage Electron Microscopy*. Microscience Microscopy Congress 2023, 4th July 2023.
- **Quigley, F.**, Downing, C., McGuinness, C., and Jones, L. *A Retrofittable Photoelectron Emitter: Improving Resolution and Functionality* . Quantitative Electron Microscopy School 2022, 5th May 2022.
- **Quigley, F.**, McBean, P., O'Donovan, P. and Jones, L. *Predicting the Performance of Low Voltage Imaging of 2D Materials*. Microscopy Society of Ireland Symposium, 7th July 2021.

Achievements Resulting from Conference Proceedings

- *Best Flash Talk*, The Microscience Microscopy Congress, Manchester, UK, 2023.
- *The Rosse Medal*, The Institute of Physics Spring Meeting, Armagh, 2023.
- *The Eric Samuel Memorial Scholarship Award*, Microscopy and Microanalysis, Portland, USA, 2022.
- *Runner Up Poster Award*, Microscopy Society Ireland conference, Online, 2021.

Several manuscripts and abstracts resulted from this research. Where this work has been included in this thesis, it has been appropriately cited.

Contents

1. Introduction **1**
1.1. The Electron Microscope 2
1.2. The Resolution of an Electron Microscope 4
1.3. Reducing Chromatic Aberration in Electron Microscopes 9
1.4. A Brief Discussion on the Electron Emitter 13
1.5. Thesis Outline 17

2. Beam Optimisation of an Electron Microscope **20**
2.1. Introduction 20
2.2. Methods of Reducing the Energy-Spread of the Electron Beam . . . 22
2.2.1. Installing a Lower Energy-Spread Electron Gun 22
2.2.2. Utilising Electron Monochromators 26
2.3. Experiment Design 28
2.3.1. The Simulated Data 31
2.3.2. Quantitatively Analysing the Results 32
2.4. Conclusion 34

3. Photoelectron Emission Theory **35**
3.1. Introduction 35
3.2. Choosing an Appropriate Photocathode 36
3.3. Determining a Suitable Light Source 39
3.4. The Theoretical ΔE of the Photoelectron Emitter 43
3.5. How the ΔE Depends on the Crystal Temperature 44
3.6. Conclusion 46

4. Designing the Photoemitter Prototype **48**
4.1. Introduction 48
4.2. Validating the Fundamental Photoemission 49
4.2.1. A Note on Laser Safety Precautions 51
4.2.2. Undertaking a Low-Risk Proof-of-Concept Experiment . . . 51
4.2.3. Evaluating the Experimental Results 54

4.3. The Initial Optical Fibre Wehnelt Prototype 58
4.3.1. Designing the Experimental Setup 58
4.3.2. Electrostatic Study of the Prototype 59
4.3.3. Pre-installation Experimental Design and Results 64
4.4. Conclusion 69

5. The Initial Retrofit of the Photoemitter onto the Electron Gun 70
5.1. Introduction 70
5.2. Installation of the Adapted Wehnelt and Initial Experimental Results 71
5.2.1. Validating Photoemission in the Electron Gun 74
5.3. Optimising the Photoelectron Emitter Setup 75
5.3.1. Design of New Light Injection Apparatus 76
5.3.2. Optimising Wehnelt Bias at Different LaB_6 Temperatures . . 77
5.4. Evaluating the Optimised Emitter 89
5.4.1. Analysing the Photoelectron Current and Laser Power Relationship 89
5.4.2. The Efficiency of the New Light Injection Apparatus 90
5.4.3. SEM Images Captured Using the Optimised Setup 93
5.5. Conclusion 93

6. The Development of a Semi-Permanent Photoemitter Installation 95
6.1. Introduction 95
6.2. The Installation of a More Powerful Laser 96
6.2.1. Running Laser Duty Cycle Experiments 97
6.2.2. Determining the Resolution of the Imaging Modes 104
6.3. The Installation of a New Optical Fibre 105
6.4. Measuring the Characteristics of the Photoelectron Emitter 106
6.4.1. Experimental Theory 107
6.4.2. Experimental Procedure to Measure Brightness and Spot Size 109
6.5. Measuring the Energy Spread of the Photoelectron Emitter 112
6.5.1. Experimental Design 112
6.5.2. Experimental Results 116
6.6. Conclusion 121

7. Future Scope and Conclusion 123
7.1. Introduction 123
7.2. Future Work 124
7.2.1. Improving the Light Injection Setup 124
7.2.2. Improving Vacuum Conditions and an Alternative Photocathode Option 126

7.3. Alternative Applications for the Retrofittable Photoelectron Emitter 127
7.4. Conclusion 128

A. Gaussian Distribution of weights **144**

B. Tableau of Simulated Images **145**

C. Quantum Efficiency Graph **151**

D. Electric Circuit Drawing of the Deconstructed Prototype **152**

E. Additional Experimental Data **153**

F. COMSOL Simulation Graph **154**

Chapter 1.

Introduction

Electron microscopes are highly specialised instruments that act as a powerful tool in a diverse set of research fields. Using fast-moving electrons as illumination instead of light, electron microscopes can generate high-resolution images down to the atomic scale. The two main types of instruments used in electron microscopy are the scanning electron microscope (SEM) and the transmission electron microscope (TEM). The SEM is a versatile piece of equipment that can examine relatively large samples, such as meteorites on the micrometre scale [1], to nanoscale materials, such as nanodots [2]. In this way, the SEM can be a frequently used laboratory apparatus capable of fulfilling multiple functions. A TEM, on the other hand, excels at more specialised atomic resolution imaging. TEMs are often used in various material science and surface science investigations, requiring precise high-resolution imaging and diffraction patterns [3, 4]. Both types of microscopes provide valuable contributions in a range of research areas. This includes quality-controlling devices in the semiconductor industry [5], investigating the surface structures of insects in the biological field [6], or studying fossils in palaeontology [7]. Unfortunately, electron microscopes, like many research-grade equipment, can be very expensive for labs which do not have large grants to support them. This high cost can be extremely exclusionary to lower-income institutions and act as a barrier to the execution of high-quality fundamental research.

Purchasing older models or second-hand microscopes is one solution to mitigate the prohibitive expense of the instruments; this however can limit researchers from performing the cutting-edge techniques of more modern machines. A new technology that could increase an older microscope's functionality and make high-resolution imaging more attainable to lower-income laboratories would be especially desirable. Focusing on the production of a device that could be retrofitted onto a microscope that is already widely in use to increase the resolution of a specific form of imaging would therefore be a valuable goal. This thesis aims to discuss the idea behind

such a technology and examine the feasibility of its installation into an electron microscope.

To provide context to this discussion, this initial chapter will outline the fundamentals of electron microscopes, describing their imaging and spectroscopic capabilities. The energy resolution of both these techniques will then be examined, and an area of imaging which would greatly benefit from improved resolution will be identified. Current solutions to increasing the resolution of this type of imaging will then be discussed. Finally, a summary of what is included in this thesis will be presented.

1.1. The Electron Microscope

An electron microscope's fundamental operation begins with its source of illumination: the electron gun. Many different types of illumination systems are available, the most basic being a thermionic electron emitter. This source produces electrons when a tungsten wire or Lanthanum Hexaboride (LaB_6) crystal is heated. Field Emission Guns (FEGs) are also popular and use an electric field to cause electrons to tunnel from their tip (usually a sharp point of tungsten) into vacuum. The many different illumination systems will be discussed in more detail in chapter 2. Whether created thermionically or via field emission, an acceleration voltage is applied to the emitted electrons which causes them to accelerate towards an anode beneath the source and subsequently pass through a condenser lens [8][9]. In the case of a TEM, the beam then interacts with the sample. Subsequently, it passes through another series of lenses before an image or diffraction pattern of the specimen is recorded on a fluorescent screen or via a digital detector [8]. A simplified schematic is shown on the left side of Figure 1.1.

A SEM's beam, on the other hand, passes through scan coils and an objective lens before reaching the sample. Using the scan coils as electromagnetic deflectors, the electrons are scanned across the surface of the specimen in a rectangular raster. During this process, the electrons interact with the sample, and the backscattered or secondary electrons are subsequently detected by electron detectors. These produce a magnified image of the specimen on a digital screen [9], as shown on the right side of Figure 1.1. In a TEM and SEM the typical acceleration voltage varies from 80kV- 200kV and 2kV-30kV respectively.

Electron microscopes can produce some magnificent high-resolution micrographs, and their functionality is not limited to their imaging capabilities. Spectroscopy also plays a big part in an electron microscope's use in a laboratory. In TEMs, Electron Energy Loss Spectroscopy (EELS) is commonly used in research for de-

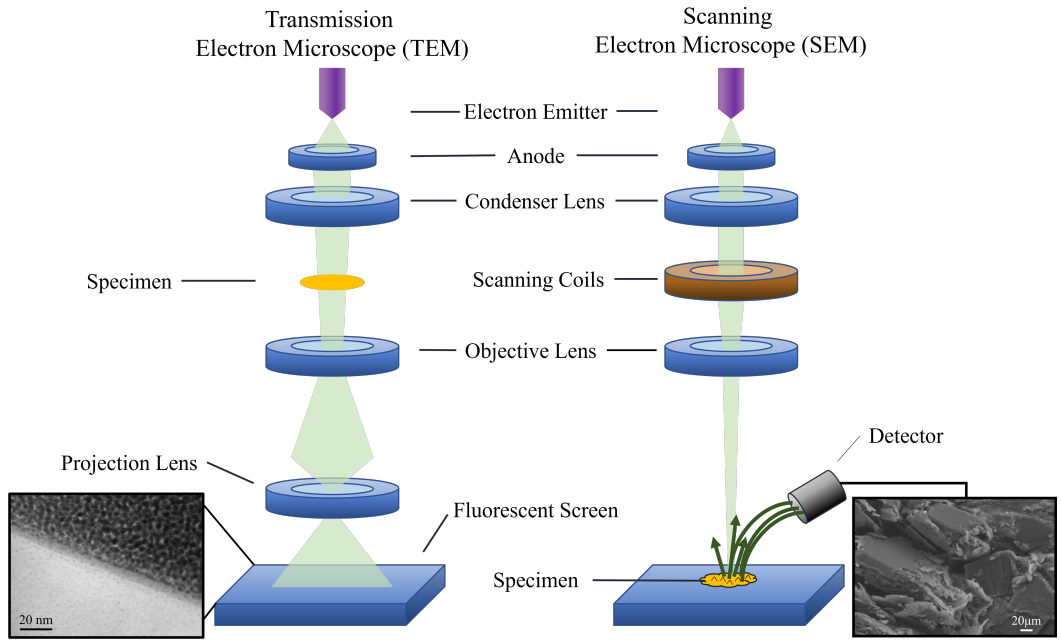

Figure 1.1.: *Simplified schematic of a Transmission Electron Microscope (left) and Scanning Electron Microscope (right) where the main lenses and components of each instrument are specified.*

termining the chemical nature of a sample and investigating the chemical shifts in a specimen when reactions are involved [10]. During EELS, the beam strikes a sample, and some electrons undergo inelastic scattering. The spectra of the energy lost by these electrons are then plotted to determine the chemical properties of the specimen [11]. A Scanning Transmission Electron Microscope (STEM) is a form of a modified TEM whereby a fine electron probe is scanned across the sample to produce an image on a digital screen. This allows STEMs to correlate images and spectroscopic data, making them particularly suitable for an analytical technique like EELS. Transmission Scanning Electron Microscopes (TSEM) are SEMs that detect the electrons after they have been transmitted through the sample through a specialised specimen holder and detector. Recently, miniaturised EELS attachments for TSEMs have been developed, allowing them to also identify elements and gather information about the sample structure [12]. Currently, EELS attachments for TSEMs have a lower resolution than those on TEMs but still provide useful information about the specimen. As low-voltage TEMs push towards ever-decreasing voltages in the coming years, the distinction between STEM and TSEM is expected to blur.

Between high-resolution imaging and the production of rich spectroscopic data, it is clear there are many uses for an electron microscope. With this in mind, understanding the factors limiting the energy resolution of these microscopes is an important endeavour.

1.2. The Resolution of an Electron Microscope

An optical system with perfect lenses is fundamentally constrained by the diffraction limit. This limit can be defined in various ways depending on the criteria employed. For example, the Abbe diffraction limit is often used in light microscopy [13], while the sparrow limit has been applied in astronomy [14]. The Rayleigh criteria is commonly used in electron microscopy and will therefore be used to define the diffraction limit in the following chapter; however, readers should be aware that other definitions exist.

The Rayleigh criteria considers two incoherent point sources being imaged in an optical system with perfect lenses. Due to the lens's finite size, the rays at the outermost collection angle of the lens are diffracted, and the two points are therefore imaged as disks [8]. These disks have an intensity profile shown as P_1 and P_2 in Figure 1.2 a).

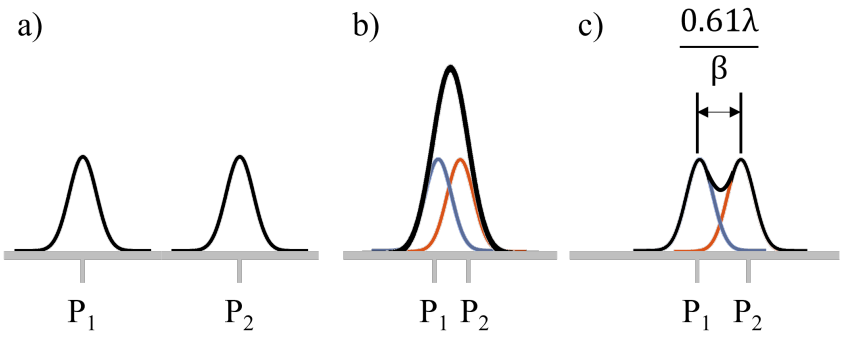

Figure 1.2.: *a) Graphs illustrating the intensity profile of two point sources which can be clearly distinguished. b) Graph illustrating two point sources so close together that their intensity profiles completely overlap, and they cannot be distinguished from one another. c) Graph of the intensity profile of two point sources that meet the Rayleigh criteria and can therefore be distinguished from one another [8]. Please note that this graph was adapted from Williams and Carter 2009 (Reference Number: [8]).*

When these intensity profiles overlap too much, the two point sources can no longer be resolved, as shown in Figure 1.2 b). The Rayleigh criteria states that the two point sources can be resolved if the maximum of one source overlaps with the minimum of the other source and the dip in the centre of the entire intensity profile is below 80 percent of the maximum intensity. The eye (or an appropriate detector) can then distinguish this as two overlapping images and, therefore, interpret that two individual objects are present; this is represented in Figure 1.2 c) [8].

This minimum separation between the two incoherent point sources is known as the diffraction limit and can be defined in terms of the diameter of the Airy disk D_d, where

$$D_d = 0.61\frac{\lambda}{\alpha}, \tag{1.1}$$

λ is the wavelength of the illumination, and α is the beam convergence semi-angle [15]. Electrons can have a wavelength that is 100,000 shorter than that of visible photons. Due to this, electron microscopes can capture images of samples at a far greater resolution than light microscopes.

Electron microscopes may have an advantage in terms of their wavelength over light microscopes, however there is still considerable room for improvement with their lenses. While glass lenses can be ground to arbitrary shapes to yield near-perfect designs, magnetic lenses in electron microscopes are limited by finite field curvature. The leading cause behind their drop in lens quality are aberrations.

Aberrations are a serious issue in degrading the resolution of an electron microscope, with spherical aberration being the most dominant at higher beam voltages. Spherical aberration occurs when an electromagnetic lens brings off-axis electrons to a premature focus on the optical axis, compared with lower-angle rays, as shown in Figure 1.3.

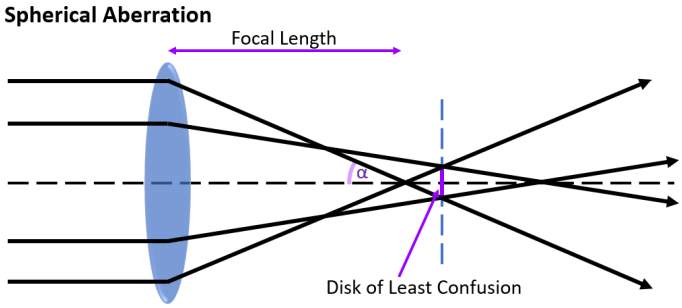

Figure 1.3.: *Simplified ray diagram illustrating spherical aberration of a generic optical element.*

Spherical aberration, C_s, can be defined in terms of the diameter of the spherically aberrated disk of electrons it produces d_{sph} (also known as the disk of least confusion illustrated in Figure 1.3). This is defined by the following equation,

$$d_{sph} = 0.5 C_s \alpha^3 \tag{1.2}$$

where α is the convergence semi-angle. For electron lenses, the spherical aberration coefficient C_s has dimensions of length (typically millimetres) and is approximately

equal to the lens's focal length [16]. In the TEM, Spherical aberration was the dominant aberration until the invention of the spherical aberration correcter in the 1990s [17, 18].

With the ability to correct C_s, chromatic aberration then became the most prominent issue in lens resolution [19]. As shown in Figure 1.4, chromatic aberration occurs when the lower energy electrons (represented by red rays) are focused prematurely on the optic axis compared to higher energy electrons (represented by the blue rays) by the electromagnetic lens [8].

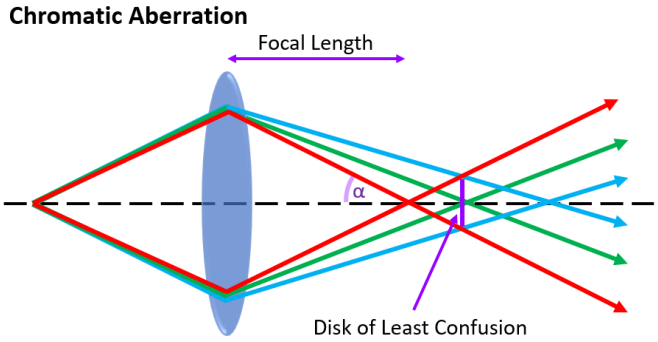

Figure 1.4.: *Simplified ray diagram illustrating chromatic aberration of a generic optical element.*

Chromatic aberration can be defined in terms of the diameter of the blurred disk of electrons it forms d_{chr}:

$$d_{chr} = C_c \frac{\Delta E}{E_o} \alpha, \tag{1.3}$$

where C_c is the chromatic aberration coefficient and E_o and ΔE are the electron beam's primary energy and energy spread, respectively [16].

Each factor determining image resolution depends on the beam semi-angle α. Plotting these contributions to beam diameter as a function of probe semi-angle in Figure 1.5a, we can visualise the resolution limiting factor of the system.

The optimum operating condition for a conventional 200kV JEOL TEM is shown by point A in Figure 1.5a). This figure shows that spherical aberration, represented by the blue line, limits the resolution of a standard system. When a spherical aberration corrector is installed, the blue line in Figure 1.5 a) shifts to the right, and we see from the position of point B in Figure 1.5b) that the red chromatic aberration line then becomes the limiting factor to resolution. Due to the chromatic defocus blur being inversely proportional to the impinging electron's energy, the chromatic aberration becomes even more dominant at lower voltages. Figure 1.5c)

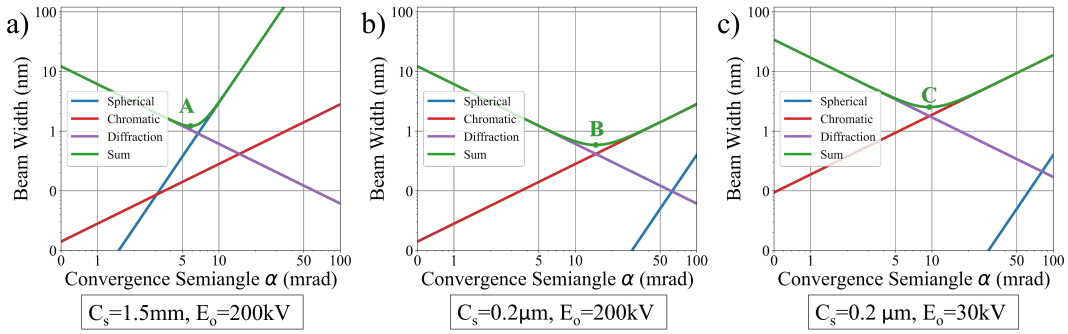

Figure 1.5.: *The contributions to beam size from spherical aberration, chromatic aberration and diffraction as a function of convergence semi-angle. Figure a) and b) are the contributions at 200kV, the typical accelerating voltage of a JEOL TEM, and Figure c) is during low voltage imaging conditions at 30kV. The microscope has a thermionic LaB_6 source with an energy spread of 1.5eV and $C_c = 1.878mm$. Figure a) is that of a standard JEOL microscope, while Figures b) and c) is the same microscope with a spherical aberration corrector installed. These plots indicate the optimum convergence angle. Note that the quadratic green line is the sum in quadrature of equations 1.1, 1.2 and 1.3.*

represents the same spherical aberration corrected TEM as Figure 1.5b) just operated at 30kV. Due to the TEM's lower acceleration voltage in Figure 1.5b), the red chromatic aberration line is shifted upwards between Figure 1.5 b) and c). Interestingly, the 200kV conventional TEM's beam diameter (point A) is smaller than that of the 30kV spherically aberration-corrected TEM (point C). This is because the diffraction limit (described in equation 1.1) is proportional to the wavelength (λ) of the electrons, which is inversely proportional to the acceleration voltage (E) of the microscope as shown in;

$$\lambda = \frac{h}{\sqrt{2m_o eE}}$$

where h, m_o and e are planks constant, the rest mass of an electron and the elementary charge of an electron, respectively. Therefore, by operating the TEM at a lower acceleration voltage in Figure 1.5 c) to Figure 1.5 a), the purple diffraction limit line is shifted upwards, and the beam diameter increases.

From an analysis of Figure 1.5c), we see that an improvement in resolution at low accelerating voltages could be realised if it were possible to decrease the effect of chromatic aberration on the microscope. For completeness's sake, it should also be mentioned that higher-order aberrations such as C_5 exist. Therefore, if chromatic aberration is corrected, these aberrations will become most prominent.

Nevertheless, improving the resolution of images at low voltages would be extremely valuable for many fields. Electrically conducting materials such as graphene, metals

and some semiconductors are easily damaged by beam heating and knock-on damage at high acceleration voltages. Imaging these materials at low voltages greatly reduces radiation damage to the sample [20] and is particularly beneficial in the semiconductor industry[5].

In SEMs, secondary electron signals are generated from a shallower depth during low-voltage imaging as the electron-sample interaction is concentrated near the surface of the specimen. Many researchers exploit this effect to investigate surface features more comprehensively [21]. An example of this can be seen in Figure 1.6 where images of 200$\mathring{A}$ thick carbon film stretched over a copper grid show very different features depending on the acceleration voltages used in the SEM [22]. At 20kV, the 200$\mathring{A}$ thick carbon film is almost invisible; however, as the acceleration voltage is reduced to 1kV, the electron interaction is concentrated near the sample's surface, and the film appears more solid in the SEM image.

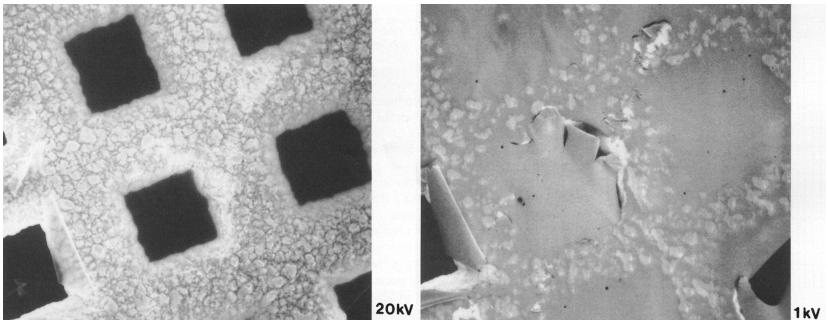

Figure 1.6.: *SEM image of 200Å thick carbon film, stretched over a copper grid, imaged at an acceleration voltage of 20kV and 1kV. Reprinted from Micron, 27, David C. Joy and Carolyn S. Joy, Low voltage scanning electron microscopy, 249, 1996, with permission from Elsevier (Reference number: [22]).*

Sample charging, whereby electrons build up on the surface of an insulated material during imaging, is also a common issue for certain specimens. By choosing a particular low acceleration voltage, a dynamic charge balance can occur, and researchers can potentially observe surface features without this charging effect [22]. Figure 1.7 shows an example of this whereby the hair of a flour beetle sputter-coated with gold was imaged at three increasing acceleration voltages. As the voltage increases, we see charge starting to build on the sample, and details on the hair's surface are subsequently challenging to observe. This dynamic charge balance has also been advantageous in biological laboratories, which have capitalised on it when imaging uncoated soft materials [23].

A wide range of research fields would benefit from improved low-voltage imaging. Therefore, examining the different methods to reduce the effect of chromatic aberration is an important research direction.

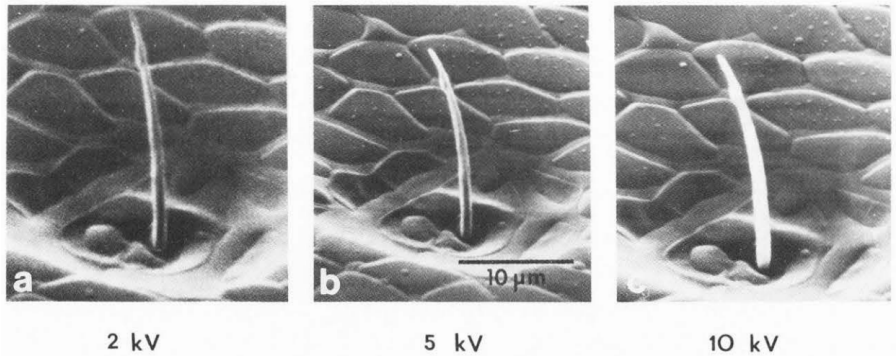

Figure 1.7.: *SEM image of the hair of a flour beetle sputter-coated with gold imaged at three increasing acceleration voltages of a) 2kV, b) 5kV and c) 10kV. Reprinted from Journal of Microscopy, 136, James Pawley, Low voltage scanning electron microscopy, 255, 2011, with permission from John Wiley and Sons. The paper is provided for free and open access by the Western Dairy Center at DigitalCommons@USU (Reference number: [5]).*

1.3. Reducing Chromatic Aberration in Electron Microscopes

There are a variety of ways to decrease the chromatic aberration affecting electron microscopes. Each involves one of the three main variables the chromatic defocus blur depends on: the C_c coefficient, the electron energy spread ΔE and the acceleration voltage of the microscope E_0.

1. Reducing the C_c coefficient

On a fundamental level, minimising the C_c coefficient would appear to be the most obvious solution to decreasing the chromatic defocus blur. This could be achieved by installing a chromatic aberration corrector onto the microscope [24]; however, this is more complex than it may seem. The Sub-Ångström Low Voltage Electron microscopy (SALVE) project group developed one such corrector. Working to produce a dedicated low-voltage TEM, they designed and installed a low-voltage quadrupole-octupole-type C_c/C_s corrector onto their column, as shown in Figure 1.8 [25].

While the TEM equipped with this C_c/C_s corrector has produced images with unprecedented contrast and demonstrated resolution comparable to only 15 times the electron wavelength [25], we see from Figure 1.8 that a great engineering burden is connected to such a feat. The corrector itself is a highly complicated piece of equipment, as shown by its variety of multipoles in Figure 1.8 b), and it should be noted that installing the corrector added 43cm of length and 185kg of extra weight to the column. It is clearly an exceptional piece of technology that can produce

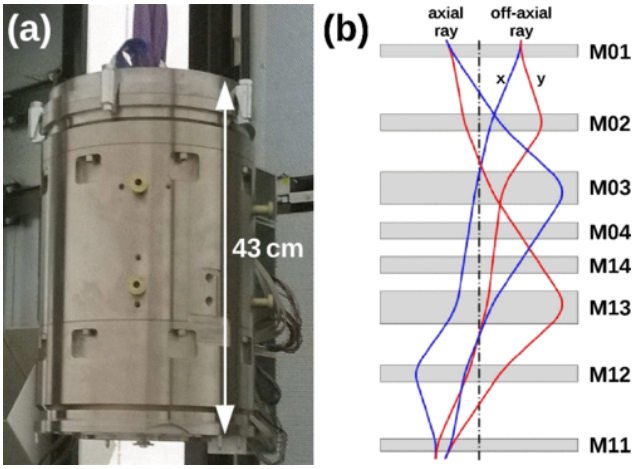

Figure 1.8.: *a) Image of the SALVE group's C_c/C_s aberration corrector installed onto a TEM microscope. It adds 43cm to the microscope and approximately 185kg of weight to the TEM. b) A simplified schematic of the interior of the corrector consisting of eight multipoles. Reprinted Figure 2 with permission from Linck, M., Hartel, P., Uhlemann, S., Kahl, F., Müller, H., Zach, J., Haider, M., Niestadt, M., Bischoff, M., Biskupek, J. and Lee, Z., Physical Review Letters, 117, 076101-2, 2016. Copyright 2016 by the American Physical Society. DOI: 10.1103/PhysRevLett.117.076101 (Reference number: [25]).*

remarkable results. However, it is currently not easily accessible to the standard TEM laboratory, either financially or in relation to having researchers with the expertise to operate and service it. Even regarding SEMs, these C_c correctors are still in a developmental stage and can be extremely expensive for users to purchase and adapt to their microscope [16].

An alternative solution is to reduce the inherent C_c coefficient of the microscope's objective lens itself. The C_s and C_c coefficients increase substantially with the size of the objective lens's pole piece gap [26]. Therefore, choosing a high-resolution pole piece with a small pole piece gap will reduce the effects of aberration on your images. However, a small gap can be limiting, especially if the sample needs to be tilted or necessitates energy dispersive X-ray analysis (EDX). Therefore, the user's requirements must be considered when deciding which sized pole piece gap to purchase during the tendering process. This solution is therefore not a very adaptable one, as once the microscope is purchased and the gap size is chosen, the user does not have the option to change it.

2. Decreasing the electron energy spread ΔE

As the chromatic defocus blur is proportional to electron energy spread (ΔE), reducing the ΔE of the electron source is another route to follow. This is an appealing solution, as reducing energy spread would also increase the sensitivity and resolution of spectroscopic techniques [11]. The smaller the energy spread of the impinging electrons on a specimen, the more precise the energy loss spectra in EELS for de-

termining small chemical shifts in a sample. It would also allow weak signals in the spectra to be more distinct.

Electron monochromators are one solution to decreasing the energy spread of the electrons once they have been emitted from an electron source [27]. They operate by filtering out electrons of a particular energy from the beam while the rest are accelerated in the microscope. In a JEOL TEM with a Schottky FEG electron source, electron monochromators can reduce the energy spread to as low as 0.08eV when the accelerating voltage is 80kV [28]. Figure 1.9 demonstrates the intricate design of this technology, displaying the schematic of an alpha-type monochromator [29]. Due to the complex nature of its operation, this technology is, unfortunately, an expensive solution to the energy spread problem, with the addition of a monochromator to a machine potentially costing the user an extra $\sim$ \$500K for installation [30].

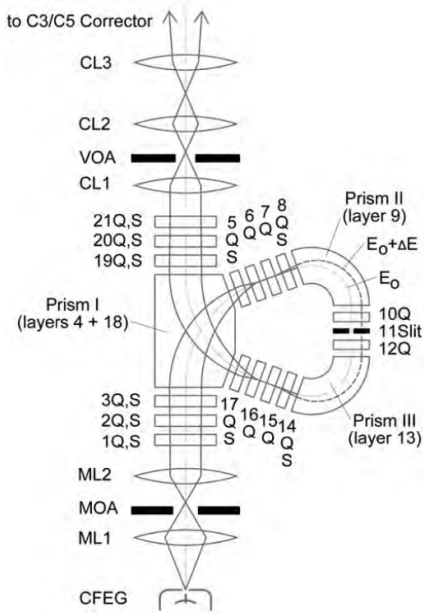

Figure 1.9.: *The cross-section of a monochromator installed in a TEM column. Please note this figure is reprinted from Krivanek, Ondrej L.; Lovejoy, Tracy C., Monochromated STEM with a 30 meV-wide, atom-sized electron probe, Microscopy, 2013, 62, 1, 3-21, by permission of The Japanese Society of Microscopy (Reference number: [29]).*

3. Increasing the acceleration voltage $\mathbf{E}_0$

With chromatic aberration being inversely proportional to the acceleration voltage of the microscope, the higher the voltage, the less of an effect chromatic defocus blur has on the image. In 1968, researchers tried to capitalise on this relationship by building a one-million-volt electron microscope [31]. Only three years later, a three million-volt electron microscope was produced, which spanned four floors and whose complex setup can be seen in Figure 1.10 [32].

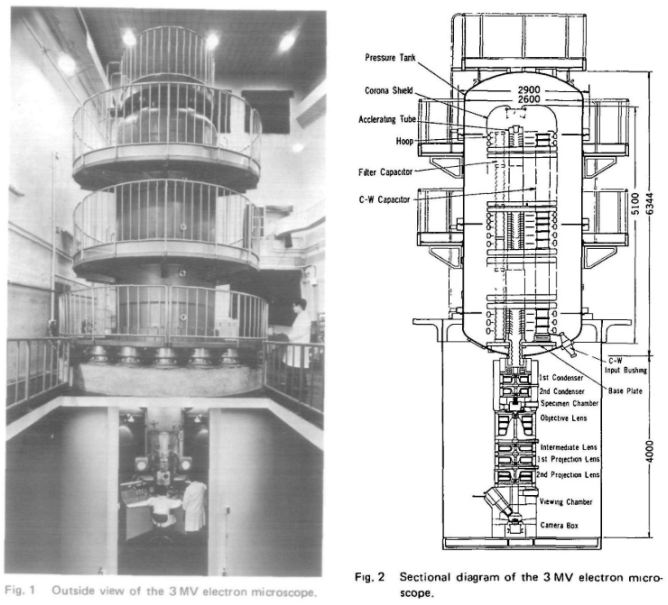

Figure 1.10.: *a) Image of the 3MV electron microscope b) A schematic of the interior of the microscope. Reprinted Figures 1 and 2 with permission from Susumu OZASA, Yasuo Kato, Hideo Todokoro, Shozo Kasai, Shinjiro Katagiri, Hirokazu Kimura, Eiji Sugata, Konosuke Fukai, Hiroshi Fujita, Katsumi Ura, 3 Million Volt Electron Microscope, Journal of Electron Microscopy, 1972, Volume 21, Issue 2, Pages 109–118 by permission of The Japanese Society of Microscopy (Reference number: [32]).*

This microscope is a great engineering feat with a resolving power of 2Å. However, being 11 meters tall and weighing 67 tons comes with some design challenges. Due to the high voltage of the TEM, it naturally requires an extremely thick X-ray shield. A high-voltage stabilising circuit is also necessary, and its construction must be vibration-proof, given its size. While a high-voltage TEM may be one solution to decreasing chromatic aberration, it is certainly not a simple, accessible or cost-effective one. This of course is an extreme case of attempting to reduce the chromatic defocus blur by increasing the acceleration voltage. The regular TEM user can naturally operate their microscope at its max acceleration voltage during standard TEM operation. However, this is not a particularly helpful solution for those wishing to undertake low-voltage imaging.

It seems all three of the main technologies mentioned above involved in reducing the chromatic defocus blur have similar caveats. They all require extremely stable electronics, have quite complicated designs and are all very expensive and not easily accessible solutions to decreasing chromatic aberration.

However, an alternative solution to reducing the electrons' energy spread has yet to be mentioned. It involves going straight to the source and upgrading the electron gun to one with a lower electron energy spread.

1.4. A Brief Discussion on the Electron Emitter

The intrinsic energy spread of emitted electrons fundamentally depends on the emission mode of the source. Figure 1.11 summarises the different mechanisms of electron emission and which electron guns are based on each method.

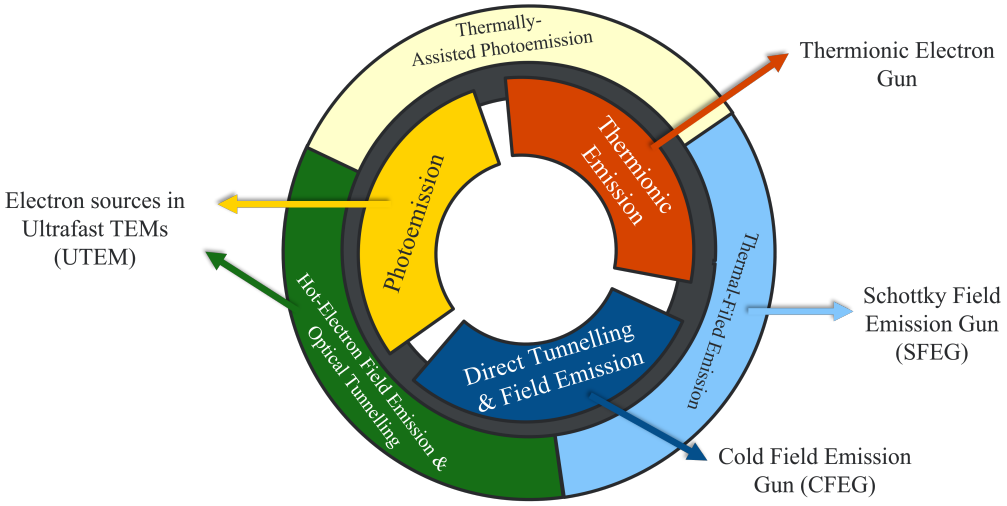

Figure 1.11.: *Centre ring: The three fundamental different types of electron emission. Outer Ring: The electron emission produced from the combination of the different fundamental forms of electron emission. The electron emitters related to the different types of emission are indicated in the illustration.*

Thermionic emitters are the most basic types of electron guns, using thermionic emission to produce electrons which have a large energy-spread relative to other electron sources found in TEMs and SEMs. The cathode's emission can be summarised by Richardson's law, where emission only occurs if the cathodes are restively heated to a sufficiently high temperature such that their electron's energy is greater than the work function of the cathode [10]. The resulting electron's energy spread is relatively large as it is related to the Maxwell-Boltzmann distribution of the temperature of the cathode. Distributions of the energy of particles with two different temperatures are shown in Figure 1.12, and it can be noted that there is not a sharp peak in the distributions but that they contain energy tails. Figure 1.12 shows that a higher temperature can cause the energy distribution of the particles to flatten and broaden. The energy spread of a standard LaB_6 emitter is 1.1eV at a 200kV acceleration voltage in a TEM [33].

Field emission guns (FEGs) produce electrons using the field emission mechanism. As indicated in Figure 1.11, Schottky FEGs operate as thermally assisted field emitters and can produce electrons whose energy spread is as low as 0.7eV. While Cold FEGs, which use direct tunnelling of electrons from a room temperature cathode,

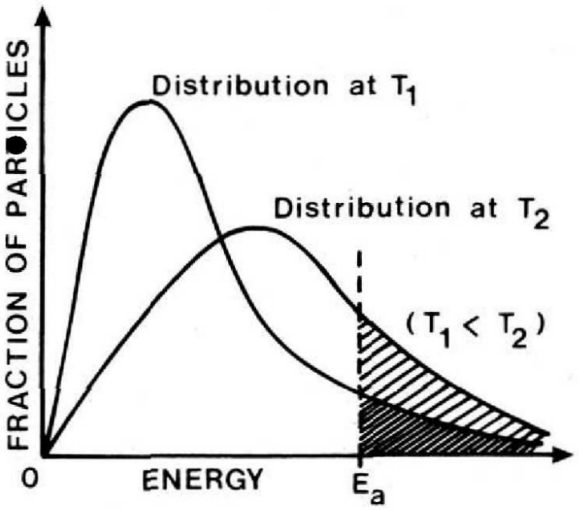

Figure 1.12.: *Maxwell-Boltzmann distribution diagram of the energy of particles at two different temperatures. E_a is the activation energy of the particles. Reprinted with permission from Gavin D. Peckham and Ian J. McNaught. Applications of Maxwell-Boltzmann distribution diagrams. Journal of Chemical Education, 69(7):554, 1992. Copyright 1992 American Chemical Society (Reference number: [34]).*

can have an energy spread as low as 0.3eV [35]. Cold FEGs have the smallest energy spread of all the primary electron sources because they lack the additional thermal spread of the Schottky FEGs and thermionic emitters [36, 37]. These energy spreads result from all emitters having an energy distribution with a tail.

A continuous source which produces electrons via photoemission is currently not commercially available in SEMs and TEMs. This is despite it being a common form of electron emission in electron guns outside of electron microscopy [38]. Photoemission has, however, been introduced as a technique to produce pulsed electron beams in TEMs. Striking a cathode which would otherwise be used for thermionic emission with a pulsed light source is one way this has been achieved [39]. Houdellier et al. is an example from a group combining field emission and photoemission to develop a laser-driven pulsed cold field emission source [40]. In their setup shown in Figure 1.13 a), they have a high-power pulsed laser beam entering their gun vacuum chamber, which is focused on the tip of a tungsten source via a series of mirrors.

The cold field emission gun's voltage is set just below the voltage required for the electrons to tunnel out. When the light strikes the tip, it gives the electrons just enough energy to tunnel out of the tip and be emitted. This allows the group to produce a very precise pulsed electron beam. While an excellent setup for the dynamic imaging required by the group, the initially more spatially confined photoelectron packets produced during imaging causes the energy spread of the beam to broaden due to the Boersch effect. The Boersch effect occurs when coulomb interaction between electrons at the source causes the energy spread of the electrons

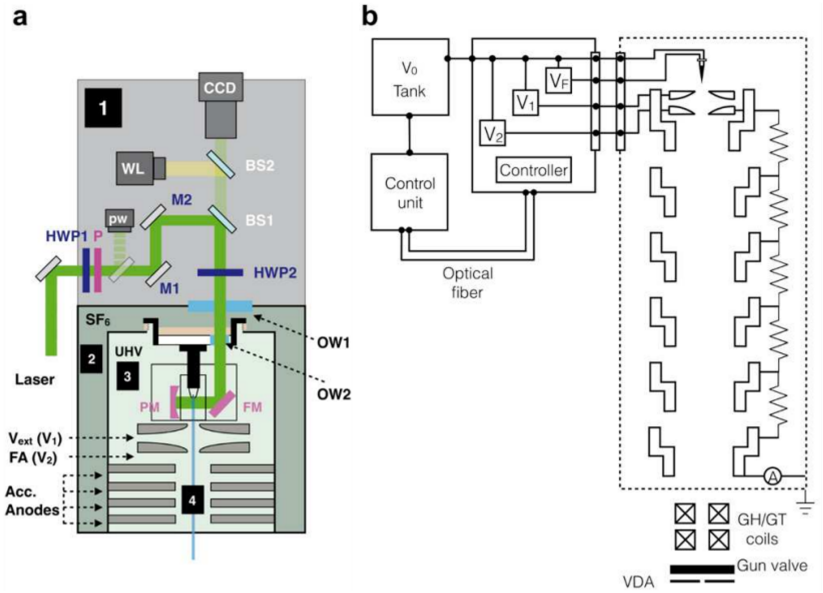

Figure 1.13.: *a) An illustration of the optical head of the ultrafast TEM electron gun. b) The high-voltage configuration of the electron gun. Reprinted from Ultramicroscopy, 186, F. Houdellier, G.M. Caruso, S. Weber, M. Kociak, A. Arbouet, Development of a high brightness ultrafast Transmission Electron Microscope based on a laser-driven cold field emission source, 11, 2018, with permission from Elsevier (Reference number: [40]).*

to broaden and is a particular problem in Ultrafast TEM's [41]. In Figure 1.13 b), the electrical configuration of the electron gun is shown. Due to the high voltages involved, careful safety precautions must be taken when installing and operating such intricate systems. The complexity of these Ultrafast TEMs, whether based on pure photoemission or field-enhanced photoemission, means they are rare to find in the average electron microscope facility.

A literature review of different emitter's and monochromator's energy-spreads was undertaken by the author. Researchers who have spent years working in the field of electron microscopy were contacted, and the approximate cost of the different technologies was gathered through private communication. A visual representation of the literature findings, which emphasises the differential cost between electron gun configurations, can be seen in Figure 1.14, which was created by the author and adapted from [30] to have the addition of a guide to the eye line through it.

In Figure 1.14, the thermionic emitters are listed as W and LaB_6 for tungsten and lanthanum hexaboride sources, respectively. Analysing the graph, we see they are the most cost-effective of all the electron guns due to their very basic and robust designs, yet they do, unfortunately, have the largest energy spreads. Being more complex and requiring stricter pumping conditions makes Schottky FEGs (SFEG)

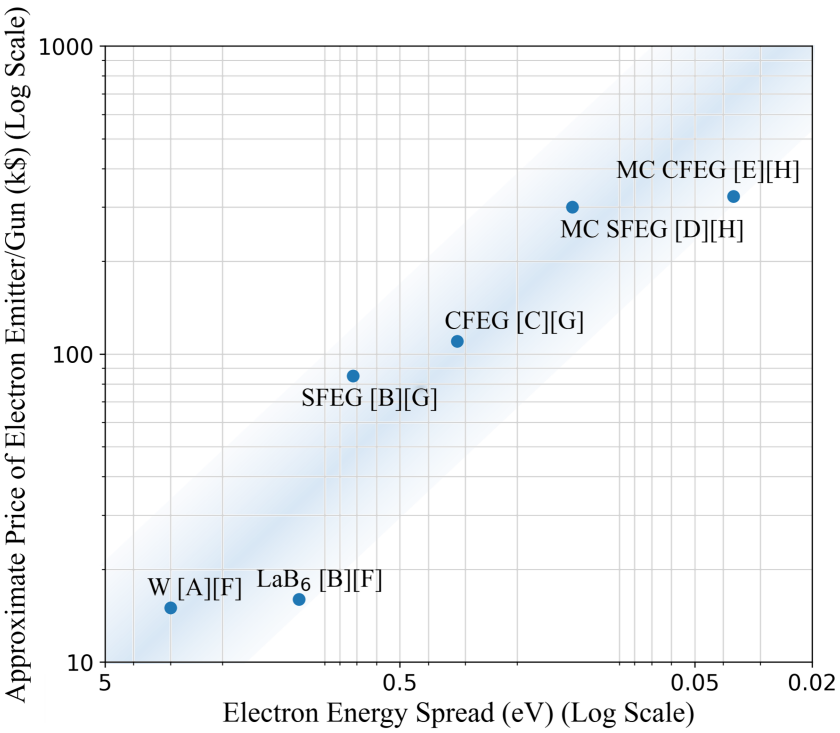

Figure 1.14.: *Comparison of energy spread and cost of electrons gun and monochromator technology. The blue band acts as a guide to the eye of the general trend in the graph. [A] Williams and Carter (2009) (Ref.: [8]), [B] Stoger-Pollach (2010) ((Ref.: [33]), [C] Sawada et al. (2009) (Ref.: [42]), [D] Kisielowski et al. (2008) (Ref.: [28]) and [E] Carpenter et al. (2014) (Ref.: [43]). Pricing data was collected via personal communications: [F] R. Beanland, December 7, 2021; [G] G. Nicotra, November 29, 2021; and [H] D. Muller, November 28, 2021. This graph was created by the author and is adapted from Quigley et al. 2022 (Reference number: [30]).*

and cold FEGS (CFEG) far more expensive than their thermionic counterparts. However, this comes with the advantage of having far lower energy-spread electron beams. Installing a monochromator will of course provide the user with the lowest electron energy-spread, but this makes them the most costly option. From our primary and secondary research, we found that there is a general trend, shown in blue, where the lower the energy spread you require, the more expensive the equipment you need to purchase. Finding a way to deviate from this trend whereby the source has a lower energy-spread at less expense to the user would be highly beneficial.

Enquiries were made into where an Ultrafast TEM would lie in Figure 1.14; however, it was found that it is not possible to separate the cost of adding additional components to a TEM to turn it into an Ultrafast TEM, and it therefore could not be included. It is known that Ultrafast TEMs are generally more costly and tend to have a much higher energy-spread than their standard TEM counterparts due to their additional functionality of dynamic imaging. Because of these reasons, we

could infer that the Ultrafast TEM would lie to the top left of the graph. However, as producing electrons with a low energy-spread is not the purpose of an Ultrafast TEM, it should be considered separate from the general trend shown in blue in Figure 1.14.

Other more niche cold field emission guns have also been created, such as ones that use nanotubes or sharpened LaB_6 tips instead of tungsten as their emitters [44, 45]. These however are currently developmental projects and are therefore not considered in Figure 1.14 with the commercial emitter technology available on the market.

Continuous photoemission is the only mechanism not commercially available to users as an electron source. As mentioned previously, continuous photoelectron sources are not uncommon in fields outside of electron microscopy [38], with different ideas for the design and operation of such emitters being proposed by many research groups [46, 47, 48, 49, 50]. Sawa et al., for example, have conducted preliminary studies with a sizeable, technically complex system which has successfully produced continuous photoelectrons [51]. However, this setup is too large to be installed into the average electron microscope gun chamber. A more compact retrofittable photoelectron source would be an appealing alternative route to follow. Where a retrofittable continuous photoelectron emitter would lie on the cost graph in Figure 1.14 would be of great interest to low-voltage electron microscope users if the energy spread of its electrons happened to be particularly low.

1.5. Thesis Outline

In this chapter the fundamentals of electron microscopes and their energy resolution have been described. It was shown that the resolution of low-voltage images and spectroscopic techniques could benefit from a reduction in the energy spread of the electron beam. It was also identified that the exploitation of photoemission as a continuous electron source has yet to be explored in electron microscopy. The following thesis will examine using a photoelectron emitter in electron microscopes. This will entail determining the properties of its emitted electrons, investigating how to build a prototype of this photoelectron emitter, and assessing where it would lie on the cost graph of Figure 1.14.

To begin, chapter two will detail the different methods of decreasing chromatic aberration and the various electron emitters currently in use. Using the software Prismatic, analyses of images with different C_c coefficients, acceleration voltages and energy spreads will be investigated for a spherical aberration corrected microscope.

These results will provide an interesting discussion on acceptable current levels for electron emitters and act as a guideline for what energy spreads users hope to obtain from their microscopes for high-resolution, low-voltage imaging.

An exploration into photoemission as a mechanism for electron production will then be undertaken in chapter three. This will include describing the fundamentals behind the photoelectric effect, leading to a discussion on suitable photocathode and light source choices for a photoemitter. This will involve analysing the quantum efficiency of the chosen photocathode and using this to advise on the optimum wavelength for the light source.

With the most suitable photocathode and light source selected, chapter four will detail the design of the initial photoemitter prototype. Firstly, an experiment will be outlined where validation of the fundamental photoemission by the chosen light source and photocathode will be described. As EELS would greatly benefit from a low energy-spread electron source, a prototype installed in a TEM would be advantageous. However, for ease of access and practicality, the initial prototype was installed in an easily accessible SEM. Solidworks models of the prototype developed as part of this research will be presented. Furthermore, this geometry was used to build COMSOL simulations of the electrostatics and electron trajectories, and the results will be discussed. Finally, this chapter will describe experiments undertaken on the prototype pre-installation into the SEM.

Chapter five will begin by outlining the installation of our prototype into the SEM. Initial experimental images with the photoelectron source were captured and will be presented. An experiment verifying that the electrons generated by the prototype are photoelectrons will be described. An upgraded light injection setup was installed, and its design will be detailed. Experiments undertaken on the effects of the Wehnelt's bias and the crystal's temperature on the photoelectron beam with this new apparatus will then be described. This will be complemented by COMSOL simulations to understand the results of the biasing experiments further. Based on simulation and experimental analyses, adjustments to the system's electron optics were implemented. After these implementations, an analysis of the relationship between laser power and photoelectron current is then discussed, and the efficiency of the new light injection apparatus is detailed. Finally, images generated by the optimised setup will be demonstrated.

Much information was garnered from the initial installation of the prototype. This included the proposal that a higher-power laser would be a beneficial upgrade to the light injection setup. Chapter 6 will begin by presenting experimental results involving our apparatus with a higher-power laser equipped and describing an in-

vestigation into the resolution of the photoelectron source. A new optical fibre was also installed into the system. The characteristics of the upgraded photoemitter will be compared to other thermionic emitters, and the results will be discussed in detail. Finally, an experiment will be described on how the system's energy spread could be measured.

Our previous experiments highlighted that the photoelectron emitter could benefit from an improvement in its brightness and resolution. Chapter seven will advise on new avenues to achieve this. This includes further upgrades to the light delivery system and examining the vacuum conditions and different methods to minimise crystal contamination. Alternative applications of our photoelectron source will also be discussed. Finally, the results of the thesis will be summarised and concluded, and the current photoelectron emitter prototype will be compared to other electron emitter technologies with respect to energy spread and cost.

Chapter 2.

Beam Optimisation of an Electron Microscope

2.1. Introduction

In the previous chapter, we reviewed the basics of electron microscopy, including how the microscopes operate and what limits their energy resolution. Furthermore, several methods for reducing chromatic aberration and the different mechanisms for electron emission were examined. The benefits of decreasing chromatic aberration for research groups that employ low-voltage imaging were also outlined. It was noted that using the beam at low voltages can enhance analysis when imaging the surface of a sample. Figures 2.1 a) and b) are a perfect example of this effect where we see a sample of carbon nanotubes on gold imaged at 5kV and 0.5kV in a SEM, respectively. The contrast of the nanotubes greatly increases when the voltage is lowered due to the electron interaction originating only from the surface of the specimen.

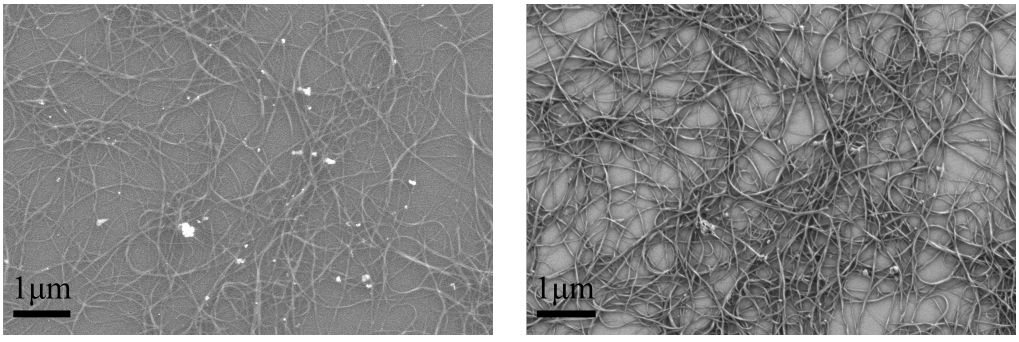

Figure 2.1.: *SEM images of carbon nanotubes on gold imaged using a secondary electron detector where the acceleration voltage was a) 5kV and b) 0.5kV. Images courtesy of Clive Downing.*

On the other hand, Figure 2.2, taken by the author, is a fitting illustration of using low-voltage imaging to reduce the effects of charging on an insulated sample. Figure 2.2 a) shows a build-up of electrons on the pine sample, represented as over-saturated bright spots on the secondary electron detector. By reducing the voltage of the beam to 2kV, this charging can be balanced, and a higher contrast image of the sample can be taken (Figure 2.2 b)). The usable magnification also increases under these conditions.

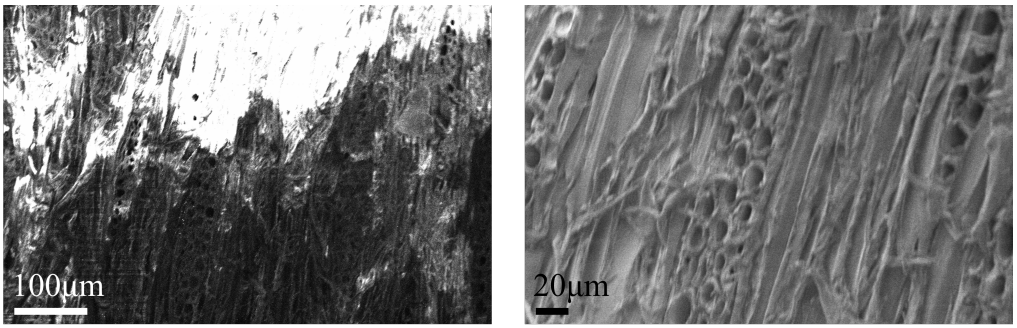

Figure 2.2.: *SEM images of uncoated pine imaged using a secondary electron detector where the acceleration voltage was a) 15kV and b) 2kV. Images taken by the author, sample courtesy of Nadezda Prochukhan.*

The low-dose community is moving towards a situation where there is a focus on getting as much information as possible from every electron. However, chromatic aberration can cause low-voltage images to lose contrast, decreasing the resolution of the technique. It is therefore an inherently beneficial research direction to attempt to lower electron energy spread and decrease the chromatic defocus blur. This would allow the user to use less current and produce sharper, higher-resolution images. This has previously been achieved by optimising the electron beam either by upgrading the electron source of the microscope or installing an electron monochromator.

The following chapter assesses the optimisation of a microscope's beam when the energy-spread of the impinging electrons are reduced. This involves examining the range of energy-spreads and currents that can be produced from the various types of electron emission at different levels of beam monochromation. This includes comprehensively discussing the array of electron emitters and monochromator technology. The software Prismatic, which can create fast simulations of STEM (Scanning Transmission Electron Microscope) images, which will be described in more detail in later sections, is used in this discussion. It generates images with different energy-spread and current conditions for a spherically aberration corrected microscope with a fixed lens C_c coefficient. Analysing the signal-to-noise ratio of these

simulations advises on how the image is affected by chromatic aberration at different energy spreads due to various levels of beam monochromation. These results act as a helpful guide as to what ranges of energy-spreads and corresponding currents can be obtained from existing electron guns and monochromator technologies for low-voltage researchers.

Please note that the simulations to be described are from the paper 'Quigley, F., McBean, P., O'Donovan, P., Peters, J. J. P. and Jones, L. (2022). "Cost and Capability Compromises in STEM Instrumentation for Low-Voltage Imaging." Microscopy and Microanalysis, 28(4), 1437-1443.'Patrick McBean performed the simulations, while Patrick McBean, the author and Lewys Jones undertook the analyses of the simulations. The majority of the manuscript was composed by the author, with excerpts composed by Patrick McBean and reviews of manuscript drafts undertaken by Patrick McBean and Lewys Jones. Sections of this chapter have been previously published in this paper.

2.2. Methods of Reducing the Energy-Spread of the Electron Beam

2.2.1. Installing a Lower Energy-Spread Electron Gun

Each electron emitter has its strengths and weaknesses. Therefore, a review of their advantages and disadvantages must be discussed to provide a complete insight into what an upgrade to a lower energy-spread electron source may entail. It is natural to start this examination with the electron gun found in the first-ever generation of electron microscopes: the thermionic emitter.

A thermionic electron gun has the largest energy spread of all the electron sources. The microscope operator applies a resistive current through its cathode which is either a tungsten filament or a crystal of Lanthanum Hexaboride (LaB_6) shown in Figure 2.3a). This current causes the cathode to heat up and thermionically emit electrons. These electrons are then accelerated via a potential gradient created by a positive anode below them. The cathode is usually held within a metal fixture called a Wehnelt. This Wehnelt has a negative bias applied to it, which can be altered such that only electrons from the very tip of the cathode are accelerated down the column.

The energy spread of an electron gun can be measured from the Zero Loss Peak (ZLP) of an EELS spectrum. The ZLP is the distribution of electrons measured by the spectrometer, which has not lost any energy travelling through the instrument.

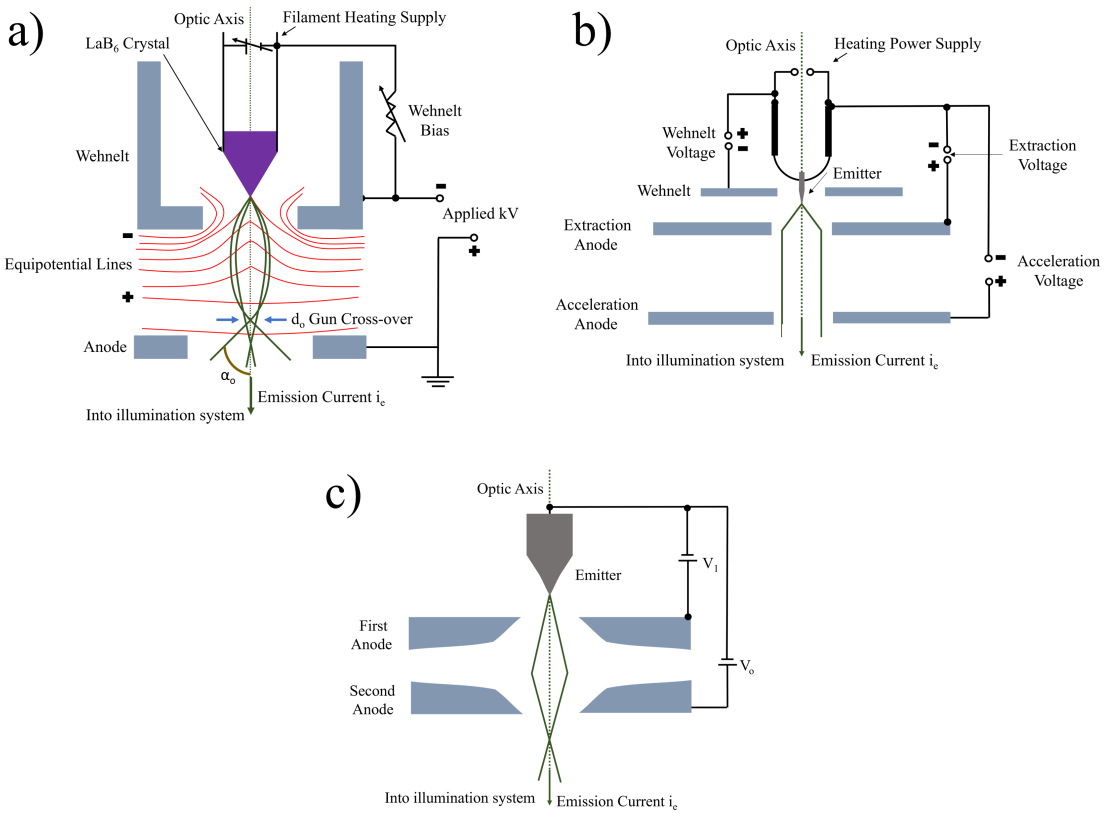

Figure 2.3.: *Schematic showing the principle components and power supplies of a a) LaB_6 thermionic emitter, b) Schottky FEG and c) cold FEG. Please note a) and c) were adapted from [8] and b) was adapted from [52].*

Therefore, this peak represents the energy distribution of the electrons emitted from the electron source, and the shape of the distribution depends on the electron emitter used. As a result, this distribution's full-width half maximum can be considered the energy spread of the electrons emitted from the source. A thermionic LaB_6 electron beam's ZLP can be seen in Figure 2.4 a) and is correlated to the high energy tail of the Fermi-Dirac distribution [48]. The Fermi Dirac distribution f(E) is represented by the following equation

$$f(E) = \frac{1}{e^{(E-E_f)/kT} + 1},$$

where E is the particle's energy, k is the Stefan-Boltzmann constant, E_f and T are the Fermi energy and temperature of the sample, respectively. As a consequence of this, its energy spread depends on the cathode's temperature. The higher the temperature of the cathode, the higher the energy spread; however, the higher the current of electrons produced. Therefore, thermionic emitters are ideal sources for applications requiring a high electron current, such as in specific electron beam

lithography experiments or energy dispersive X-ray analysis (EDX) mapping [53]. However, for applications which require a low energy-spread source, a field emitter gun (FEG) may be a required upgrade.

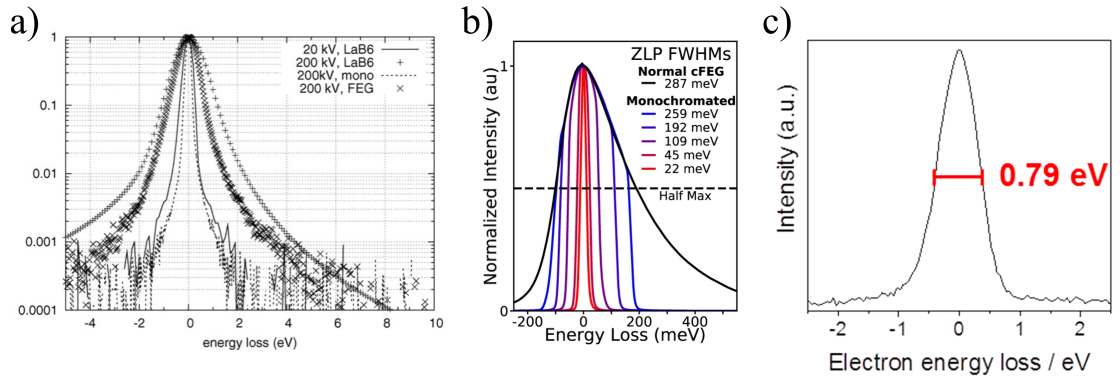

Figure 2.4.: *a) ZLP graph of a LaB_6-TECNAI microscope at an acceleration voltage of 20kV and 200kV. It also includes the ZLP of a monochromated and unmonochromated Schottky FEG in a FEG-TECNAI at 200kV. Note that the maxima of the ZLPs are normalised to one to aid with the comparison between the graphs [33]. b) ZLP of an unmonochromated cold FEG (black) and the same gun monochromated to several different levels in a 60kV aberration-corrected high energy resolution monochromated EELS-STEM [54]. c) ZLP of an ultrafast TEM EELS spectrum in photoelectron mode where the laser is at a low intensity [39]. Please note a) is reprinted from Micron, 41, M. Stöger-Pollach, Low voltage TEM: Influences on electron energy loss spectrometry experiments, 8, 2010, with permission from Elsevier [33]. b) Is reprinted from Hachtel et al.'s paper [54] and c) is reprinted from Ultramicroscopy, 171, K. Bücker, M. Picher, O. Crégut, T. LaGrange, B.W. Reed, S.T. Park, D.J. Masiel, F. Banhart, Electron beam dynamics in an ultrafast transmission electron microscope with Wehnelt electrode, 11, 2016, with permission from Elsevier [39].*

Schottky field emitters operate similarly to thermionic sources, as shown in Figure 2.3 b). They are constructed from a thin piece of tungsten wire, heated up resistively slightly below the temperature at which electrons would be emitted. They employ the Schottky effect, where an electric field is applied to them, which lowers the work function of the tungsten and allows electrons from a specific energy range to be emitted from the material. This effect produces a much more coherent source than a simple thermionic emitter, drastically reducing its energy spread to approximately 0.7eV [8]. This can be seen in Figure 2.4 a), whereby we note the FWHM of the Schottky FEG ZLP at 200kV is smaller than that of the LaB_6 electron gun at the same acceleration voltage. This quite infallible emitter is commonly used in TEMs and SEMs for its stability, low energy-spread and high current beam. Please note the acceleration voltages found in Figure 2.4 are higher than those mentioned in Figures 2.1 and 2.2 because Figure 2.4 is referring to electron guns in a TEM or STEM while Figures 2.1 and 2.2 are SEM images. As mentioned in chapter one TEM's and STEM's operate at higher acceleration voltages than SEM's.

For completeness' sake, Ultrafast TEMs (UTEM) can also be reviewed in this discussion. UTEMs fundamentally can be considered as producing a pulsed electron beam via photoemission. Determining the energy spread of this beam is not so straightforward as it inherently depends on the operation mode of the system. When the stimulating laser is operated at a low intensity, the energy spread will be close to the photon energy minus the work function of the cathode, such as that shown by the ZLP in Figure 2.4 c). However, as the laser intensity and frequency of the pulses get larger, the electron energy-spread can increase due to space charge and Boersch effects [55]. As mentioned in chapter one, the aim of UTEMs is not to produce low energy-spread electrons but rather to create a pulsed electron beam to examine dynamic phenomena at the nanoscale [39]. Therefore, while they are excellent for their intended use, they are not currently a viable option when wishing to upgrade to a lower energy-spread electron gun. A cold field emission source is, however, a potential contender.

Cold FEGs operate slightly differently from the three emitters mentioned above. Figure 2.3 c) shows an extremely sharp piece of tungsten wire with only a few atoms at its tip. An electric field is applied to it, which causes electrons to tunnel from the tip. This produces a highly coherent low energy-spread electron beam as all the electrons originate from a virtual point behind the tip. This results in the lowest energy-spread source of all the electron emitters. This is demonstrated in the ZLP in Figure 2.4 b), where we note its FWHM is over half as small as that of the Schottky FEG in Figure 2.4 a).

Unfortunately, this low energy-spread does come at the cost of electron current and stability. Firstly, cold FEGS operate at room temperature and, therefore, can be contaminated after several hours due to the adsorption of residual gases found in the TEM chamber to the tungsten tip. This adsorption can occur even in an Ultra High Vacuum (UHV) chamber. This contamination (which will be discussed in more detail in Chapter 3 section 3.5) gradually reduces the beam's current throughout the day and increases the energy spread of the gun. The tip must be heated up to clean off contamination (also known as flashing the tip). Flashing must be undertaken daily, if not more frequently, depending on the electron beam current required by the user. For example, a researcher hoping to undertake Energy-dispersive X-ray spectroscopy (EDS or EDX) might need to flash the tip before each session to get the current required for this analytical technique. Unfortunately, this flashing can also slightly reduce the beam's stability. The source itself must also be operated in UHV vacuum conditions with very stable power supplies. All of these factors increase the cost of the gun to the user [56], which often needs to be accounted for if a laboratory is considering upgrading its electron gun when purchasing a new

microscope.

2.2.2. Utilising Electron Monochromators

The primary method that can be used to decrease the energy-spread of electrons once they have been emitted is using an electron monochromator [27]. Monochromators are an expensive but effective solution to the energy-spread problem of impinging electrons. They usually involve using small magnetic prisms and an energy-selecting slit, as shown in Figure 2.5.

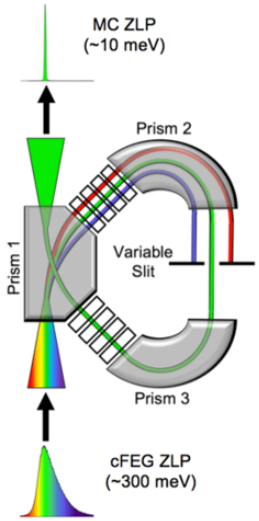

Figure 2.5.: *Schematic of an electron monochromator performing the monochromation of an electron beam between the electron gun and the condenser lenses. This graph was reproduced from Hachtel et al. 2018 (Reference Number: [54]).*

Figure 2.5 shows that the prisms cause electrons of different energies to disperse in the beam. The variable slit then selects electrons with a specific energy, thereby reducing the overall energy-spread of the beam. To highlight how this would affect the microscope's resolution, Figure 2.6 a) and b) were plotted, which compares a spherical aberration corrected JEOL microscope operated at 80 kV with and without a monochromator attached, respectively.

With the monochromator installed, the red chromatic aberration line shifts downwards between Figure 2.6 a) and b), which causes the beam width to decrease. In summary, the reduction in energy-spread by the monochromator significantly reduces the contribution of chromatic aberration, allowing the user to image at a higher resolution.

Regarding resolution, a low current means a decrease in the signal-to-noise ratio in the images produced. This is a result of Poisson noise, which refers to the statistical variation of the number of electrons detected in an electron microscope. This noise

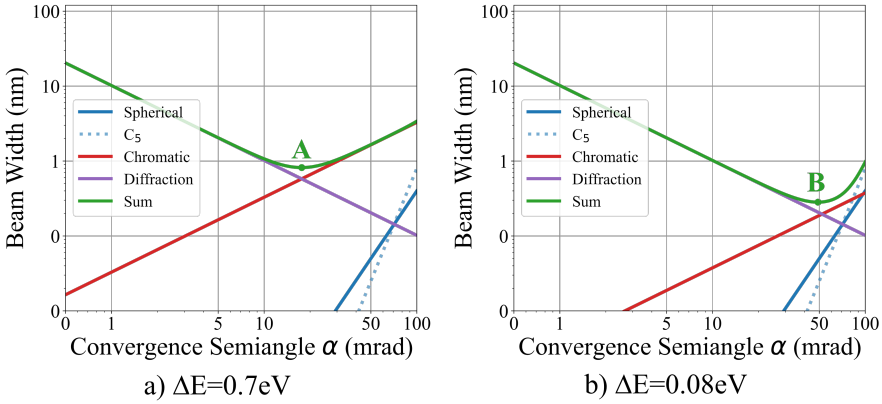

Figure 2.6.: *Graphs of the range of beam diameters due to spherical aberration, fifth-order spherical aberration (C_5), chromatic aberration and the diffraction limit at 80keV in a JEOL microscope with $C_s = 0.2\mu m$ and $C_c = 1.878mm$. Figures a) and b) simulate a JEOL with a Schottky FEG as the electron source; however, b) is a microscope with a monochromator installed.*

can dominate when imaging with low electron beam currents, leading to a loss of resolution. For a complete picture of how the image's resolution is limited, the electron beam current must also be considered. Figure 2.4 a) and b) show the ZLPs of a monochromated Schottky and Cold FEG, respectively. The beam current can be calculated as the area under their ZLPs. From the reduction of the FWHMs of the ZLPs, we see that after the monochromation of the emitted beams, the tails of the ZLPs were reduced, causing the energy spread of the impinging electrons to be decreased. Unfortunately, this in turn decreases the integral of the ZLP, which indicates a reduction in total beam current and, consequently, a loss of resolution.

To explore how this reduction in current and energy-spread via monochromation can affect experimental images, we refer to Figure 2.7 from Hachtel et al.'s paper [54] below. We see from Figure 2.7 that the image of silicon produced with the max amount of monochromation (Figure 2.7d)) does not necessarily correlate to the highest resolution image, which in this case appears to be Figure 2.7 c). This is evidence that current and energy-spread must be balanced to produce the highest-resolution image.

Based on these observations, it is a more meaningful metric to consider an image's signal-to-noise ratio as the beam is attenuated and locate where the optimal beam conditions occur at different levels of monochromation and utilising a range of electron guns. To achieve this, a series of simulations of gold nanoparticles imaged at different conditions were performed.

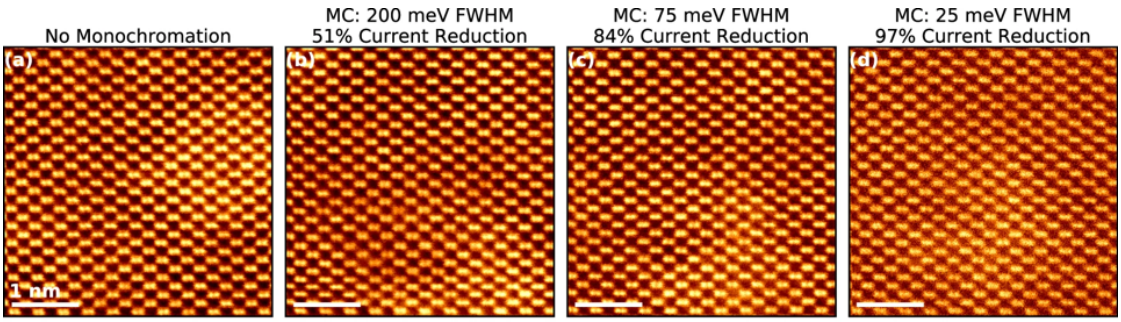

Figure 2.7.: *Images of Silicon < 110 > zone axis taken at various levels of monochromation using high angle annular dark field STEM at a 60kV acceleration voltage. Please note that this graph was reproduced from Hachtel et al. 2018 (Reference Number: [54]).*

2.3. Experiment Design

The following STEM image simulations were performed using the PRISM algorithm implemented in the Prismatic 2.0 package [57], an open-source GPU-accelerated STEM simulation software. Prismatic is based on the multislice approach, which divides the sample into several thin slices alternating between transmission and propagation steps. These simulations involved modelling a Schottky and cold FEG in a spherically aberration corrected STEM producing Annular Dark Field (ADF) images of Au nanoparticles. ADF imaging involves collecting the scattered electrons from an annulus around the beam using an ADF detector. The nature of this type of imaging allows EELS to be performed simultaneously with the main beam, therefore, the energy-spread of the electrons can be recorded alongside each image produced. The ADF image simulations were performed at various acceleration voltages, C_c coefficients, and levels of beam monochromation. Various values for properties used in the simulations are shown in Table 2.1.

Detector angle range	**Probe semi-angle of aperture**	**Pixel dwell time**	**Exposure time of each image**	**Schottky FEG energy spread**	**Cold FEG energy spread**
40–150 mrad	28 mrad	40 μs [58]	8.35 s	0.65 eV [59]	0.287 eV [54]

Table 2.1.: *Various values for properties used in the Prismatic simulations.*

Across the simulations, the appropriate electron wavelength was used, corresponding to each acceleration voltage. As the scattering cross section also depends on wavelength, the simulations necessarily reflect changes in scattering with voltage. The simulation was averaged across 10 frozen phonons to account for thermal diffuse scattering. Using post-processing techniques, chromatic aberration, finite source size, and Poisson noise were included in the simulated images. The chromatic aberration can be approximated by taking a weighted average of a spread of defocused images [60], while the defocus values and weightings were chosen from a Gaussian

distribution (see Appendix A). Previously, Prismatic assumed a point source for electron emission at the gun, but a source-size contribution was added in this work. A mixed Gaussian-Cauchy distribution has been shown to describe source effects accurately [61]. However, as the trends across the data are of primary interest, a purely Gaussian distribution was chosen for simplicity, where the source size (after demagnification) determines the FWHM of the Gaussian distribution. The source size for a Schottky FEG is lifetime dependent [62], and a mid-range estimate of 80 pm was chosen from literature [62, 63, 64, 65]. For the cold FEG, a mid-range estimate of 40 pm was chosen [66, 67, 68]. This source size contribution is added to the ADF image as a 2D convolution post-processing step. It also should be noted that changing monochromator dispersion has some effect on effective source size; however, there is insufficient data on this in the literature, so it was not modelled here. Finally, Poisson noise was added after scaling the relative dose by 1.5x in the case of the cold FEG due to its higher brightness [8, 69].

The beam current reduction of the two electron emitters from various levels of monochromation was determined from the EELS ZLP of the Schottky and cold FEG in Figure 3 of [59] and Figure 2a of [54], respectively. The remaining beam current for both FEGs with increasing levels of monochromation was calculated by integrating the graph at their respective FWHM of various energy-spreads (see Figure 2.8). These values were then used in the following image simulations.

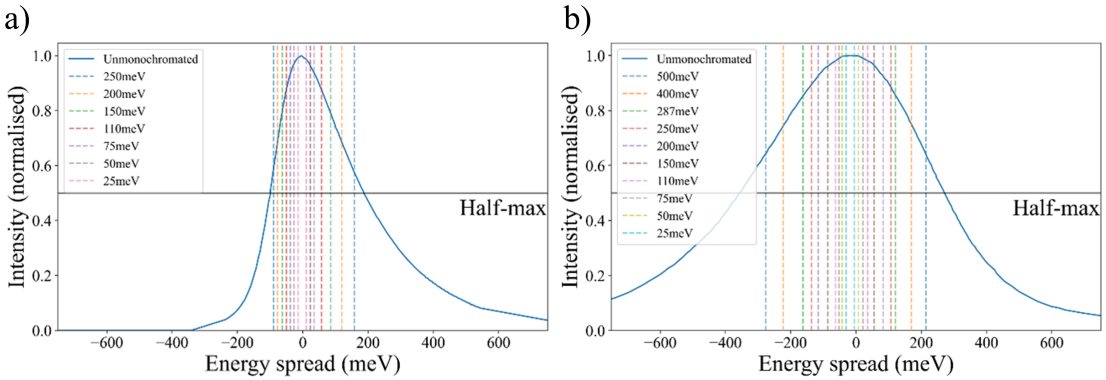

Figure 2.8.: *a), b) ZLP of an unmonochromated (solid blue) cold FEG and Schottky FEG, respectively, data taken from [54] and [59] respectively. The dashed lines in each graph indicate the positions at which the curve of the ZLP is cut off due to various levels of monochromation. Image reprinted from the supplemental information of Quigley et al. 2022 (Reference Number: [30]).*

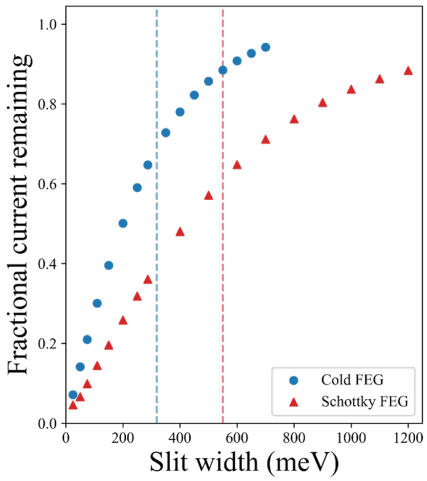

Figure 2.9.: *The fractional current remaining after monochromation versus the slit width at the various levels of monochromation. This relative current was utilised for the simulations to determine the dose for Poisson noise. The dashed lines indicate the maximum 500 meV (red) and 250 meV (blue) monochromation for the Schottky FEG and cold FEG, respectively. Image reprinted from the supplemental information of Quigley et al. 2022 (Reference Number: [30]).*

After the remaining area was integrated, it was then compared to the total area to determine the fractional reduction in current, shown in Figure 2.9. These have been extended beyond the maximum 500 meV and 250 meV monochromation for the Schottky FEG and cold FEG indicated by red and blue dashed lines, respectively, to display the full trend. For a given dwell time, the fractional reduction in current equals the fractional reduction in dose.

Metallic nanoparticles are susceptible to knock-on damage [70], whose effects can be reduced by imaging at lower acceleration voltages. This makes them a relevant candidate for optimising STEM performance at lower voltages. The simulations showed a gold nanoparticle on a carbon support imaged at three different acceleration voltages (E = 15, 30, and 60 keV). These acceleration voltages were arbitrarily chosen to span a wide range of low-voltage imaging conditions. Here, only a C_s-corrected STEM was considered where the C_s coefficient was fully corrected (0 mm). The simulations for the Schottky FEG were evaluated for eleven different electron energy-spreads spanning the range from severe monochromation to its usual electron energy-spread (ΔE = 25, 50, 75, 110, 150, 200, 250, 287, 400, 500, and 650 meV), while the cold FEG was only evaluated for eight different energy-spreads (ΔE = 25, 50, 75, 110, 150, 200, 250, and 287 meV) as it had an initial lower energy-spread of 287 meV.

These simulations were also run for four different objective lenses (OL) C_c coefficients to represent a variety of OLs available during tendering [C_c= 1.1, 1.8, and 3.0

mm [71]] as well as, for comparison, a STEM with a chromatic aberration corrector installed (C_c= 0 mm) (see Appendix B Figures B.1 - B.6). As this is a simulation study, sample damage and scan distortion effects [72, 73] are omitted, so the images produced only show a best-case scenario. However, as this is consistent across all the data sets investigated, it is still a fair comparison between all the simulations. To calculate the SNR of the simulated images, the final image (with all effects included) and the ground truth image (i.e. the zero defocus plane image, with source size applied) are both mean-subtracted to examine only the undulations in the signal which produce the visual contrast. The ground truth was then subtracted from the final image to give just the noise. The SNR could then be calculated using the following equation;

$$SNR = \frac{RMS(signal - mean(signal))}{RMS(noise - mean(noise))},$$

where RMS is the root mean square. The signal is defined as the ground truth image which is the image simulated at the zero defocus plane which has source size applied to it but not the effects of Poisson noise or chromatic defocus blur. The noise is defined as the difference once the signal is subtracted from the image inclusive of dose and chromatic effects. As SNR was chosen as a proxy for resolvability, noise and chromatic blur are both together considered to be deleterious behaviours. These SNRs were plotted to determine the optimum energy-spread for a STEM with either a Schottky or cold FEG based on its C_c coefficient and the acceleration voltage.

2.3.1. The Simulated Data

A sample of the images of the Au nanoparticles simulated under different conditions can be seen in Figure 2.10, and a whole tableau of all the simulated images can be found in Appendix B. Figure 2.10 a) are nanoparticles imaged at a 60keV acceleration voltage with the energy-spread of a monochromated Cold FEG and Figure 2.10 b) are imaged at a 30kV acceleration voltage with the energy-spread of a monochromated Schottky FEG.

The top row in Figure 2.10 a) and b) can be viewed as having a chromatic aberration corrector installed in the microscope as numerically, this is equivalent to reducing the chromatic aberration coefficient to near zero. At the same time, the other rows are indicative of pole pieces with increasingly larger gaps with subsequently increasingly larger C_c coefficients. Inspecting the different rows in Figure 2.10 a)

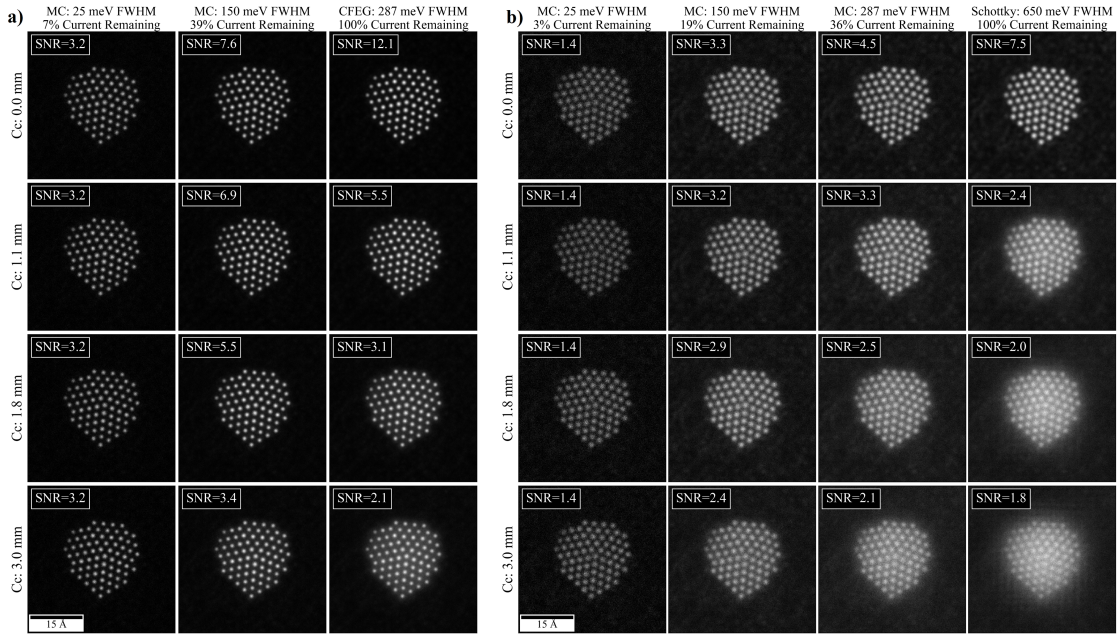

Figure 2.10.: *Images of Au nanoparticles simulated in a $C_s$corrected STEM at a) an acceleration voltage of 60keV with a cold FEG and b) an acceleration voltage of 30keV with a Schottky FEG. a) and b) are at various levels of monochromation. The energy-spread and current remaining after monochromation for each image are indicated above each column. Each image's C_c coefficients are indicated on the left of each row. The scale bar is 15 Å. Image reprinted from Quigley et al. 2022 (Reference Number: [30]).*

and b), it can be noted that as the chromatic aberration coefficient decreases, the image's resolution increases. This can be attributed to a decrease in the effect of chromatic aberration.

The columns in Figure 2.10a) and b) indicate the energy-spread of the emitted electron beam and the percentage of current remaining after monochromation. Figure 2.10 a) and b) shows that the lowest resolution image has the largest energy-spread and C_c coefficient in the bottom right-hand square. Naively, it would also be logical to assume that the highest resolution image would be the one taken with the lowest C_c coefficient and energy-spread in the top left-hand corner of the tableau. However, the SNR of this image is less than that of slightly higher energy-spread images. This is due to an increase in Poison noise at this level of current reduction. This indicates that analysing the SNR of each simulated image could tell where the balance between energy-spread and current reduction needs to be struck.

2.3.2. Quantitatively Analysing the Results

In order to quantitatively analyse the tableau of simulated images, Figure 2.11 was plotted. These graphs plot the SNR of the different tableau images versus their

energy-spread.

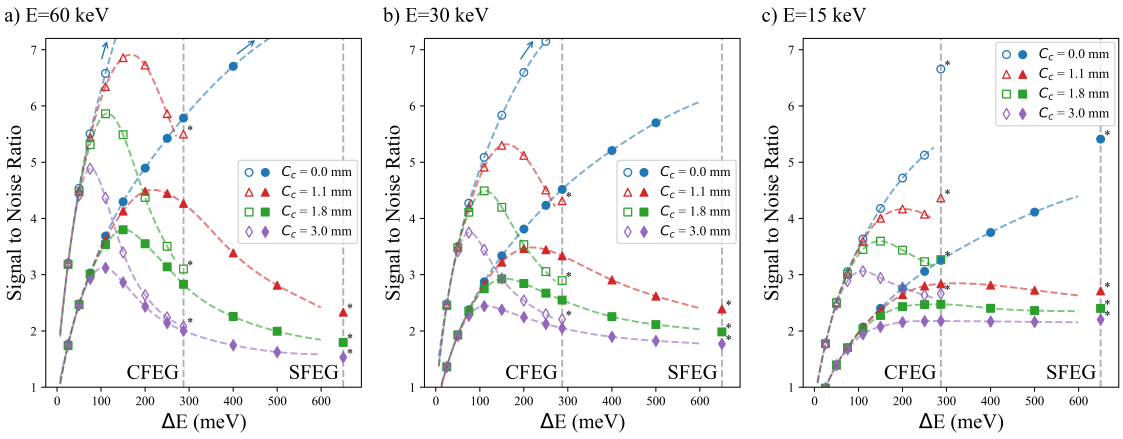

Figure 2.11.: *SNR versus energy-spread for images simulated at an acceleration voltage of a) 60keV, b) 30keV and c) 15keV, respectively. The unfilled-in markers represent the cold FEG data points, while the filled-in markers represent the Schottky FEG data points. The data points marked with an asterisk are unmonochromated. Image reprinted from Quigley et al. 2022 (Reference Number: [30]).*

Figure 2.11 a) shows the SNR of a monochromated cold FEG and Schottky FEG for different C_c Coefficients at an acceleration voltage of 60keV. Looking first at the monochromated Schottky FEG, indicated by the filled markers on the graph, we see a general trend occurring as the energy-spread is reduced. At high energy-spreads, the SNR is low; as the energy-spread decreases, the SNR increases due to the decreasing effects of chromatic aberration. After a peak in SNR at a certain energy-spread, this SNR then starts to decline sharply due to a reduction in current, causing an increase in Poisson noise. Therefore, this peak in SNR is the optimum current and energy-spread to operate the microscope at a particular pole piece gap.

The exception to this trend in Figure 2.11 a) is that of the images with a C_c coefficient of 0, representing the simulation of a chromatic aberration corrector installed in the microscope. As is expected, we see that the SNR of the images simulated with lower C_c coefficients are higher. However, those simulated with a C_c of 0 do not peak due to the higher energy-spread having a negligible effect on the image due to the lack of chromatic aberration. We can also note that the cold FEG generally has higher SNR values than the Schottky FEG's images simulated under equivalent levels of monochromation and C_c coefficient conditions. This is because the cold FEG starts with an inherently lower energy-spread value; its current reduction is not quite as high as the Schottky FEG and is subsequently not as impacted by Poisson noise. The initial higher brightness of the cold FEG compared to the Schottky FEG also contributes to the larger SNR values.

We note Figures 2.11 b) and c) are the same imaging conditions as Figure 2.11 a),

only differing by their acceleration voltages, which are 30keV and 15keV for Figures 2.11 b) and c), respectively. From Figure 2.10 a) to c), we see the overall SNR of the images decreases respectively. This aligns with our expectations that the lower the acceleration voltage, the larger effect chromatic defocus blur has on the resolution and, therefore, the SNR of the image.

It is evident that for most instruments, the default emitter's energy-spread can limit the machine's resolution during low-voltage imaging, but this can be improved with monochromation. It is apparent from the experimental paper published by Hachtel et al. [54] that even with the low energy-spread produced from a cold FEG, users still desire even lower energy-spreads for their applications and therefore look towards adding a monochromator to their system. While monochromators have many benefits, they are a costly upgrade to the user [30] and can be out of the reach of less funded laboratories. An alternative solution to fulfilling users' low energy-spread needs that does not require an electron monochromator would certainly interest low-voltage researchers.

2.4. Conclusion

In this chapter, we discussed the different ways of optimising beam current, which included the different methods for decreasing chromatic aberration. Prismatic simulations were then run of gold nanoparticles for various acceleration voltages, C_c coefficients and energy-spread conditions for a spherically aberration corrected STEM. The analysis of the SNR values of these simulations was used to advise on the optimal energy-spread for a monochromated electron emitter. With the ability to reduce knock-on effects, charging and increase surface sensitivity, there is a motivation for researchers to move towards lower acceleration voltages. This chapter's investigation indicated that users are looking towards even lower energy-spreads for their low-voltage experiments and that monochromators are currently the only solution to achieving beams with energy-spreads less than a cold FEG. The next chapter will look towards an alternate solution to producing a low energy-spread beam by utilising the photoelectric effect.

Chapter 3.

Photoelectron Emission Theory

3.1. Introduction

Chapter two described in detail the different types of electron emitters and monochromator technology that can be involved in reducing the energy spread of an electron source. Analysing STEM simulations of gold nanoparticles imaged in a microscope with different objective lenses, acceleration voltages and levels of monochromation provided insight into how to optimise the electron beam to produce the largest signal-to-noise ratio during low-voltage imaging. The main takeaway from this investigation was that low energy-spreads are becoming increasingly more desirable for researchers who wish to perform low-voltage microscopy. However, to reach these extremely low energy-spreads, an electron monochromator is required, which has the caveat of being relatively expensive and not accessible to less funded institutions. Considering this, a potentially different route is to produce low energy-spread electrons via the photoelectric effect.

The photoelectric effect occurs when sufficiently energetic photons collide with a material and an electron, or other free carriers, in the material absorbs the photon's energy and gets emitted. An illustration of this can be seen in Figure 3.1.

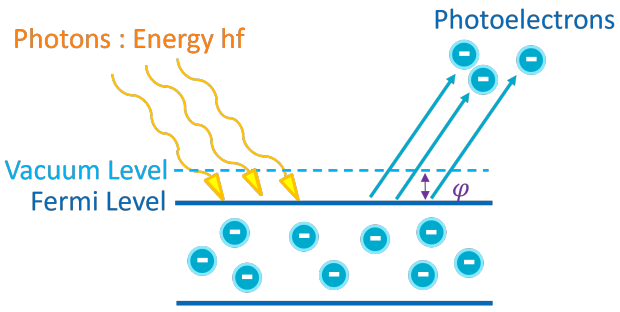

Figure 3.1.: *Illustration of the photoelectric effect whereby ϕ is the work function of the sample and is equal to the vacuum level minus the Fermi level of the material.*

If the photon's energy is greater than the work function of the sample ϕ, photoelectrons will be produced. The energy spread of the emitted photoelectrons depends on the energy and energy spread of the photon energy and the work function of the sample. A low energy spread electron source could be produced by carefully selecting the photoelectron emitter's components. By choosing low-cost, off-the-shelf parts, this photoelectron emitter could be an alternative option to the more expensive electron monochromator or cold FEG.

The following chapter will explore the design for such a photoelectron emitter. Firstly, how light sources of different photon energies can affect the energy spread of the emitted photoelectrons will be examined. A suitable photocathode and light source will then be chosen, and a discussion into whether a photoelectron emitter made from these components could act as a low energy spread electron source in an electron microscope will be conducted.

Please note that excerpts of this chapter have been previously published in 'Quigley, F., Downing, C., McGuinness, C., Jones, L. (2023) "A Retrofittable Photoelectron Gun for Low Voltage Imaging Applications in the Scanning Electron Microscope." Microscopy and Microanalysis, 29(5), 1610-1617 '. Regarding the delegation of responsibilities between the paper's authors, the author of this thesis ran the experiments, conducted the analyses of the results and composed the paper's manuscript. Lewys Jones, Cormac McGuinness and Clive Downing aided in analysing the results and reviewing drafts of the manuscript, while Clive Downing also assisted in some of the experimental setups.

3.2. Choosing an Appropriate Photocathode

Before selecting a suitable photocathode, the fundamental interaction between the photons and the cathode material must be considered. This interaction can be represented in Figure 3.2 a) and b) (which is after previous work by Sawa ([51])). These figures show the Fermi distributions of a material struck by two light sources with different photon energies (E_A and E_B, respectively). It describes how electrons will be emitted when the energy of the photon $h\omega$ is greater than the sample's work function (ϕ). Whereby the maximum energy of the photoelectrons (E_{max}) is given by the following equation:

$$E_{max} = h\omega - \phi \tag{3.1}$$

where h is Plank's constant and ω is the frequency of the photon, which is equal to

the speed of light divided by the wavelength of the light source ($\omega = \frac{c}{\lambda}$).

Choosing a photocathode with a low work function is therefore beneficial for a photoelectron gun as it would not require a light source with an excessively high photon energy to stimulate photoelectron production. Other factors should also be considered, including whether the cathode is cost-effective and how adaptable it would be to current electron microscopes.

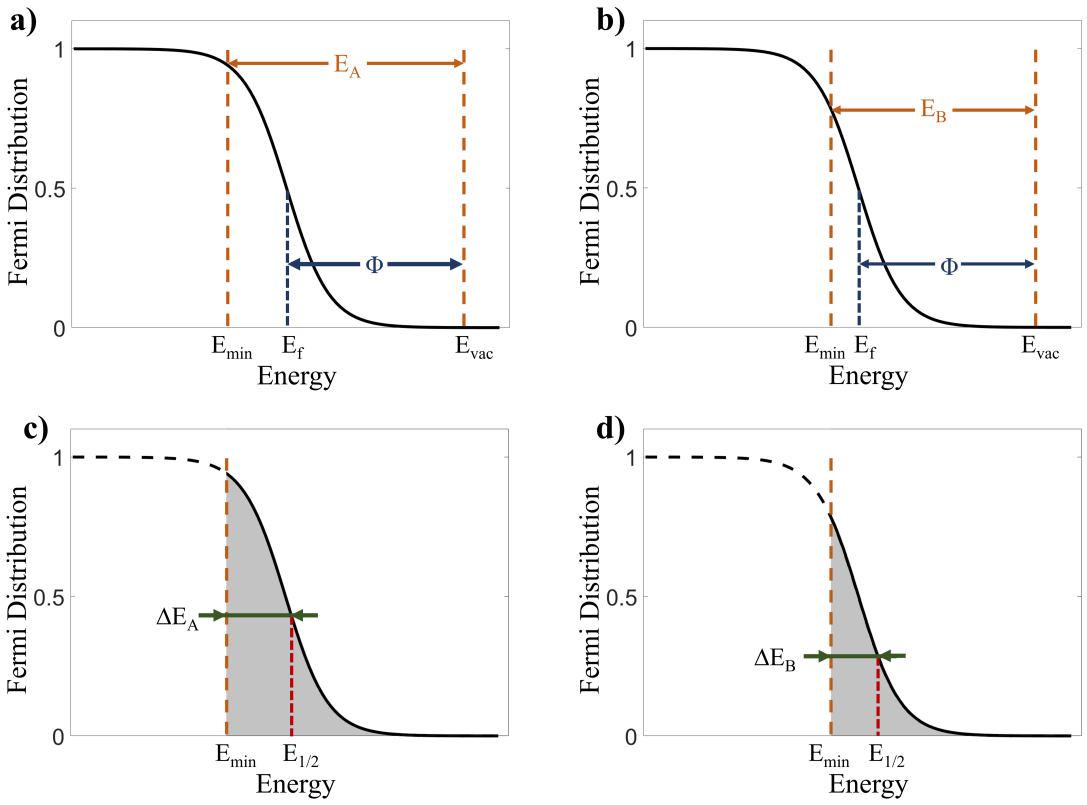

Figure 3.2.: *a), b) Graphs of the Fermi distribution displaying the minimum energy level (E_{min}) a photon of energy E_A and E_B can excite an electron, respectively. The work function is represented by ϕ, which is equal to the vacuum level (E_{vac}) minus the Fermi level (E_f) of LaB_6. c), d) Graphs of the Fermi distribution displaying the energy spread (ΔE_A and ΔE_B, respectively) of the emitted photoelectrons between the green arrows where $E_{\frac{1}{2}}$ satisfies the equation $f(E_{\frac{1}{2}})=f(E_{min})/2$. This graph is after Figure 5 in Sawa et al. [51] and is reprinted from Quigley et al. 2023 (Reference Number: [74]).*

One material that meets all of these criteria would be the crystal Lanthanum Hexaboride (LaB_6). To start, LaB_6 is a low work function material which has been well investigated for its use as a photocathode in literature [47, 48, 49, 50, 75], making it a strong candidate for a photoelectron source. LaB_6 is a monovalent, non-magnetic compound [76], which has a simple cubic crystal structure [77]. Its work function is anisotropic, increasing and decreasing with different crystal orientations [78]. This is taken advantage of by cathode manufacturers, and an image of a standard fila-

ment is shown in Figure 3.3 a), where Figure 3.3 b) is a SEM image of the tip of the crystal captured by the author. It has been constructed such that the microflat at the tip is a $< 100 >$ orientated single crystal with a low work function of 2.69eV.

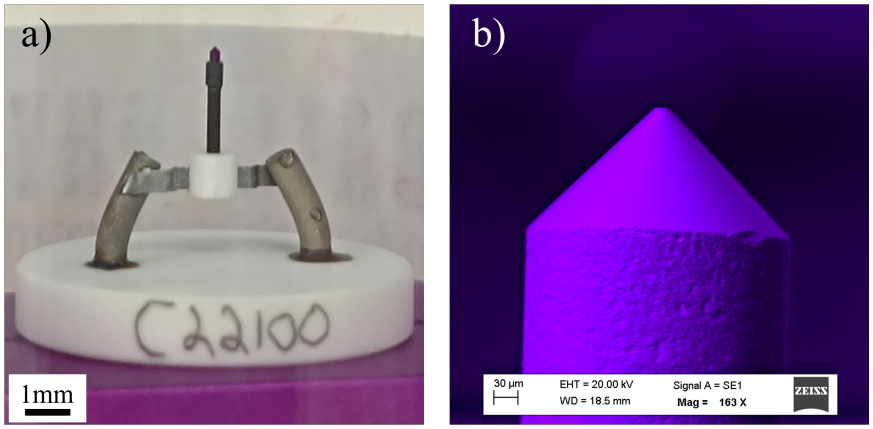

Figure 3.3.: *a) Image of Lanthanum Hexaboride crystal in a carbon ferrule, a standard crystal mount for thermionic electron guns. b) SEM image of the LaB_6 crystal tip artificially coloured.*

As LaB_6 is commonly found as a cathode in thermionic electron guns, it is already easily adaptable to thermionically driven electron microscopes through commercially available mounts. The Kimball Physics holder in Figure 3.3 a) is an example of such a mount, where thermionic emission occurs when the carbon ferrule the LaB_6 is mounted on applies a current through the crystal. This resistive heating also cleans the tip of the cathode from contamination. This would be a valuable operation to perform prior to photoemission to avoid the crystal's work function increasing due to this contamination (which is described in more detail in section 3.5) [75]. The LaB_6's availability to be purchased commercially makes it relatively cost-effective as a custom holder is not required for installing the crystal into thermionically driven microscopes.

Cerium Hexaboride (CeB_6 or CeBix) is another very similar material to LaB_6 [79] and is offered by a few filament manufacturers. It is currently not widely used in TEMs and SEMs, making it slightly more expensive than its lanthanum counterpart.

Other photoelectron sources using negative electron affinity (NEA) photocathodes have previously been investigated for low voltage SEM imaging [80]. These sources have achieved brightnesses as high as a Schottky FEG at an energy spread estimated to be less than 0.2eV [81]. While a LaB_6 photocathode may potentially be unable to reach these levels of brightness, these NEA photocathodes usually require extra space in the vacuum chamber for surface preparation devices to clean the cathode, need illumination ports to introduce the laser light and usually operate in an extremely high vacuum chamber [82]. The photoemitter to be built is focused on using

low-cost, off-the-shelf components where possible and the ability to be retrofittable on a conventional SEM or TEM would be preferable. Therefore, a commercially available LaB_6 crystal, which can be easily cleaned via resistive heating, was chosen for this retrofittable photoelectron emitter design.

3.3. Determining a Suitable Light Source

When aiming to construct a practical emitter with a usable electron beam-current, the quantum efficiency (η) of LaB_6 is another critical variable to consider when deciding on the light source, as it can be used to determine what variables influence the photoelectron current (I_{PE}). The quantum efficiency of LaB_6 (η) defines the efficiency of photons of a certain wavelength to convert electrons into photoelectrons in the LaB_6 crystal. Its most basic definition is as follows;

$$\eta = \frac{Number\ of\ Photoelectrons\ produced}{Number\ of\ Impinging\ photons} \tag{3.2}$$

This efficiency depends on the wavelength of the impinging photons and the optical power of the laser. The quantum efficiency of LaB_6 at different wavelengths has been determined experimentally in many papers for many different types of light sources. However, the method of calculating the quantum efficiency varies slightly between the different literature. Qian et al. defined the quantum efficiency as

$$\eta = \frac{(I_{pe}\Delta t)h\omega}{E_\lambda}, \tag{3.3}$$

where E_λ is the laser energy, I_{pe} is the photocurrent, t is time, and $h\omega$ is the impinging photon's energy [49]. Konishi et al., on the other hand, calculated the quantum yield from the photoemission current and the intensity of the incident photon [83]. In Oettinger et al.'s research, the quantum efficiencies of the LaB_6 at three different wavelengths were calculated from the experimentally measured photocurrent and the measured laser power [50]. Sawa et al. had the same method, defining quantum efficiency in terms of photocurrent (I_{pe}), the optical power of the light source (P) and impinging photon energy (E_{ph}) in the form of the equation

$$\eta = \frac{I_{pe}/e}{P/E_{ph}} \tag{3.4}$$

where e is the charge of an electron [51]. Given the breadth of literature available, comparing quantum efficiency versus the light sources' photon energy would be

useful. This information was gathered by the author and plotted in Figure 3.4. It is interesting to note that some of the values of quantum efficiency in Figure 3.4 appear to vary quite widely between different photon energies, for example between point [G] and [C]. This may be due how the cathodes were prepared before each experiment. In [C] the crystal was cleaned via Argon ion sputtering before each experimental measurement while the cathode in [G] was cleaned via resistive heating. The Argon ion sputtering could produce a cleaner cathode surface with a potentially lower work function for enhanced photoemission and therefore increased quantum efficiency. This highlights the importance of preparing a clean cathode surface before photoemission in order to obtain the maximum quantum efficiency from the crystal.

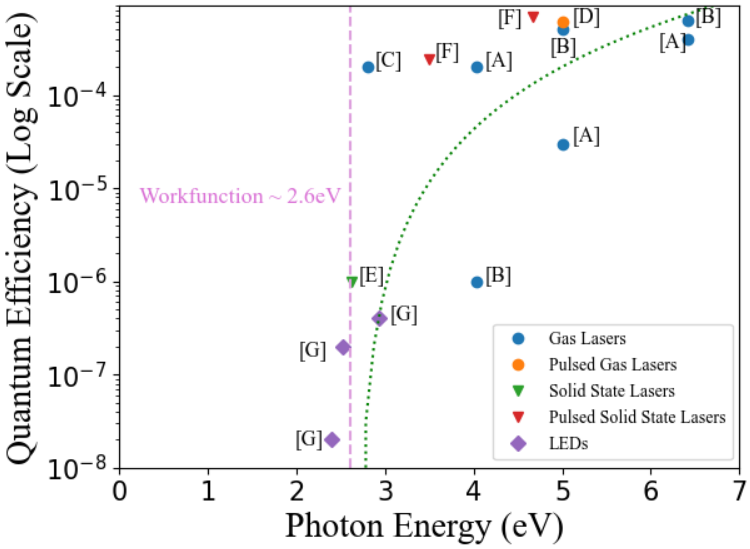

Figure 3.4.: *The quantum efficiency of LaB_6 versus photon energy for the literature values; [A] Oettinger et al. 1990 [50], [B] Lafferty et al., 1951 [46], [C] May et al., 1990 [47], [D] Qian et al., 1995 [49],[E] Sawa et al., 2017 [51],[F] Leblond et al., 1996 [75] and [G] Konishi et al., 2012 [83]. The dashed line indicates the approximate work function of LaB_6 2.6eV. The trendline plotted in green is from Figure C.1 in Appendix C. This graph is reproduced from supplemental Figure 1 from Quigley et al. 2023 (Reference Number: [74]).*

A similar graph of quantum efficiency versus photon energy minus the work function of the sample given in each paper was also plotted and can be seen in Figure C.1 in Appendix C. The trendline of this graph was plotted in green in Figure 3.4 and is given as;

$$Quantum\ Efficiency\ (\eta) = 2.056 \cdot 10^{-5} \cdot (Photon\ Energy\ -\ Work\ Function)^{2.719} \tag{3.5}$$

Based off literature the quantum efficiency is known to be proportional to $(Photon\ Energy\ -\ Work\ Function)^2$ at the weak electric field limit [51]. So equation 3.5 of the trendline from Figure C.1 which has quantum efficiency proportional to $(Photon\ Energy\ -\ Work\ Function)^{2.719}$ approximately follows this relationship. Using equation 3.5, the quantum efficiency of light sources at different photon energies can be predicted.

It is interesting to note from Figure 3.4 that there is a sharp drop off in the quantum efficiency the closer the photon energy gets to the work function of the LaB_6 at approximately 2.6eV. This is a nice verification of the initial equation behind photoemission: $E_{max} = h\omega - \phi$.

The next step when trying to determine the most suitable light source is to rearrange the quantum efficiency equation 3.4 in terms of photoelectron current I_{PE};

$$I_{pe} = \frac{\eta \cdot e \cdot P_e \cdot \eta_{electrical}}{E_{ph}} \tag{3.6}$$

whereby the optical power P has been replaced by total electrical power P_e multiplied by the optical-electrical efficiency $\eta_{electrical}$. The wavelength λ of the light source can easily be converted to the energy of the photons in eV (E_{ph}) using the relation $E_{ph} = \frac{hc}{\lambda}$ where h is Planck's constant in eV and c is the speed of light. In addition to this, the laser's power and opto-electrical efficiency can be determined from the light sources specification sheet. Equation 3.5 can then be used to calculate the quantum efficiency η. Therefore, equation 3.6 is extremely useful as the photocurrent that would theoretically be produced from a light source can be calculated by simply inputting these values.

With the ability to determine the photocurrent produced by each light source, we can start to compare the different light sources from different manufacturers. The survey of literature in Figure 3.4 indicates that many of the high photon energy light sources which produce a high quantum efficiency are gas or pulsed laser systems, which are not the most cost-effective. When choosing a light source with photon energy close to the work function of LaB_6, LEDs and laser diodes were the leading choice in literature and were therefore a point of focus in the search for a suitable light source. LEDs tend to have a large angular ($\sim$120 degrees) and wavelength spread ($\sim\pm$10 nm) relative to the laser diodes ($\sim$21 degrees and $\sim\pm$5 nm), (shown in Figure 3.5), however they do tend to be more cost-effective. Comparing the right-hand images in Figure 3.5, we see that the source size of the laser diodes also tends to be smaller than LEDs due to their smaller angular spread.

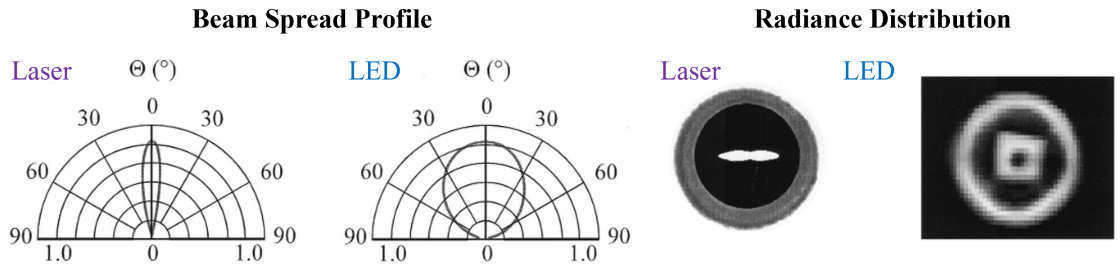

Figure 3.5.: *The difference between the beam spread profiles and radiance distributions of laser diodes and LEDs. Please note this figure was reprinted from the International Commission on Non-Ionizing Radiation Protection, ICNIRP Statement on Light-Emitting Diodes (LEDs) and Laser Diodes: Implications for Hazard Assessment, Health Physics: The Radiation Safety Journal, 78, 6, 744-752, journal URL: https://journals.lww.com/health-physics/citation/2000/06000/icnirp_statement_on_light_emitting_diodes__leds_.20.aspx (Reference number: [84]).*

It also should be noted that LEDs can have higher quantum efficiency values than those shown in Figure 3.4. The reason the LEDs show the lowest quantum efficiency values in Figure 3.4 is because the LEDs chosen in the literature the data points were taken from ([G] Konishi et al., 2012 [83]) have a lower photon energy compared to the other light sources. If a higher photon energy LED was used a higher quantum efficiency would most likely have been recorded.

In order to inform on the choice of a light source, a metric was created where the photocurrent that would be emitted from LaB_6 due to stimulation from different LEDs and laser diodes was calculated using equation 3.6. This value in nA was divided by the cost of the light source, its theoretical energy spread (calculated from equation 3.7 to be described below) and the angle spread of the source taken from its specification sheet. After researching various commercially available light sources, Figure 3.6 was plotted, which compares many different LEDs and laser diodes based on this metric and their wavelength.

This metric takes into account that it would be ideal to select a light source which produces the maximum amount of photocurrent, while striving for low cost, low energy-spread and low angle-spread. The light source with the largest value of this metric is the optimal light source to purchase. Based on Figure 3.6, continuous wave laser diodes of wavelength 405nm +/- 5nm (3.06eV $\pm$ 0.038eV), which are commonly used in a variety of applications from laser engravers to curing resin in 3D printers, were chosen as the light source. The laser packages selected have an additional focussing lens to make their optical path more parallel and are priced within the range of $\sim$ €10-€60, depending on the required power.

With a suitable photocathode and light source chosen, the energy spread of the

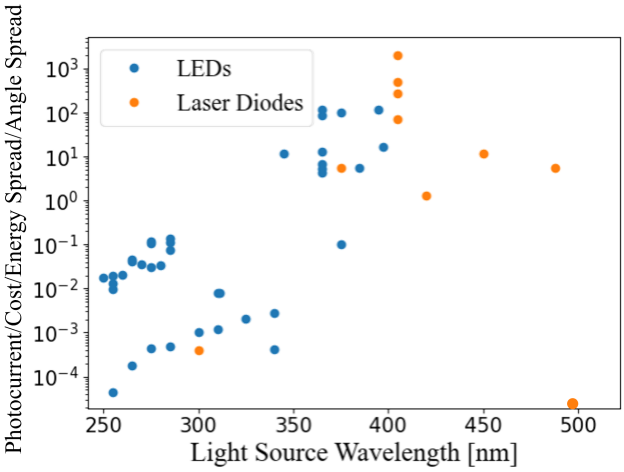

Figure 3.6.: *Comparison of commercially available LEDs and laser diodes based on their different properties.*

photoelectrons emitted using a source composed of the selected components can be determined.

3.4. The Theoretical △E of the Photoelectron Emitter

Sawa et al. used the following equation to theoretically predict the energy spread (ΔE_e) of their electron source;

$$\Delta E_e = k_B T \; ln \left[2 \exp\left(-\frac{E_{ph} - \phi}{k_B T} \right) + 1 \right] + E_{ph} - \phi \tag{3.7}$$

where E_{ph} is the photon energy, k_B is the Boltzmann constant and T and ϕ are the temperature and work function of the LaB_6 crystal [51]. Using equation 3.7, the theoretical energy spread of our electron source with a LaB_6 cathode with ϕ=2.69 which is struck by a light source of E_{ph}=3.06eV ± 0.038eV is ΔE_e=0.37±0.04 eV. This energy spread is similar to that of a cold FEG.

It would of course be desirable to use a light source with photon energy that would stimulate photoelectrons with an energy spread less than 0.3eV, such as that used in Sawa et al.'s paper (ΔE_e=0.11eV) [51]. However, based on equation 3.4, the smaller the photon energy, the smaller the quantum efficiency and subsequently, from equation 3.6, the smaller the photoelectron current produced from the light

source. Therefore, for initial experiments, an electron energy spread of 0.37eV is acceptable as it is important to have a large enough detectable photoelectron current when designing the prototype. When the initial prototype is created and the design optimised, a lower photon energy light source could be then installed to produce lower energy-spread electrons.

Previous literature corroborates the theoretical prediction of 0.37eV based on Sawa's work. Curtis et al. have simulated the kinetic energy distributions of photoelectrons stimulated from LaB_6 using three different photon energies [85]. In their work, the electron energy distribution decreases as the photon energy decreases. This once again highlights that the closer the photon energy is to the work function of your sample, the lower the photoelectron energy spread. Figure 7 in Mogren and Reifenberger's work experimentally supports these simulations, displaying the same trend of a decrease in photon energy striking the LaB_6 resulting in a decrease in photoelectron energy distribution [48]. Konishi and colleagues used photons with energies of 2.40eV, 2.52eV and 2.93eV to strike a LaB_6 crystal. Using a retarding-field type electron energy analyser, they measured the energy spread of the emitted photoelectrons. Their energy spreads were found to be 0.05 eV, 0.15eV and 0.4eV, respectively [83]. This further experimentally supports the theory that low energy spread electrons can be produced via photoemission. Finally, Sawa and their team used a laser diode with a photon energy of 2.62eV to stimulate their photoelectrons. As the light source energy was close to the work function of the LaB_6 crystal, an energy spread of 0.11eV was recorded [51], around one-third of the energy spread of a cold FEG [54]. The collection of these literature findings would imply that the theoretical prediction of energy spread based on Sawa et al.'s calculations should apply to our photoemitter setup.

3.5. How the $\triangle$E Depends on the Crystal Temperature

With the theoretical energy spread predicted, another area to examine is how this energy spread would depend on the temperature of the crystal. This is important to discuss as if the goal is to potentially retrofit these components onto a thermionic electron emitter, the vacuum of the gun chamber must be considered. Photoelectrons will only be stimulated if the photon energy is above the work function of the crystal. A poor vacuum chamber can cause monolayers of gas to be deposited on the surface of the LaB_6. These pollution effects can affect the work function of the crystal and subsequently decrease the lifetime of the photocathode [51][75]. Fortu-

nately, applying permanent thermal assistance to the cathode by slightly heating it can minimise contamination effects in poorer vacuum conditions [75]. However, based on equation 3.7, the energy-spread of the photoelectrons can increase with increasing LaB_6 temperature.

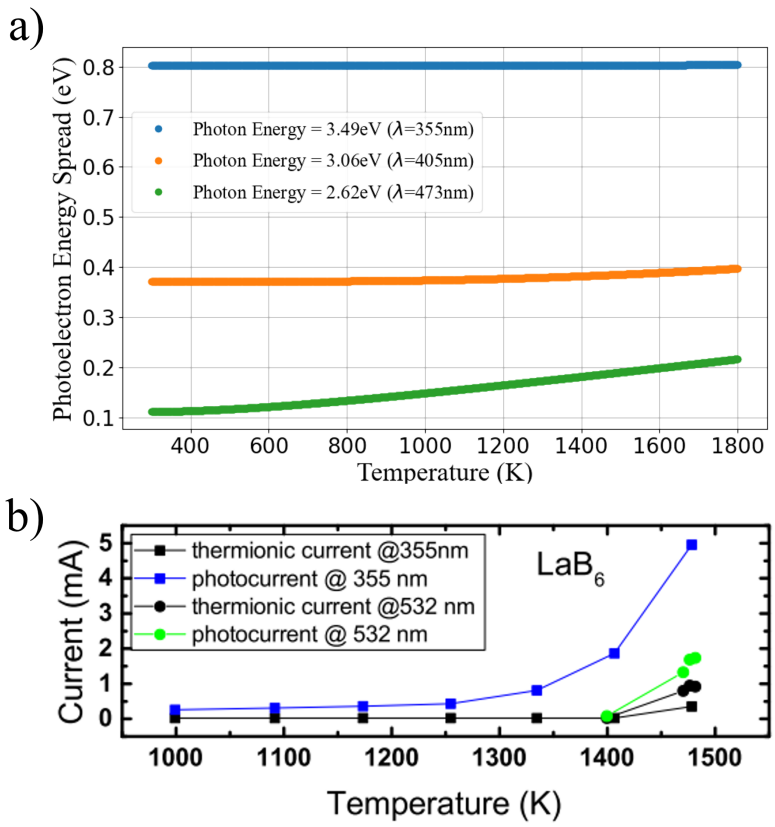

Figure 3.7.: *a) Simulated data of how the energy spread of photoelectrons from three different light sources changes with the temperature of the LaB_6 crystal. b) Plot of how the thermionic and photoelectron beam current changes with LaB_6 temperature for two light sources with different wavelengths. Please note that b) is reprinted from K. Torgasin, K. Morita, H. Zen, K. Masuda, T. Katsurayama, T. Murata, S. Suphakul, H. Yamashita, T. Nogi, T. Kii, K. Nagasaki, and H. Ohgaki, Thermally assisted photoemission effect on CeB_6 and LaB_6 for application as photocathodes, Physical Review Accelerators and Beams, DOI: 10.1103\PhysRevAccelBeams.20.073401 (Reference Number: [79]).*

To demonstrate how this may affect the energy-spread for light sources of three different photon energies, Figure 3.7 a) was plotted for the photon energy 2.62eV found in Sawa et al. [51], 3.49eV found in Torgasin et al. [79] and the photon energy of our chosen light source 3.06eV.

From Figure 3.7 a), it was found that the change in energy spread between room temperature (300K) and the standard thermionic operating temperature of the crystal (1800K) is 0.0017eV, 0.026eV and 0.10eV for light sources with 3.49eV,

3.06eV and 2.62eV photon energy respectively. This shows that photons with energy closer to the work function of the sample (2.69eV) are more likely to have larger energy spread changes with temperature. This is something to be aware of in the future emitter design if slight heating is required to keep the crystal contamination-free.

It should also be noted that thermally assisted photoemission can occur when the crystal temperature is increased. The energy distribution of electrons in the material can be changed due to thermal excitation. It can cause some electrons to occupy higher energetic states. This can increase the probability of the electron being extracted by a photon and will also increase the energy of the extracted electron. This can cause the quantum efficiency and, subsequently, the photoelectron current to increase [79]. Torgasin et al. investigated and demonstrated this effect. Using light of wavelength 355nm, as the LaB_6 temperature was increased, the photocurrent also increased [79]. This is something to consider when deciding whether to increase the cathode temperature in future prototypes. Up to a certain temperature, the photoelectron current increases while the thermionic current remains relatively constant, as shown in Figure 3.7 b) taken from Torgasin et al.'s paper [79]. However, as there is no way of separating the thermionic and photoelectric current, the energy spread of the beam will then start to increase with this increasing temperature and subsequent thermionic current. Based on Sawa et al.'s experimental work, operating the LaB_6 crystal at around 1200K appears not to increase the beam's energy spread significantly. To the author's knowledge, measurements of the energy spread from a photoelectron source above this LaB_6 temperature do not appear to be recorded in literature. However, analysing Figure 3.7 b), we see the thermionic current starts to increase above 1200K. Therefore, caution should be applied when operating above 1200K as an increase in energy spread could potentially occur due to the addition of more thermionic electrons. As mentioned previously operating the crystal at lower temperatures can causes an increase in crystal contamination in poor vacuum chambers causing a decrease in photoelectron current due to a subsequent increase in workfunction. Therefore a balance may need to be struck when selecting the crystal temperature when operating the emitter in a poor vacuum chamber.

3.6. Conclusion

In this chapter, an analysis of the properties of a photocathode and light source required to produce low energy-spread electrons was examined. LaB_6 was subsequently selected as a low work function, commercially available photocathode. A laser diode of wavelength 405nm was chosen as an appropriate, cost-effective light

source, which would produce sufficient photoelectron current from the LaB_6 crystal. The energy spread of photoelectrons emitted from a source using these specific components was then determined to be ΔE_e=0.37±0.04 eV, which is near the energy spread of a cold FEG. With the foundation parts of a photoelectron emitter selected, the next step is to design an operational photoelectron source.

Chapter four will begin this task by describing an experiment to prove that photoemission can occur with our chosen components. With this complete, a discussion of the design of a photoemitter prototype, including the safety aspect of using a UV laser diode in the setup, will be undertaken. This initial photoelectron source prototype will then be presented, and an analysis of provisional experimental results from this emitter will be examined.

Chapter 4.

Designing the Photoemitter Prototype

4.1. Introduction

Chapter three focused on the fundamentals of photoelectron emission. It discussed the photoelectric effect and what factors can affect the photoelectron current and the energy spread of the emitted electrons. These insights led to selecting LaB_6 as a suitable photocathode and a 405nm UV laser diode as an appropriate light source for a photoelectron emitter prototype. With the building blocks of the source identified, the not-inconsiderable feat of designing the retrofit of the photoelectron emitter into an electron microscope remains.

As outlined previously, electron microscopes are costly instruments regularly used in the lab. Suppose one were to shut down the operation of the microscope and retrofit a photoelectron emitter that does not work; this might damage the machine and cause unnecessary downtime for other users. To ensure our research direction is valid, this chapter focuses on designing and implementing a low-risk proof-of-concept experiment before committing to expensive hardware and installing any equipment into an actual electron microscope. I used the 3D CAD design software SOLIDWORKS to design a prototype that retrofits the chosen laser diode onto a commercially available electron microscope's LaB_6 thermionic electron gun. Based on the schematic designed in SOLIDWORKS, we manufactured a deconstructed version of this prototype for an experiment to verify that photoelectrons can be produced with our fundamental cathode and light source components. With this achieved, I used the modelling software SOLIDWORKS and COMSOL to design an apparatus that would allow the photoelectron emitter to integrate into a working electron microscope. Finally, the experimental results of this design pre-installation into the electron microscope are outlined.

Please note excerpts of sections 4.3.1 and 4.3.2 of this chapter have been previously published in 'Quigley, F., Downing, C., McGuinness, C., Jones, L. (2023) "A Retrofittable Photoelectron Gun for Low Voltage Imaging Applications in the Scanning Electron Microscope." Microscopy and Microanalysis, 29(5), 1610-1617 '.

4.2. Validating the Fundamental Photoemission

While the future photoelectron emitter will hopefully enhance the resolution of low-voltage images, its low energy-spread will also be extremely helpful for EELS. As EELS is predominately found in TEMs, the initial photoelectron emitter design was modelled for a JEOL 2100 TEM containing a thermionic LaB_6 electron gun. This instrument is located in the Advanced Microscopy Laboratory, Trinity College Dublin, and is a potential candidate for future prototype installations. The proposed photoelectron gun would consist of lanthanum hexaboride struck with UV photons from a small UV laser diode. This whole setup must be contained within a component that could be retrofitted into a transmission electron microscope's electron gun.

A schematic of a generic TEM thermionic electron gun adapted from Williams and Carter 2009 [8] can be seen in Figure 4.1.

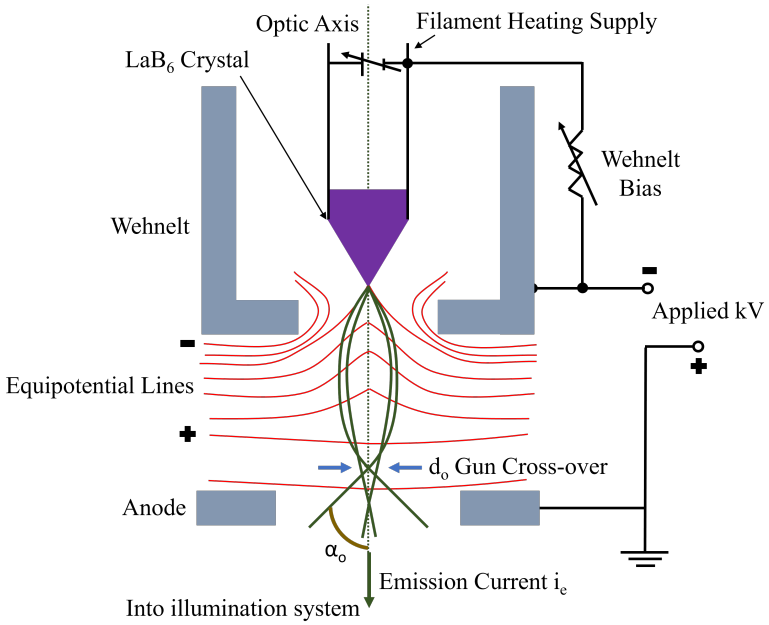

Figure 4.1.: *A schematic of a generic TEM Thermionic electron gun adapted from Williams and Carter 2009 (Reference number: [8]).*

It consists of a Wehnelt, a large cone of shaped metal with a negative bias applied to it to help focus the electron beam. The LaB_6 cathode is held inside the Wehnelt,

where it can be heated resistively to produce electrons. A balance between the bias of the Wehnelt, anode and LaB_6 is struck to ensure the electrons are accelerated away from the source down the column. To produce a stable beam current for the highest quality of illumination, it is advantageous to adjust the filament heating current to achieve a condition known as 'saturation'. During saturation the electrons are only emitted from the very tip of the LaB_6 and are focussed into a tight bundle by the Wehnelt's negative bias voltage. This is achieved through a self-regulating negative feedback process. An increase in filament heating current causes an increase in emission current. This increase in emission current flowing through the bias resistor causes the negative Wehnelt bias to increase, which opposes the emission current increase. This self-regulating feature creates a stable beam current [9].

Avoiding altering the Wehnelt by cutting or drilling into it mitigates the risk of permanently damaging the component and negatively affecting the emitter's electrostatics. The modelled prototype was designed so that its effects on the Wehnelt are reversible, and the machine is still usable if the prototype were to fail. The Wehnelt of a thermionic electron gun has holes to allow easy access to its interior for vacuum pumping. Therefore, the SOLIDWORKS software package was used to design a metal holder clipping into the Wehnelt's holes, angling the laser diode so that its light strikes the LaB_6. This clip-on method ensures that the Wehnelt is still operational even if the prototype is removed. This design can be seen in Figure 4.2, where the wiring for these prototypes could be fed out through the vacuum pumping tubes of the electron gun chamber. Before designing an experiment around this simulated model, to validate that photoemission can be realised with our chosen light source and cathode, certain laser safety precautions needed to be considered.

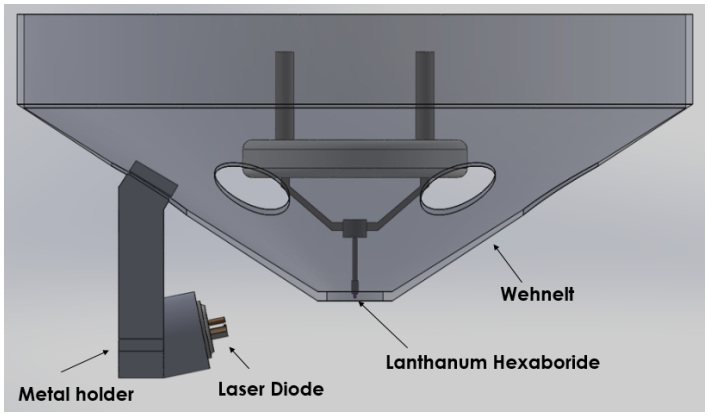

Figure 4.2.: *SOLIDWORKS design of the laser diode placed outside a JEOL 2100 TEM Wehnelt in a metal holder.*

4.2.1. A Note on Laser Safety Precautions

In the following work, a range of laser diodes were used in various experiments. The author attended a college-approved laser safety seminar to ensure all experiments were undertaken safely. The laser's wavelength and wattage combination was assessed during each experiment, and a laser safety risk assessment was undertaken. This involved consulting the laser safety officer and ensuring all necessary precautions were undertaken. This included building enclosures, installing safety signage, and purchasing appropriate laser safety glasses for the experiments.

4.2.2. Undertaking a Low-Risk Proof-of-Concept Experiment

A proof-of-concept experiment was then designed to determine whether the simulated prototype can produce photoelectrons in a vacuum. This was achieved by modelling a deconstructed prototype of the SOLIDWORKS rendered photoelectron emitter. Using SOLIDWORKS, an experiment holder was designed such that the laser diode would slot in and strike the secured LaB_6 at the same angle and distance that it would be positioned as in Figure 4.2. The 3D printed holder was fabricated in a Realizer SLM 50, a selective laser melting printer and can be seen in Figure 4.3a) - 4.3c).

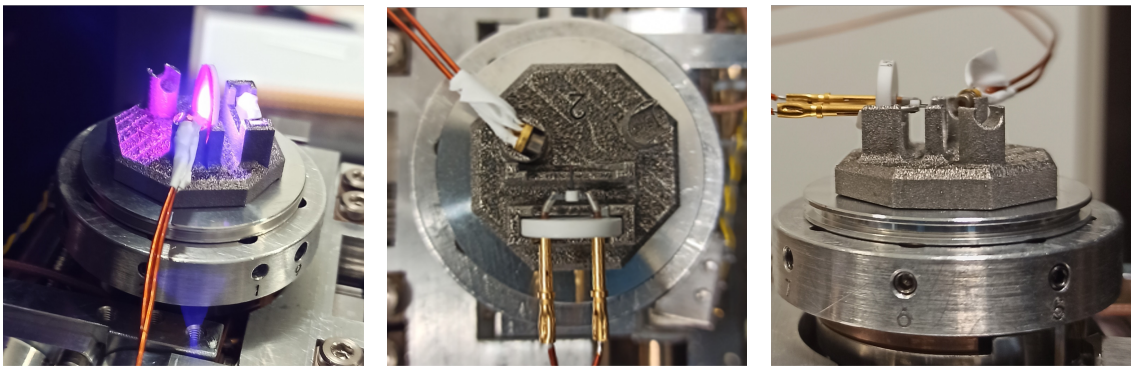

(a) (b) (c)

Figure 4.3.: *a) The laser diode in the 3D printed holder striking the alignment disk, causing it to fluoresce. b), c) A top and side view of the LaB_6 and laser diode holder setup on the stage of the SEM, respectively.*

The energy of the light source's photons ($h\omega$) is 3.06± 0.03eV, and the work function of the LaB_6 (ϕ) is 2.69±0.05eV, hence the maximum energy of any emitted photoelectron ($E_{max} = h\omega - \phi$) is expected to be 0.37±0.08eV. Due to the low energy of these photoelectrons, a sensitive electron detector was required. The experimental holder was therefore placed in a SEM vacuum chamber. The SEM's secondary electron (SE2) detector is very sensitive to low-energy electrons and would thus be

suitable for detecting these photoelectrons.

To integrate the electronics of the experimental setup into the SEM, an electronic feedthrough flange was installed into the microscope's door to provide access to the chamber's interior for the components' wiring. To prove the positioning of the laser diode is correct, it was fitted into the 3D printed holder opposite an alignment disk, as shown in Figure 4.3a). The fluorescing of the alignment disk in front of the LaB_6 holder slot proves that the laser beam will strike the LaB_6 at the correct angle in the holder. The LaB_6 was then inserted into the 3D printed holder opposite the laser diode, as shown in Figures 4.3b and 4.3c. The driving circuit for this setup can be seen in Figure D.1 in Appendix D.

The SE2 detector would only switch on if the acceleration voltage controlling the SEM's electron beam was also turned on. However, for our experiments, we only wanted to detect electrons generated by our deconstructed prototype in the main vacuum chamber. Therefore, the electron beam emitted by the SEM's electron gun was blanked during the following experiments.

As the detector contains a photomultiplier tube, it was found that it is sensitive to both electrons and photons. When an electron or photon is detected, it produces a grey-scale signal intensity, with examples shown in Figure 4.4. Interestingly while a photomultiplier is used in this SEM detector, electron multipliers are commonly used as image intensifiers in TEM detectors.

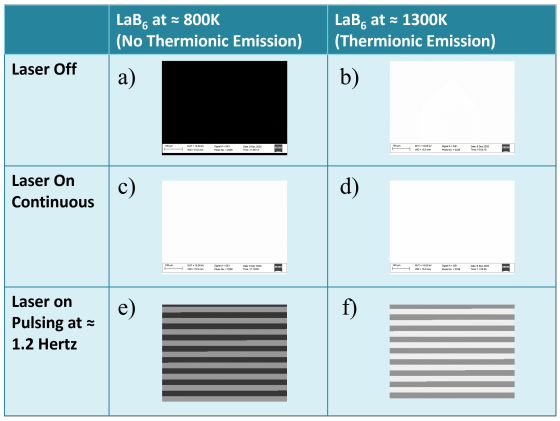

Figure 4.4.: *The images the SE2 detector produces when the laser diode and LaB_6 are at various settings. e) and f) are taken from the red boxes in Figure 4.7, which had a total frame time of 20.2s while the laser frequency was set to approximately 1.2 Hertz.*

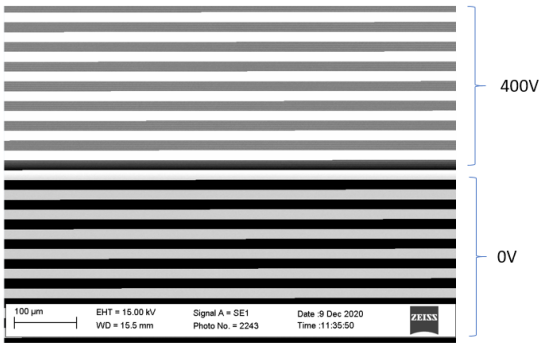

Figure 4.5.: *SEM image produced when the LaB_6 emits thermionic electrons as the laser diode pulses at approximately 3.3 hertz while the electron detector is at a bias of 400V and then switched to 0V. The frame time of this image is 5.1 seconds.*

In Figure 4.4 b), we see that when the LaB_6 was thermionically emitting lots of electrons, the SE2 detector would record a high value, resulting in a brighter image.

However, if the LaB_6 were below the temperature threshold for thermionic emission, approximately 800K, the SE2 detector would produce a black image as no electrons would be detected (Figure 4.4 a)). A similar scenario occurs when the laser is turned off and on (Figure 4.4 a) and c), respectively)). We found that using the laser diode to strike the ∼800K heated LaB_6 crystal at a frequency of approximately 1.2 hertz caused the SE2 detector to produce a zebra-striped image. Black for when the laser diode is off, white for when the laser diode struck the LaB_6 and photoelectrons were produced and were subsequently detected with the laser photons (Figure 4.4 e)).

From Figure 4.4 e) and f), we see a clear contrast between the thermionic emission of electrons when the LaB_6 is at different temperatures. This contrast also occurs when the bias of the electron detector is changed from 400V to 0V, as shown in Figure 4.5. At the start of Figure 4.5, the laser is pulsing, and the LaB_6 is at approximately 1300K emitting thermionic electrons; however, halfway through taking the image, the bias is changed from 400V to 0V. The electrons are no longer attracted to the detector, and when the laser is off, the detector reads black as it detects neither electrons nor photons.

This setting was used to verify that photo-emission was occurring in our trials, even if it cannot be directly seen due to the intensity of the photons striking the detector. This was achieved by setting the laser pulsing at approximately 1.2 hertz and capturing a SEM image at a frame time of 20.2 seconds using the SE2 detector while performing the following experimental steps;

1. The LaB_6 was set to a temperature of 1300K for 6 seconds so that photoemission and thermionic emission occur.

2. The temperature of the LaB_6 was then reduced to 800K over 6 seconds, so photoemission is still occurring, but there is a reduction in thermionic emission.

3. The temperature of the LaB_6 was then left at 800K for the remaining 6 seconds of the image, so only photoemission is occurring.

An example of a SE2 image taken after following these steps for a detector at bias 400V can be seen in Figure 4.6.

This experiment was repeated for detector biases ranging from 0V to 400V, as seen in Figure 4.7. At higher detector biases, the electrons from the LaB_6 are visible; however, as the detector bias decreases, so does the intensity of the electrons in the image, as they are no longer attracted to the detector.

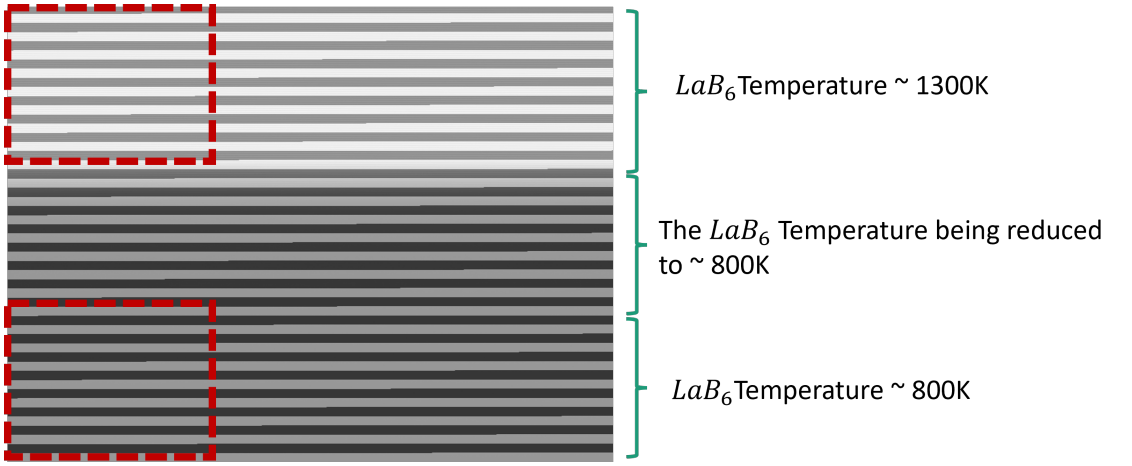

Figure 4.6.: *The experimental setup at a detector bias of 400V. The LaB_6 emits thermionic electrons as the laser diode pulses at approximately 1.2 hertz. The LaB_6 temperature is then turned down to no longer emit thermionic electrons. The total frame time of this image is 20.2s. The red boxes indicate where Figures 4.4 e) and f) were cropped from.*

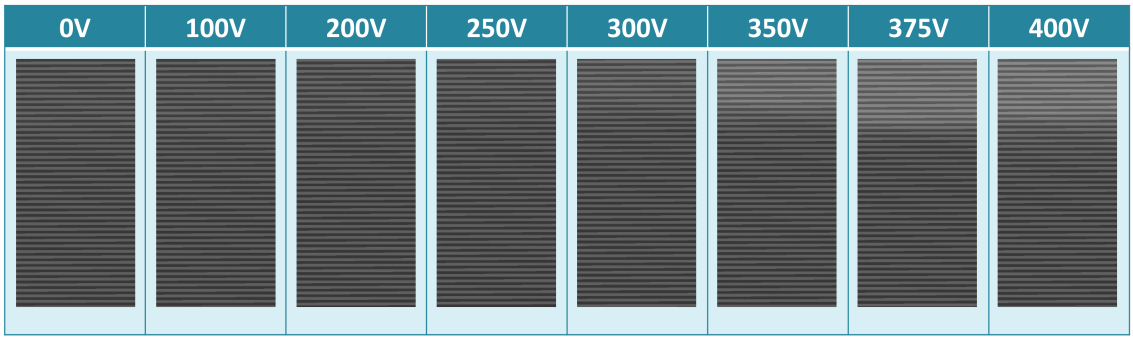

Figure 4.7.: *Images recorded on the SEM as the bias ranges from 0V to 400V. During all these images, the LaB_6 emits thermionic electrons as the laser diode pulses at approximately 1.2 hertz. The LaB_6 temperature is then turned down such that it is no longer emitting thermionic electrons.*

4.2.3. Evaluating the Experimental Results

A time-series of pixel intensity versus time was extracted using MATLAB code for each image in Figure 4.7 to analyse the data more quantitatively. This involved reshaping the image into a 1D time-series of their greyscale intensity. This comprises of a series of peaks and troughs, as seen for a detector bias of 400V (blue) and 0V (orange) in Figure 4.8.

These time-series appear to follow the pattern of a square wave that follows a sigmoid shape. The square wave shows when the laser diode is on (the peaks) and when it is off (the troughs). For the 400V time-series, the sigmoid shape it follows demonstrates how the intensity of the electrons detected is high when the LaB_6 is emitting thermionic electrons and thermionically induced photons, however after six seconds, the temperature of the LaB_6 is turned down, causing the overall

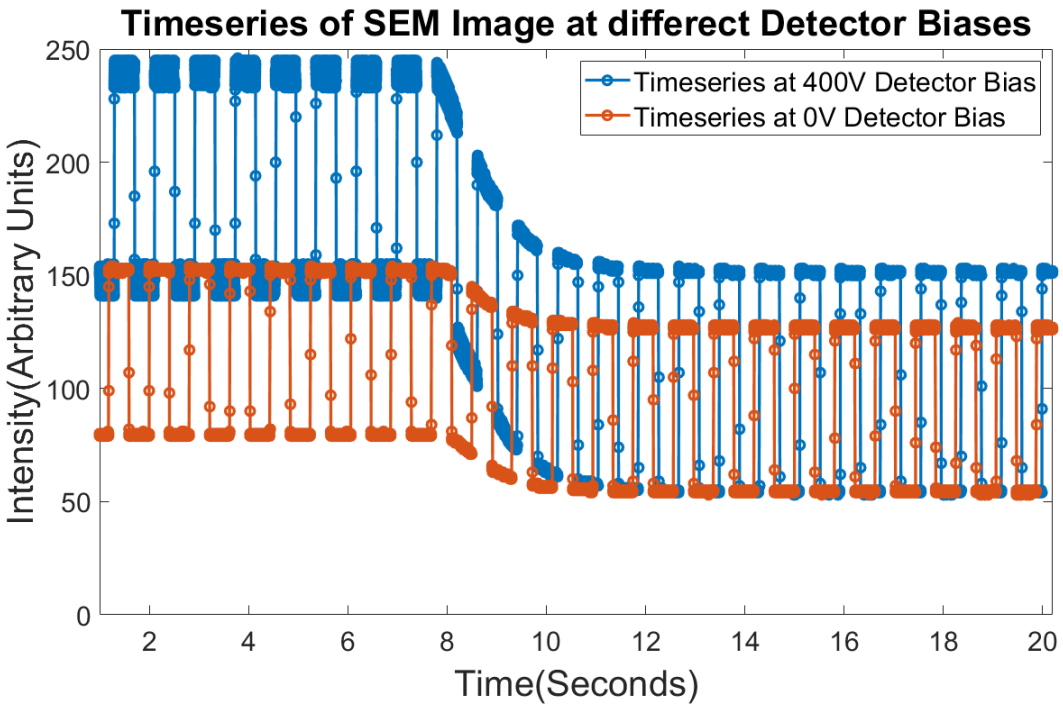

Figure 4.8.: *The time-series of pixel intensity versus time at a detector bias of 400V (blue) and 0V (orange).*

intensity to drop as fewer thermionic electrons and photons are detected. This effect plateaus at approximately twelve seconds when the LaB_6 no longer emits thermionic electrons; therefore, only the intensity of laser photons, residual thermionic photons and potential photoelectrons are being detected.

To analyse this 400V time-series data, we extract the intensity of the time-series' peaks and troughs and the square wave's amplitude. MATLAB's curve fitting tool was used to fit the equation of a sigmoid and square wave to this time series. The plot of this fit can be seen in dark orange in Figure 4.9.

The sigmoid shifted upwards on the y-axis by the black level offset value of the image system is plotted in purple in Figure 4.9 with the time-series and the MATLAB fitted equation. To plot the peaks (yellow) and troughs (green), this sigmoid was shifted up and down by half the amplitude of the square wave, respectively.

The peaks include the intensity of the thermionic electrons (e_t^-) and photons (P_t), as well as the laser's photons (P_L) and photoelectrons (e_L^-), i.e. $\text{Peaks}_{400\text{V}} = e_t^- + P_t + P_L + e_L^-$. The troughs on the other-hand include: $\text{Troughs}_{400\text{V}} = e_t^- + P_t$. The time-series when the detector was at 0V is shown in Figure 4.8 in orange. This time-series separated into its peaks and troughs using the MATLAB custom fit tool can be found in Appendix E Figure E.1. As no electrons are detected at 0V we can infer that $\text{Peaks}_{0\text{V}} = P_t + P_L$, while as the laser is off, the $\text{Troughs}_{0\text{V}} = P_t$.

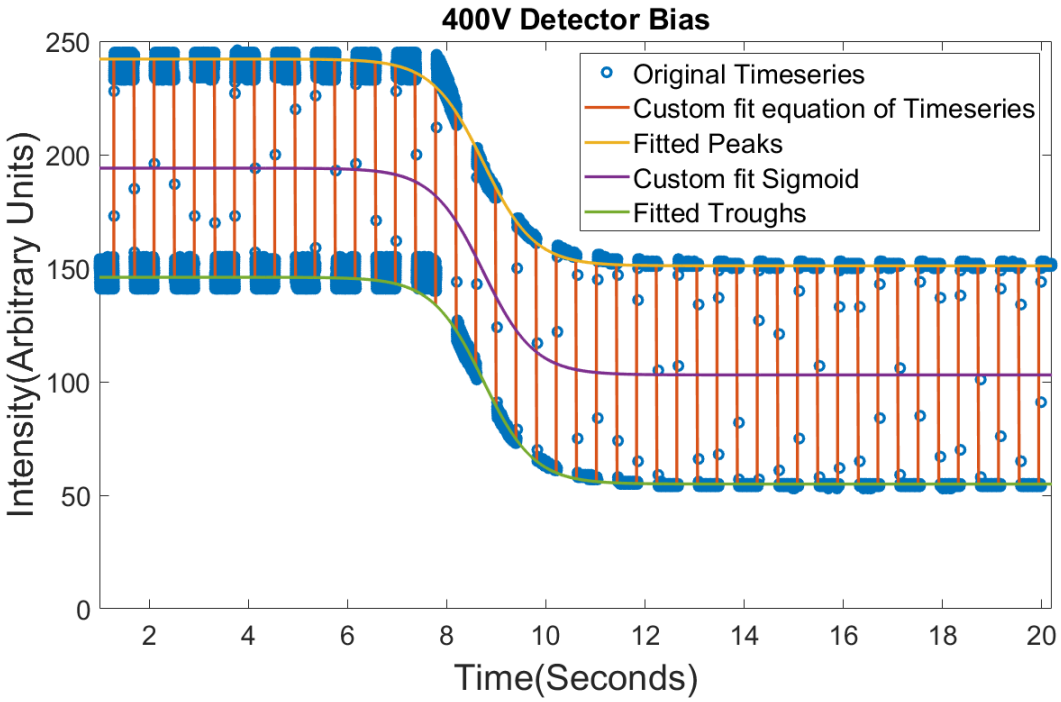

Figure 4.9.: *Time-series at a detector bias of 400V (blue), including the custom fit equation of this time-series (orange) and the sigmoid derived from this equation (purple), which has been shifted up and down by half the amplitude of the square wave to determine the peaks (yellow) and troughs (green) respectively of the time-series.*

The amplitude of the time-series of the detector at 400V ($\text{Amp}_{400\text{V}}$) and 0V($\text{Amp}_{0\text{V}}$) is simply the peaks minus the troughs. Therefore, $\text{Amp}_{400\text{V}} = P_L + e_L^-$ while $\text{Amp}_{0\text{V}}$ can be used to calculate the laser photon's intensity as

$$\begin{aligned} \text{Laser photons } P_L &= \text{Amp}_{0\text{V}} \\ &= \text{Peaks}_{0\text{V}}\text{-Troughs}_{0\text{v}} \\ &= P_t + P_L - P_t \\ &= P_L. \end{aligned} \tag{4.1}$$

We also previously mentioned that the thermionic photon intensity can be inferred as

$$\begin{aligned} \text{Thermionic photons } P_t &= \text{Troughs}_{0\text{v}} \\ &= P_t. \end{aligned} \tag{4.2}$$

From these equations, we can also calculate the intensity of the Photoelectrons (e_L^-)

and Thermionic electrons (e_t^-) as

$$\begin{aligned} \text{Photoelectrons } e_L^- &= \text{Amp}_{400\text{V}}\text{- Amp}_{\cdot 0\text{V}} \\ &= (P_L + e_L^-) - (P_L) \\ &= e_L^- \end{aligned} \tag{4.3}$$

$$\begin{aligned} \text{Thermionic electrons } e_t^- &= \text{Troughs}_{400\text{V}}\text{-Troughs}_{0\text{v}} \\ &= (e_t^- + P_t) - (P_t) \\ &= e_t^-. \end{aligned} \tag{4.4}$$

The intensities of the photons and electrons produced in the experiment based on Equations 4.1-4.4 are plotted in Figure 4.10. Analysing Figure 4.10, we see that the laser photons have the highest intensity and are constant throughout the experiment. This is understandable as the intensity of the photons emitted from the laser are independent of the LaB_6 temperature or detector bias. The intensity of the thermionic electrons and photons are represented in red and yellow, respectively. As expected, they follow the same sigmoid shape as the crystal's temperature is reduced. Finally, the purple line represents the photoelectrons that appear to be successfully produced in this experiment. This proves that this setup, including our chosen cathode and light source, can produce photoelectrons.

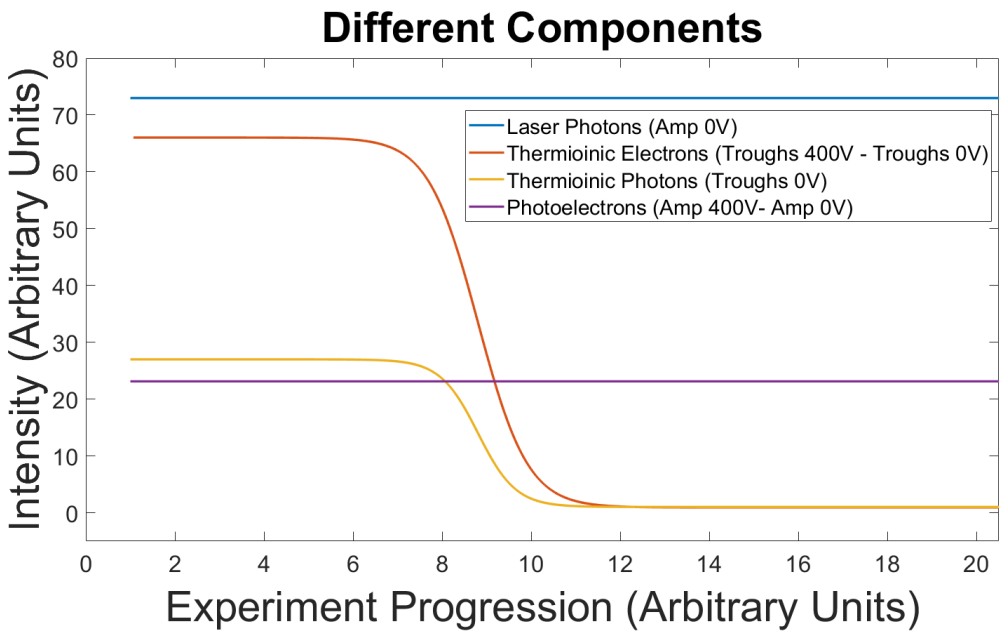

Figure 4.10.: *The intensity of the photoelectrons (e_L^-), laser photons (P_L) and thermionic electrons (e_t^-) and photons (P_t) calculated using equations 4.1, 4.2, 4.3 and 4.4 respectively.*

4.3. The Initial Optical Fibre Wehnelt Prototype

With the initial proof-of-concept results complete, the next stage was to design a prototype to be installed in an electron microscope. As mentioned, the deconstructed prototype was based on a JEOL TEM Wehnelt. However, as the AML has an older SEM, which was not often used, the initial prototype will be designed for a ZEISS EVO SEM to further lower risk. Once the prototype is complete with this lower-cost test bed, we can reassess adapting the prototype to a TEM.

4.3.1. Designing the Experimental Setup

Using SOLIDWORKS, I designed a setup in which a photoemission source could be retrofitted onto the thermionic electron gun of a ZEISS EVO SEM. The Wehnelt for this electron microscope varies from its previously seen TEM counterpart in that its base is flat, as shown in Figure 4.11. It was initially thought that a laser diode could be attached to the Wehnelt via a holder to introduce the light to the LaB_6 crystal. However, as the Wehnelt is biased and relatively close to the first anode, it was thought that having a large laser diode in the chamber could disrupt the electrostatic field that shapes the electron beam. Due to this, it was decided that introducing the laser light via vacuum-compatible optical fibres would be a less invasive approach and allow flexibility in changing the power and wavelength of the light introduced to the crystal.

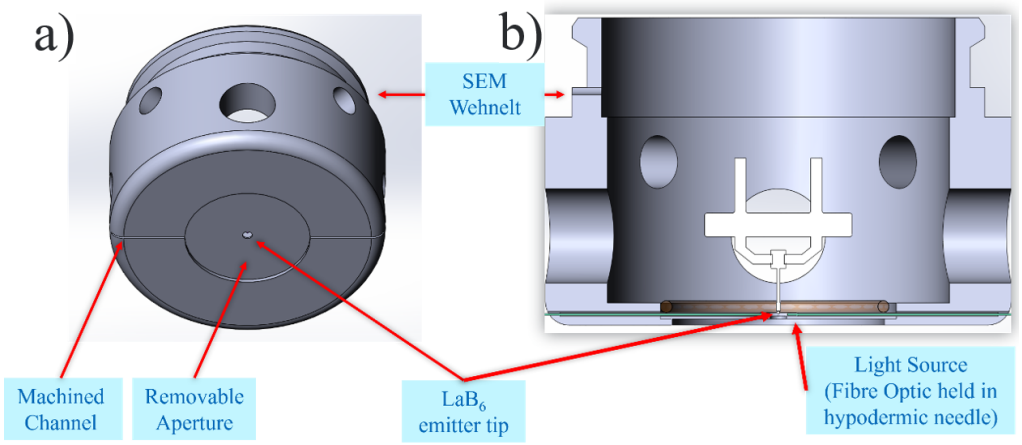

Figure 4.11.: *Model of the a) exterior and b) interior of a ZEISS EVO Wehnelt replicated in SOLIDWORKS with the adaptations of installing optical fibres into the Wehnelt included.*

A removable aperture is directly below the LaB_6 tip. This aperture dictates the shape of the electric field around the crystal, which significantly influences the

electron beam. Therefore, when deciding how to install the optical fibres, it is essential to alter this aperture as little as possible.

To retrofit optical fibres into the Wehnelt, components were required to securely hold and align the fibres such that the light exiting would strike the LaB_6. Considering this prototype aims to be low-cost, off-the-shelf hypodermic needles were chosen for this task. Being made of stainless steel, hypodermic needles are vacuum-compatible and have a small enough inner hole to hold appropriately chosen optical fibres securely. In SOLIDWORKS, the Wehnelt was adapted such that two slits were cut into it, and two modelled hypodermic needles were placed within these slits. The optical fibres could then be fed through the hypodermic needles so that the light could strike the LaB_6 crystal. This schematic can be seen in Figure 4.11, where we note that the removable aperture is unaltered by this retrofit.

4.3.2. Electrostatic Study of the Prototype

When designing this adapted Wehnelt, the removable aperture was kept intentionally unmodified to avoid affecting the electrostatics surrounding the LaB_6 crystal. Despite this, we must still investigate whether our introduction of optical fibres and hypodermic needles affects the electrostatics of the emitter and particle trajectories of the electrons. This was achieved using the multiphysics simulation software COMSOL.

Modelling of the Electrostatics

In the COMSOL electrostatics module, the following well-known equation is used to model electrostatic fields:

$$\mathbf{E} = -\nabla V \tag{4.5}$$

whereby E is the electric field, and ∇V is the derivative of the electric potential. To account for the polarisation within the solids of the model, the following equation is used:

$$\nabla \cdot \mathbf{D} = \rho_v \tag{4.6}$$

where $\mathbf{D}$ is described as the displacement field of an object when an electric field is applied to it. $\nabla \cdot \mathbf{D} = \rho_v$ accounts for the free charge in the object, with ρ_v being the free charge density of the object. To simulate the equipotential surfaces

in a model, we define the potential of each of the components, and COMSOL will simulate a graph of the equipotential surfaces. COMSOL can then convert these electric potential surfaces into electric fields using $\mathbf{E} = -\nabla V$. These electric fields can then be inputted into the charged particle tracing module to determine the electric forces applied to the emitted electrons.

Defining the Correct Electric Field

Before simulating our photoemitter prototype, we should consider the shape of the electric field we wish to produce to accelerate the particles down the column. The Wehnelt acts as a suppression field, dictating the shape of the electric field and, thus, the shape of the electron beam. In all thermionic electron emitters, this value for Wehnelt bias needs to be carefully chosen to create the positive gradient between the LaB_6 and the anode which can accelerate the electrons down the column. Figures 4.12 a) and c) show examples of the COMSOL geometry where both simulations have the same voltages on their components, only varying by the Wehnelt potential of -15275V in a) and -15175V in c).

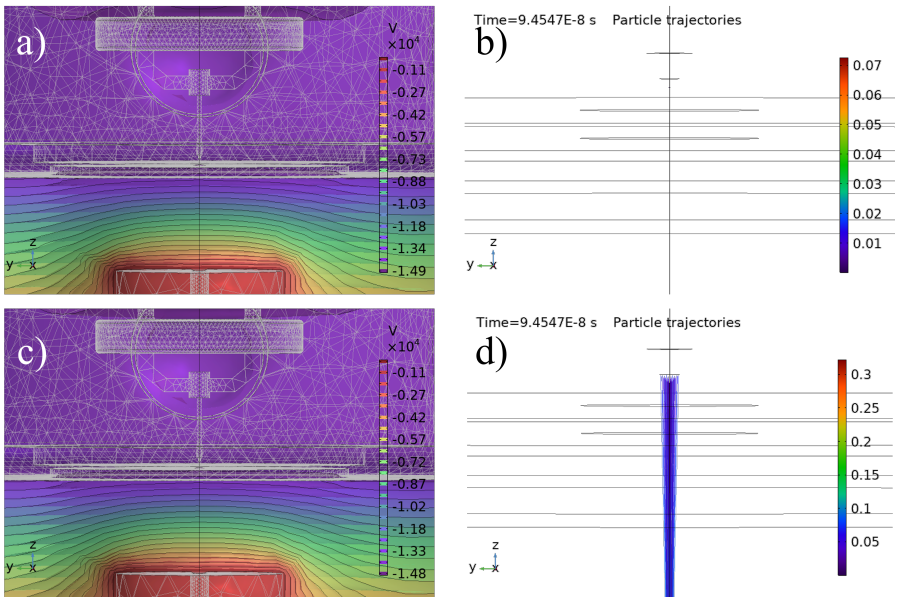

Figure 4.12.: *a) Electrostatics applied to the electron gun when the Wehnelt is too negatively biased. b) Particle trajectories of the electrons calculated from the electric fields in a). The electrons are not accelerated off the source and remain on the surface of the crystal. c) Electrostatics applied to the electron gun when the Wehnelt is biased correctly. Electrons are accelerated off the source towards the anode. d) Particle trajectories of the electrons calculated from the electric field in c). Note the colour axis in b) and d) indicates how radially far away the electrons are from the optic axis and is given in mm.*

Because the change in Wehnelt potential is so small between Figures 4.12 a) and c) it is very difficult to observe the difference in equipotential lines between the two

images. This small change in bias however does have a large impact on the particle trajectories of the electrons which can be seen in Figures 4.12 b) and d).

In Figure 4.12 a), the Wehnelt is too negatively biased, and the electrons remain on the surface of the source (Figure 4.12 b)). Figure 4.12 d) shows that the 200V reduction in the suppression voltage creates a positive potential gradient for the electrons to be accelerated down. Therefore, to achieve the required field, we must negatively bias the LaB_6 and the Wehnelt such that the electrons are repelled from the source and attracted towards the positively biased anode.

Of course, the size of the Wehnelt hole, the position of the LaB_6 relative to the hole and the distance between the anode and the Wehnelt hole also contribute to whether the electrons will be accelerated. However, all of these variables are fixed, besides the position of the LaB_6 relative to the Wehnelt hole, which was chosen as the standard positioning distance during Wehnelt installation for ease of future maintenance.

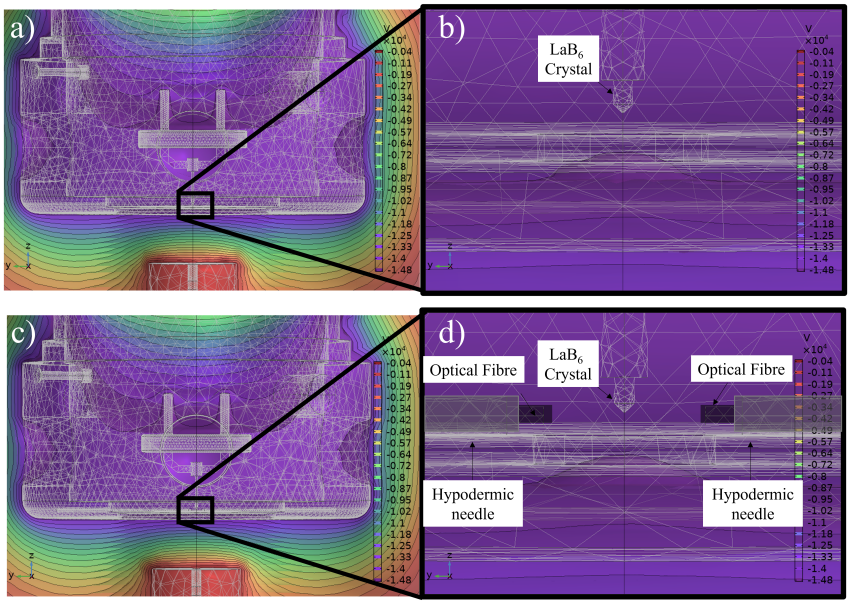

Figure 4.13.: *a) c) Electrostatics of the adapted electron gun without and with the hypodermic needles and optical fibres installed. b) and d) zoomed-in images of the components within a) and c) respectively, where the needles and hypodermic needles are highlighted in grey in d). Please note that this image was reprinted from the supplemental information of Quigley et al. 2023 (Reference number: [74]).*

Two electrostatic simulations of the Wehnelt were then compared. The first simulation was of the electrostatics of the Wehnelt without any extra equipment installed (Figure 4.13 a) and b)). The second a simulation of the Wehnelt with the needles and fibres installed (Figure 4.13 c) and d)). In this simulation the metal needles which contained the optical fibres were in contact with the Wehnelt and assumed

to be at the same potential. These electric fields calculated in the electrostatics module was then be inputted into the COMSOL charged particle tracing module to calculate the emitted electrons' trajectories. This step will be described in the next section.

Charged Particle Tracing Simulations

The charged particle tracing module in COMSOL can simulate a range of charged particles being released from a boundary or point. This module was used to determine how the simulated electric fields will affect the released electrons' trajectories. It is possible to set the number of particles, their initial energy, their shape and the position of their release point. Once the particles are released, how other factors influence them in the simulation can also be established. In our simulation model, the particles were defined as electrons by setting their charge as -1 and their mass to that of an electron (m_p). The force $\mathbf{F}_t$ that would then be applied to the electrons was defined by

$$\mathbf{F}_t = \frac{d(m_p \mathbf{v})}{dt} \tag{4.7}$$

where $\mathbf{v}$ is the velocity of the electron and dt is the change in time. This is a Newtonian description of the release of particles. However in the SEM electrons have an acceleration voltage applied to them, varying from 15keV for standard operation to 1 or 2keV for low voltage imaging. In either case this would accelerate the electrons to relativistic speeds therefore the relativistic correction term was applied to the following simulations. By turning on this correction the relativistic effects on the particle's mass were taken into account, and the mass m_p is calculated as

$$m_p = \frac{m_r}{\sqrt{(1 - \mathbf{v} \cdot \mathbf{v}/c^2)}} \tag{4.8}$$

where m_r is the rest mass and c is the speed of light in vacuum.

Next, wall conditions were set such that if the electrons were to strike any boundaries in the system's geometry, they would freeze, and their recorded velocities would be recorded as the velocity they had when they struck the wall ($\mathbf{v}_c$). Some secondary electrons may be released during such collisions in a real electron gun, but modelling these is not practical or necessary.

The electric force on the particle $\mathbf{F}_e$ was then described by the formula $\mathbf{F}_e = eZ\mathbf{E}$

where e is the magnitude of the electron's charge, Z is the electron's charge number, and $\mathbf{E}$ is the applied electric field. The particle beam is defined in terms of the Twiss parameter β and the I-RMS beam emittance ϵ_{rms}. The twiss parameter provides a general idea of the transverse size of the particle beam. While the I-RMS beam emittance ϵ_{rms} is the calculated average spread of the particles in phase space. These were defined as $\beta = 0.0101$m and $\epsilon_{rms} = 2.47 \times 10^{-10}$m, where the particles were set to be released from the 20μm microflat on the tip of the LaB_6 crystal. Electrons were also set to be released from the side walls of the LaB_6 by setting them to emit tangentially to the walls.

Finally, we specified the longitudinal velocity of the particles by defining the initial kinetic energy of the electrons $E_o = 0.37eV$. This was calculated from the equation $E_o = hf - \phi$ where hf is the impinging photon's energy and ϕ is the work function of the LaB_6 crystal. The initial velocity of the electrons $\mathbf{v}_o$ was then calculated from the initial energy (E_o) using the equation

$$|\mathbf{v}_o| = c\sqrt{1 - \frac{1}{(\frac{E_o}{m_r c^2} + 1)^2}} \tag{4.9}$$

where $m_r = m_e = 9.10938356 \cdot 10^{-31}kg$ the rest mass of an electron and c is the speed of light. The initial velocity of the electrons was therefore calculated to be $|\mathbf{v}_o| = 3.61 \cdot 10^5 m/s$.

With these parameters inputted charge particle tracing for both electrostatic models of the adapted Wehnelt with and without needles inserted was undertaken, and the results can be seen in Figure 4.14.

Based on the particle trajectories calculated, the adapted Wehnelt with the needles and fibres have no detrimental effect on the trajectory of the emitted electrons. There remains a possibility that the glass fibres may experience some charging because of our geometry, which may lead to some minor astigmatism after installation in the SEM. However, this could not be decoupled from other sources of astigmatism corrected by the operator during imaging.

As the removable aperture was unmodified in the design of this adapted Wehnelt (Figure 4.11), adding the slit to the Wehnelt does not appear to affect the electron beam's particle trajectories. Therefore, whether the needles and fibres are installed in the Wehnelt or not, it could still operate as a standard thermionic electron gun.

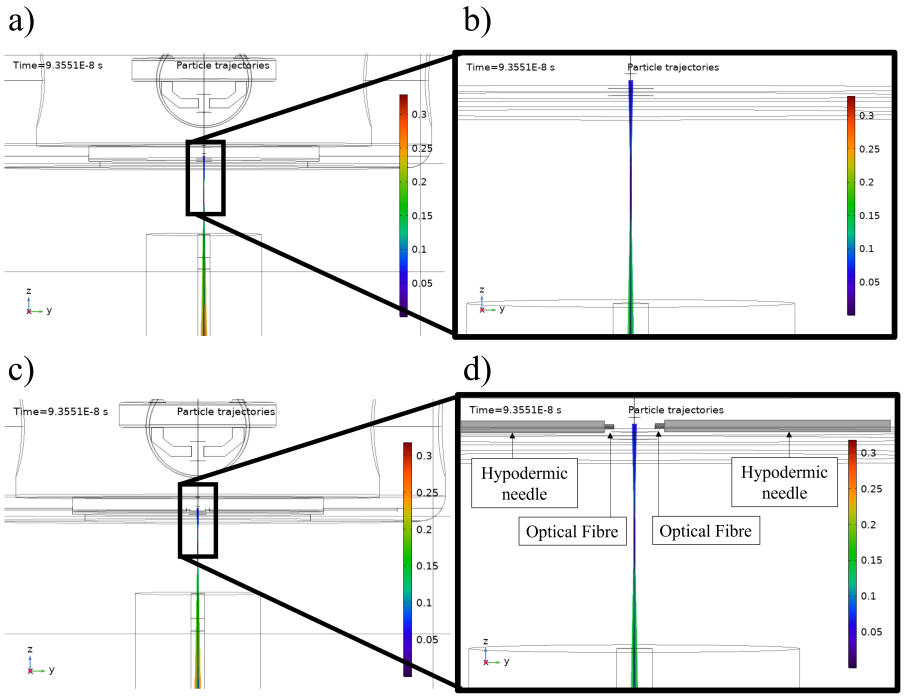

Figure 4.14.: *a),c) Particle trajectories of the model without and with needles. b) and d) are zoomed-in images of a) and c), respectively, where the needles and hypodermic needles are highlighted in grey in d). Note the colour axis indicates how radially far away the electrons are from the optic axis and is given in mm. Please note that this image was reprinted from the supplemental information of Quigley et al. 2023 (Reference number: [74]).*

4.3.3. Pre-installation Experimental Design and Results

With a model of the adapted Wehnelt complete and confirmation that the fundamental operation of the gun would not be affected by the alterations, hypodermic needles, which had an inner diameter of 0.159mm and an outer diameter of 0.312mm, were selected. Ultra-high vacuum-compatible optical fibres from Thor labs were chosen to be fed through the needles to guide the light to the LaB_6 crystal. The MV11L1 fibres were made of a differently doped silica core and cladding with a polyimide coating. They had an NA of 0.22 NA and were compatible with wavelengths between 250nm-1200nm. The core, cladding and coating had diameters of 100 ± 3 µm, 120 ± 3 µm and 140 ± 4 µm, respectively, as shown in Figure 4.15.

An electrical discharge machine (EDM) was used to cut a slit to match the needle dimensions (0.33mm diameter and 1.16mm depth) into a spare ZEISS EVO Wehnelt. The circlip, which holds down the Wehnelt's removable aperture, was positioned to clamp down on both the aperture and the hypodermic needles, securing them in the slit as shown in Figure 4.16 a).

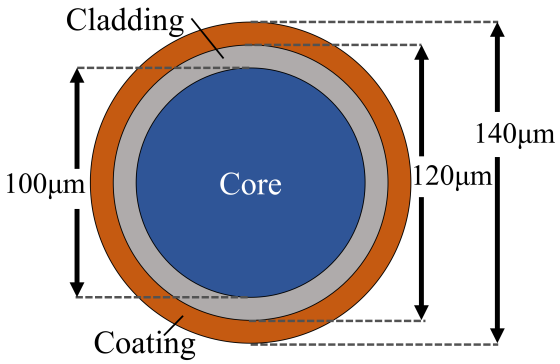

Figure 4.15.: *Diagram indicating the diameters of the core, cladding and coating of the chosen UHV optical fibre.*

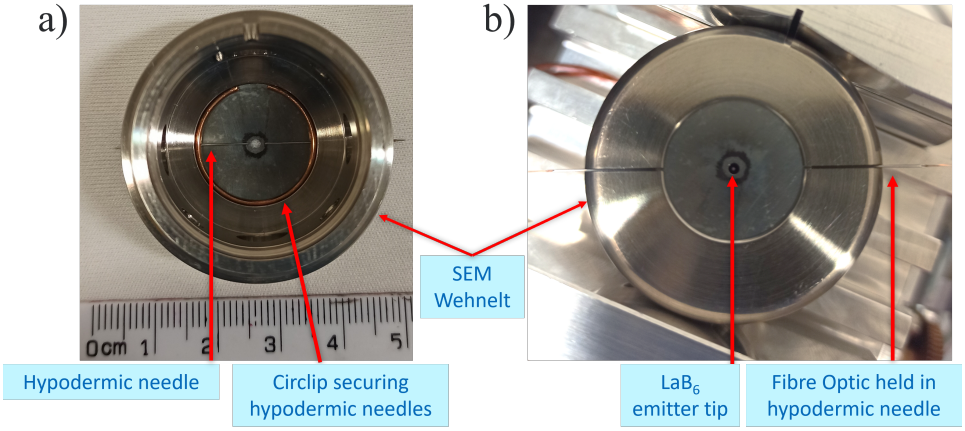

Figure 4.16.: *a) Hypodermic needle secured into Wehnelt slit via circlip. b) Optical fibres and hypodermic needles installed into the adapted Wehnelt.*

A simplified schematic of the position of the fibres relative to the LaB_6 in the Wehnelt and the angle at which the light exits them can be seen in Figure 4.17. The needles and ends of the fibres were positioned to be ∼1.6mm and ∼0.7mm away from the LaB_6 tip, respectively. The exposed length of the fibres outside the needle does not allow deviation from the light's initial trajectory towards the crystal. Assuming the maximum angle that the light can exit the fibre is the same as the maximum incidence angle of 12.71°, the radius of the cone of light when it strikes the crystal would be ≈0.162mm. Therefore, this cone is large enough to cover the 20μm microflat and side walls of the crystal. The light from the fibre should therefore strike the LaB_6 tip as they were positioned, as shown in Figure 4.17. Please note that as we are dealing with relatively high power lasers, it was too difficult to experimentally measure the final angular distribution intensity of the light due to safety reasons.

With all of the components installed, a proof-of-concept experiment was performed. The adapted Wehnelt was electrically isolated using PTFE tape and placed in

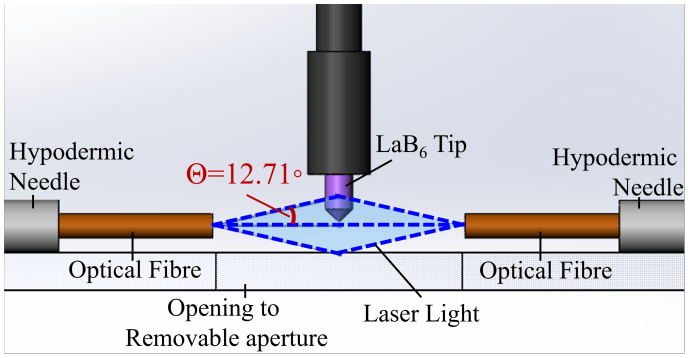

Figure 4.17.: *Simplified ray diagram of how the light exits the optical fibre to strike the LaB_6 tip. The needles and ends of the fibres are positioned ∼1.6mm and ∼0.7mm away from the LaB_6 tip, respectively.*

the vacuum chamber of the SEM. The Wehnelt aperture was then covered with aluminium foil such that any electrons produced would strike the interior of the Wehnelt or the foil covering. A picoammeter was connected to the Wehnelt via kapton wire, which entered the chamber through a flange containing an electrical connector. I then designed and 3D printed a holder to support and align the lasers and multimode collimators. These collimators couple the laser light to the vacuum-compatible optical fibres attached to a fibre feedthrough flange installed in the SEM chamber's door, as shown in Figure 4.18.

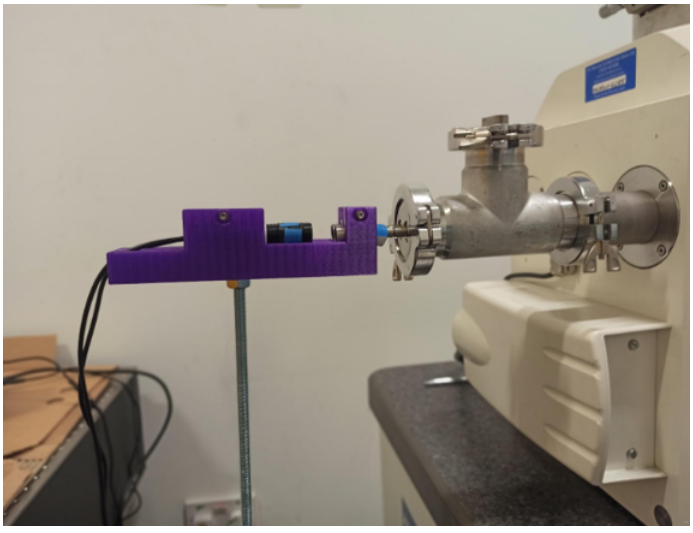

Figure 4.18.: *3D printed holder positioning the laser diodes such that they are coupled to the optical fibres via the multimode collimators.*

As vacuum conditions in the main chamber of the SEM were poor ($\sim 10^{-6}$ mbar), the crystal was heated to 1500K to prevent contamination. 405nm laser light from 10mW to 250mW was then set to strike the crystal continuously. Once again, it should be highlighted that a risk assessment was undertaken for this experiment with appropriate signage to prevent unauthorised users from entering the light-tight

room and the author operating the experiment wearing suitable laser safety glasses.

To separate the photoelectron current from the thermionic current produced by the crystal at 1500K, the current was recorded when the laser was on and off at different wattages. By subtracting both values, the photoelectron current could be calculated, and a graph of photoelectron current versus laser wattage can be seen in Figure 4.19.

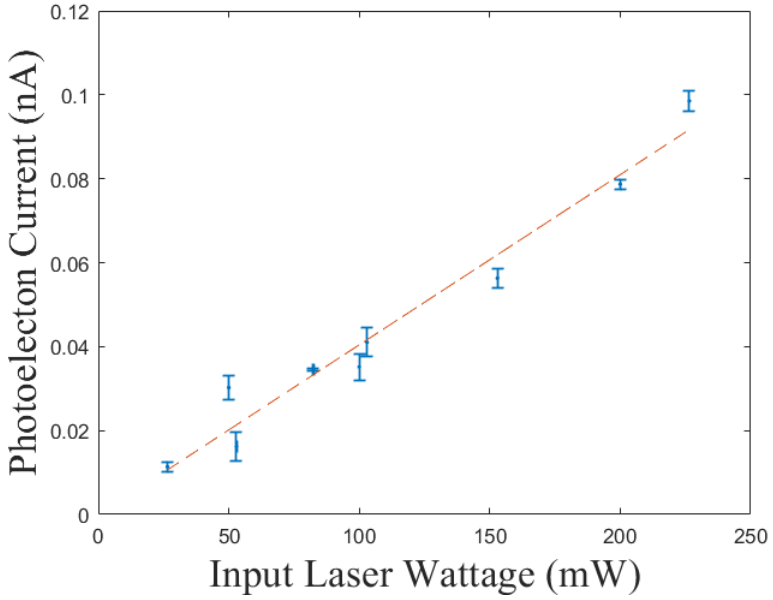

Figure 4.19.: *Graph of laser wattage versus detected photoelectron current from a laser continuously striking a LaB_6 crystal at 1500K.*

From Figure 4.19, we see that photoelectrons were detected at various laser wattages and that as the wattage increased, so did the photoelectron current.

Figure 4.19 was then used to calculate the quantum efficiency (η) of the LaB_6 struck with our 405nm (E_{ph}=3.06eV) laser diode. Photoelectron current (I_{ph}) versus the wattage of the laser (P_e) can be related by the following equation

$$I_{pe} = \frac{\eta \cdot e \cdot \eta_{electrical}}{E_{ph}} \cdot P_e, \tag{4.10}$$

where $\eta_{electrical}$ is the electrical efficiency of the laser and e is the charge of an electron. Equation 4.10 was derived in chapter 3, section 3.3. We see equation 4.10 is in the form

$$y = slope \cdot x + c \tag{4.11}$$

where is this case c=0. The slope of Figure 4.19 is therefore equal to;

$$slope = \frac{\eta \cdot e \cdot \eta_{electrical}}{E_{ph}}. \tag{4.12}$$

Rearranging equation 4.12, we can calculate the quantum efficiency η as follows;

$$\eta = \frac{slope \cdot E_{ph}}{e \cdot \eta_{electrical}}. \tag{4.13}$$

The energy of the photons produced from our 405nm laser is E_{ph}=3.06eV. The slope of Figure 4.19 was determined to be $0.4054 \cdot 10^{-9}$. The electrical efficiency of our laser can be calculated by dividing the optical power by the inputted power. For the 50mW, 100mW and 200mW lasers, this was calculated to be 0.1, 0.125 and 0.182, respectively. Taking the average of these values, the value for electrical efficiency used was $\eta_{electrical}$=0.1357. Inputting all these values into equation 4.13, the quantum efficiency was calculated to be $9.14 \cdot 10^{-9}$. Figure 4.20 plots our calculated quantum efficiency in chapter three's Figure 3.4, a graph of the quantum efficiency of LaB_6 versus photon energy for various literature values.

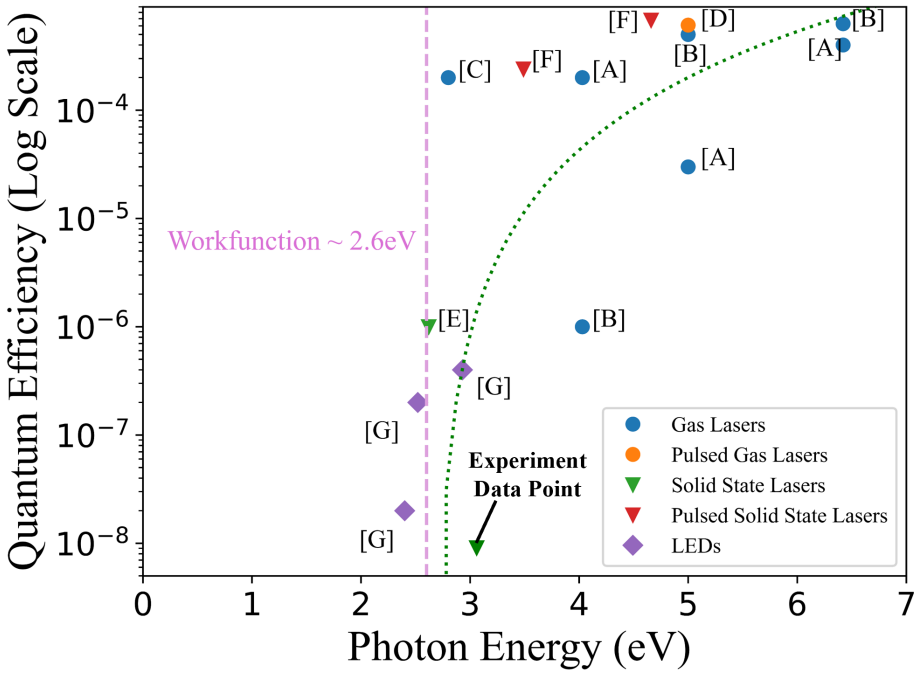

Figure 4.20.: *Replotted chapter 3 Figure 3.4 with our 405nm laser diode experimentally calculated quantum efficiency alongside the literature values; [A] Oettinger et al. 1990 [50], [B] Lafferty et al., 1951 [46], [C] May et al., 1990 [47], [D] Qian et al., 1995 [49],[E] Sawa et al., 2017 [51],[F] Leblond et al., 1996 [75] and [G] Konishi et al., 2012 [83]. The dashed line indicates the approximate work function of LaB_6 2.6eV. The trendline plotted in green is from Figure C.1 in Appendix C. This graph is reproduced from supplemental Figure 1 from Quigley et al. 2023 (Reference Number: [74]).*

Analysing our computed quantum efficiency plotted in Figure 4.20, we see that it generally aligns with the trendline calculated from our literature values. It may be slightly lower than expected, but this could be because not all of the photoelectron current is being detected by the picoammeter, given the simplicity of our experimental setup. Nonetheless, these were quite promising results, given the poor vacuum found in the vacuum chamber.

4.4. Conclusion

This chapter outlined a derisking experiment we undertook to validate that photoemission can occur from a setup containing a consumer-grade, as opposed to complicated research grade, 405nm laser diode and the LaB_6 cathode selected in the previous chapter. After successfully validating this initial proof-of-concept experiment, I created a model of a retrofittable prototype to be installed in a ZEISS EVO SEM. This was modelled in SOLIDWORKS, while COMSOL was used to confirm that the electrostatics and trajectories of the electrons, either thermionically or photoelectrically produced, would not be affected by the Wehnelt alterations. After confirming that the modifications would not affect the electrostatics, the adapted Wehnelt was assembled, and a bench test of its performance was performed in a vacuum chamber. Photoelectrons were detected when laser light at different wattages was directed to strike the LaB_6 crystal in the Wehnelt. The quantum efficiency of the LaB_6 struck with our 405nm laser light was then calculated to be $9.1 \cdot 10^{-9}$. This result is lower than expected but could be due to the picoammeter not collecting all the photoelectron current emitted. It also should be noted that this was calculated by using the work function specified in the LaB_6 manufacturers specification sheet.

With the essential operation of the prototype verified, the next step is to install it in the gun of the ZEISS EVO SEM. This process will be described in the next chapter, along with how the SEM parameters may need to be adjusted to optimise the functionality of the photoelectron emitter prototype.

Chapter 5.

The Initial Retrofit of the Photoemitter onto the Electron Gun

5.1. Introduction

Initial experimental results involving the prototype photoemitter were presented in chapter four. Proof that photoemission can occur with our chosen photocathode and light source was described, and details of the design of the initial photoemitter prototype were outlined. This included examining the electrostatics of the electron emitter and verifying that any adaptations to the original electron gun would not affect the emitted electrons' trajectories. The optical fibres were then installed into the adapted Wehnelt, and we ran a bench test which proved that photoemission could occur from the setup.

With this complete, the following chapter focuses on installing the prototype into the ZEISS EVO SEM. Initial images generated using the photoemitter are presented, and proof that photoemission is occurring, not thermionic emission from the laser heating up the crystal, is described. Issues with the initial light injection apparatus are then outlined, and a design of a new, improved light injection setup is detailed. An investigation is given into how the Wehnelt bias can be adjusted to extract the optimum amount of current from the electron gun. This analysis is accompanied by COMSOL simulations. A measure of photoelectron current produced during different laser power injections is then described. Finally, an investigation into beam current and SEM images generated after all the optimisations are applied is outlined.

Excerpts of this chapter are from 'Quigley, F., Downing, C., McGuinness, C., Jones, L. (2023) "A Retrofittable Photoelectron Gun for Low Voltage Imaging Applications in the Scanning Electron Microscope." Microscopy and Microanalysis, 29(5), 1610-

1617 '. Please note Clive Downing assisted with the installation of the adapted Wehnelt into the ZEISS EVO SEM.

5.2. Installation of the Adapted Wehnelt and Initial Experimental Results

Installing the adapted Wehnelt into the electron gun of the ZEISS EVO SEM needed to be carefully planned. This involved determining how the optical fibres installed in the Wehnelt would be fed out through the pumping tree of the EVO. I achieved this by building a digital twin of the electron gun chamber and pumping tree of the EVO using Solidworks (Figure 5.1). After examining the geometry of this virtual replica, it was decided that adding a t-piece to the pumping tree would allow the optical fibres to be introduced to the Wehnelt through an Accu-Glass FO1UV-2-K40 optical fibre feedthrough flange. This KF-40 flange had two inputs with an operating wavelength of 200-800nm, designed to be connected to 100μm core optical fibres. Note the KF in KF-40 stands for Klein Flansche where KF-40 is a standard size flange, sized by the largest nominal inner diameter tube that can be welded to it. In this case the largest nominal inner diameter is 40mm. Figure 5.1 shows this setup.

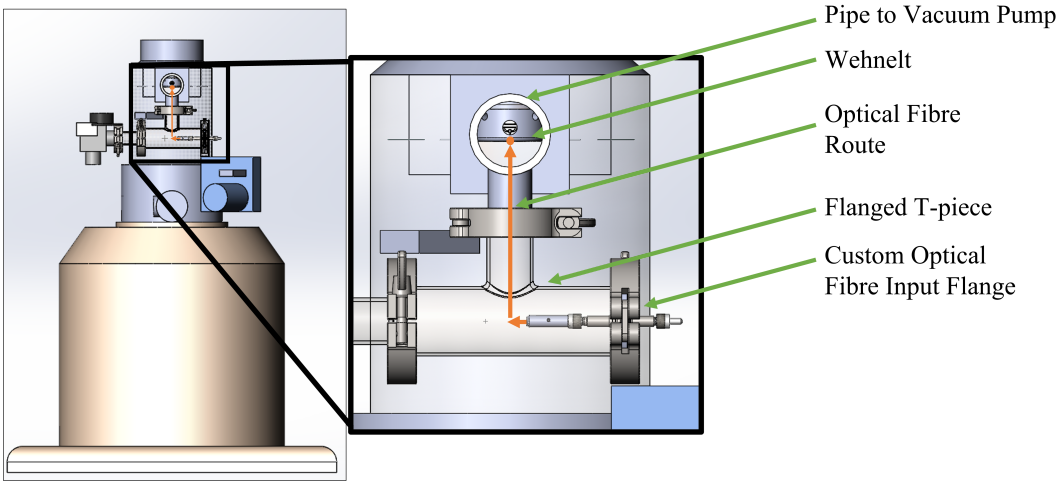

Figure 5.1.: *(Left) Digital twin of the ZEISS EVO SEM with the addition of a T-piece to introduce the optical fibres to the adapted Wehnelt. (Right) Magnified view of the vacuum side of the feedthrough flange. The vacuum compatible optical fibres are fed into the gun chamber through the pumping tree, as indicated by the orange arrows.*

These components were then installed into the SEM. Figure 5.2 a) shows the before and after images of the t-piece installed, demonstrating that any changes made to

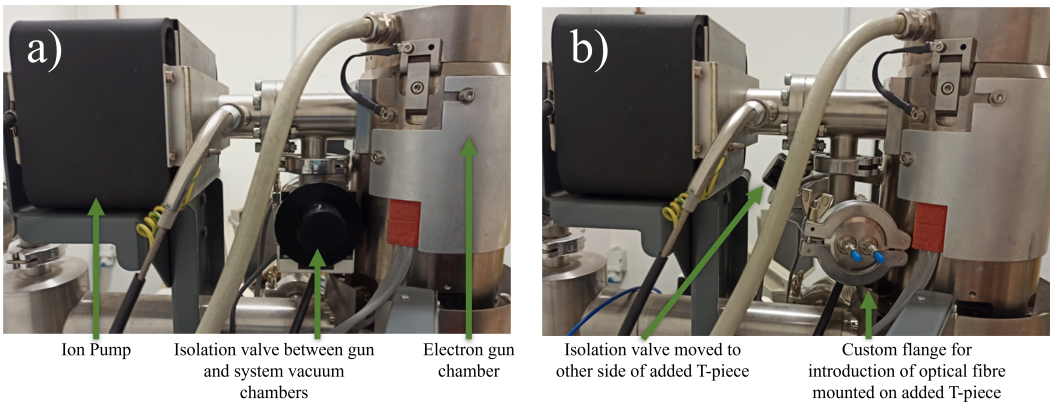

Figure 5.2.: *a), b) Pumping tree of ZEISS EVO SEM before and after the t-piece was mounted, respectively.*

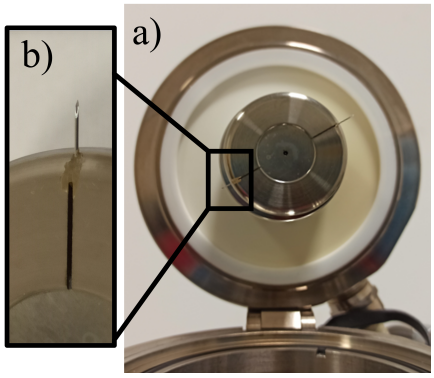

Figure 5.3.: *a) Adapted Wehnelt with needles installed, mounted in the lid of the electron gun chamber. b) Magnified image of Silver DAG securing the hypodermic needles in the Wehnelt.*

the pumping tree are reversible and do not affect the standard operation of the SEM.

The Wehnelt installed into the electron gun chamber just before the optical fibres were fed through the t-piece into the needles can be seen in Figure 5.3 a). Silver DAG was placed between the needles and the Wehnelt to ensure the needles would be secure when installed. The circlip was then used to clamp the needles in place. Silver DAG is a vacuum-compatible conductive paste commonly used in SEMs to make an electrically conductive path between an insulated sample and ground. Its vacuum compatibility and adeptness at adhering relatively light components together made it an excellent choice for securing the needles, as shown in Figure 5.3 b). Silver DAG was also used to ensure the optical fibres remained in the correct position once installed by applying the paste between the end of the needle and the fibre.

The light injection apparatus was then set up. An improved 3D printed holder used

in the pre-installation adapted Wehnelt experiments described in chapter four was used. This holder positioned the optical fibres so the laser light would be coupled into the multimode collimators hooked up to the feedthrough flange installed on the t-piece. Two continuous wave laser diodes of wavelength 405nm +/- 5nm (3.06eV ± 0.038eV) of power 100mW and 200mW in 16mm diameter cylindrical casings, were mounted in the 3D printed holder, as can be seen in Figure 5.4 a). Figure 5.4 b) highlights the laser cover placed over the laser diodes during experimentation to protect the SEM user.

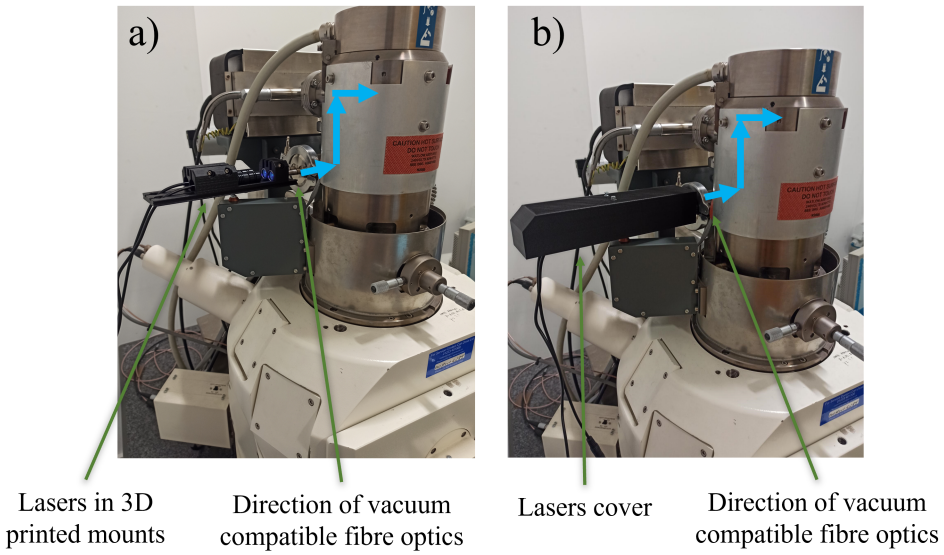

Figure 5.4.: *a) Laser diodes mounted onto the 3D printed holder installed onto the exterior of the ZEISS EVO SEM. b) Laser cover over laser diodes to protect the SEM user.*

A sample of titanium powder (often used in metal 3D printing) mounted on a carbon tab was then placed in the SEM sample stage. To prevent contamination, the crystal was cleaned by leaving it resistively heating at ∼1443K (via a 1.4A resistive current) for 20 minutes. The temperature of the crystal was then reduced, and Figure 5.5, one of the very first SEM images taken using the photoemitter prototype, was acquired when the laser was switched on and off multiple times.

Figure 5.5 shows that the titanium balls were successfully imaged when the laser was turned on and the light was striking the crystal. The intensity of the image then dropped to a negligible value when the laser was turned off.

After these initial promising images were taken, it was found that while two fibres were installed in the setup, one fibre seemed to deliver a superior amount of light to the crystal, indicated by a larger amount of photocurrent detected in a Faraday cup on the stage. This could be because the fibre shifted during installation and is therefore no longer directly pointing at the crystal tip and could be striking it at a

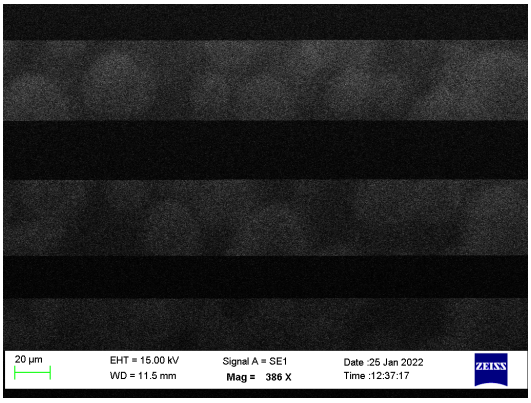

Figure 5.5.: *Preliminary image taken in the ZEISS EVO SEM of titanium balls, which were imaged when the laser was on and were not imaged when the laser was off.*

less than optimal angle. Due to this reason, only one laser diode and one fibre were used for all future experiments.

5.2.1. Validating Photoemission in the Electron Gun

With the installation of the adapted Wehnelt complete and some initial images captured, a key test in our experimental work was to verify that photoelectrons, not thermionic electrons, were being produced from the emitter when struck by the laser light. The LaB_6 crystal was heated to ∼1443K (via a 1.4A resistive current) for 20 minutes to remove contamination from the surface. Then, it was left at a resistive current of 0.96A (LaB_6 temperature of ∼1064K) for 20 minutes. A laser diode of wavelength 405nm and power of 200mW (Figure 5.6 a)) was then used to take a SEM image of the titanium powder. Halfway through the SEM image, the laser was turned off, and we see the intensity of the SEM image immediately decrease to a negligible intensity. This result confirms that the electrons were produced from the light striking the LaB_6 crystal.

The experiment was then repeated with a laser of wavelength 650nm with an identical power of 200mW. The wattage of the lasers were matched to ensure that the heat load on the crystal in both experiments were identical. This laser (at 650nm / 1.91eV) emits photons with insufficient energy to yield photoelectrons. A SEM image was then taken with the laser on/off again (Figure 5.6 d)). It is clear from Figure 5.6 d) that there is no change in intensity when the laser is on or off, and the intensity remains relatively negligible independent of the state of the laser. In both Figure 5.6 b) and d) laser light of the exact same wattage is striking the crystal therefore the heat load on the crystal is the same. The only difference in both experiments is that the light from the laser of wavelength 650nm would not have

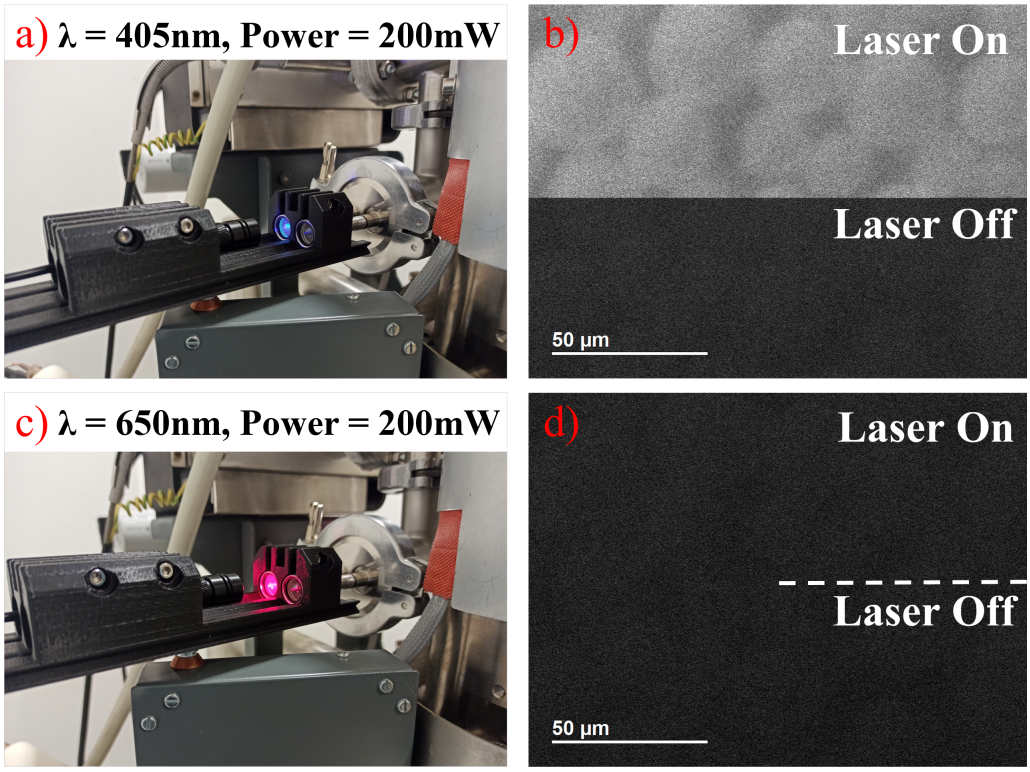

Figure 5.6.: *a) The exterior light injection setup containing a laser diode with wavelength=405nm and power=200mW. b) SEM image taken when the laser in a) is on and then switched off. c) The same setup as a) except with a laser of wavelength 650nm and power 200mW. d) SEM image taken when the laser in c) is on and then switched off. Please note this image was reprinted from the paper Quigley et al. 2023 (Reference number: [74]).*

the energy to stimulate photoelectrons. As an image of the titanium balls was only recorded in Figure 5.6 b) and not Figure 5.6 d), this confirm that the electrons being produced by the UV laser are not thermionic electrons being emitted due to the laser wattage heating the LaB_6 crystal, as in both cases, the heat load on the crystal is the same. This results, in turn, verify that the intensity seen with the 405nm laser was photoemission.

5.3. Optimising the Photoelectron Emitter Setup

Figures 5.6 b) and d) proved that photoelectrons were being produced from the photoemitter prototype. However, the image when the laser is on (Figure 5.6 b)) needs to be of a higher resolution and up to the standard of typical thermionic imaging in the ZEISS EVO SEM. The photoelectron emitter was operating under sub-optimum conditions, and improvements to its design could lead to improved image resolution.

Two avenues were followed to achieve this. Firstly the light injection setup was upgraded such that the laser diode was coupled more accurately to the multimode collimator, and subsequently, more light could be delivered to the surface of the LaB_6. Secondly the Wehnelt's bias was investigated such that it could be adjusted to draw an optimal amount of photocurrent from the crystal. What value to set this bias depends on the temperature the crystal is operating at, so this was also researched. All of these optimisations were examined in detail and presented below.

5.3.1. Design of New Light Injection Apparatus

While the 3D printed mount was a useful initial choice for the light injection setup, it unfortunately came with some disadvantages. Firstly, when the laser diode is in operation, the process of generating and forming the laser beam within the diode can cause the laser diode and it's surrounding casing to heat up. In general, the higher the power of the laser, the larger the amount of this waste heat is generated. While not a massive issue with the powers we are currently operating at, it would be beneficial to have the laser module contained in a heat sink to absorb some of this excess heat. As our 3D-printed mount was made out of plastic, it was quite an inefficient heat sink. A new holder made of a more thermally conductive material, such as metal, would be a helpful upgrade.

Secondly, the laser diodes must be aligned very accurately with the multimode collimators, or photoemission will not occur. Unfortunately, the 3D-printed mount was very rigid and did not allow sensitive adjustments in the alignment of the two components. Therefore, a light injection apparatus that would allow a more precise approach to aligning the laser diodes was required. This led to our design of a new light injection setup shown in Figure 5.7 b).

This light injection setup consists of two precision kinematic mounts to hold the laser diode and multimode collimator such that they are aligned on an optical rail. In this setup, an optical fibre FG200UEA from Thorlabs with a 0.22 NA, 200 μm $\pm$ 4 μm core, which accepts wavelengths between 250 - 1200 nm, was used to connect the multimode collimator to the flange with the fibre optic feedthrough. Its core, cladding and coating were made from pure silica, fluorine-doped silica, and acrylate, respectively. While its cladding and coating diameter were 220 $\pm$ 2 μm and 320 μm $\pm$ 16 μm, respectively.

It was found that this new light injection setup was far superior at allowing precise alignment between the laser diode and the multimode collimator. This was indicated by larger current readings being detected via a Faraday cup in the SEM

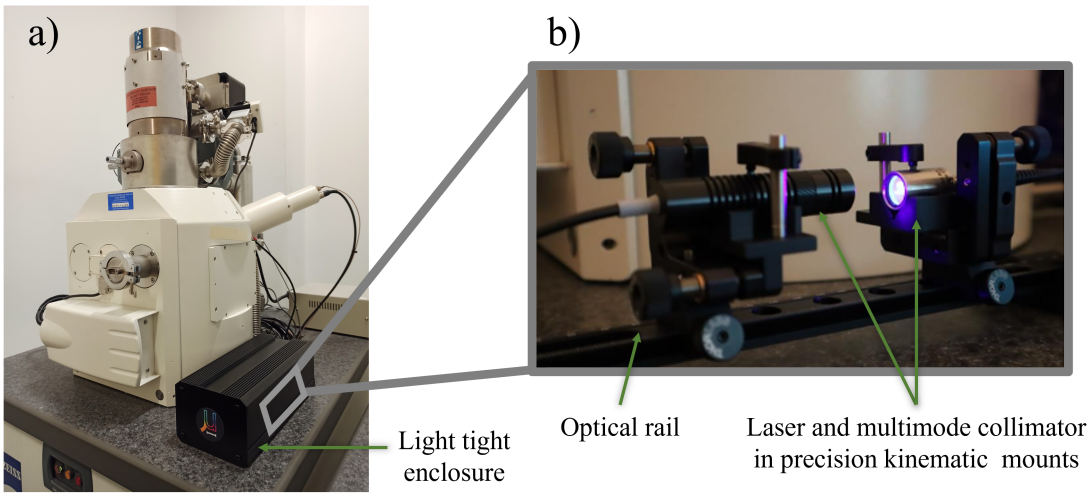

Figure 5.7.: *a) A light-tight enclosure containing b) the new light injection setup using Thor Labs kinematic mounts to align the laser diode to the multimode collimator, which is connected to the custom flange via an optical fibre.*

chamber compared to the old setup with the same laser diode and SEM operating parameters. In addition to this, as the precision kinematic mounts were metallic, they acted as a better heat sink for the laser diode. This improved heat absorption was an especially useful addition as a higher-power 400mW 405nm laser was installed into the apparatus. The substitution of the laser was performed as an increase in laser power should lead to a rise in photoelectron current. This new setup was placed in an improved light-tight metal enclosure, as seen to the left of the EVO in Figure 5.7 a).

5.3.2. Optimising Wehnelt Bias at Different LaB_6 Temperatures

With a new light injection setup implemented, the effect of the Wehnelt bias on the electron beam was investigated. The Wehnelt serves two principal functions: to focus the electron beam optimally through the anode and to extract electrons from only the very tip of the LaB_6 cathode. The former function was touched upon briefly during the previous chapter's COMSOL simulations, but Figure 5.8 illustrates the effect of focusing the electron beam more clearly.

Figure 5.8 a) demonstrates the shape of the electron beam when no bias is applied to the Wehnelt. No focussing effect occurs, the electron beam is spread out, and some current is lost, striking the anode and Wehnelt as it travels down the column. In Figure 5.8 b), we see the effect of optimal Wehnelt bias being applied to the electron beam. This bias focuses the electrons from the tip of the LaB_6 source such that they travel through the anode. It is crucial to focus electrons from the very tip of the crystal as they are more spatially coherent than those emitted at

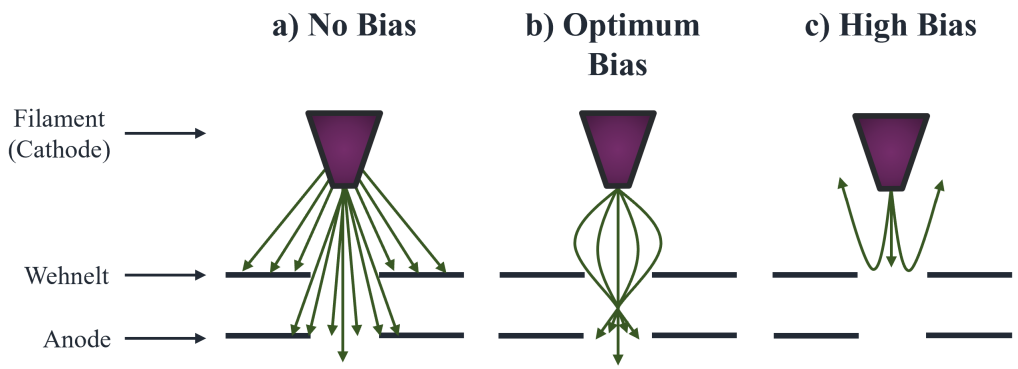

Figure 5.8.: *a) Illustration of the electron beam when no Wehnelt bias is applied and, therefore, no focusing effect occurs. b) Illustration of when there is an optimum Wehnelt bias, the electron beam is focussed optimally through the anode. c) Illustration of when the Wehnelt bias is too high, and the electrons are repelled away from the Wehnelt.*

high angles from the side walls of the source [86]. Spatial coherency reflects the phase difference of an emitted electron beam. If a source is perfectly spatially coherent all the electrons would be emitted from the same point on the source, therefore spatially coherency is governed by source size where the smaller the source the better the coherency. Finally, when the Wehnelt bias is too high (Figure 5.8 c)), the electrons are repelled away from it, and no current makes it through the anode. The energy of the electrons produced via photoemission and thermionic emission will be fundamentally different due to the nature of their production and will therefore be affected differently by a change in Wehnelt bias. This effect was therefore investigated to optimise the Wehnelt bias at extracting photoelectrons.

COMSOL Simulation of the Wehnelt Bias's Effects on Thermionic Emission

Figure 5.9 shows the geometry of a COMSOL model of the electron gun during thermionic operation. This model was built to simulate how a change in Wehnelt bias affected the electron beam. The settings used were as follows: LaB_6 temperature = 1324K (equivalent to 1.25A resistive current), LaB_6 potential = -15kV and anode potential = 0V. Electrostatic simulations were run, varying the Wehnelt bias between 0V to -15.32kV and using these, the particle trajectories were calculated. The LaB_6 tip can be viewed on the right hand side of Figure 5.9. The very top of the tip has a conical shape terminating with a 20μm microflat. The microflat has a <100> orientated single crystal at the tip which has a low work function for increased electron emission. The crystal is shaped in this way by the manufacturer such that the electrons will be selectively emitted from the tip by the wehnelt bias for a more spatially coherent source.

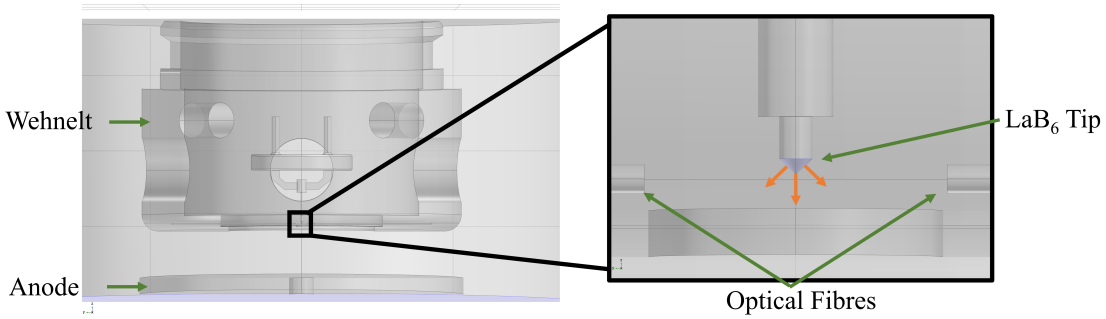

Figure 5.9.: *(Left) Image of the geometry of the Wehnelt and anode used in the COMSOL simulations. When the emitted electrons hit the purple boundary highlighted on the bottom, they were counted as having travelled through the anode. (Right) Magnified image of LaB_6 tip and optical fibres used in the COMSOL simulations. Note that the orange arrows indicate the boundaries and direction the electrons were emitted from during the charged particle tracing module.*

The particle release module in these simulations determined the velocity at which the electrons would be emitted by re-sampling the speed of the particles from a distribution based on the temperature of the boundary, which was set as the crystal temperature 1324K. Five particle trajectory simulations for different biases are shown in Figure 5.10.

After each simulation, the number of electrons to strike a wall below the anode was recorded (shown as the purple boundary wall in Figure 5.9). In this way, we could determine the intensity of electrons to travel through the anode versus the Wehnelt bias. A graph of this was plotted and is shown at the bottom of Figure 5.10, where a graph of the full range of Wehnelt biases from 0kV to -15.32kV can be seen in Figure F.1 in Appendix F. We see from Figure 5.10 a)-b) that as expected, as the Wehnelt bias increases, the more the electron beam is focused through the anode and the more the current travelling through the anode increases. This trend continues until the electrons begin to be retarded by the Wehnelt, causing the current to decrease and emission to occur only from the tip of the LaB_6 source (Figure 5.10 c) - d)). Despite the drop in current, the electron beam in Figure 5.10 d) would be the optimum condition to operate the emitter to achieve the most coherent electron beam for the highest quality of illumination [87]. Finally we see the current drop off to zero at the maximum bias in Figure 5.10 e).

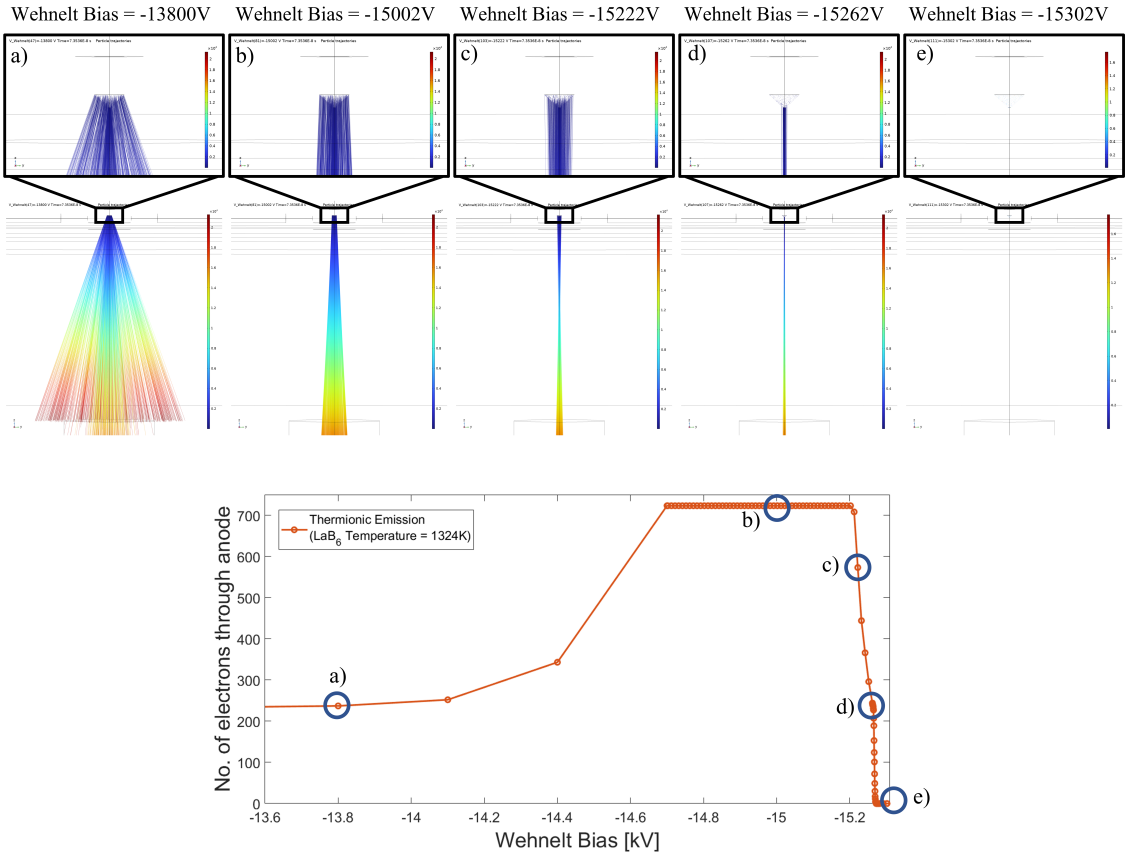

Figure 5.10.: *(Top) Images of particle trajectories at five different Wehnelt biases. (Bottom) Graph of the number of electrons to get through the anode versus change in Wehnelt bias. The Wehnelt biases in a)-e) are indicated on the graph. The optimum condition to operate the emitter to achieve the most coherent electron beam for the highest quality of illumination would be point d) (further details found in text).*

Experimental Results and Analyses

With the thermionic simulations complete, experiments were run in the EVO to see how electron beam current was affected by the change in Wehnelt bias during thermionic emission and photoemission. The schematic for the experimental setup can be seen in Figure 5.11, where the stage specimen current monitor was disconnected to electrically isolate the stage. An electrically isolated Faraday cup was placed on the sample carousel and connected to a picoammeter to record the electron beam current.

The crystal was heated to ∼1443K (via a 1.4A resistive current) for 15 minutes to minimise contamination. The crystal was then held at ∼1324K (via 1.25A resistive current) for 15 minutes, and the acceleration voltage of the SEM was set to 15kV. Unfortunately, we cannot directly control and cycle through Wehnelt bias. However, as advised by a ZEISS technician, changing "Beam Current" in the SEM software can indirectly change the Wehnelt bias. Therefore, different values of "Beam cur-

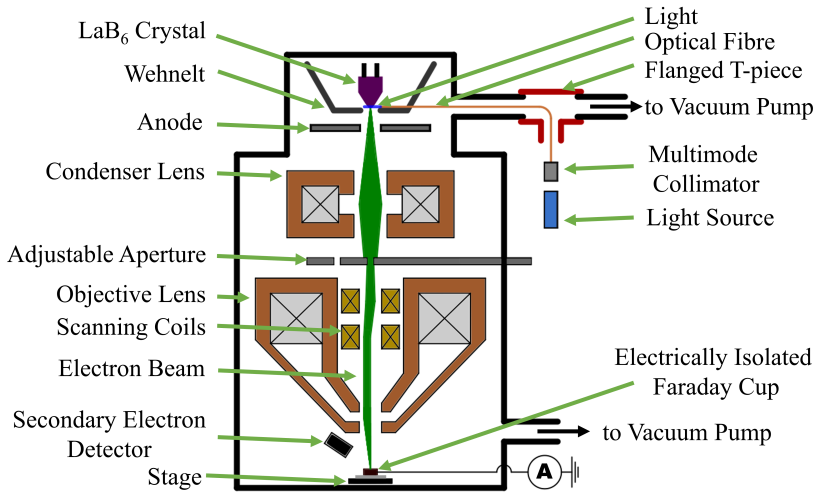

Figure 5.11.: *Schematic of the experimental setup of Faraday cup installed in ZEISS EVO SEM. Please note this image was reprinted from the paper Quigley et al. 2023 (Reference number: [74]).*

rent", which will from now on be referred to as Wehnelt bias with arbitrary units, were cycled through as the laser was set to pulse off and on every 20 seconds as the current was recorded on the picoammeter. The new light injection apparatus containing a 405nm, 400mW laser described in section 5.3.1 was used for these experiments.

Matlab was used to calculate the average beam current recorded over ten seconds after the laser had been on/off for five seconds. This value was taken as the recorded current at the corresponding Wehnelt bias. This experimental method and analyses were then repeated for the crystal temperatures of approximately 1443K, 1404K, 1264K, and 1282K, corresponding to a resistive current of 1.4A, 1.35A, 1.3A, and 1.2A applied to the crystal, respectively. The results of the current recorded when the laser was off and on versus the Wehnelt bias can be seen in Figure 5.12.

In Figure 5.12, all the current versus Wehnelt bias graphs were plotted together to analyse their overall trend as the cathode temperature increased. As expected, the greater the temperature of the crystal, the larger the current detected. Subsequently, when the laser was switched on, at certain biases, the total current was larger than when the laser was switched off. This current increase implies that photoemission occurs when the light strikes the crystal. To analyse these results in more detail, the current recorded at different temperatures was plotted on separate graphs, as shown in Figure 5.13.

Inspecting Figure 5.13 b), we see the current when the laser is off (orange) drops off at a Wehnelt bias around 6.5, while the current when the laser is on (yellow) drops

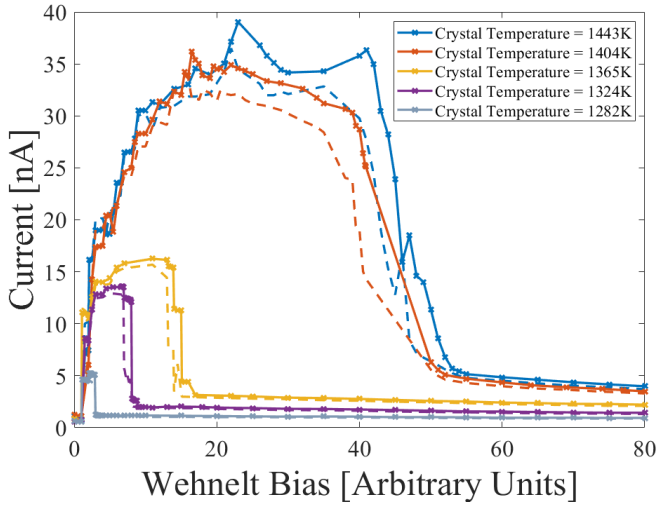

Figure 5.12.: *Current recorded versus the Wehnelt bias at different crystal temperatures. The solid line indicates the current measured when the laser was on, and the dashed line indicates the current measured when the laser was off at the indicated temperature.*

off at 8. This effect of the laser on current dropping off at larger Wehnelt biases than the laser off current can similarly be seen in Figures 5.13 c)-e). Thermally assisted photoemission (TAPE), previously mentioned in chapter three, section 3.5, could explain this phenomenon. TAPE can occur when the temperature of a cathode is increased. The thermal excitation causes changes in the electron energy distribution, which can result in some electrons occupying higher energetic states. This increases the probability of electrons being extracted by photons and can also increase the extracted electron's energy. This can increase the quantum efficiency and, subsequently, the photoelectron current [79].

This definition of TAPE corresponds to what we observe in the experimental graphs in Figure 5.13. As the Wehnelt bias increases, the purely thermionic current (produced when the laser was off) drops off faster than the current generated when the laser was on. This implies that when the laser is on, electrons with a higher energy are being produced compared to those produced during purely thermionic emission, as a more significant Wehnelt bias is required to retard them. This aligns with the idea that TAPE is occurring as photoelectrons generated in this way have a higher energy.

If the electrons being stimulated have a higher energy due to TAPE, chromatic aberration could also explain why the current when the laser is on drops off slower than the purely thermionic current. Chromatic aberration is the premature focus of lower energy electrons on the optic axis compared to higher energy electrons. Bücker et al. observed the phenomenon of slower (or lower energy electrons) being

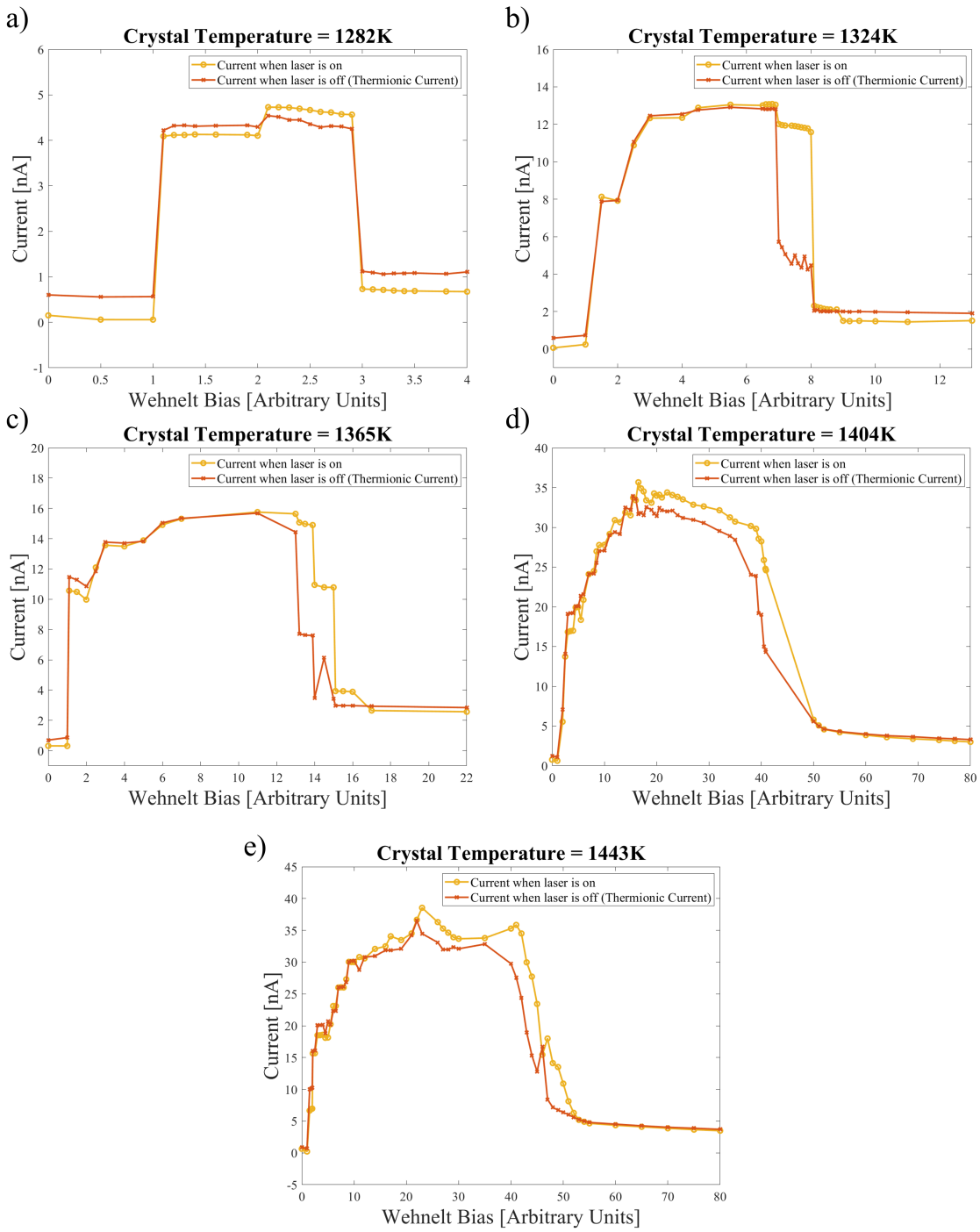

Figure 5.13.: *Graphs of current versus Wehnelt biases recorded when the laser was on and off for LaB_6 temperatures a) 1282K, b) 1324K, c) 1365, d) 1404K, and e) 1443K. Please note that the x and y axes have different scales in a)-e).*

filtered out of the electron beam by being blocked by an aperture due to chromatic aberration in the Wehnelt as shown in Figure 5.14 [39]. This could explain why the lower energy thermionic electrons are being filtered out at lower Wehnelt biases compared to the higher energy TAPE electrons.

The results here are consistent with the combination of chromatic aberration in the

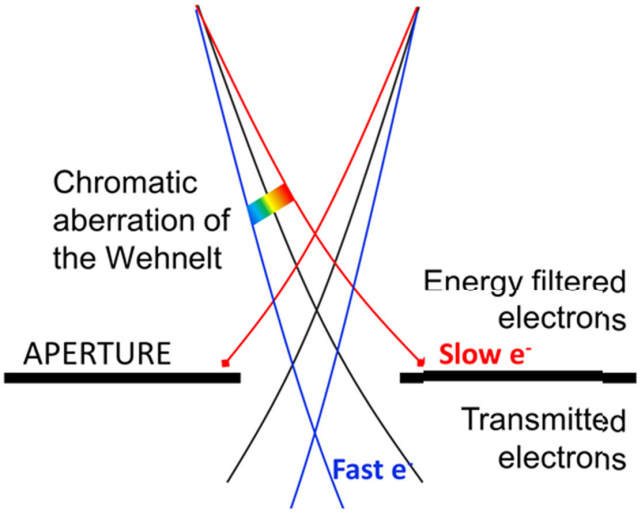

Figure 5.14.: *Graph of chromatic aberration in the Wehnelt causing lower energy electrons to be blocked by the aperture while higher energy electrons are focused through the opening. Reprinted from Ultramicroscopy, 171, K. Bücker, M. Picher, O. Crégut, T. LaGrange, B.W. Reed, S.T. Park, D.J. Masiel, F. Banhart, Electron beam dynamics in an ultrafast transmission electron microscope with Wehnelt electrode, 11, 2016, with permission from Elsevier (Reference number: [39]).*

Wehnelt and the electrons being of such a high energy that more Wehnelt bias is required to retard them, being the cause of the laser on current to drop off slower than the purely thermionic current.

A Comparison of COMSOL Simulations and the Experimental Results

With an initial analysis of the experimental findings complete, it would be helpful to reproduce the TAPE effect in COMSOL to see if it aligned with our experimental results and to further understand if our explanation for how the current changes with bias is correct. Unfortunately, reproducing the TAPE effect in COMSOL does not appear to be possible. The particle release module calculates the velocity of the emitted electrons by two different methods;

1. By using the inputted energy of the electrons.
2. By re-sampling the speed of the particles from a distribution based on the temperature of the boundary they are emitted from.

The first method could be used if the electrons were produced solely via photoemission. The value of 0.37eV could be set as the starting energy of the photoelectrons calculated from the equation; photoelectron energy = photon energy (3.06eV) - LaB_6 work function (2.69eV). For thermionic electrons, we could use the second option by putting in the temperature of the crystal during the experimental run.

However, to simulate TAPE, we would need to add 0.37eV to the simulated Boltzmann distribution of the temperature of the crystal in COMSOL.

Two simulations were run to see whether either of the two methods were approximately similar to the TAPE effect. The first simulation calculates the velocity of the electrons using their inputted starting energy. This starting energy was set as the energy the electrons would initially have when emitted ($E_{Emitted\,e^-}$). We defined this energy as;

$$E_{Emitted\,e^-} = E_{Photoemission} + E_{Thermionic\,emission} \tag{5.1}$$

where $E_{Photoemission}$ is the energy of electrons emitted via photoemission and $E_{Thermionic\,emission}$ is the energy of electrons thermionically emitted, in this case at 1324K. $E_{Photoemission}$ was previously calculated as 0.37eV. While the energy of the thermionically emitted electrons ($E_{Thermionic\,emission}$) at T=1324K was computed using the equation

$$E_{Thermionic\,emission} = kT, \tag{5.2}$$

where k is Boltzmann's constant in terms of electron volts. $E_{Thermionic\,emission}$ was calculated as 0.11eV, and the energy inputted into the COMSOL software was therefore $E_{Emitted\,e^-}$=0.48eV.

The second simulation involved method two, where the velocity of the emitted electrons was calculated from a distribution based on the temperature of the boundary they're emitted from. To define this boundary temperature we converted the photostimulated electrons energy of 0.37eV into a temperature using equation 5.2 rearranged to

$$T = \frac{E_{Photoemission}}{k}. \tag{5.3}$$

Using equation 5.3, the surface temperature of a cathode emitting electrons with an energy of 0.37eV was calculated to be 4294K. This temperature was added to the temperature of the crystal, 1324K. Therefore, 5618K was inputted as the boundary temperature of the crystal. Please note this temperature was inputted into the software in order to try calculate the energy range of electrons generated by the TAPE effect. This would not be the actual temperature of the crystal during any form of normal operation and is purely inputted for simulation purposes.

Besides the change in the initial release method of the electrons, both simulations

were run with the exact same parameters as the 1324K thermionic COMSOL simulation described previously. The graph of electrons detected through the anode versus Wehnelt bias can be seen in Figure 5.15 for all three simulations.

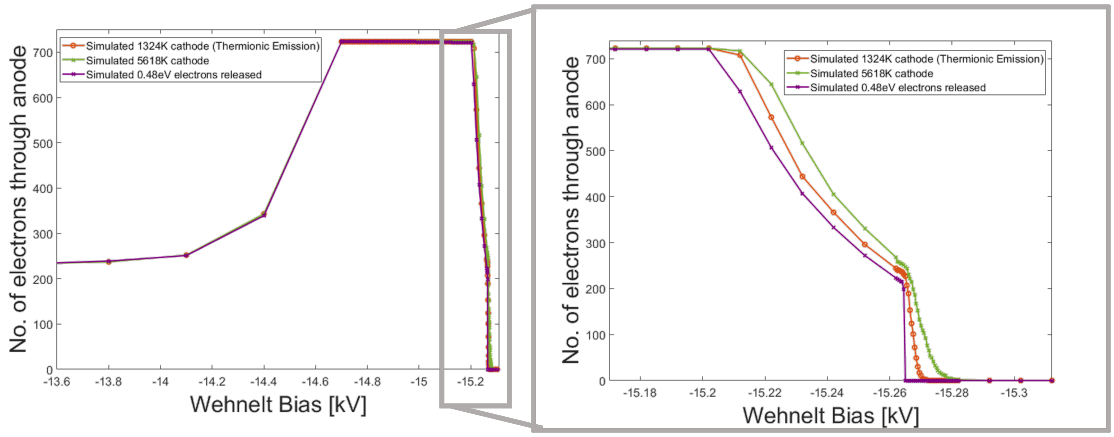

Figure 5.15.: *Graphs of the number of electrons to travel through the anode versus the bias of the Wehnelt for three simulations with different emission release conditions (please see text for more details).*

From the right-hand graph in Figure 5.15, we find that as the 5618K cathode simulation has a sizable thermal spread, its electrons drop off slower than that of the lower thermal spread 1324K cathode simulated electrons, with the 0.48eV electrons dropping off the quickest due to having had no thermal spread at all. Realistically, any electrons emitted from a source will have some sort of energy-spread; therefore, it is not viable to compare the 0.48eV simulation with the experimental results. The simulation of the 5618K plot's shape and slope matches the experimental results of the laser-on current more closely and was therefore used in the following comparison of the experimental and simulated data. For this comparison, the current when the laser was on and off was subtracted from one another for the experimental data recorded when the crystal temperature was 1324K, (plotted in Figure 5.16 a)).

In Figure 5.16 a), we see the curve in blue (the difference between the on and off current), peaks at a high Wehnelt bias when the thermionic current begins to drop off. In Figure 5.16 b), the 5618K simulated cathode graph was subtracted from the pure thermionic emission 1324K cathode graph in Figure 5.15. We observe that the blue curve peaks at a high Wehnelt bias, just as in the experimental results.

It is clear, however, from Figure 5.16 that the simulations do not exactly match the experimental results. The two main differences are the number of electrons detected at high Wehnelt biases and the ratio of the peak of the blue curve to the thermionic curve. Comparing Figure 5.16 a) to b), we notice that in the simulations, the electrons drop to zero at high Wehnelt biases, while in the experimental results, the

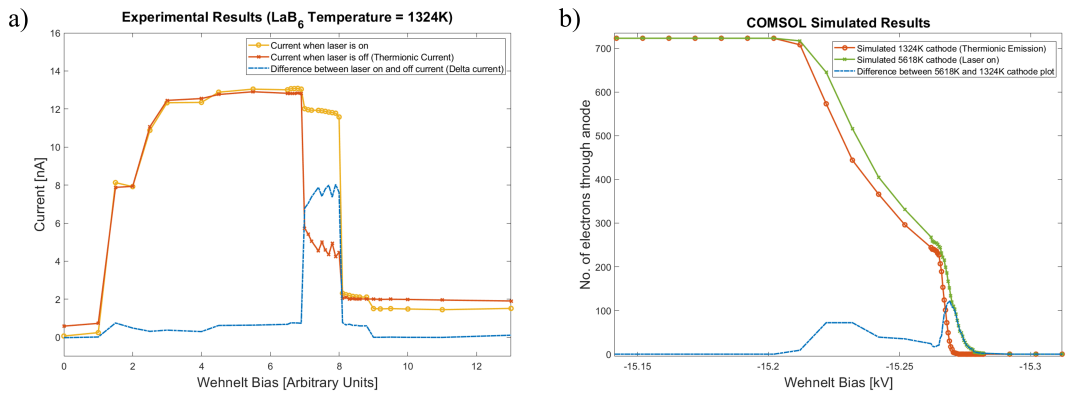

Figure 5.16.: *a) Graph of the current versus the Wehnelt bias when the laser was on and off and the difference between the two currents. These experimental results were recorded when the crystal temperature was 1324K. b) Graph of the COMSOL simulated results for a cathode simulated at 1324K and 5618K, and the difference between the number of electrons to have traveled through the anode for the two results. Please note the y-axis in a) and b) have difference units. This is because we could not directly control and cycle through Wehnelt bias in our experiments. However, as advised by a ZEISS technician, changing 'Beam Current' in the SEM software can indirectly change the Wehnelt bias and can be referred to as Wehnelt bias with arbitrary units. This value for Wehnelt bias was used in our y-axis in Figure a). In our simulations the Wehnelt bias can be directly measured as shown in b). This is the reason the y-axis varies in values between a) and b) and why it is the overall trend of the graphs that must be considered when comparing them.*

electrons drop off to a baseline current, in this case, ∼2nA. Interestingly, during all of the different crystal temperature experiments (Figure 5.13 a)-e)), the thermionic current always appears to have a larger current at these biases than when the laser is on. This could be because the Wehnelt bias is being swept through indirectly during our experiments via the "Beam current" parameter in the SEM software. The software could have built-in limits, not allowing a bias to be introduced that causes no electrons to travel down the column. This is supported in a paper by Bigelow, who notes that because the emission current self regulates its bias voltage, if there's no electron emission, there would be no emission current which means no bias voltage. However if there is no bias voltage, there would be nothing to prevent electron emission. Therefore as the gun is self-biased it is impossible to completely cut off the electron emission [86]. This self-biasing effect is not taken into account in our comsol simulations and explains why the current is completely cut off at high biases. More information about how the self-biasing operates can be found in Chapter 4 Section 4.2. A potential reason more thermionic electrons than TAPE electrons are being detected could be because the EVO would have been aligned for thermionic electrons. Thermionic electrons could therefore travel down the column more efficiently than the higher energy TAPE electrons.

The ratio of the current at the peak of the blue curve to the current of the thermionic curve at the same bias value in Figures 5.16 a) and b) is another discrepancy between the experimental and simulation results. In the experimental results, this ratio is ∼0.54, while the ratio in the simulation is ∼0.25. It seems our simulations' results are inconsistent with the experimental findings. This could be due to two reasons. Firstly, a more accurate depiction of the TAPE effect would be simulating the emitted electrons energy from a range where an energy of 0.37eV was added to a Boltzmann distribution at a temperature of 1324K. Unfortunately, this was not possible to do with our COMSOL model. Secondly, we believe chromatic aberration may be occurring in the Wehnelt. However, the effects of chromatic aberration have not been included in our simulations. These reasons could cause the discrepancies between our experimental and simulated results.

Alongside the simulation's limitations, the experiments proved quite challenging, with the picoammeter being very sensitive to any electrical noise in the room. Therefore, based on literature, we can only infer that the TAPE effect is causing the general trends seen in our results. However, for future work, more rigorous simulations and higher-quality instrumentation would be very beneficial in more conclusively determining how the Wehnelt bias impacts the electron beam current during different forms of electron emission.

Wehnelt bias and Cathode Temperature

Based on our analyses of the Wehnelt Bias's effects on current, it is evident that at a certain bias, there is a higher ratio of thermally assisted photoelectrons to thermionic electrons. For Figures 5.13 a)-e) the laser on and off currents were taken from one another, and this difference will be called the delta current for simplicity. A plot of the laser on, off, and delta currents at the bias that produces the peak delta current for all the different temperatures can be seen in Figure 5.17. The ratio of the maximum delta current to the current of the laser off at the same bias value was then calculated and can be seen rounded to two decimal places above each temperature in Figure 5.17.

Figure 5.17 can be used to determine which temperature would produce the maximum ratio of TAPE to thermionic current. We see that at high temperatures, the thermionic current dominates. As the temperature is reduced, the thermally assisted photoelectrons start to increase as the thermionic current decreases. This trend peaks at 1324K, and then the thermionic current dominates again. This is most likely due to the crystal contaminating at lower temperatures, causing an increase in cathode work function and a decrease in photoemission. With our current

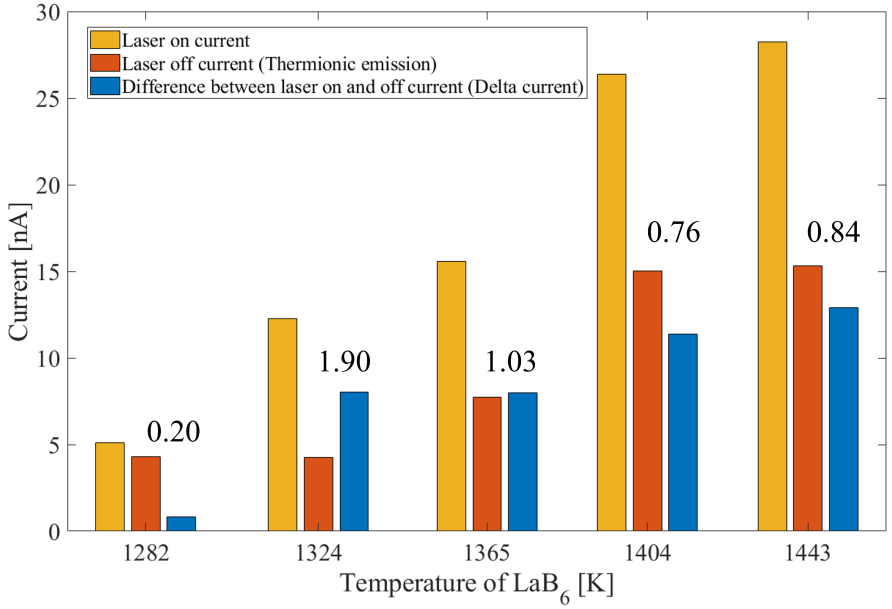

Figure 5.17.: *Bar chart indicating the laser on, off, and delta current at different LaB_6 temperatures. The numbers above each of the bars indicate the ratio of the max delta current to the current of the laser off (thermionic current) at the same bias value.*

photoelectron emitter setup, we see that 1324K is the optimal temperature to operate it at when hoping to image with thermally assisted photoelectrons. It should be noted, however, that as mentioned in chapter three, section 3.5, operating the cathode at a temperature above 1200K can cause the energy-spread of the electrons to increase. This is something to be aware of when designing future prototypes. A higher vacuum such as that in the $10^{-8} - 10^{-9}$ mbar range or a cathode that contaminates less easily in a poor vacuum would be preferred so that operation of the emitter at lower cathode temperatures is a viable option.

5.4. Evaluating the Optimised Emitter

5.4.1. Analysing the Photoelectron Current and Laser Power Relationship

A higher-power laser was used in the new light injection setup to increase photoelectron current. To determine the effectiveness of this upgrade, a quantitative investigation into the impact of the laser power on the electron beam current was performed. The same setup as Figure 5.11 was used where a Faraday cup was electrically isolated, connected to a picoammeter, and placed in the SEM chamber. The LaB_6 was heated to ~1443K (via a 1.4A resistive current) for 15 minutes to

minimise contamination. The crystal was then set at ∼1324K (via 1.25A resistive current), the optimum temperature of thermally assisted photoemission over thermionic emission. The Wehnelt bias was then set so that an optimum number of thermally assisted photoelectrons were emitted relative to thermionic electrons.

A Thor Labs step variable neutral density filter was used to determine how the electron current changes with laser power. Each section of the neutral density filter had a different optical density and would reduce the intensity of the light and, therefore, the laser power by a set amount. The filter was placed between the 400mW, 405nm laser, and multimode collimator in the new light injection setup shown in Figure 5.7. The laser light was turned on and off for 20 seconds at each section three times, and the average on, off and delta currents were calculated. A plot of the calculated laser wattage versus the detected current in the Faraday cup for the laser off and delta current can be seen in Figure 5.18.

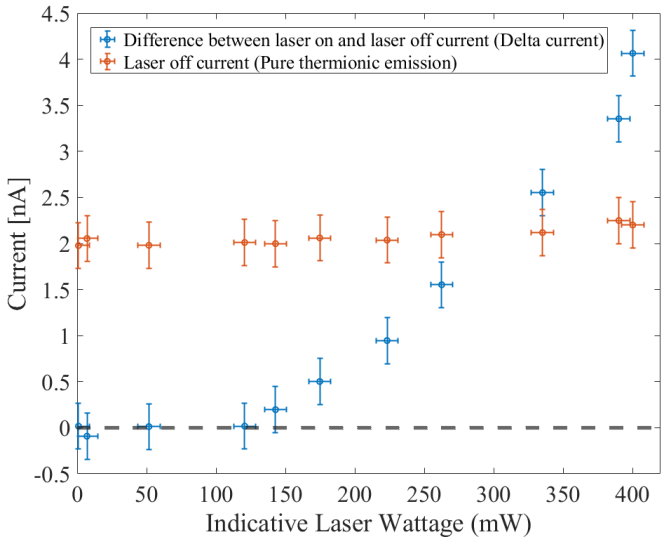

Figure 5.18.: *Graph of the laser off current and delta current at different laser wattages.*

We find that as the laser wattage increases, the thermionic current remains constant, and the thermally assisted photoelectron current (delta current) increases. This implies that the larger the laser power, the more thermally assisted photoelectrons are produced. This demonstrates that the higher-power 400mW laser was a useful upgrade and means that an even higher-power laser could benefit future prototypes.

5.4.2. The Efficiency of the New Light Injection Apparatus

An analysis of the performance of our light injection setup would be helpful in determining its efficiency. The photoelectron current (I_{ph}) and thermionic current (I_{th})

to strike the sample was estimated to accomplish this. This was achieved by disconnecting the stage specimen current monitor (i.e., electrically isolating the stage) and measuring the current I_{ph} at the SEM stage using a Faraday cup connected to a picoammeter. The largest possible aperture of 750 µm was placed in the SEM for the following experiments to minimise measurement uncertainty. Technicians mainly use this 750μm aperture for servicing the microscope, and it is comparable to having no aperture in the SEM. The current when the laser (405nm and power 400mW) was off was taken as I_{th}, and the current when the laser was on minus I_{th} was taken as I_{ph} (formally known as the delta current).

To determine the efficiency of the emitter, the ratio of the thermionic current at the microflat for LaB_6 temperatures between ∼1282K-1443K (1.2A-1.4A resistive current) versus the thermionic current at the stage (I_{th}) needed to be determined during normal thermal emission. The current emitted at the LaB_6 at a specific temperature needed to be calculated to compute this ratio. Our crystal was a Kimball Physics LaB_6 cathode, model ES-423E, style 90-20. This means it had a 20 µm diameter microflat at its tip. Kimball Physics has released a LaB_6 specification sheet with a graph of the emission current versus the heating current of the crystal for 15,40,100,200 µm diameter microflats. Using a Matlab gridded interpolation function, we can calculate the emission values for a 20 µm diameter microflat from the specification sheet's values. The specification sheet also gives the heating current versus the true temperature of the LaB_6 crystal, so the temperature of the crystal versus the emission current can also be calculated. The ratio of the thermionic current at the sample divided by the thermionic current at the tip can then be computed. For example, at 1282K, the thermionic emission at the tip was determined to be ∼19.6 nA, the current detected by the Faraday cup was ∼4.5nA, so 23.2% of the current made it down the column to the sample. From 1282K-1443K, the percentage of the current that passes down the column varied between 9.8% and 29.6%. Please note that this value does not consider any thermionic electrons generated outside the microflat of the crystal, however, the bias of the Wehnelt has been set to try optimally select electrons from the microflat and suppress those electrons emitted elsewhere from the crystal.

Using this thermal ratio and the I_{ph} measured at the sample, the number of photoelectrons generated at the tip of the LaB_6 could be calculated. This calculation assumes that this thermal ratio between the thermionic electrons generated at the tip and those detected at the sample is the same as the ratio of photoelectrons stimulated at the tip and detected at the sample. Using the Faraday cup, the difference in the current detected when the laser was on and off was taken as the photoelectron current at the sample I_{ph}. By dividing I_{ph} by the ratio of the thermionic current to

make it down the column at the same LaB_6 temperature, we can therefore calculate the photocurrent emitted at the tip. At the previous LaB_6 temperature of 1282K, the I_{ph} detected was 0.8nA, so the computed photoemission at the tip would be ∼3.6nA.

Using equation 4.10 derived in chapter 3 section 3.3;

$$I_{pe} = \frac{\eta \cdot e \cdot P_e \cdot \eta_{electrical}}{E_{ph}} \tag{5.4}$$

we can calculate the total photocurrent produced if 100% of the light emitted by the laser were to strike the crystal. The expected quantum efficiency of LaB_6 with our crystal's work function of 2.69eV (value provided by the manufacturer) struck by a photon with energy 3.06eV is taken from corresponding the value given in the trendline in Figure C.1 in Appendix C (more details on this graph can be found in chapter 3 section 3.3). From equation 5.4, it was calculated that theoretically, 182nA of photocurrent should be produced from a 400mW 405nm laser diode. This is clearly an overestimation and implies only 2% of laser light gets from the diode through the optical components to strike the LaB_6 tip and cause photoemission at a crystal temperature of 1282K. For crystal temperatures ∼1282K-1443K, this value was between 2%-72%. We believe this number varies so largely with temperature because it is a product of the efficiency of the light to strike the crystal and the efficiency of the photoelectron emission from the crystal. As photoemission efficiency will increase with increased crystal temperature this could influence our calculation of the percentage of light to travel through the optical components and cause photoemission, and therefore cause the percentage to vary largely from 2%-72%. This number indicates a large scope for design improvement in implementing the photoemitter.

This could include parabolic mirrors or ball lenses to improve the focusing of the laser, as in the current setup, the fibres are simply pointed at the crystal, and the large angle at which the light exits the fibre ensures some photons will strike the tip of the crystal. Some of the light lost could also be due to laser losses, such as reflectivity at the LaB_6 surface. It is also possible that a sizable fraction of laser light would have been lost coupling the 100μm core fibre to the 200μm core fibre, but no more than 50%. To eliminate this, a future iteration could replace the 200μm core fibre with a more suitable core fibre, eliminating this as a possible source of loss in delivering the laser light to the LaB_6 tip.

5.4.3. SEM Images Captured Using the Optimised Setup

With the improved light injection setup and the knowledge of how to optimise the Wehnelt bias complete, we captured new images of the titanium balls in the SEM at a cathode temperature of 930K (Figure 5.19 b)). It should be noted that none of the previously described Wehnelt bias experiments were run at a cathode temperature below 1264K due to the picoammeter's inability to detect the low levels of current produced. However, the secondary electron detector was sensitive enough to detect the current generated at such low temperatures; therefore, images could be formed below 1264K, especially if low scan speeds were used. Now that the general shape of the current versus the Wehnelt bias curve was understood, the bias could be adjusted so that the maximum amount of photoelectron current was detected via the secondary electron detector for our new images.

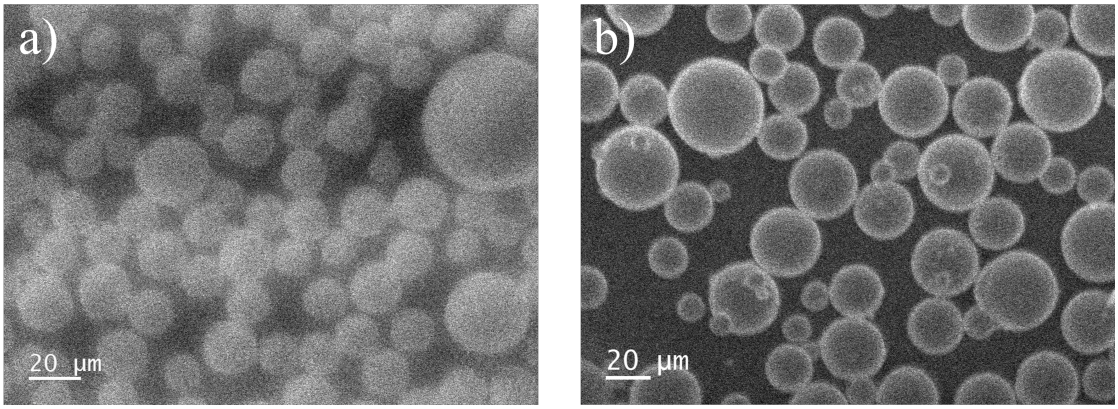

Figure 5.19.: *a) SEM image of Titanium balls imaged using the old light injection setup operating at sub-optimum biasing conditions with a 400mW laser at a LaB_6 temperature of 930K. b) SEM image of Titanium balls at an optimised Wehnelt bias using the new light injection apparatus with a 400mW laser at a LaB_6 temperature of 930K.*

Figure 5.19 a) was an image taken using the old 3D-printed light injection setup, which had no adjustments to the biasing of the Wehnelt. Between Figure 5.19 a) and b), we see the contrast in b) is much sharper and much improved over the old light injection setup operating at sub-optimum conditions in a).

5.5. Conclusion

This chapter described our successful installation of the adapted Wehnelt into the ZEISS EVO SEM electron gun. Initial proof-of-concept photoelectron images were taken, and we ran experiments validating that photoelectrons were being produced when the light struck the cathode. I then designed a new light injection setup for a

more precise alignment of the light source with the multimode collimator. After its installation, an analysis of the optimisation of the Wehnelt bias was performed. This involved comparing COMSOL simulations to experimental results, and from this, it was deduced that when the laser is on, thermally assisted photoemission is most likely occurring. My evaluation of the beam current at different crystal temperatures was then described. The results indicated that operating the photoemitter in a higher vacuum or with a cathode that contaminates less easily in a poor vacuum would be preferable. An experiment into the relationship between beam current and the laser power inputted was also performed. This experiment demonstrated that upgrading the light source to an even higher-power laser could be useful in future prototypes to increase the beam current. Finally, I assessed the efficiency of the new light injection setup. It was found that while it was an improvement over the old 3D printed apparatus, the current light injection setup was inefficient and that a sizable fraction of light was lost coupling the 200μm to the 100μm core optical fibre. These results advised that the current optical fibre should be replaced with a more suitable 100μm core optical fibre. It was also demonstrated that there is much space for design improvement in the photoemitter setup, such as parabolic mirrors or ball lenses to improve the focusing of the light on the crystal. Finally, a SEM image was taken using the new setup, and an improvement in contrast is evident compared to an image taken with previous sub-optimal conditions and apparatus.

Analysing all these experiments is instrumental in advising the next stage of improving the photoelectron emitter. Chapter seven will apply the insights from these results to a new semi-permanent photoelectron emitter. This will involve using a higher-power laser and upgrading the optical fibres. We will assess the performance of this new photoemitter, and an evaluation of how the photoelectron emitter's energy-spread could be measured will be outlined.

Chapter 6.

The Development of a Semi-Permanent Photoemitter Installation

6.1. Introduction

Chapter five described our initial installation of the photoelectron emitter and the experiments validating that it produces photoelectrons. The setup was optimised, and valuable information on how to improve our photoelectron emitter design was gathered. It was observed that an increase in laser power results in an increase in photoelectron current. We also noted that the light injection setup was losing light due to inefficient coupling between 100μm and 200μm core optical fibres. The following chapter will build on these observations to improve the photoelectron emitter. Firstly, installing a higher-power laser into the light injection setup will be implemented and described. A new, more suitable 100μm optical fibre will then be chosen to replace the existing 200 μm core fibre. With the higher-power laser and new fibre installed, the characteristics of the photoelectron emitter will then be measured. Finally, one of the key uses of this emitter is that its low energy spread could help improve low-voltage imaging. An experiment which aims to measure the energy spread of the photoelectron emitter will therefore be described and its results discussed.

Excerpts of this chapter are from 'Quigley, F., Downing, C., McGuinness, C., Jones, L. (2023) "A Retrofittable Photoelectron Gun for Low-Voltage Imaging Applications in the Scanning Electron Microscope." Microscopy and Microanalysis, 29(5), 1610-1617 '. Please note that during the characterisation of the electron emitter described in section 6.4, Armin Hayn, a ZEISS technician, was heavily involved in the experimental analysis and aided with the experimental setup. Jonathan Peters

assisted with developing the electronic circuitry for the new light injection setup described in section 6.2. Igor Chunin also aided with early designs of the retarding field energy analyser, and Jonathan Peters and Cormac Mcguinness assisted with its experimental setup described in section 6.5. All other work, including all of the experiments, was run by the author.

6.2. The Installation of a More Powerful Laser

In the previous chapter, it was found that if the power of the laser was increased from 10mW to 400mW, the photoelectron current increased while the thermionic current remained constant. An 800mW 405nm laser diode was purchased to capitalise on this relationship. This laser diode was contained in a laser dot module, meaning its light could be focussed using an inbuilt lens such that it was emitted as approximately parallel rays. This feature is beneficial when coupling the light into the multimode collimator, as shown in the right-hand image of Figure 6.1.

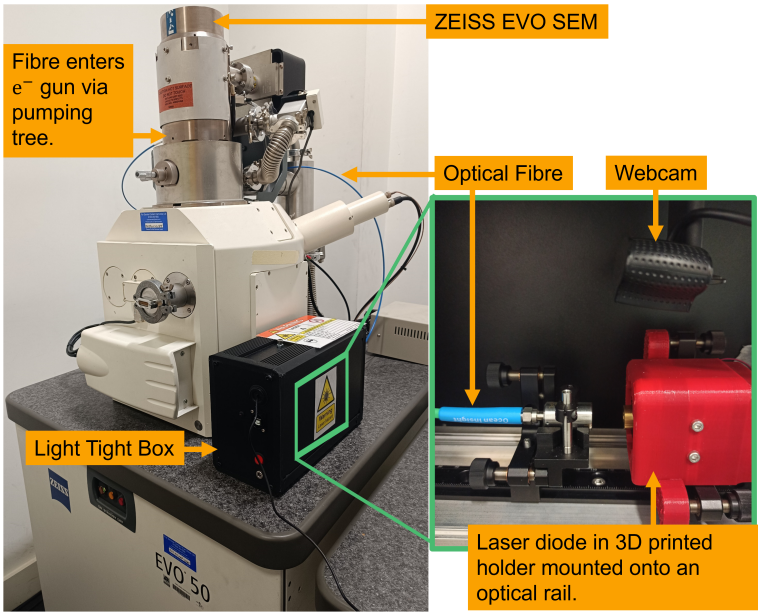

Figure 6.1.: *The exterior of the ZEISS EVO SEM, which has the photoelectron emitter setup installed. The green box displays the interior of the light-tight box, which contains the light injection setup.*

The module's casing also contains a fan, ensuring the high-power laser will not overheat. The laser module was enclosed in a 30mm × 30mm × 66.5mm rectangular housing, significantly larger than the 16mm diameter cylindrical casings used in previous experiments. To accommodate its larger size, I designed a bespoke 3D-printed holder. This holder supports the laser module on the kinematic mounts used in the previous light injection setup so that it is aligned with the multimode

collimator, as shown in the right-hand image of Figure 6.1.

Due to the high power of the purchased laser module, it was categorised as a class 4 laser and appropriate safety precautions were implemented. As shown in the left-hand image of Figure 6.1, a custom aluminium light-tight box was designed for this system. The right-hand image of Figure 6.1 shows the interior of this box with the optical rail bolted into its base and a webcam bolted into its roof. This webcam allows the user to view the box's interior when shut to ensure the laser is operating correctly. The optical fibre and the electronics of the webcam and laser module are fed out of the box through light-tight rubber seals. We installed a LED on the exterior of the box. This LED was interconnected with the laser module's circuitry such that when the laser was on, the LED would light up, and its brightness would even correlate to the laser power being emitted by the laser diode. Finally, appropriate laser safety signage was attached to the box's exterior, indicating the class of laser contained within the setup.

With the design and safe installation of the higher-power laser complete, experiments were run to establish how the photoelectron current would be affected by this higher-laser-power setup.

6.2.1. Running Laser Duty Cycle Experiments

The new 800mW laser module came with circuitry which allowed its average laser power to be controlled by pulsed width modulation (PWM) using a digital signal. Figure 6.2 demonstrates how PWM operates where the percentage duty cycle indicates the percentage of time the signal is on over a period of time and can be used to control the average output power [88].

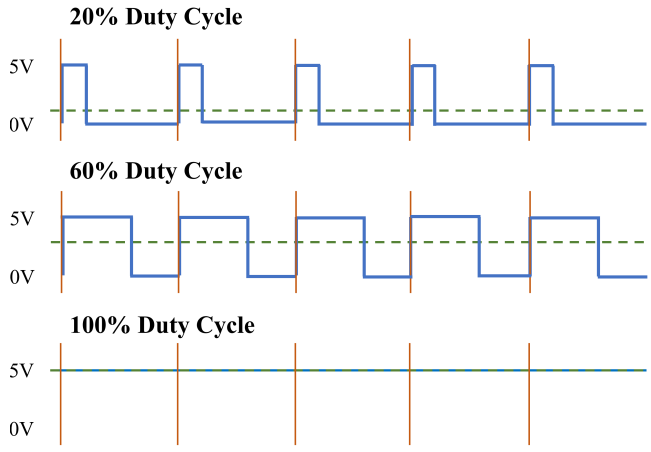

Figure 6.2.: *Illustration of how the duty cycle operates where the dashed green line indicates the average output voltage.*

For example, as shown in Figure 6.2, a 100% duty cycle means the laser is on 100% power for 100% of the time; therefore, the average output power would be 100%. Whereas a 20% duty cycle means the laser is on 100% power for 20% of the time, and the average output power is, therefore, 20%. There is a linear relationship between the duty cycle and the average output power of a laser during PWM [88].

We then ran an experiment where the LaB_6 crystal was cleaned via resistive heating at ∼1443K (1.4A resistive current) for 30 minutes and afterwards set to ∼1282K (1.2A resistive current). The Wehnelt bias was then set to optimally select photoelectrons. Using PWM on the 800mW 405nm laser, the duty cycle could be changed to decrease the power of the light striking the crystal. At an acceleration voltage of 15kV, SEM images of titanium balls on a carbon sample when the laser was on and then turned off were taken for different duty cycle percentages when an aperture of 750μm and 30μm were inserted into the SEM (see Figure 6.3 and Figure 6.4, respectively). The brightness and contrast were kept the same for each image in each tableau. Note that 30μm is a standard aperture size for SEM operation, while technicians mainly use the 750μm aperture for servicing the SEM, and it is comparable to having no aperture in the SEM at all.

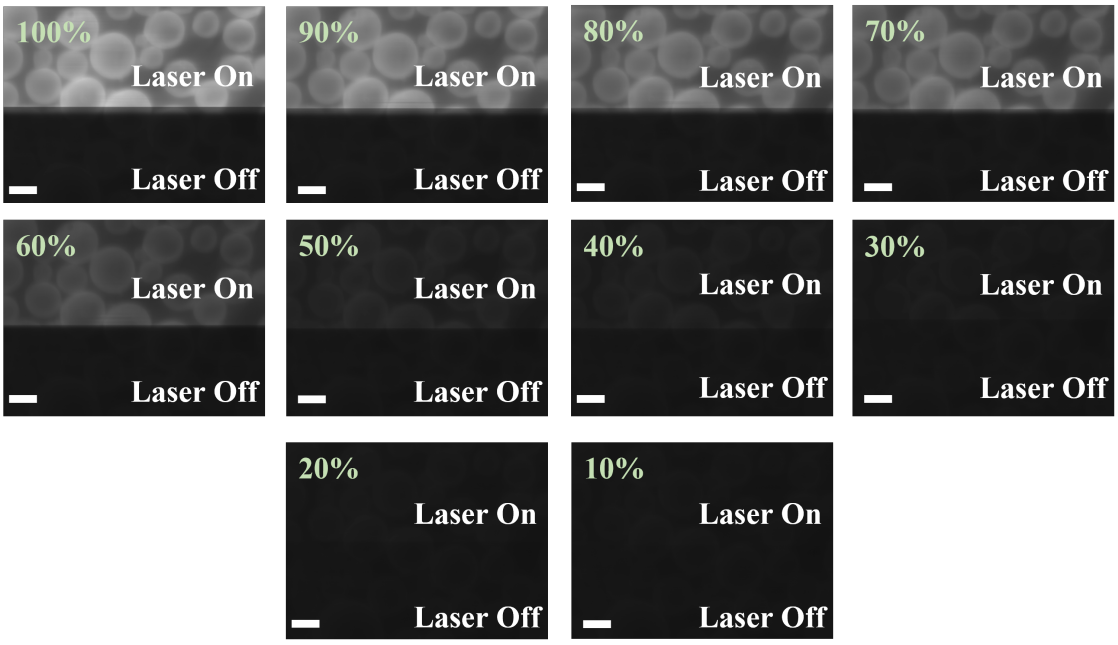

Figure 6.3.: *The SEM images captured when the laser was on and off at different duty cycle percentages indicated on the image's top left corner. When these images were taken, an aperture of 750µm was in the SEM. The scale bar is 20µm. Please note that this image was reprinted from the supplemental information of Quigley et al. 2023 (Reference number: [74]).*

The images in Figure 6.4, which were captured with a regularly sized aperture of 30μm, have a higher resolution than those taken when an aperture of 750μm was

in the SEM, as shown in Figure 6.3. The smaller aperture reduces the effect of spherical aberration on the image, causing the resolution to be improved compared to the images taken with the larger aperture.

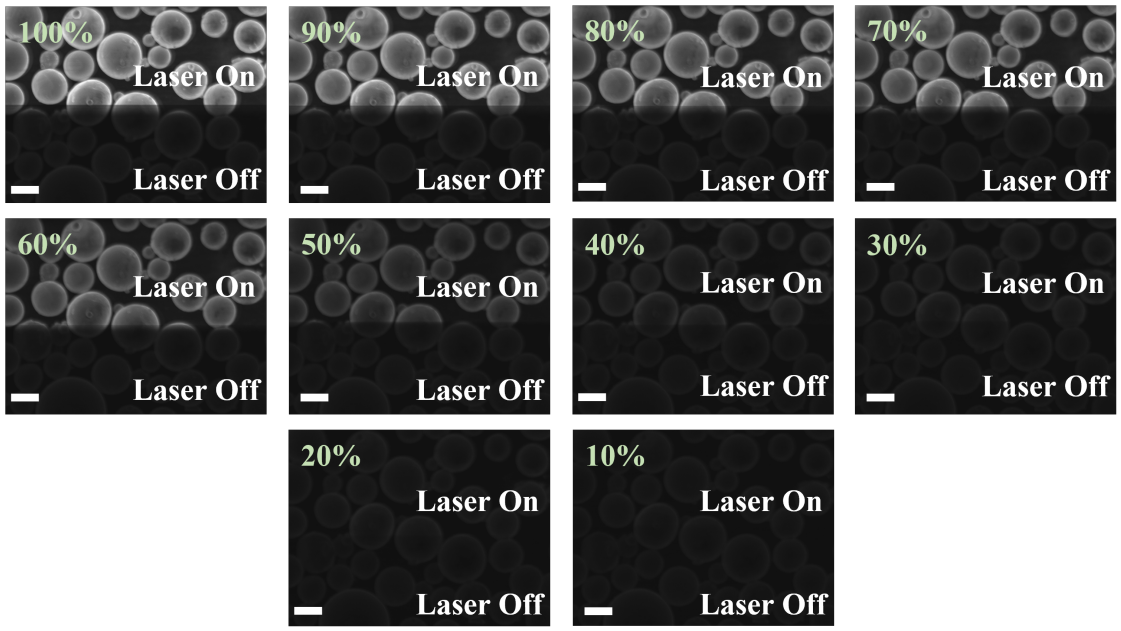

Figure 6.4.: *The SEM images captured when the laser was on and off at different duty cycle percentages indicated on the image's top left corner. When these images were taken, an aperture of 30μm was in the SEM. The scale bar is 20μm. Please note that this image was reprinted from the supplemental information of Quigley et al. 2023 (Reference number: [74]).*

To run a more quantitative investigation on how average output power affects current, an experiment was completed where a Faraday cup was electrically isolated and placed on the SEM stage. Using a picoammeter connected to the Faraday cup, the thermionic current (I_{th}) was taken as the current recorded when the laser was off, and the difference in current when the laser was on and off was taken as the photoelectron current (I_{ph}). Applying the same experimental parameters used to take the SEM images in Figures 6.3 and 6.4, I_{ph} and I_{th} were then measured at different laser powers using decreasing duty cycles when an aperture of 750μm was placed in the SEM. Figure 6.5 b) shows the current versus duty cycle recorded.

We see in Figure 6.5 b) that the thermionic current (I_{th}) remains the same independent of the duty cycle; however, the photoelectron current (I_{ph}) increases with an increasing duty cycle, as observed in our previous experiment with the 400mW laser in chapter 5. There also appears to be some minimum duty cycle at which the photoelectrons are stimulated. For ease of reference, Figure 6.5 a) corresponds to images taken at the same experimental conditions at four of the different duty cycles in Figure 6.5 b) and displays a more visual representation of the thermionic

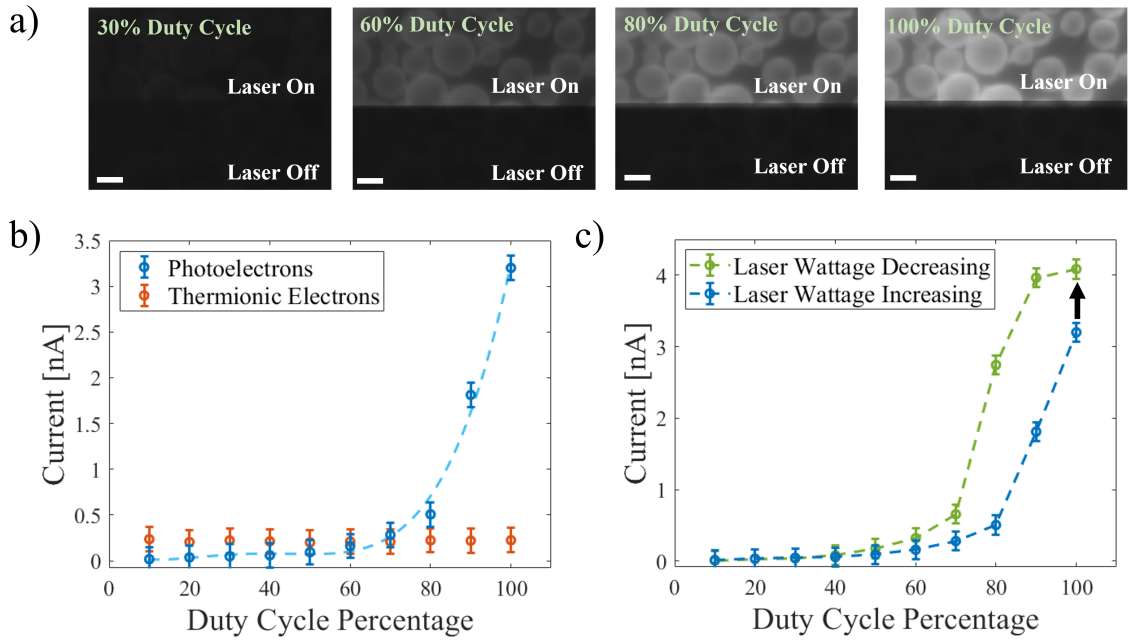

Figure 6.5.: *a) Subset of SEM images from Figure 6.3. The duty cycles indicated on each image are a subset of the duty cycles in b). The scale bar is 20µm. b) Plot of thermionic and photoelectron current detected at different PWM duty cycles of an 800mW laser with an aperture of 750µm in the SEM. c) Plot of photoelectron current recorded when the laser was increased in power and then decreased in power. Please note that a) and b) were reprinted from the paper Quigley et al. 2023 (Reference number: [74]).*

and total laser on current present when imaging.

Figure 6.5 c) shows the photoelectron current recorded in Figure 6.5 b) (blue). In the experiment run in Figure 6.5 b), the laser wattage was increased as the current was recorded. Under the same experimental conditions, this experiment was repeated with the laser wattage decreasing as the current was recorded (green curve in Figure 6.5 c)). We see in Figure 6.5 c) that the decreasing wattage green curve starts out at a higher photoelectron current, and its overall current is higher at the equivalent duty cycle percentage as the blue laser wattage increasing curve. This would imply that at higher wattages the laser may have been cleaning the crystal. This would reduce crystal contamination and allow more photoelectron current to be stimulated. As the green curve began with a higher wattage the crystal may have remained slightly cleaned for longer allowing more photoelectron current to be produced. In both experiments in Figure 6.5 c) the thermionic current remained constant throughout.

Inspecting Figure 6.5 b), we see a curve in the photoelectron current, which may result from a multiphoton effect. The multiphoton effect occurs when two or more photons are absorbed and excite a molecule (in this case, an electron) from a lower

to a higher energy state [89]. This process is non-linear where the peak photoelectron current (I_{ph}) is proportional to the peak laser intensity (I_0) by the following relationship

$$I_{ph} \propto I_0^m (m = 2, 3, 4, ...) \tag{6.1}$$

where m is the number of photons involved in the elementary photoemission process [89]. Therefore, the number of photons being absorbed is proportional to the power (m) of the intensity of the light source [90].

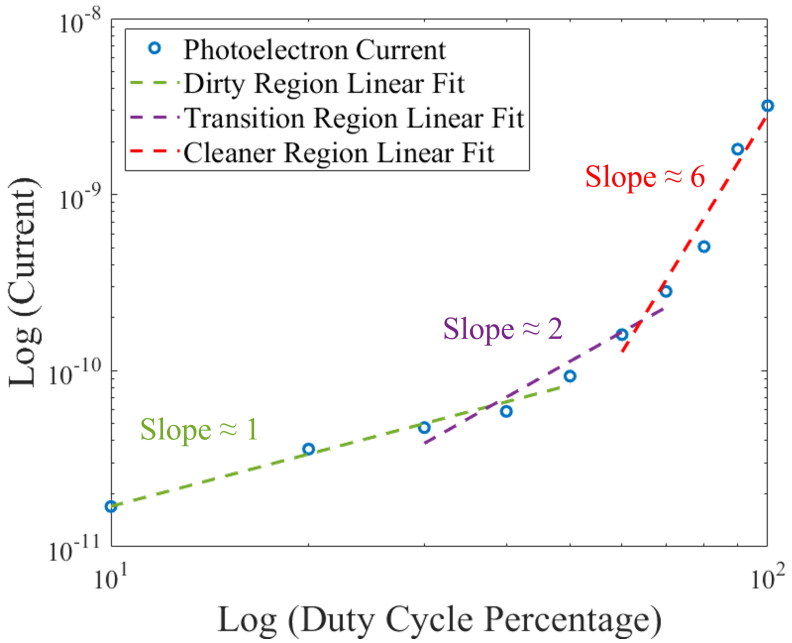

Figure 6.6.: *Log plot of Figure 6.5 b) with three linear fits through different logged data point regions.*

Figure 6.6 shows the log graph of Figure 6.5 b). The slope of this log graph should indicate how many electrons are absorbed during this multiphoton effect process. However, it is evident that this is not a completely linear graph. If the laser is slightly cleaning the crystal as the wattage increases, it may explain the shape of the curve. There may be three regions on the graph which indicate three different crystal contamination states:

1. The lower laser wattage region where the crystal is slightly dirty due to the relatively poor vacuum conditions in the SEM gun chamber.

2. A transitional region while the laser is cleaning the crystal.

3. A region where the crystal is cleaner at the highest wattage.

A linear fit was plotted through all three of these regions in Figure 6.6, and their slopes were found to be 0.98, 2.10 and 6.09 for the dirty, transition and cleaner regions, respectively. Accounting for some experimental uncertainty, the slope calculated shows that a two-photon absorption is likely occurring in the transitional region and potentially greater than two photon absorption is occurring in the cleaner region. This may increase the energy spread of the electron beam as electrons photoemitted through multiphoton absorption can have a larger energy than those emitted through single photon photoemission.

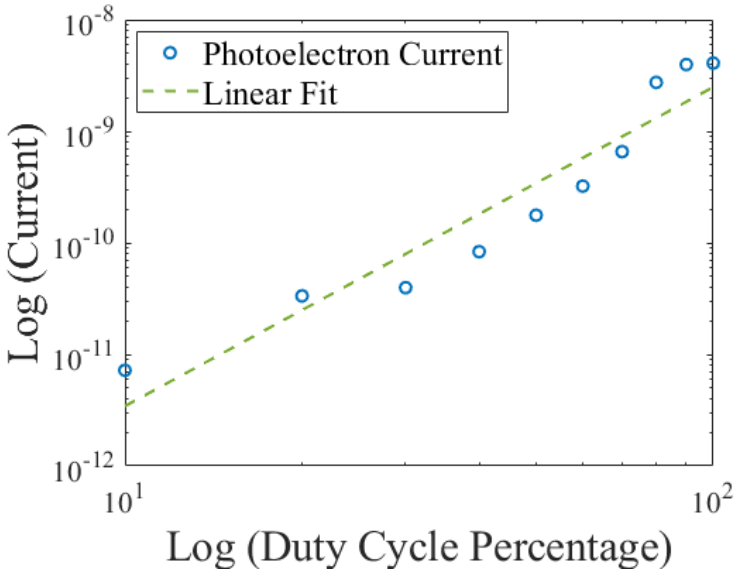

Figure 6.7.: *Log plot of the green laser wattage decreasing plot in Figure 6.5 c) with a linear fit through the logged data points.*

Figure 6.7 is a log-log graph of the green laser wattage decreasing plot in Figure 6.5 c). A linear fit was plotted through all of its data points and was found to have a slope of 2.9. This slope implies multiphoton absorption may be occurring from the crystal which is most likely cleaner after having had the laser striking it before the experiment recordings were begun.

The same experiment with the same experimental parameters was then repeated, where I_{ph} and I_{th} were measured at different laser powers using decreasing duty cycles; however, this time, an aperture of 30μm was placed in the SEM. An image of the current versus duty cycle percentage produced from the experimental results can be seen in Figure 6.8 a).

As expected, the thermionic current remains relatively constant as the duty cycle increases and the photoelectron current increases after a particular duty cycle percentage. Due to the addition of the smaller aperture, the overall current recorded is much smaller than that recorded with the larger aperture in Figure 6.5. The inser-

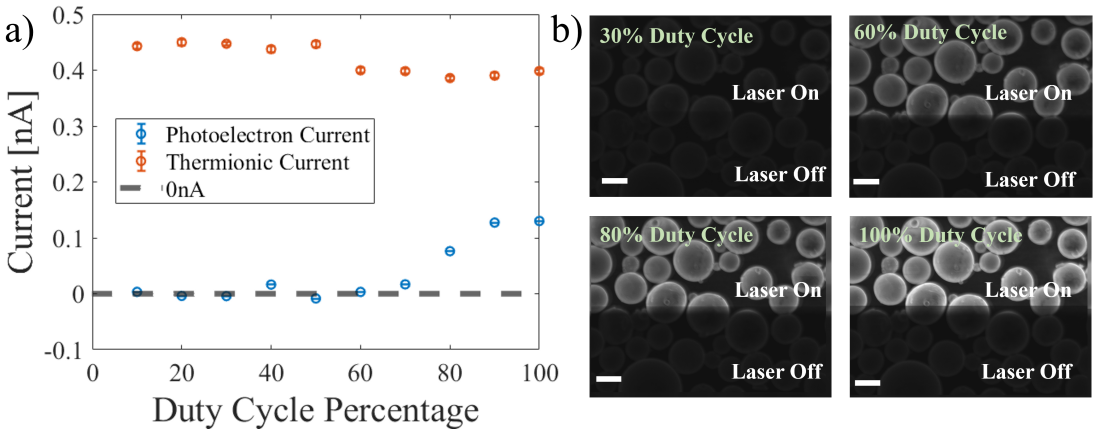

Figure 6.8.: *a) Plot of thermionic and photoelectron current detected at different PWM duty cycle percentages of an 800mW laser with an aperture of 30µm in the SEM. b) SEM images captured of titanium powder on a carbon tab when the laser was on and then off at the duty cycles indicated on the top left-hand corner of the image. These duty cycles correlate with the duty cycles indicated in a). The contrast and brightness were kept the same for each image, and the scale bar is 20µm. Please note this image was reprinted from the paper Quigley et al. 2023 (Reference number: [74]).*

tion of the aperture also appears to have an interesting effect on the photoelectron current as, in this case, the photoelectron current never becomes larger than the thermionic current, even when the laser is at its maximum output power.

Analysing our experimental results, we see that when the smaller aperture of 30 μm was placed in the SEM, the max photoelectron current produced at a duty cycle of 100% was reduced from ~3.19nA to ~0.12nA. Operating the SEM in normal thermionic mode (at ~1707K with a 1.8A resistive current) with a 30 μm aperture inserted, we found ~3.00nA of current was detected using the specimen current monitor. This will be a slight underestimation of the current due to some backscatter electrons not being recorded by the specimen current monitor. There is an apparent disparity between the operating current with the standard aperture in during thermionic and photoelectron mode. While the level of photocurrent produced was high enough to form images at slow scan speeds with the 30 μm aperture inserted, it is clear from these experiments that the current design of the photoelectron emitter is producing sub-optimal photocurrent for the everyday operation of the SEM, which may require even smaller apertures. This decrease in photoelectron current could also be due to the SEM being optimised for thermionic electrons. The thermionic electrons could be optimised to travel through the system, while the photoelectrons are not focussed as accurately due to their different energy, causing them to be cut off by apertures.

6.2.2. Determining the Resolution of the Imaging Modes

To further compare both imaging modes, the resolution of the SEM in thermionic and photoelectron mode was assessed using the titanium balls on a carbon sample with a 30 µm aperture placed in the SEM. Visually comparing Figure 6.9 a) taken in thermionic mode and Figure 6.9 c) taken in photoelectron mode we note that the features in image b) seem sharper than image a) and that more details of the Titanium balls seem to appear in image a). We also observe that the edges of the titanium balls in c) are very bright. We believe this is due to the edge effect, where more secondary electrons leave a sample at its edges, compared to flat areas, leading them to appear brighter [91]. This is more evident in image a) over image c) and is due to how the brightness and contrast were initially set in the SEM software and has nothing to do with the mode of operation of the gun. Figure 6.9 a) and b) were used for a resolution test, which was taken as the distance between the 10% and 90% drop-off of the line profile of an edge.

As the photoelectron current is lower than expected, both images were run at non-optimal condenser lens settings to prevent a poor signal-to-noise ratio in the photoelectron-generated images, which would occur if operated at a small spot size. From the line profiles in Figure 6.9 c) and d), the SEM was found to have a resolution of 0.66 μm in thermionic mode and 0.95μm in photoelectron mode, respectively. The resolution of the SEM during photoelectron mode appears to be slightly worse than in thermionic mode. We believe this is because the tip is not saturated during photoelectron mode, therefore not producing a beam as coherent as that formed during the thermionic mode [87].

Our results show that the lack of current being produced during photoelectron mode, when a regular aperture of 30μm is inserted in the SEM, affects the resolution of the images produced. As mentioned previously, it was believed that light may be lost coupling the 100μm and 200μm core optical fibres. Replacing the 200μm core fibre with a 100μm fibre will hopefully increase the light reaching the LaB_6 tip and, subsequently, the photoelectron current. The following section will describe the installation of a more suitable optical fibre and discuss experimental results from the setup with the new component.

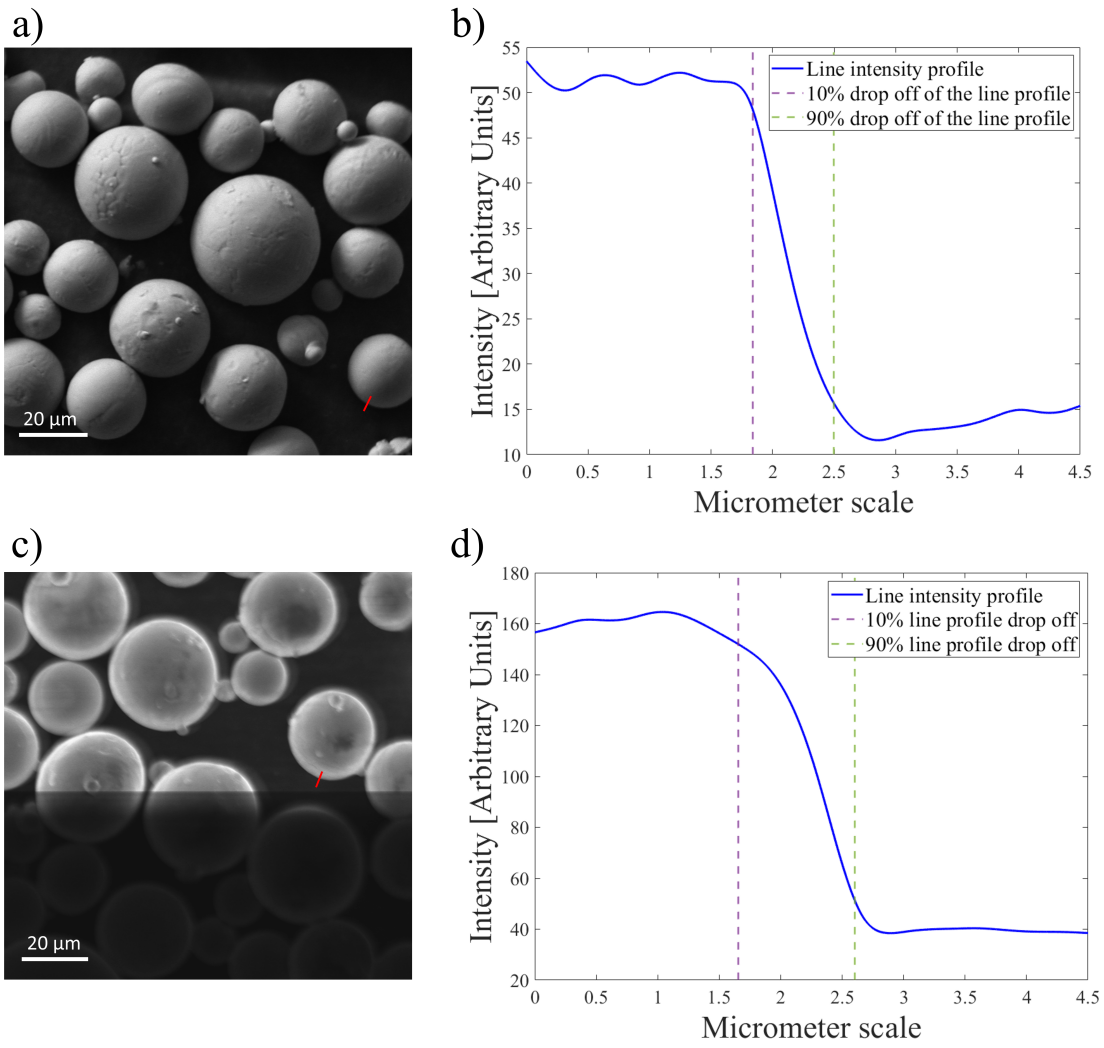

Figure 6.9.: *a) ZEISS EVO SEM image captured during normal thermionic mode with the laser off. The LaB_6 temperature was ∼1761K during this image. c) SEM image captured with the laser on then off at a duty cycle of 100% for the 800mW laser diode. The LaB_6 temperature was ∼1282K during this image. Both a) and c) were captured using the secondary electron detector when an aperture of 30µm was in the SEM where the acceleration voltage was 15kV. The red line in each image indicates where the line profile was taken for the resolution test. b) and d) are the line intensity profiles calculated at the positions of the red lines in images a) and c), respectively. Please note that this image was reproduced from the supplemental information of Quigley et al. 2023 (Reference number: [74]).*

6.3. The Installation of a New Optical Fibre

Our light injection setup involves a laser diode directed at a multimode collimator. This multimode collimator couples the laser light into a 200μm core optical fibre. This optical fibre guides the light into a custom flange with a 100μm core vacuum-compatible optical fibre attached to its vacuum side. The 200μm core optical fibre was replaced with a 100μm ± 3μm core P100-2-UV-VIS optical fibre from Ocean

Insight, which accepts wavelengths between 300nm-1100nm. Its jacket was made from a PVDF zip tube, and its buffer materials were made from polyimide. While its cladding and primary buffer outer diameters were 12μm $\pm$ 5μm and 17μm $\pm$ 3μm, respectively. Due to the smaller core diameter of this new optical fibre, it should couple the laser light into the vacuum compatible optical fibre far more effectively than the previous larger core fibre. A SEM image of titanium balls on carbon captured before and after the optical fibre was replaced can be seen in the left and right-hand image of Figure 6.10, respectively.

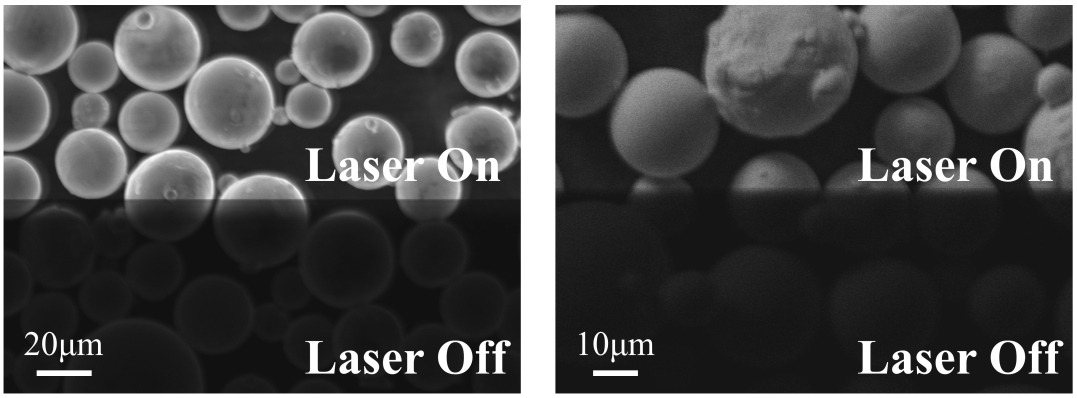

Figure 6.10.: *SEM image of Titanium balls on a carbon tab taken when the 800mW 405nm laser was on then off with (Left) the original 200µm fibre installed with LaB_6 Temperature = ∼1282K (1.2A resistive current), (Right) the new 100µm optical fibre installed with LaB_6 Temperature = ∼1331K (1.259A resistive current). EHT=15kV and aperture size=30 µm for both images.*

We see that with the addition of a more suitable optical fibre, the photoelectron current has increased due to increased light striking the crystal. This results in a higher resolution image at even higher magnifications, as shown in the right-hand image of Figure 6.10 where we note the scale bar is 10μm in comparison to 20 μm in the left-hand image. Once again it should be noted that the edges of the titanium balls in the left-hand image of Figure 6.10 are very bright most likely due to the edge effect [91]. This is more evident in the left-hand over the right-hand image and once again is due to how the brightness and contrast were initially set in the SEM software and has nothing to do with replacing the optical fibre.

6.4. Measuring the Characteristics of the Photoelectron Emitter

Several characteristics of our photoelectron emitter can then be measured using our new setup, which contains a higher-powered laser and new optical fibre. We wish to

measure source diameter, brightness and angular intensity during thermionic and photoelectron emission to compare and contrast both modes.

To achieve this, a ZEISS technician, Armin Hayn, was contacted. Armin Hayn is an expert on the ZEISS EVO SEM. The following experiment procedure to measure these characteristics was designed by him based on the theory found in Bronsgeest et al.'s research [92] and will be outlined below. The experimental procedure involved images being taken on the ZEISS EVO SEM in the different emission modes. The author undertook this, and Armin Hayn kindly processed these images to determine the properties of the emitter, and Table 6.1 contains the values he has calculated. Armin Hayn also generously provided results from two standard tungsten and LaB_6 ZEISS EVO SEMs to assist in comparing our emitter to unaltered emitters. This included Figures 6.12 and 6.15. The experimental theory, results and procedure will be described in detail below.

6.4.1. Experimental Theory

The brightness of an electron source is a very useful parameter as it is one of the key factors in determining the performance of an electron microscope. Interestingly, brightness is conserved through the electron microscope, so the brightness recorded at the sample should indicate the approximate brightness at the electron source. The brightness (β) of an electron gun can be defined as

$$\beta = \frac{4I_{Beam}}{\pi^2 d_o^2 \alpha_o^2} \tag{6.2}$$

where I_{Beam} is the beam emission current, d_o is the spot size or source diameter, and α is the beam semi-angle.

Analysing equation 6.2, we see that to determine the brightness of an emitter, a suitable measure of the source diameter needs to be chosen. This can be achieved by selecting a measure that assumes no particular shape of the probe intensity profile by choosing a diameter that contains a fraction of the probe current [92]. The fraction chosen in the following experiments was 50%.

If we assume the brightness is maintained as the beam travels through the column, equation 6.2 can be expressed in the image plane (i.e. the plane at the specimen) as follows;

$$\beta = \frac{4I_{Probe}}{\pi^2 d_3^2 \alpha_3^2} \tag{6.3}$$

where d_3 is the spot size at the image plane excluding lens aberrations, I_{Probe} is the probe current, and α_3 is the beam semi-angle at the image plane, as seen in Figure 6.11. Therefore, using equation 6.3, the brightness can be calculated from the spot size at the specimen.

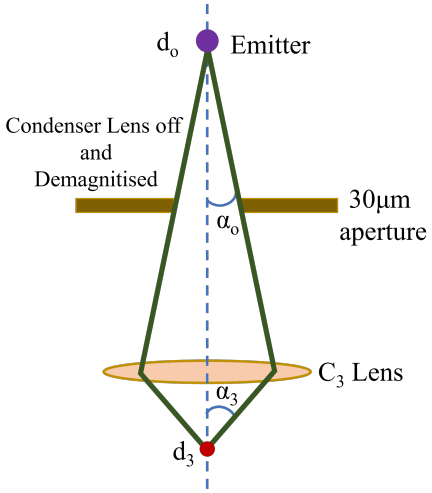

Figure 6.11.: *Simplified schematic of the interior setup of the SEM during the experimental measurement of spot size and brightness. Please note that this image is a reproduction of a schematic drawn by Armin Hayn.*

To assess this spot size, a Python program can be used that conducts a 1d Fourier Transform (line and frame) on a SEM image which contains suitably small features, such as the one shown in Figure 6.12 a) of a universal tin on Carbon sample. The Fourier-Transform of an image such as this one can be seen in Figure 6.12 b).

The maximum frequency of the signal f_{max} where the signal level is above the noise level can be determined from the Fourier transform. Unfortunately, the noise level makes it difficult to determine the exact frequency; however, we will use the average of the first five points below the noise level in the Python program as our value of f_{max}. The spot size of the specimen can then be defined as;

$$d_3 = \frac{pixel\ size}{f_{max}}. \tag{6.4}$$

If we assume a Gaussian distribution, the spot size containing 50% of the probe current can be derived as;

$$d_{3_{50\%}} = d_3\sqrt{ln(2)} \tag{6.5}$$

and brightness can subsequently be given as;

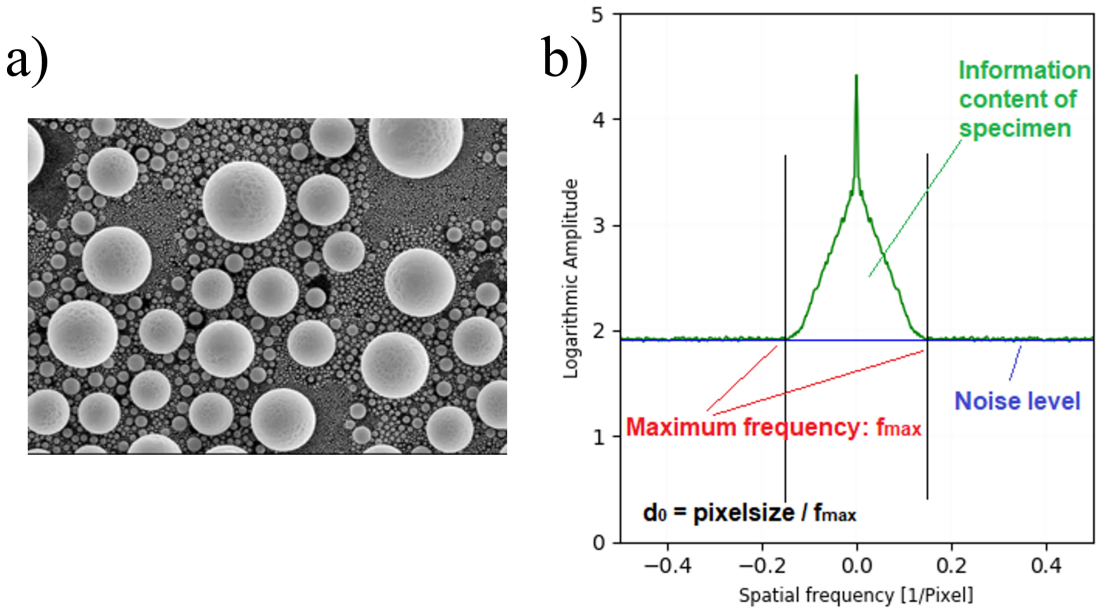

Figure 6.12.: *a) SEM image of universal tin on carbon sample. b) Fourier-Transform taken of a tin on carbon specimen SEM image.*

$$\beta = \frac{4I_{Probe}}{ln(2)\pi^2 d_3^2 \alpha_3^2}. \tag{6.6}$$

The following section will describe how we experimentally determined I_{Probe}, d_3 and α_3 so that equation 6.6 can be used to calculate brightness.

6.4.2. Experimental Procedure to Measure Brightness and Spot Size

The ZEISS EVO SEM itself can be used to measure our emitter's spot size and brightness. To achieve this, the condenser lenses C1 and C2 were turned off. These lenses are then demagnified to ensure no unwanted magnetic fields are inside the column. This was accomplished by using a built-in hysteresis removal feature in the SEM. These steps ensure that only the objective lens (C3) is used to focus the beam, and the electron source will be projected onto the specimen. ZEISS have undertaken electron optical modelling of the ZEISS EVO SEM; therefore, fundamental elements such as dimensions of the column and the aberration coefficient of the C3 objective lens are known.

The following tools are required to measure the desired parameters: a Faraday cup to measure the probe current and an appropriate sample to assess spot size (source and image plane). To assess our adapted ZEISS EVO SEM, we chose titanium balls

on carbon as our sample as it would contain balls of various sizes. When taking the image of this sample, the magnification needed to be high enough so that the image appears slightly blurry so that the maximum frequency of the signal level could be determined. In previous experiments, a Faraday cup, which was a block of metal with a deep hole, was used. For these experiments, a hypodermic needle electrically isolated was chosen as the Faraday cup as we believed its depth would improve the signal gathered. Figure 6.13 shows a SEM image of this Faraday cup.

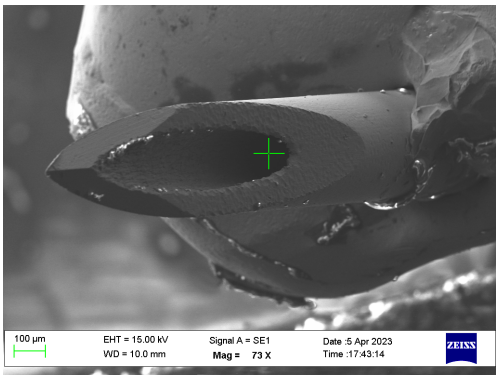

Figure 6.13.: *SEM image of the Faraday cup composed of a hypodermic needle, which was electrically isolated and connected to a picoammeter. The green crosshair indicates the point at which the beam was positioned during the current readings.*

When taking the current reading, spot mode on the SEM was used. Spot mode stops the beam from scanning and focuses the beam on one specific spot. The green cross in Figure 6.13 indicates the approximate position the beam was fixed at in the following experiments. Figure 6.14 a) and b) displays SEM images taken of the titanium balls during thermionic emission when the laser was off, the crystal temperature was ∼1708K (1.802A resistive current), the acceleration voltage was 15kV, and an aperture of 30μm was inserted in the SEM. With the same aperture and acceleration voltages, the crystal was cleaned resistively at 1443K for 15 minutes. After being set at a crystal temperature of ∼1331K (1.259A) for 20 minutes, images were then taken when the laser was on at an 85% duty cycle, as shown in Figure 6.14 (c) and d)). Figure 6.14 a) and c) are the images taken under standard SEM lens operating conditions, whereas b) and d) are the images taken when the C1 and C2 lenses are turned off, and we see the images are slightly less well resolved.

Armin Hayn also repeated this experimental procedure in two other standard ZEISS EVO SEMs, one containing a tungsten filament and one with a LaB_6 cathode. A universal tin-on carbon sample was used as his specimen. Figure 6.15 a) and c) displays the SEM images taken of the sample with the C1 and C2 lenses turned off, while Figure 6.15 b) and d) are SEM images of the Faraday cup used in his experiments with the grey crosshairs indicating the position the beam was in when

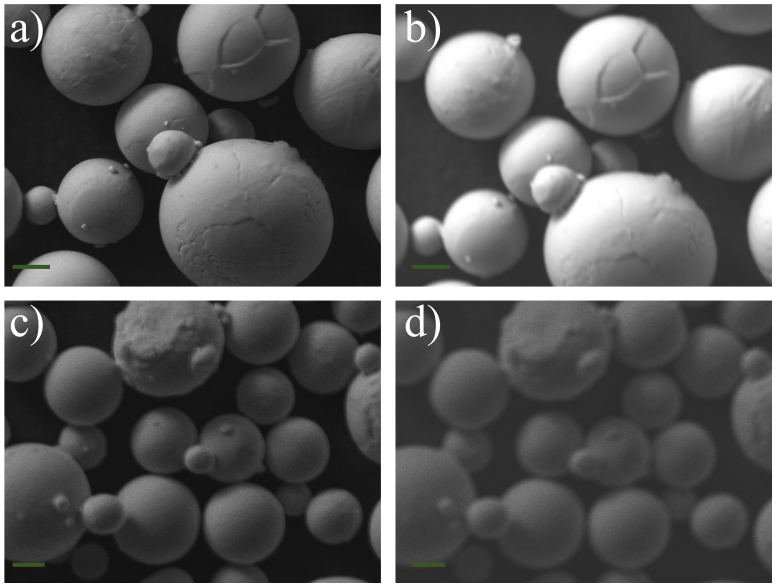

Figure 6.14.: *a) and c) SEM images of titanium balls on a carbon tab taken when the laser was off and on, and the crystals were at ∼1708K and ∼1331K, respectively. b) and d) are taken under the same experimental conditions as a) and c), respectively, except the C1 and C2 lenses were turned off during the imaging. The green scale bar in all four images is 10µm in length.*

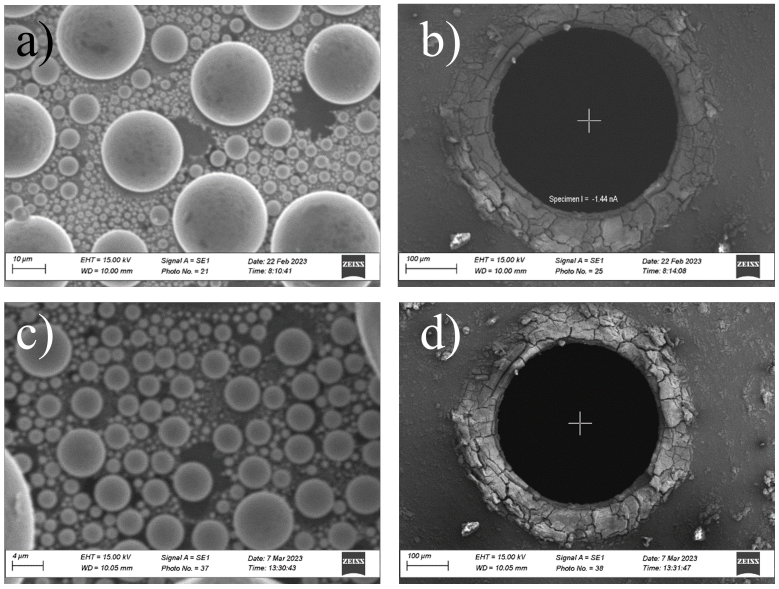

Figure 6.15.: *a) and b) SEM images of a universal tin on carbon sample taken when the C1 and C2 lenses were turned off using a ZEISS EVO SEM, containing a tungsten filament and LaB_6 cathode, respectively. b) and d) SEM images of the Faraday cup used to measure the currents emitted from the tungsten and LaB_6 cathodes, respectively. The crosshairs indicate the point at which the beam was positioned during the current readings.*

the current was recorded.

With the experimental images captured and the probe current recorded, the images

could be inputted into a Python program to plot their Fourier transform and determine the maximum frequency of the images. Armin Hayn kindly undertook this step. These recorded values could then be used to calculate the emitters' source diameter, brightness and angular intensity. A summary of these values for the different emitters can be seen in Table 6.1 below.

	ZEISS EVO SEM		Adapted ZEISS EVO SEM	
Cathode Type	Tungsten	LaB_6	LaB_6	LaB_6
Emission Mode	Thermionic	Thermionic	Thermionic	Photoemission
Brightness at 15 kV [A/(m^2× sterad)]	0.711×10^9	2.43×10^9	4.16×10^9	1.05×10^6
Source Diameter [µm]	11.94	6.9	7.81	26.93
Angular Intensity [A/sterad]	7.97×10^{-2}	9.08×10^{-2}	19.9×10^{-2}	0.05×10^{-2}

Table 6.1: *Summary of the values calculated from the SEM images captured on two standard ZEISS EVO SEMs and the adapted ZEISS EVO SEM.*

This table shows that our adapted ZEISS EVO SEM operating with thermionic emission mode has a similar brightness to that recorded on a standard EVO SEM with a LaB_6 cathode. However, the brightness produced during photoemission mode is almost 1000 times less than in thermionic mode. The brightness during photoemission is even less than that recorded from the tungsten cathode. We also note that the angular intensity of the emitter during photoelectron mode is a lot less than that during thermionic mode. This could be explained again by the crystal not being fully saturated, causing a decrease in angular intensity, brightness and resolution. Upgrading the way light is delivered to the crystal should increase the photoelectron current and would, therefore, benefit future emitter designs.

6.5. Measuring the Energy Spread of the Photoelectron Emitter

6.5.1. Experimental Design

One of the main motivations behind building the photoelectron emitter is that it would produce low energy-spread electrons that would reduce the effect of chromatic aberration on SEM images. In chapter three, the theoretical energy spread of our emitter built with a LaB_6 cathode and 405nm laser diode was calculated to be 0.37±0.04 eV. From literature, the approximate energy spread of a LaB_6 emitter in thermionic mode is between 1-2 eV [9]. Based on experiments undertaken in

chapter four, we believe that because we must have the crystal heated to mitigate contamination due to the poor vacuum in the gun chamber, thermally assisted photoemission could be occuring when our laser strikes the resistively heated LaB_6 crystal. Therefore, the energy spread of the photoelectrons may be even higher than those generated during regular thermionic emission. Measuring the energy-spread of the photoelectrons would provide further insight into this.

A retarding field energy analyser (RFEA) is a commonly used instrument for measuring the energy-spread of an electron source. RFEAs operate by recording the current striking a collector component placed before the electron source. An electrode is positioned in front of this component. Increasingly negative potentials are applied to the electrode until all the electrons are repelled, and no electrons strike the collector. The differential of the current detected versus the retarding bias can be plotted, and the full-width half maximum (FWHM) of the peak in this graph indicates the energy spread of the source. Lee et al. have released a paper that provides guidelines on building a RFEA [93], and their method has been followed for our experimental procedure. The top image in Figure 6.16 a) shows the schematic of the instruments used in Lee et al.'s research.

Lee et al.'s experimental setup contained a Schottky FEG in a vacuum chamber, producing an electron beam. Due to the large amount of current being emitted, a shield was placed in front of the lens apparatus, so only a fraction of the electron beam was being analysed by the setup, as seen in Figure 6.16 a). The lens was set to a certain voltage such that the beam was focused at the entrance of the retarding electrode. The electrons that travelled through the electrodes were then detected by the collector connected to a picoammeter. At a particular negative potential applied to the retarding electrode, all the electrons are completely retarded.

This retarding potential is controlled by a sourcemeter which can also detect if any current strikes the retarding electrode. This can be seen in more detail in Figure 6.16 b)-d).

In Figure 6.16 b)-d) we see how different lens acceleration voltages affect the electron beam's focus. The optimum focusing occurs when the electrons do not collide with the electrodes during the retarding process, as shown in Figure 6.16 c).

To measure the energy spread of the source, the electron current detected by the collector differentiated by the retarding voltage versus the retarding voltage needs to be plotted. This is shown in Lee et al.'s work in Figure 6.17 for three different Schottky tip temperatures.

Taking the full-width half maximum (FWHM) of each curve, the energy spread of

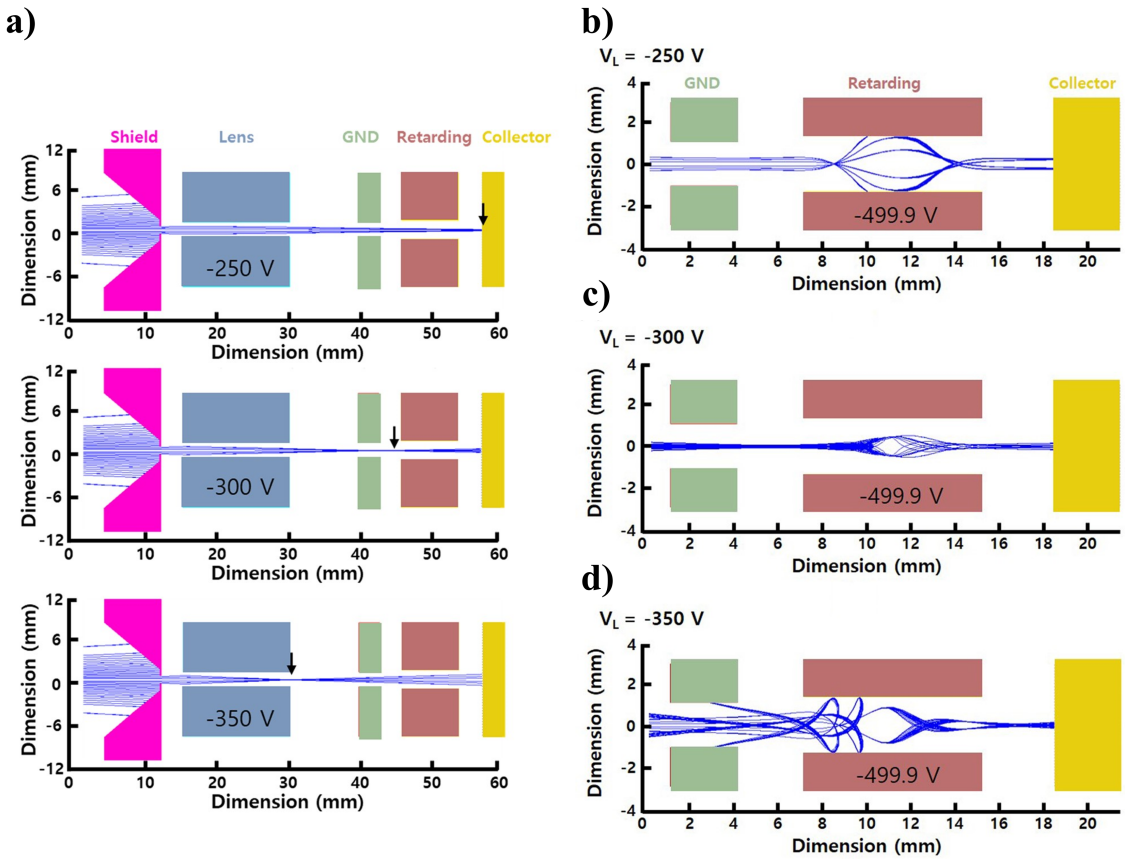

Figure 6.16.: *a) Illustration of Lee et al.'s experimental setup at different retarding voltages. b)-d) Illustration of the electron trajectories in Lee et al.'s experimental setup at different lens voltages. Reprinted from Lee, Ha Rim; Hwang, Junhyeok, High-Performance Compact Pre-Lens Retarding Field Energy Analyzer for Energy Distribution Measurements of an Electron Gun, Microscopy and Microanalysis, 2022, 28, 6, 1989–1997, by permission of Oxford University Press (Reference Number: [93]).*

the electron source at the different temperatures can be calculated. Lee et al.'s experimental setup produces very accurate results, with energy-spreads as low as 0.8eV being measured. This setup would therefore be suitable for the sensitive measurement we require to record the energy-spread of our source.

A modified replica of Lee et al.'s apparatus was designed for our experiments. In Lee et al.'s setup, a shield was required to block the majority of the electron current as the Schottky FEG was in the same vacuum chamber as the RFEA equipment, and only a fraction of the current was needed to analyse the energy spread. Our electron source is located in the gun chamber of the SEM. The electrons emitted travel through several apertures as they enter the main system vacuum chamber and travel down the column. Therefore, only a fraction of their current reaches the sample stage, and a shield is not required in our experimental setup.

Lee et al. found that the lens's voltage could be optimally adjusted such that

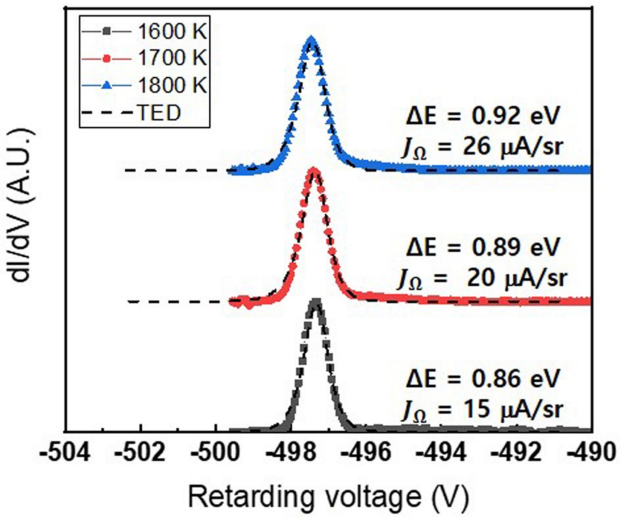

Figure 6.17.: *Plot of incremental current versus the retarding voltage for different Schottky tip temperatures. The energy spread at the different temperatures is indicated beside each curve. Reprinted from Lee, Ha Rim; Hwang, Junhyeok, High-Performance Compact Pre-Lens Retarding Field Energy Analyzer for Energy Distribution Measurements of an Electron Gun, Microscopy and Microanalysis, 2022, 28, 6, 1989–1997, by permission of Oxford University Press (Reference Number: [93]).*

the retarding process could occur without the electron beam colliding with the electrodes, as shown in Figure 6.16 b). Lee et al. determined that adjusting the voltage to focus the electron beam just before the retarding analyser produced this result [93]. Our electron source is contained within a SEM that already has a series of lenses for focusing the electron beam on a sample. An extra lens was therefore unnecessary, and the SEM itself could be used to simply focus the electron beam on the entrance boundary of the retarding electrode. The electron beam could then be shifted to the centre hole of the apparatus and set to spot mode such that the beam is focussed on the correct plane in the right position to operate the setup as executed by Lee et al..

While the shield and lens were not required for our experimental setup, the ground electrode, retarding electrode and collector were necessary components. The electrodes were built by cutting a stainless steel cylindrical bar to the same dimensions of width, height and interior hole size as Lee et al.'s apparatus shown in Figure 6.16 a). Small holes were then drilled through the electrodes so ceramic spacers could be inserted, separating them to the same distances as Lee et al.'s apparatus in Figure 6.16 a). A Faraday cup from an old electron gun was used for the collector. The flat metallic plate was placed in a ceramic holder, which could be mounted onto the same apparatus as the electrodes via ceramic spacers. Figure 6.18 a) shows this setup with the components positioned at approximately the same distance as Lee

et al.'s setup shown in Figure 6.16 a).

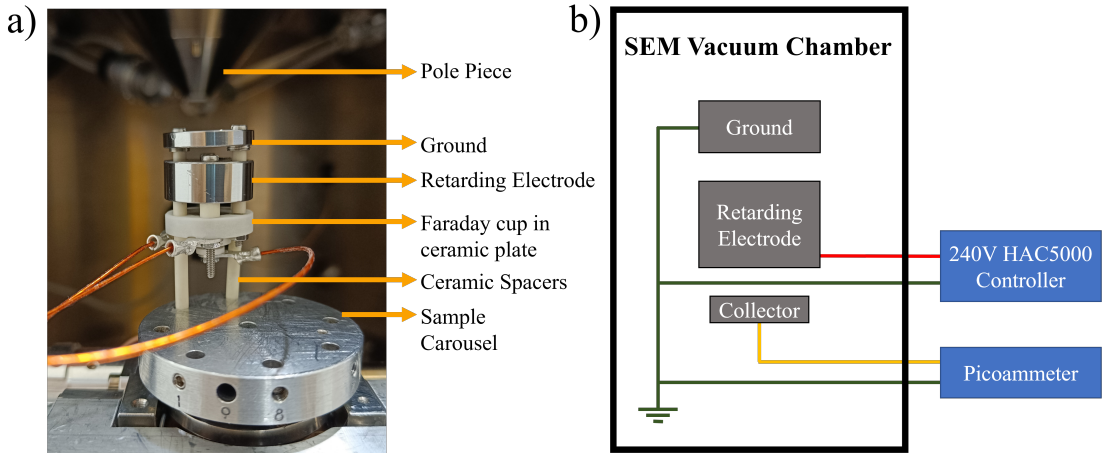

Figure 6.18.: *a) Image of retarding field energy analyser apparatus with all the key components labelled. b) Electric circuit drawing of our retarding field energy analyser. Please note that ground, in this case, is the chassis of the SEM.*

Hex bolts were fed down through some of the ceramic spacers, and kapton wire was connected securely to these nails via bolts to connect the different components to ground, a controller and a picoammter, as indicated by the electric circuit drawing in Figure 6.18 b).

A critical difference between our setup and that of Lee et al.'s is that we do not have a source-meter attached to our retarding electrode. Instead, we are using a repurposed electron spectrometer controller. This 240V HAC5000 controller allows us to apply a precise voltage in 0.01V increments to the retarding electrode; however, as it is not a source-meter, we cannot simultaneously read current while applying this voltage. Unlike Lee et al.'s setup, we also do not have a picoammeter attached to the ground electrode. When running our experiments, we therefore do not know if some current is striking the retarding or ground electrode, however as mentioned previously, if we focus our beam in the same manner as that in Lee et al.'s work, the beam should be optimised to not strike the electrodes during the retarding process.

6.5.2. Experimental Results

With the setup complete, experiments were run where the retarding voltage was swept through while the current detected by the collector was measured. The 240V HAC5000 controller's voltage could go up to -5kV; however, the wiring of the apparatus limited the maximum voltage that could be applied to the retarder electrode to -300V. The acceleration voltage of the SEM was therefore set to -270V such that the retarder voltage could be swept up to -276V to fully retard the beam.

The first experiment run was when the source was in standard thermionic emission mode with the LaB_6 temperature set to ∼1707K (1.8A resistive current). This was done for two reasons; firstly, the energy spread of a LaB_6 thermionic emitter is known from literature. Therefore, initially operating the experiment in thermionic mode allows us to validate if our energy analyser can measure an energy-spread that aligns with the values recorded in the literature. Secondly, at such low acceleration voltages, the current detected by the picoammter was relatively low in the picoamp regime. Standard thermionic emission from our adapted Wehnelt produces a larger amount of current than photoemission, so analysing the energy-spread in thermionic mode provides us with more current to check that the energy analyser is sensitive enough for our energy-spread measurement requirements.

Due to how low the acceleration voltages were, the Wehnelt bias was simply set to its minimum value to ensure the small amount of current accelerated could travel through the system. The largest aperture of 750μm was inserted into the SEM to ensure the maximum current reached the collector. The retarding voltage was swept from 0V to -276V, and the picoammeter recorded the current. Figure 6.19 a) and b) shows the experimental results recorded.

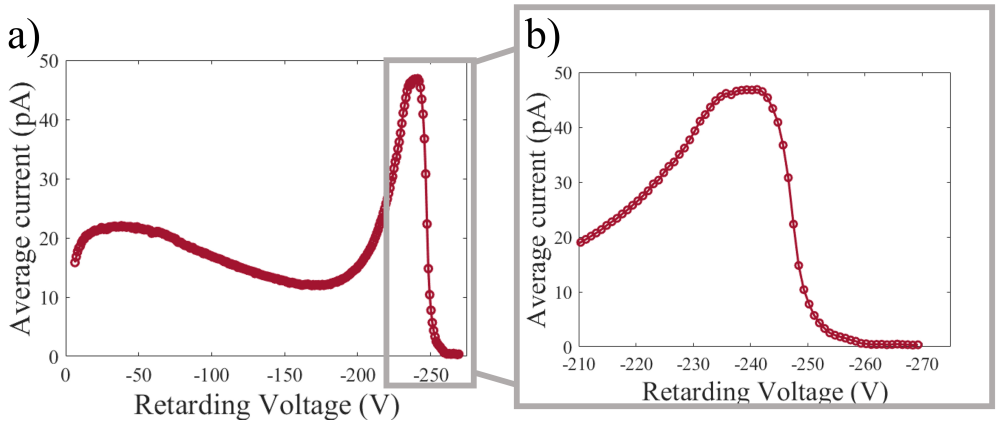

Figure 6.19.: *a) and b) Plot of the average current detected by the collector versus the retarding voltage from 0 to -276V and -210 to -276V, respectively, when the LaB_6 temperature was ∼1707K (1.8A resistive current).*

When recording the current collected versus retarding voltage, it was expected that the current would remain high. Then, when the voltage was close to the acceleration voltage of the SEM, the current would start to drop-off until it reached zero, with all the electrons being repelled away from the electrode. However, this differs from our experimental results in Figure 6.19 a). Instead, the current rises and then falls at different voltages; finally, around -240V, it peaks and then starts to drop off abruptly until its current reaches zero. These peaks and troughs in the current before -240V could potentially be due to the electron beam not being optimally

focussed by the SEM lenses. This can be explained by looking at Lee et al.'s results in Figure 6.16 b)-d) where we see how different lens acceleration voltages affect the electron beam's focusing.

The optimum focusing condition occurs when the electrons do not collide with the electrodes during the retarding process. Figure 6.20 a) and b) show plots of the current striking the collector, retarding electrode and ground electrode at different acceleration voltages for a lens voltage of -310V and -314V, respectively. At -310V in Figure 6.20 a), the focusing is not optimised, and electrons strike the boundary of the electrodes as shown in the peak in the red and blue retarding and ground curves, respectively. This current striking the electrodes means the current detected by the collector is decreased, as shown by the dip in the grey curve at approximately -495V in Figure 6.20 a). Figure 6.20 b) shows the optimised focussing conditions with a lens voltage of -314V. While the current still strikes the ground electrode, it is much less than before and does not affect the smooth decreasing shape of the collector's current represented by the grey curve. We see no current striking the retarding electrode represented by the red line under these conditions.

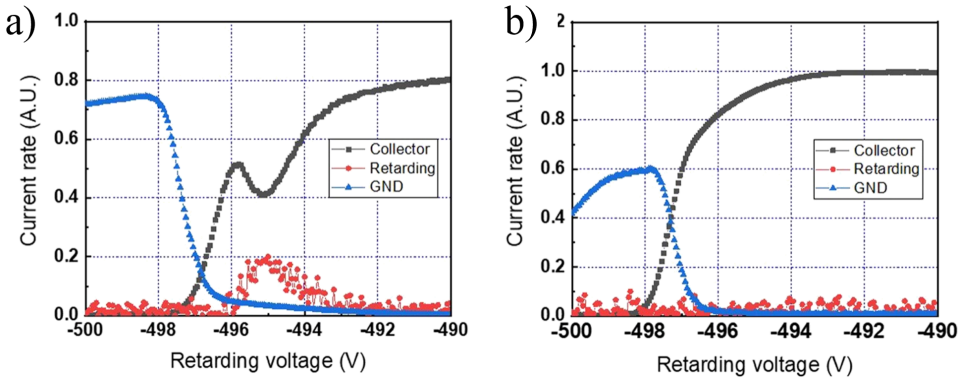

Figure 6.20.: *a) and b) Graph of the current recorded striking the collector, retarding electrode and ground electrode at a lens voltage of -310V and -314V, respectively. Reprinted from Lee, Ha Rim; Hwang, Junhyeok, High-Performance Compact Pre-Lens Retarding Field Energy Analyzer for Energy Distribution Measurements of an Electron Gun, Microscopy and Microanalysis, 2022, 28, 6, 1989–1997, by permission of Oxford University Press (Reference Number: [93]).*

Looking at Figure 6.20 a) taken from Lee et al.'s paper, we see that when the current strikes the retarding electrode, it causes a dip in the collector current. This focusing effect could explain the drops in current occurring in Figure 6.19 a), perhaps causing the beam to strike the boundaries of the electrodes until it is correctly focussed through the electrode at approximately -240V. After this point, the retarding voltage may then operate as expected, causing the electrons to start being repelled until the current drops to zero.

Figure 6.19 b) shows this current drop-off in more detail. Interestingly, it was expected that the drop-off would occur closer to -270V, the acceleration voltage of the electrons. While the current is at zero by -270V, the drop-off occurs much earlier than expected. Figure 6.21 from Lee et al.'s results compares the collector current when the lens bias is optimised at -314V and when there is no biasing at 0V. We see from Figure 6.21 that there is a sharper drop-off in current when the lens focuses the beam. This implies that having an incorrect bias applied could cause the current to drop off earlier than expected and could explain our earlier drop off in current (Figure 6.19 b)).

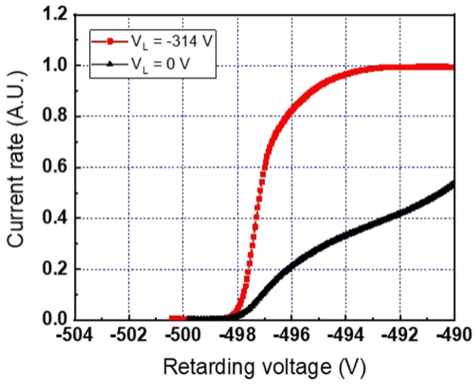

Figure 6.21.: *Current recorded by the collector at the optimised lens acceleration voltage of -314V and 0V. Reprinted from Lee, Ha Rim; Hwang, Junhyeok, High-Performance Compact Pre-Lens Retarding Field Energy Analyzer for Energy Distribution Measurements of an Electron Gun, Microscopy and Microanalysis, 2022, 28, 6, 1989–1997, by permission of Oxford University Press (Reference Number: [93]).*

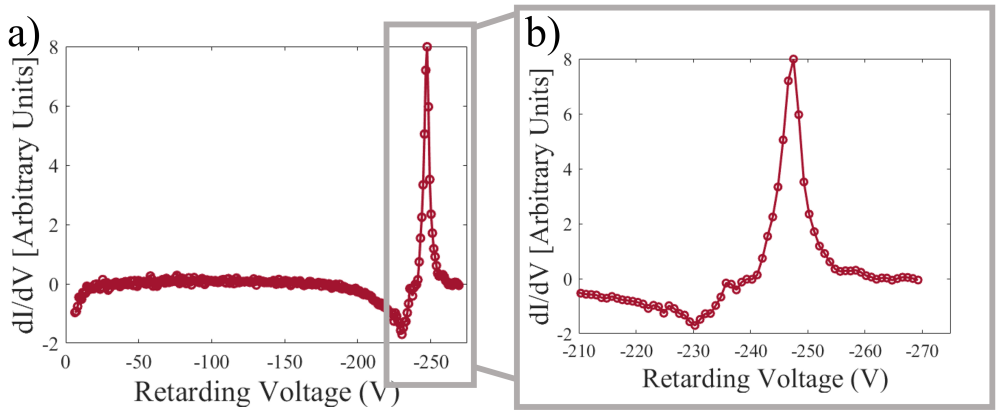

Figure 6.22.: *a) and b) Plot of the differential of the average current detected by the collector with respect to voltage versus the retarding voltage from 0 to -276V and -210 to -276V, respectively.*

To further analyse the results, the gradient of the current with respect to voltage was taken and plotted in Figure 6.22 a) and b). Figure 6.22 a) shows a large peak

at the position where the electrons are dropping off in Figure 6.19 a). Inspecting this peak in Figure 6.22 b), we note that its approximate full-width half maximum, which is supposed to indicate its energy spread is 4.533V. As these are electrons we are referring to, this energy spread can be given in units of eV as 4.533eV. For reference, the energy spread of a LaB_6 SEM thermionic emitter in literature is 1-2eV [9]. Therefore, the value we have recorded is off by a factor of ∼2.5eV. Additionally, this experiment, operated during thermionic emission, did not have very good repeatability. While the current would drop off during every run close to the acceleration voltage of the SEM, it did not follow the same peaks and troughs as shown between 0 and -240V in Figure 6.19 a).

There appear to be issues with the experimental setup that it reads such large energy-spread values and that the current recorded varied so widely before its drop-off. For completeness sake, the experiment was repeated with a LaB_6 temperature of ∼1443K (1.4A resistive current). With the same aperture and Wehnelt bias, the 800mW laser was turned on, and the retarding voltage was swept from -213V to -276V while the picoammeter recorded the current. This was then repeated with the laser turned off. The results of this experiment can be seen in Figure 6.23 a).

Figure 6.23 a) shows that the current drops off close to the SEM's acceleration voltage when the laser is on and off. Figure 6.23 b) shows the gradient of these graphs, where we note the FWHM of both curves is approximately 10V (or 10eV). This value for energy spread is way above the thermionic energy-spread recorded in literature and even the value recorded during the previous ∼1707K thermionic emission experiment. Furthermore, considering the noise the picoammeter records, the current measured when the laser was on and off was virtually indistinguishable.

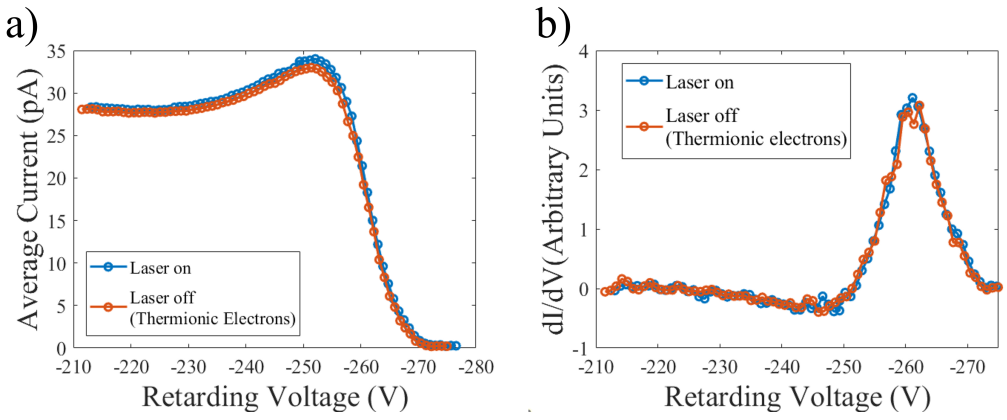

Figure 6.23.: *a) Plot of the average current detected by the collector versus the retarding voltage when the LaB_6 temperature was ∼1443K (1.4A resistive current). b) Plot of the differential of the average current detected by the collector with respect to voltage versus the retarding voltage.*

It seems the low currents produced at such low acceleration voltages mean that it is not possible to distinguish between photoemission and thermionic emission.

Based on our experimental results, the RFEA built is not operating correctly. This could be due to several reasons. Firstly, the SEM column was never designed to handle such low acceleration voltages. It is most likely not optimised for it and may need more stability for such a sensitive experiment. Secondly, in Lee et al.'s paper, a sourcemeter was connected to the retarding electrode and a picoammeter to the ground electrodes. This allowed them to record if any current was striking the electrodes. This would be particularly useful in our experiments as we could not determine if the focusing of the beam through the electrodes was fully optimised. Finally, the energy analyser we have built is relatively primitive due to all these limitations, and the currents generated at such low acceleration voltages are relatively low. Therefore, detecting photoelectrons with this RFEA setup might be impossible.

Due to all these reasons, conclusions cannot be reached on the difference between the laser on and off curves in Figure 6.23 a) and b), nor can the values of full width half maximum recorded be taken as an accurate reading of the energy-spread of the source. In future work, upgrading the apparatus so that a higher bias can be applied to the retarding electrode, which would allow the acceleration voltage of the electron beam to be subsequently increased, would be a good starting point. This would allow more current to be detected by the collector and hopefully allow photoelectron current to be distinguished from thermionic emission. Using a high voltage sourcemeter to apply a potential to the retarding electrode and let current striking the electrode to be recorded would also be a valuable addition to the setup. Unfortunately, operating high-voltage equipment requires careful safety precautions to be implemented, and these upgrades and subsequent experiments are, therefore, outside the scope of this research.

6.6. Conclusion

This chapter outlined the installation of a more powerful laser into our light injection setup. Results of duty cycle experiments with this setup were then described, and issues with the photoelectron current yield when a standard aperture was placed inside the SEM were identified. To try to increase the photoelectron current, a 200μm core optical fibre in the light injection setup was replaced with a more suitable 100μm optical fibre. SEM images taken pre and post the new fibre's installation were subsequently compared, and it was deduced that the new fibre did increase

the photoelectron yield and, therefore, the overall resolution of the SEM images captured.

Different characteristics of the photoelectron emitter were then measured with the upgraded light injection setup, and it was determined that the brightness during photoemission mode was lower than that during thermionic mode. We believe this is because the photoelectron current is still not of a high enough level to saturate the LaB_6 cathode, and the image's resolution is therefore, suffering due to the use of an incoherent source [87].

Finally, an experiment measuring the energy-spread of the photoelectron emitter using a retarding field energy analyser was described. Unfortunately, the equipment used in this setup was not sensitive enough to measure the beam's energy-spread. Repeating the experiment with upgraded equipment with a higher acceleration voltage could allow the energy-spread to be measured.

In conclusion, while a successful photoelectron emitter has been retrofitted into a ZEISS EVO SEM, its performance is not currently reaching its full potential. Many avenues could be followed to improve the operation of the photoelectron emitter. This includes optimising how the light strikes the crystal in the gun chamber, improving the vacuum conditions to minimise the contamination of the LaB_6 crystal, or even examining the installation of an alternative photocathode that would not contaminate so quickly in a poor vacuum. The following chapter will discuss these options in detail and outline other applications of this photoelectron emitter. Finally, a conclusion will be drawn on the overall research undertaken in this thesis.

Chapter 7.

Future Scope and Conclusion

7.1. Introduction

In chapter six, upgrades to the photoelectron emitter were outlined. Installing a higher-power laser and more suitable optical fibre proved successful, with increased photoelectron current detected and higher-resolution images captured. An attempt to analyse the energy-spread of the photoelectron emitter using a retarding field energy analyser (RFEA) was also presented. However, no conclusions could be formed due to issues with the experimental setup.

After characterising the brightness and resolution of the upgraded photoelectron emitter, it was concluded that a preliminary photoelectron emitter has successfully been retrofitted onto the ZEISS EVO SEM but is not operating to its maximum ability. Decreasing the acceleration voltage only further reduces the brightness and resolution of an image [5]. Therefore, as the original aim of producing the low energy-spread electron source was for low-voltage imaging, improving this low brightness and resolution is an important research direction. Options for improving these properties will be described in the following chapter, in section 7.2.1. This will include examining how the light source can be focused more effectively on the LaB_6 crystal to increase the photoelectron yield.

In addition to the brightness and resolution issue, it was determined in chapter five that the energy spread of our photoelectrons may be affected by having our crystal slightly heated to prevent contamination due to the poor vacuum conditions in the electron gun chamber. When the UV light struck the heated crystal we found that thermally assisted photoemission (TAPE) was most likely occurring indicated by a higher Wehnelt bias being required to retard the electrons. It was noted that operating in this mode may increase the energy-spread of the photoelectrons produced. Therefore, section 7.2.2 will focus on the different options that would

allow us to operate our photoelectron emitter at lower crystal temperatures.

Despite not currently operating at its full potential, there are still many applications for this photoelectron emitter. Alternative uses for the source outside those involving a low energy-spread electron beam for low-voltage imaging will be detailed. Finally, a discussion into where the photoelectron emitter lies on the emitter technology versus cost graph presented in chapter one will be undertaken, and a conclusion to the research presented in this thesis will be performed.

Please note excerpts of this chapter are from 'Quigley, F., Downing, C., McGuinness, C. and Jones, L. (2023) "A Retrofittable Photoelectron Gun for Low Voltage Imaging Applications in the Scanning Electron Microscope." Microscopy and Microanalysis, 29(5), 1610-1617 '.

7.2. Future Work

7.2.1. Improving the Light Injection Setup

From chapter 6, it was found that the brightness during photoelectron mode was 1000 times less than both an adapted and unadapted LaB_6 thermionic source operating under the same 15kV conditions. We believe the photoelectron emitter's issues with resolution and brightness are due to the LaB_6 tip not being saturated. An unsaturated source means the electron current is lower than it should be, and the electron beam is not as spatially coherent as one produced during thermionic mode because the electrons are being emitted from the side walls of the LaB_6 crystal and not the microflat on the tip [87]. Both of these factors will cause a decrease in brightness and resolution. Fortunately, increasing the photoelectron yield can resolve the issue of the tip not being saturated. This can be achieved by increasing the light striking the crystal.

In chapter six, the installation of a higher-power laser was described, and it was found that the image's resolution did increase due to the resulting increase of photoelectron current. Installing an even higher-power laser into our light injection setup is certainly a potential option to improve the photoelectron yield. However, the higher the laser power, the more safety precautions that need to be implemented and the higher the risk of injury to the SEM user. An alternative solution would be to upgrade and improve the light injection setup so that more light generated from the laser strikes the crystal. This solution was demonstrated throughout my research, firstly when the 3D printed holder was replaced with precise kinematic mounts for coupling the laser and multimode collimator and secondly when the

200μm core optical fibre was replaced with a more suitable alternative. In both cases, more light was delivered to the LaB_6 tip, and the contrast of the SEM images increased due to an increase in photoelectron current.

At this stage, the exterior of the light injection setup has been reasonably optimised. However, the light's delivery in the SEM interior could potentially be improved. The vacuum-compatible optical fibres are simply pointed at the crystal in the current design. The large angle at which the light exits the fibre ($\sim 12°$) ensures some photons will strike the tip of the crystal, as shown in Figure 7.1.

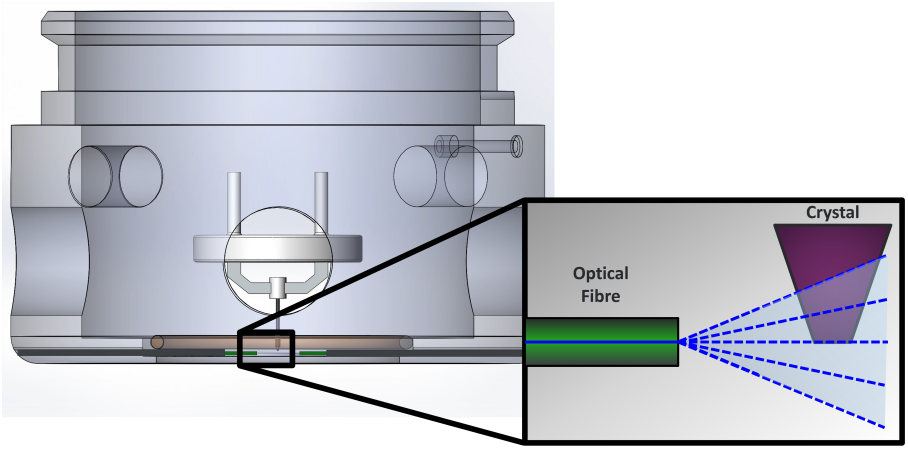

Figure 7.1.: *The Wehnelt in the Zeiss EVO SEM gun chamber, where the black box contains a magnified image of a simplified ray diagram of the light from the optical fibre striking the LaB_6 crystal.*

Improving the focusing of the laser on the LaB_6 tip could vastly increase the amount of light striking the crystal and the photoelectron yield. This could include using parabolic mirrors within the Wehnelt or placing a spherical ball lens at the end of the fibre as shown in Figure 7.2 . Whichever method is chosen, this route could be taken advantage of for increasing photoelectron yield.

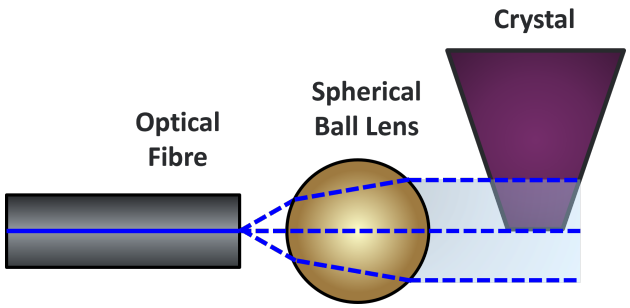

Figure 7.2.: *Simplified ray diagram of the light from an optical fibre with a spherical ball lens attached, striking a LaB_6 crystal.*

7.2.2. Improving Vacuum Conditions and an Alternative Photocathode Option

In chapter five, the evaluation of beam current detected at different crystal temperatures during photoemission was described. The results indicated that there would be a higher ratio of photoelectron current to thermionic current at a certain crystal temperature and that the photoemission was most likely thermally assisted. As we hope to produce a low energy-spread electron beam, it would be beneficial to operate the crystal at a temperature where only non-thermally assisted photoelectrons were being generated, with a negligible amount of thermionic current being emitted.

Unfortunately, due to the poor vacuum in the SEM gun chamber, the LaB_6 crystal contaminates quite easily at low temperatures. This causes its work function to increase, subsequently decreasing its photoelectron yield. The most apparent solution to this issue would be to improve the vacuum conditions in the electron gun chamber. However, this is more complex than it initially seems. Thermionic electron gun chambers have not been designed to accommodate ultra high vacuum (UHV) conditions (10^{-7}-10^{-12}mbar), so many of their entry ports involve KF flanges, which contain o-rings. O-rings are rubber seals used in high vacuum chambers (10^{-3}-10^{-7}mbar). While o-rings help maintain an acceptable vacuum level for regular thermionic electron gun operation, in an UHV chamber, they would be considered porous due to various gases from the air outside the chamber leaking through them. A more powerful ion pump cannot simply be added to improve the vacuum of a thermionic electron gun. The chamber's leak rate would also have to be reduced by replacing the KF flanges with conflat flanges, which create a stronger seal. Only some of these o-rings have commercially available substitutes, too. For example, the lid of the electron gun chamber has two large o-rings for mechanical alignment, which are certainly not straightforward to replace. In summary, the vacuum conditions could be improved to an extent by replacing easily accessible KF flanges, such as the gun shut valve, with conflat flanges and by upgrading to a more powerful ion pump. However, with the prohibitive cost of purchasing a more powerful pump and replacing the seals, there are more economically viable options than this one.

An alternative, perhaps more accessible route, is to replace the LaB_6 crystal with a cathode which contaminates less quickly in a poor vacuum: Cerium Hexaboride (CeB_6 or CeBix). CeB_6 is a very similar material to LaB_6 and is offered by a select few filament manufacturers at a slightly more expensive cost. While LaB_6 may have a higher electron emissivity than CeB_6 when operated at the same temperature,

CeB_6 has a higher resistivity to carbon contamination. It has also been found that CeB_6 has a lower evaporation rate when running in thermionic mode, causing it to have a longer lifetime than LaB_6 [79]. This resistance to carbon contamination could allow the crystal to photoemit at lower temperatures in a poor vacuum more efficiently than LaB_6. Replacing the LaB_6 cathode with a CeB_6 crystal is one route to increase the photoelectron to thermionic electron ratio if vacuum conditions cannot be improved.

7.3. Alternative Applications for the Retrofittable Photoelectron Emitter

The initial motivation behind building this retrofittable photoelectron emitter was to produce a low energy-spread electron beam for improved low-voltage imaging. While the current photoelectron emitter requires some improvements to its design before it can be practically useful for low-voltage imaging, it still has many other beneficial applications.

Our photoelectron emitter has a level of control over the emitting current that is not afforded to other guns. A thermionic emitter, for example, is limited by its fundamental operation of using resistive heating to generate the electron beam. Its resistive heating means it cannot be immediately turned down in temperature to produce a lower beam current. The crystal would need time to cool to the required temperature to produce the necessary current. In standard operation, this decrease should also be undertaken relatively slowly and with care to prevent damage to the crystal from thermal shock [8].

While Schottky and cold field emitters have more control over their current, it is still to a limited capacity. Schottky emitters, for example, usually have five settings for current. This is not ideal in experiments where you may want to precisely control the fluence (the number of electrons per unit area) and flux (the number of electrons per unit area per second) of electrons on a sample [94]. A monochromator can afford you this level of control, but as mentioned previously, it can be a costly upgrade for a microscope.

However, the design of our photoelectron emitter allows for control of the electron beam in a programmable way. The current generated from a photoelectron source can be easily modulated by adjusting the wattage of the light source and the subsequent power of the light striking the crystal. The laser currently installed is capable of switching at 19kHz. Therefore, depending on the user's requirements, the pho-

toelectron current can be turned on and off or reduced in very small increments using pulsed width modulation of the laser power. Applications of this include modulation of the beam during the flyback time [95], and for use in electron beam lithography, which benefits from control of the current and current density of the beam [53].

The design of this prototype's light delivery apparatus also allows for the use of a pulsed light source in the system. This could potentially allow for time-resolved SEM studies to be undertaken with this setup. Still, it should be noted that a pulsed operation of the system may increase the electron energy-spread due to space charge and Boersch effects [55]. As we were focused on using low-cost retrofittable components for our design, more expensive pulsed light sources were not considered. However, our design should accommodate pulsed operation if that is one of the areas of research the user requires.

7.4. Conclusion

This thesis aimed to investigate the viability of photostimulation for the development of a low energy-spread electron source for an electron microscope. **Chapter 1** presented a discussion highlighting the importance of electron microscopy in various research areas. It was then identified that due to the increasing popularity of low-voltage imaging, the technique would benefit from improved resolution by reducing chromatic aberration in the microscope. Many different methods for reducing chromatic aberration were discussed, including, but not limited to, using a C_c corrector, installing an electron monochromator or purchasing a microscope with a smaller pole piece gap. All these options proved to be quite expensive and rigid, and instead, an examination of low energy-spread electron emitters was discussed. A graph was plotted of the cost of different electron emitter technologies versus their energy-spread. A general trend was identified whereby the lower the energy-spread the user sought, the more expensive the equipment required to be purchased. Our analyses determined that while pulsed photoelectron sources could be found in Ultrafast TEMs, a continuous photoemitter has not been heavily researched for use in electron microscopes, and its position on the emitter cost versus energy-spread graph was unknown.

To gain context into the discussion of users requiring low energy-spread electron beams, a more detailed examination into optimising a beam using monochromators and low energy-spread electron emitters was undertaken in **Chapter 2**. An investigation was performed into the effect of acceleration voltage, C_c coefficients and

energy-spread conditions on an image of gold nanoparticles in a spherical-aberration corrected STEM. This was achieved using multislice simulations and the analyses of the signal-to-noise ratio values from each image advised on the optimal energy-spread for a monochromated electron emitter. This investigation indicated that users are looking towards even lower energy-spread electron beams for their low-voltage experiments. It highlighted that currently, monochromators are the only technology available to achieve beams with energy-spreads less than a cold FEG.

Chapter 3 proposed a low-cost continuous photoelectron source as an alternative approach to monochromator technology. After examining the fundamentals of photoemission, it was determined that a light source with a suitably chosen wavelength close to the work function of an appropriate photocathode could produce low energy-spread electrons. With this information, an investigation into the construction of a continuous photoelectron source was begun. Firstly, various photocathodes were examined, and lanthanum hexaboride (LaB_6), a low work function compound already commonly found in thermionic emitters, was chosen. My investigation into the dependence of quantum efficiency on the light source's photon energy based on literature values was then presented. Equipped with this knowledge, various commercially available LEDs and laser diodes were compared, and a 405nm laser diode was chosen. Using the same method outlined by Sawa et al. [51], the energy-spread of an emitter constructed of a LaB_6 photocathode and 405nm light source was calculated and found to be ΔE_e=0.37±0.04 eV. This is similar to a cold FEG's energy-spread and is an excellent starting point for a low energy-spread photoelectron emitter.

With the base elements of the photoemitter selected, a low-risk proof-of-concept experiment was constructed in **Chapter 4**. We designed a 3D printed holder to mount the two components, and the secondary electron detector in the SEM at different biases was used to detect the different photons and electrons generated. After separating the signals emitted during thermionic and photoemission using Matlab, we concluded that we had successfully generated photoelectrons with our setup. Building on these results, I designed a method, using COMSOL and Solidworks, of positioning an optical fibre in the Wehnelt such that light would strike the LaB_6 crystal without affecting the electrostatics of the electron gun. After running a series of experiments with a picoammeter attached to the Wehnelt, we found we could detect photoelectron current and that this current increased with increasing laser wattage.

Chapter 5 described our installation of this adapted Wehnelt into the SEM electron gun chamber. The production of initial SEM images when the laser was on

indicated a successful instalment. A laser with a wavelength unable to stimulate photoelectrons was then used to verify that photoelectrons, not thermionic electrons from the laser heating up the crystal, were being generated. An examination of how to improve the quality of the SEM images generated was then undertaken. This involved improving the light injection apparatus from 3D printed components to kinematic mounts to increase the amount of light delivered to the crystal. An analysis of how Wehnelt bias affected the beam current at different LaB_6 temperatures then revealed an interesting result. I found that it is most likely thermally assisted photoemission (TAPE) occurring when the light strikes the LaB_6, as our crystal needed to be operated at a slightly heated temperature to prevent contamination. In addition to this, these results highlighted that at a certain Wehnelt bias, the thermally assisted photoelectrons could be selected as our imaging beam over those generated via pure thermionic emission. It also showed that at a particular LaB_6 temperature, there is a higher ratio of photoelectrons to thermionic electrons.

Under these temperature and Wehnelt bias conditions, the photoelectron current and laser power relationship was examined. As expected, it was found that an increase in laser power resulted in an increase in photoelectron current and suggested that installing a higher-power laser could improve our photoelectron to thermionic electron ratio. The efficiency of the new light injection apparatus was also investigated. It was deduced that the optical fibre would need to be replaced to couple the laser light into the vacuum-side optical fibre effectively. With an understanding of the optimum Wehnelt bias and LaB_6 temperature, a new SEM image was taken with the upgraded kinematic mounts. The image quality was much higher than the one captured with the previous sub-optimal setup.

Chapter 6 outlined our systematic investigation into the laser wattage's effects on electron beam current and the installation of a higher-power 800mW laser into our light injection setup. The laser's power could be controlled via pulsed width modulation, allowing us to run experiments whereby the current detected and the SEM images generated at different laser duty cycles could be recorded. Much was learned from these results. Firstly, from the shape of the graph produced of current versus duty cycle percentage, when an aperture of 750μm was placed in the SEM, it was found that a multiphoton effect may be occurring. We also identified that when a standard aperture of 30μm was placed in the SEM, the photoelectron current decreased far more than the thermionic current. This potentially indicates that the C1 and C2 lenses need to be adjusted to more optimally select photoelectrons over thermionic electrons. Based on our analyses of the efficiency of our light injection setup, a new 100μm core optical fibre was installed to replace the 200μm core optical fibre, whose core was too large for our coupling requirements. This vastly improved

the quality of our SEM images captured.

As a final analysis of the practical operation of our emitter, we measured the brightness and spot size of different electron sources. This was achieved by taking SEM images when the C1 and C2 detectors were turned off and recording the electron beam current. After processing these images, it was found that our photoelectron emitter's brightness was 1000 times less than the emitter operating during thermionic emission. It was believed this was due to the photoelectron current being too low such that the tip was not saturated and an incoherent beam was being produced [87]. We also attempted to evaluate the energy-spread of the electron beam but found that, unfortunately, our experimental apparatus was not sensitive enough for such measurements.

The analyses of our photoelectron emitter indicated that it was not working to its full potential. **Chapter 7** discussed the two main issues with the setup. Firstly, that the tip was not being saturated; therefore, the user was imaging with an incoherent source, and this was causing low brightness and resolution. Secondly, the crystal had to be operated slightly heated to prevent contamination, which may lead to an unwanted increase in electron energy-spread. Fortunately, all our previous experimental investigations provided great insight into how to improve the overall setup to solve these issues. This included upgrading the light injection setup in the electron gun chamber such that the light would be more focused on the LaB_6 crystal, as an increase in light would increase photoelectron yield. An increase in image resolution could then potentially occur with a completely saturated source. There is also the option of improving the vacuum conditions such that the LaB_6 crystal could be operated at lower temperatures during photoelectron mode. It was found that a more accessible option would be to replace the LaB_6 crystal with a CeB_6 (cerium hexaboride) cathode, which contaminates less easily at low temperatures.

Despite the upgrades required to make our photoelectron emitter practically useful for low-voltage imaging, we found that it still has many other applications. The ability of the photoemitter's beam current to be precisely controlled by pulsed width modulation of the laser power gives it an advantage over other electron sources. This gun property is particularly beneficial when the user wants to control the flux and fluence of the electrons on the sample. The control of the electron emitter in a programmable way makes it applicable in many research areas, such as modulation of the beam during flyback time and for use in electron beam lithography. Due to the flexibility of our design, upgrading the laser diode may even allow time-resolved SEM studies to be undertaken with a pulsed light source.

Considering everything, a question proposed in chapter one has yet to be answered.

In the graph comparing the cost versus energy-spread of different monochromator and electron emitter technology, where would a continuous photoelectron source lie? Based on the literature, a photoemitter could have an energy-spread between a monochromated TEM and a cold FEG [51][83]. While its cost can vary depending on the components it's composed of, it will most likely be more expensive than a thermionic electron gun but potentially less expensive than field emitters, which are more complex and require very stringent pumping conditions [56]. The approximate continuous photoelectron emitter region is therefore shown in Figure 7.3.

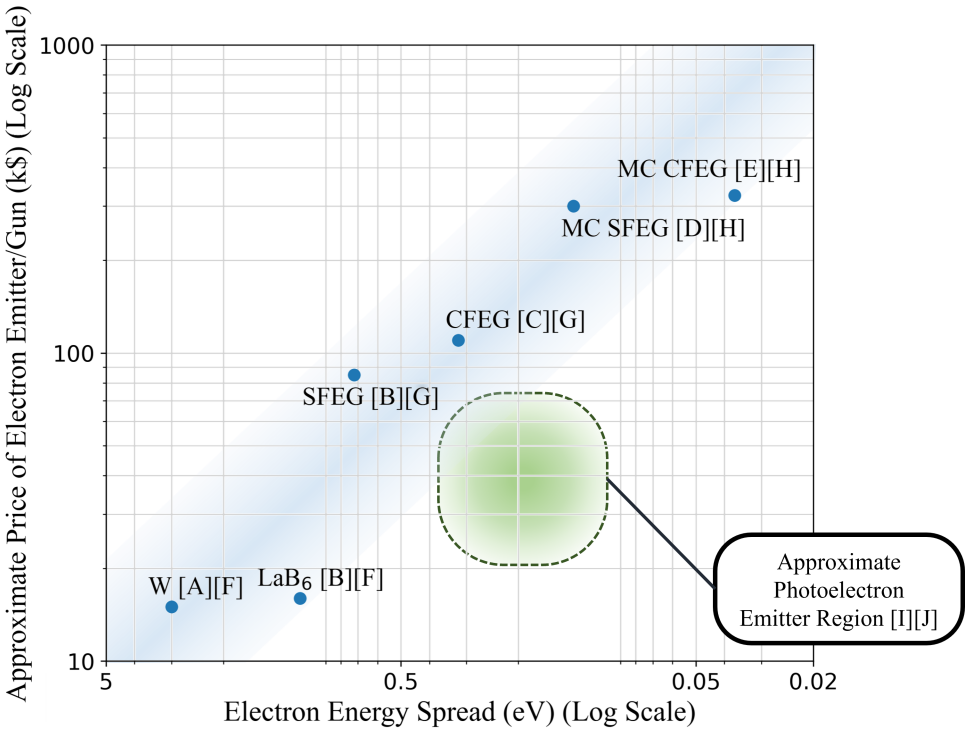

Figure 7.3.: *Reproduced graph comparing the approximate price of electron emitter and monochromator technology, and the electron energy-spread. The blue band acts as a guide to the eye of the general trend in the graph. The bottom left green region indicates the approximate electron emitter region. [A] Williams and Carter (2009) (Ref.: [8]), [B] Stoger-Pollach (2010) ((Ref.: [33]), [C] Sawada et al. (2009) (Ref.: [42]), [D] Kisielowski et al. (2008) (Ref.: [28]), [E] Carpenter et al. (2014) (Ref.: [43]), [I] Sawa et al. (2017) (Ref.: [51]) and [J] Konishi et al. (2012) (Ref.: [83]). Pricing data was collected via personal communications: [F] R. Beanland, December 7, 2021; [G] G. Nicotra, November 29, 2021; and [H] D. Muller, November 28, 2021. This graph was created by the author and was adapted from Quigley et al. 2022 (Reference Number: [30]).*

Figure 7.3 shows that the photoelectron emitter technology is in precisely the right region that would interest low voltage microscopy researchers. This region deviates from the current trend, which requires the user to purchase more expensive equipment to acquire a lower energy-spread electron beam. If cost-effective parts are chosen, an energy-spread less than a cold FEG could be achieved at a fraction

of the cost of a monochromator to manufacture. This ethos has been the basis for this thesis. During the whole process, commercially available low-cost components were used to build a retrofittable photoelectron emitter that could upgrade the functionality of older thermionic SEMs. The emitter we have built could have an energy-spread as low as ΔE_e=0.37±0.04 eV with its 405nm light source. Our flexible design means that in the future, light sources with a wavelength closer to the work function of the cathode could be installed to produce a beam with an even lower electron energy-spread. While the photoelectron emitter we have built may not be operating at its full potential, future directions to improving the design of the source to reach this goal have been presented. In addition to this, many more promising applications of the photoemitter have been outlined. These additional benefits further show the improvement this retrofit has had on increasing the functionality of this older SEM.

In conclusion, the feasibility of photostimulation for developing a low energy-spread electron source for an electron microscope has been investigated. A low-cost retrofittable photoelectron emitter with a potential energy-spread of ΔE_e=0.37±0.04 eV was successfully built. Experiments were undertaken to characterise the source, and further improvements to the emitter have been proposed such that it can be practically useful for low voltage imaging. Other applications for the emitter have been presented, including its potential use in beam modulation and time-resolved SEM studies.

Bibliography

[1] A. Brecher and M. Cutrera, "A Scanning Electron Microscope (SEM) Study of the Magnetic Domain Structure of Iron Meteorites and Their Synthetic Analogues," *J. Geomag. Geoelectr.*, vol. 28, pp. 31–45, 1976.

[2] Y. Nakata, K. Tsubakimoto, N. Miyanaga, A. Narazaki, T. Shoji, and Y. Tsuboi, "Laser-induced transfer of noble metal nanodots with femtosecond laser-interference processing," *Nanomaterials*, vol. 11, no. 2, pp. 1–10, 2021.

[3] C. Kübel, A. Voigt, R. Schoenmakers, M. Otten, D. Su, T. C. Lee, A. Carlsson, H.-J. Engelmann, and J. Bradley, "Recent advances in electron tomography: TEM and HAADF-STEM tomography for materials science and IC applications," *Microscopy and Microanalysis*, vol. 11, no. 5, pp. 378–400, 2005.

[4] M. Batzill, "The surface science of graphene: Metal interfaces, CVD synthesis, nanoribbons, chemical modifications, and defects," *Surface Science Reports*, vol. 67, no. 3-4, pp. 83–115, 2012.

[5] J. B. Pawley, "Low Voltage Scanning Electron Microscopy," *Scanning Electron Microscopy*, vol. 3, no. 1, pp. 253–272, 1984.

[6] F. Friedrich, Y. Matsumura, H. Pohl, M. Bai, T. Hörnschemeyer, and R. G. Beutel, "Insect morphology in the age of phylogenomics: Innovative techniques and its future role in systematics," *Entomological Science*, vol. 17, no. 1, pp. 1–24, 2014.

[7] M. F. Teaford, "Scanning electron microscope diagnosis of wear patterns versus artifacts on fossil teeth." *Scanning microscopy*, vol. 2, no. 2, pp. 1167–1175, 1988.

[8] D. B. Williams and C. B. Carter, *Transmission Electron Microscopy: A Textbook for Materials Science*. Boston, MA: Springer US, 2009, pp. 3–17.

[9] J. I. Goldstein, D. E. Newbury, P. Echlin, D. C. Joy, C. E. Lyman, E. Lifshin, L. Sawyer, and J. R. Michael, "The SEM and Its Modes of Operation," in

Scanning Electron Microscopy and X-ray Microanalysis. Boston, MA: Springer US, 2003, pp. 21–60.

[10] C. B. Carter and D. B. Williams, *Transmission electron microscopy: Diffraction, imaging, and spectrometry*. Springer, 2016.

[11] R. F. Egerton, "Electron energy-loss spectroscopy in the TEM," *Reports on Progress in Physics*, vol. 72, no. 1, 2009.

[12] T. Luo and A. Khursheed, "Transmission EELS attachment for SEM," *IEEE Transactions on Device and Materials Reliability*, vol. 6, no. 2, pp. 182–185, 2006.

[13] P. C. Hackley, A. M. Jubb, R. J. McAleer, B. J. Valentine, and J. E. Birdwell, "A review of spatially resolved techniques and applications of organic petrography in shale petroleum systems," *International Journal of Coal Geology*, vol. 241, no. April, p. 103745, 2021.

[14] C. M. Sparrow, "On Spectroscopic Resolving Power," *American Astronomical Society*, 1874.

[15] H. Sawada, T. Sasaki, F. Hosokawa, and K. Suenaga, "Atomic-resolution STEM imaging of graphene at low voltage of 30 kV with resolution enhancement by using large convergence angle," *Physical Review Letters*, vol. 114, no. 16, p. 166102, Apr 2015.

[16] D. C. Joy, "The Aberration Corrected SEM," *AIP Conference Proceedings*, no. 1, p. 535, sep.

[17] O. L. Krivanek, N. Dellby, A. J. Spence, R. A. Camps, and L. M. Brown, "Aberration correction in the STEM," in *Electron Microscopy and Analysis Group Conference*, Cambridge, 1997, pp. 35–40.

[18] M. Haider, S. Uhlemann, E. Schwan, H. Rose, B. Kabius, and K. Urban, "Electron microscopy image enhanced," *Nature*, vol. 392, no. 6678, pp. 768–769, Apr 1998.

[19] R. Klie, "Reaching a new resolution standard with electron microscopy," *Physics*, vol. 2, p. 85, 2009.

[20] R. F. Egerton, "Choice of operating voltage for a transmission electron microscope," *Ultramicroscopy*, vol. 145, pp. 85–93, 2014.

[21] J. Liu, "High-resolution and low-voltage FE-SEM imaging and microanalysis in materials characterization," *Materials Characterization*, vol. 44, no. 4, pp. 353–363, 2000.

[22] D. C. Joy and C. S. Joy, "Low Voltage Scanning Electron Microscopy," *Micron*, vol. 27, no. 3, pp. 247–263, 1996.

[23] J. Liang, X. Xiao, T. M. Chou, and M. Libera, "Analytical Cryo-Scanning Electron Microscopy of Hydrated Polymers and Microgels," *Accounts of Chemical Research*, vol. 54, no. 10, pp. 2386–2396, May 2021.

[24] J. Zach and M. Haider, "Aberration correction in a low voltage SEM by a multipole corrector," *Nuclear Inst. and Methods in Physics Research, A*, vol. 363, no. 1-2, pp. 316–325, 1995.

[25] M. Linck, P. Hartel, S. Uhlemann, F. Kahl, H. Müller, J. Zach, M. Haider, M. Niestadt, M. Bischoff, J. Biskupek, Z. Lee, T. Lehnert, F. Börrnert, H. Rose, and U. Kaiser, "Chromatic Aberration Correction for Atomic Resolution TEM Imaging from 20 to 80 kV," *Physical Review Letters*, vol. 117, no. 7, p. 076101, 2016.

[26] K. Tsuno and D. A. Jefferson, "Design of an objective lens pole piece for a transmission electron microscope with a resolution less than 0.1 nm at 200 kV," *Ultramicroscopy*, vol. 72, no. 1-2, pp. 31–39, Apr 1998.

[27] K. Tsuno, "Monochromators in electron microscopy," *Nuclear Instruments and Methods in Physics Research, Section A: Accelerators, Spectrometers, Detectors and Associated Equipment*, vol. 645, no. 1, pp. 12–19, 2011.

[28] C. Kisielowski, B. Freitag, M. Bischoff, H. Van Lin, S. Lazar, G. Knippels, P. Tiemeijer, M. Van Der Stam, S. Von Harrach, M. Stekelenburg, M. Haider, S. Uhlemann, H. Müller, P. Hartel, B. Kabius, D. Miller, I. Petrov, E. A. Olson, T. Donchev, E. A. Kenik, A. R. Lupini, J. Bentley, S. J. Pennycook, I. M. Anderson, A. M. Minor, A. K. Schmid, T. Duden, V. Radmilovic, Q. M. Ramasse, M. Watanabe, R. Erni, E. A. Stach, P. Denes, and U. Dahmen, "Detection of single atoms and buried defects in three dimensions by aberration-corrected electron microscope with 0.5-Å information limit," *Microscopy and Microanalysis*, vol. 14, no. 5, pp. 469–477, 2008.

[29] O. L. Krivanek, T. C. Lovejoy, N. Dellby, and R. W. Carpenter, "Monochromated STEM with a 30 meV-wide, atom-sized electron probe," *Journal of Electron Microscopy*, vol. 62, no. 1, pp. 3–21, 2013.

[30] F. Quigley, P. McBean, P. O'Donovan, J. J. P. Peters, and L. Jones, "Cost and Capability Compromises in STEM Instrumentation for Low-Voltage Imaging," *Microscopy and Microanalysis*, vol. 28, no. 4, pp. 1437–1443, Mar 2022.

[31] M. Watanabe, Y. Hinaga, M. Yamamoto, O. Nakamora, T. Someya, T. Goto, K. Konno, T. Yanaka, and N. Takahashi, "1 Million Volt High Voltage Electron Microscope," *Journal of Electron Microscopy*, vol. 17, no. 4, pp. 289–300, 1968.

[32] S. Ozasa, Y. Kato, H. Todokoro, S. Kasai, S. Katagiri, H. Kimura, E. Sugata, K. Fukai, H. Fujita, and K. Ura, "3 Million Volt Electron Microscope," *Journal of Electron Microscopy*, vol. 21, no. 2, pp. 109–118, Jan 1972.

[33] M. Stöger-Pollach, "Low voltage TEM: Influences on electron energy loss spectrometry experiments," *Micron*, vol. 41, no. 6, pp. 577–584, 2010.

[34] G. D. Peckham and I. J. McNaught, "Applications of Maxwell-Boltzmann distribution diagrams," *Journal of Chemical Education*, vol. 69, no. 7, p. 554, 1992.

[35] K. Kimoto and Y. Matsui, "Software techniques for EELS to realize about 0.3 eV energy resolution using 300 kV FEG-TEM," *Journal of Microscopy*, vol. 208, no. 3, pp. 224–228, 2002.

[36] R. F. Klie, I. Arslan, and N. D. Browning, "Atomic resolution electron energy-loss spectroscopy," *Journal of Electron Spectroscopy and Related Phenomena*, vol. 143, no. 2-3 SPEC. ISS., pp. 105–115, 2005.

[37] K. Naydenova, G. McMullan, M. J. Peet, Y. Lee, P. C. Edwards, S. Chen, E. Leahy, S. Scotcher, R. Henderson, and C. J. Russo, "CryoEM at 100keV: A demonstration and prospects," *IUCrJ*, vol. 6, pp. 1086–1098, 2019.

[38] S. Mogren and R. Reifenberger, "Field emission and photofield emission energy distributions from LaB6," *Surface Science*, vol. 254, no. 1-3, pp. 169–181, 1991.

[39] K. Bücker, M. Picher, O. Crégut, T. LaGrange, B. W. Reed, S. T. Park, D. J. Masiel, and F. Banhart, "Electron beam dynamics in an ultrafast transmission electron microscope with Wehnelt electrode," *Ultramicroscopy*, vol. 171, pp. 8–18, 2016.

[40] F. Houdellier, G. M. Caruso, S. Weber, M. Kociak, and A. Arbouet, "Development of a high brightness ultrafast Transmission Electron Microscope based on a laser-driven cold field emission source," *Ultramicroscopy*, vol. 186, pp. 128–138, 2018.

[41] E. Kieft, K. B. Schliep, P. K. Suri, and D. J. Flannigan, "Communication: Effects of thermionic-gun parameters on operating modes in ultrafast electron microscopy," *Structural Dynamics*, vol. 2, no. 5, 2015.

[42] H. Sawada, Y. Tanishiro, N. Ohashi, T. Tomita, F. Hosokawa, T. Kaneyama, Y. Kondo, and K. Takayanagi, "STEM imaging of 47-pm-separated atomic columns by a spherical aberration-corrected electron microscope with a 300-kV cold field emission gun," *Journal of Electron Microscopy*, vol. 58, no. 6, pp. 357–361, 2009.

[43] R. W. Carpenter, H. Xie, S. Lehner, T. Aoki, J. Mardinly, M. Vahidi, N. Newman, and F. A. Ponce, "High energy and spatial resolution EELS band gap measurements using a nion monochromated cold field emission HERMES dedicated STEM," *Microscopy and Microanalysis*, vol. 20, no. 3, pp. 70–71, 2014.

[44] F. Houdellier, A. Masseboeuf, M. Monthioux, and M. J. Hÿtch, "New carbon cone nanotip for use in a highly coherent cold field emission electron microscope," *Carbon*, vol. 50, no. 5, pp. 2037–2044, 2012.

[45] H. Zhang, J. Tang, J. Yuan, and L. C. Qin, "Ultrabright and monochromatic nanowire electron sources," *MRS Bulletin*, vol. 42, no. 7, pp. 511–517, 2017.

[46] J. M. Lafferty, "Boride cathodes," *Journal of Applied Physics*, vol. 22, no. 3, pp. 299–309, 1951.

[47] P. G. May, R. R. Petkie, J. M. Harper, and D. S. Yee, "Photoemission from thin-film lanthanum hexaboride," *Applied Physics Letters*, vol. 57, no. 15, pp. 1584–1585, 1990.

[48] S. Mogren and R. Reifenberger, "Thermionic and Threshold Photoemission Energy Distributions from LaB6 (110)," *Surface Science*, vol. 186, pp. 232–246, 1987.

[49] M. quan Qian, M. rong Yang, Q. Pan, K. song Hu, R. pei Deng, J. jun Shi, Z. cong Tao, J. bo Cheng, Q. jun Ran, and Z. lun Lin, "Photoemission studies on LaB 6 and pure metals using a nanosecond KrF excimer laser," *Nuclear Inst. and Methods in Physics Research, A*, vol. 358, no. 1-3, pp. 280–283, 1995.

[50] P. E. Oettinger, "Measured brightness of electron beams photoemitted from multicrystalline LaB6," *Applied Physics Letters*, vol. 56, no. 4, pp. 333–334, 1990.

[51] H. Sawa, M. Anzai, T. Konishi, T. Tachibana, and T. Hirayama, "Development of a UHV-compatible low-energy electron gun using the photoelectric effect," *58th Vacuum Symposium Proceedings*, vol. 60, no. 12, pp. 467–470, 2017.

[52] JEOL Ltd., "Schottky-emission electron gun, SE electron gun, Glossary of SEM Terms."

[53] R. F. W. Pease, "Electron beam lithography," *Contemporary Physics*, vol. 22, no. 3, pp. 265–290, 1981.

[54] J. A. Hachtel, A. R. Lupini, and J. C. Idrobo, "Exploring the capabilities of monochromated electron energy loss spectroscopy in the infrared regime," *Scientific Reports*, vol. 8, no. 1, pp. 1–10, dec 2018.

[55] L. Piazza, D. J. Masiel, T. LaGrange, B. W. Reed, B. Barwick, and F. Carbone, "Design and implementation of a fs-resolved transmission electron microscope based on thermionic gun technology," *Chemical Physics*, vol. 423, pp. 79–84, 2013.

[56] L. E. Franken, K. Grünewald, E. J. Boekema, and M. C. Stuart, "A Technical Introduction to Transmission Electron Microscopy for Soft-Matter: Imaging, Possibilities, Choices, and Technical Developments," *Small*, vol. 16, no. 14, p. 1906198, 2020.

[57] L. R. Dacosta, H. G. Brown, P. M. Pelz, A. Rakowski, N. Barber, P. O. Donovan, P. Mcbean, L. Jones, J. Ciston, M. C. Scott, and C. Ophus, "Prismatic 2.0 - Simulation Software for Scanning and High Resolution Transmission Electron Microscopy (STEM and HRTEM)," *Micron*, vol. 151, p. 103141, 2021.

[58] T. Mullarkey, C. Downing, and L. Jones, "Development of a Practicable Digital Pulse Read-Out for Dark-Field STEM," *Microscopy and Microanalysis*, vol. 27, no. 1, pp. 99–108, 2021.

[59] W. Grogger, F. Hofer, G. Kothleitner, and B. Schaffer, "An introduction to high-resolution EELS in transmission electron microscopy," *Topics in Catalysis*, vol. 50, no. 1-4, pp. 200–207, 2008.

[60] T. Aarholt, Y. K. Frodason, and Ø. Prytz, "Imaging defect complexes in scanning transmission electron microscopy: Impact of depth, structural relaxation, and temperature investigated by simulations," *Ultramicroscopy*, vol. 209, no. October 2019, p. 112884, 2020.

[61] J. Verbeeck, A. Béché, and W. Van den Broek, "A holographic method to measure the source size broadening in STEM." *Ultramicroscopy*, vol. 120, pp. 35–40, sep 2012.

[62] J. M. Lebeau, S. D. Findlay, X. Wang, A. J. Jacobson, L. J. Allen, and S. Stemmer, "High-angle scattering of fast electrons from crystals containing heavy elements: Simulation and experiment," *Physical Review B - Condensed Matter and Materials Physics*, vol. 79, no. 21, p. 214110, 2009.

[63] J. M. Lebeau, S. D. Findlay, L. J. Allen, and S. Stemmer, "Quantitative atomic resolution scanning transmission electron microscopy," *Physical Review Letters*, vol. 100, no. 20, p. 206101, 2008.

[64] R. Erni, M. D. Rossell, C. Kisielowski, and U. Dahmen, "Atomic-resolution imaging with a sub-50-pm electron probe," *Physical Review Letters*, vol. 102, no. 9, p. 096101, 2009.

[65] H. G. Brown, Z. Chen, M. Weyland, C. Ophus, J. Ciston, L. J. Allen, and S. D. Findlay, "Structure Retrieval at Atomic Resolution in the Presence of Multiple Scattering of the Electron Probe," *Physical Review Letters*, vol. 121, no. 26, p. 266102, 2018.

[66] L. Jones and P. D. Nellist, "Three-dimensional optical transfer functions in the aberration-corrected scanning transmission electron microscope," *Journal of Microscopy*, vol. 254, no. 2, pp. 47–64, May 2014.

[67] H. G. Brown, R. Ishikawa, G. Sánchez-Santolino, N. R. Lugg, Y. Ikuhara, L. J. Allen, and N. Shibata, "A new method to detect and correct sample tilt in scanning transmission electron microscopy bright-field imaging," *Ultramicroscopy*, vol. 173, no. November 2016, pp. 76–83, 2017.

[68] G. Sánchez-Santolino, N. R. Lugg, T. Seki, R. Ishikawa, S. D. Findlay, Y. Kohno, Y. Kanitani, S. Tanaka, S. Tomiya, Y. Ikuhara, and N. Shibata, "Probing the Internal Atomic Charge Density Distributions in Real Space," *ACS Nano*, vol. 12, no. 9, pp. 8875–8881, 2018.

[69] Y. Xin, J. Kynoch, K. Han, Z. Liang, P. J. Lee, D. C. Larbalestier, Y. F. Su, K. Nagahata, T. Aoki, and P. Longo, "Facility implementation and comparative performance evaluation of probe-corrected TEM/STEM with schottky and cold field emission illumination," *Microscopy and Microanalysis*, vol. 19, no. 2, pp. 487–495, 2013.

[70] J. C. Azcárate, M. H. Fonticelli, and E. Zelaya, "Radiation Damage Mechanisms of Monolayer-Protected Nanoparticles via TEM Analysis," *Journal of Physical Chemistry C*, vol. 121, no. 46, pp. 26 108–26 116, 2017.

[71] JEOL, "Jem-2100 Electron Electron," *Microscope*, 2004.

[72] L. Jones, H. Yang, T. J. Pennycook, M. S. Marshall, S. Van Aert, N. D. Browning, M. R. Castell, and P. D. Nellist, "Smart Align—a new tool for robust non-rigid registration of scanning microscope data," *Advanced Structural and Chemical Imaging*, vol. 1, no. 1, pp. 1–16, 2015.

[73] S. Van Aert, A. De Backer, L. Jones, G. T. Martinez, A. Béché, and P. D. Nellist, "Control of Knock-On Damage for 3D Atomic Scale Quantification of Nanostructures: Making Every Electron Count in Scanning Transmission Electron Microscopy," *Physical Review Letters*, vol. 122, no. 6, p. 066101, 2019.

[74] F. Quigley, C. Downing, C. McGuinness, and L. Jones, "A Retrofittable Photoelectron Gun for Low-Voltage Imaging Applications in the Scanning Electron Microscope," *Microscopy and Microanalysis*, vol. 29, no. 5, pp. 1610–1617, Jul 2023.

[75] B. Leblond, G. Kuznetsov, and M. Batazova, "Short pulse photoemission from LaB6-based materials," *Nuclear Instruments and Methods in Physics Research, Section A: Accelerators, Spectrometers, Detectors and Associated Equipment*, vol. 372, no. 3, pp. 562–566, 1996.

[76] P. Teredesai, D. V. Muthu, N. Chandrabhas, S. Meenakshi, V. Vijayakumar, P. Modak, R. S. Rao, B. K. Godwal, S. K. Sikka, and A. K. Sood, "High pressure phase transition in metallic LaB6: Raman and X-ray diffraction studies," *Solid State Communications*, vol. 129, no. 12, pp. 791–796, 2004.

[77] L. Bai, N. Ma, and F. Liu, "Structure and chemical bond characteristics of LaB 6," *Physica B: Condensed Matter*, vol. 404, no. 21, pp. 4086–4089, 2009.

[78] C. Oshima, E. Bannai, T. Tanaka, and S. Kawai, "Thermionic work function of LaB6 single crystals and their surfaces," *Journal of Applied Physics*, vol. 48, no. 9, pp. 3925–3927, 1977.

[79] K. Torgasin, K. Morita, H. Zen, K. Masuda, T. Katsurayama, T. Murata, S. Suphakul, H. Yamashita, T. Nogi, T. Kii, K. Nagasaki, and H. Ohgaki, "Thermally assisted photoemission effect on CeB6 and LaB6 for application as photocathodes," *Physical Review Accelerators and Beams*, vol. 20, no. 7, p. 073401, 2017.

[80] T. Ohshima and M. Kudo, "Electron beam brightness from negative-electron-affinity photocathodes for scanning electron microscopy application," *Japanese Journal of Applied Physics*, vol. 43, no. 12, pp. 8335–8340, 2004.

[81] H. Morishita, T. Ohshima, M. Kuwahara, Y. Ose, and T. Agemura, "Resolution improvement of low-voltage scanning electron microscope by bright and monochromatic electron gun using negative electron affinity photocathode," *Journal of Applied Physics*, vol. 127, no. 16, p. 164902, 2020.

[82] T. Ohshima, "NEA photocathode for SEM application," *Microelectronic Engineering*, vol. 67-68, pp. 951–954, 2003.

[83] T. Konishi, S. Jinno, and T. Hirayama, "Development of a low energy electron beam source using the photoelectric effect," *Journal of Physics: Conference Series*, vol. 388, no. PART 14, p. 142021, 2012.

[84] W. Cornelius, D. Courant, P. J. Delfyett, S. Diemer, V. P. Gabel, W. Honk, G. Lidgard, R. Matthes, I. Mellerio, T. Okuno, M. B. Ritter, K. Schulmeister, D. H. Sliney, B. B. Stuck, E. Sutter, and J. Tajnai, "ICNIRP statement on light-emitting diodes (LEDS) and laser diodes: Implications for hazard assessment," *Health Physics*, vol. 78, no. 6, pp. 744–752, 2000.

[85] W. A. Curtis and D. J. Flannigan, "Toward Å-fs-meV resolution in electron microscopy: Systematic simulation of the temporal spread of single-electron packets," *Physical Chemistry Chemical Physics*, vol. 23, no. 41, pp. 23 544–23 553, 2021.

[86] W. C. Bigelow, "Notes on Electron Gun Saturation and Stabilization... An Older Man's Lectures," *Microscopy Today*, vol. 18, no. 3, pp. 26–30, 2010.

[87] S. Chapman, "The Life and Death of a Tungsten Hairpin Filament," *Microscopy Today*, no. April, pp. 104–132, 2003.

[88] P. Horowitz and W. Hill, *The Art of Electronics*. Cambridge University Press, 2015, vol. 3.

[89] G. S. He, *Laser Stimulated Scattering and Multiphoton Excitation*. Oxford University Press, 2022.

[90] N. V. Tkachenko, *Optical spectroscopy: methods and instrumentations*. Elsevier, 2006.

[91] M. Bekeris, T. Truong, S. Carron, Z. Karimi, H. Feng, U. Nze, M. Beeman, R. D. Sochol, and R. Warren, "Rapid Quantification of Nanosphere Lithography Packing Defects Using Scanning Electron Microscopy Edge Effects," *Physica Status Solidi - Rapid Research Letters*, vol. 14, no. 11, pp. 1–6, 2020.

[92] M. S. Bronsgeest, J. E. Barth, L. W. Swanson, and P. Kruit, "Probe current, probe size, and the practical brightness for probe forming systems," *Journal of Vacuum Science and Technology B: Microelectronics and Nanometer Structures*, vol. 26, no. 3, p. 949, 2008.

[93] H. R. Lee, J. Hwang, T. Ogawa, H. Jung, D. J. Yun, S. Lee, and I. Y. Park, "High-Performance Compact Pre-Lens Retarding Field Energy Analyzer for Energy Distribution Measurements of an Electron Gun," *Microscopy and Microanalysis*, vol. 28, no. 6, pp. 1989–1997, 2022.

[94] M. Ilett, M. S'Ari, H. Freeman, Z. Aslam, N. Koniuch, M. Afzali, J. Cattle, R. Hooley, T. Roncal-Herrero, S. M. Collins, N. Hondow, A. Brown, and R. Brydson, "Analysis of complex, beam-sensitive materials by transmission electron microscopy and associated techniques: TEM of Beam Sensitive Materials," *Philosophical Transactions of the Royal Society A: Mathematical, Physical and Engineering Sciences*, vol. 378, no. 2186, 2020.

[95] H. Hashiguchi, K. Yagi, Y. Jimbo, R. Sagawa, R. S. Bloom, B. Reed, S. T. Park, D. J. Masiel, and I. Ohnishi, "Ways to Suppress Electron Beam Damage Using High-Speed Electron Beam Control by Electrostatic Shutter in Sample Observation and Analysis," *Microscopy and Microanalysis*, vol. 28, no. S1, pp. 2200–2201, 2022.

Appendix A.

Gaussian Distribution of weights

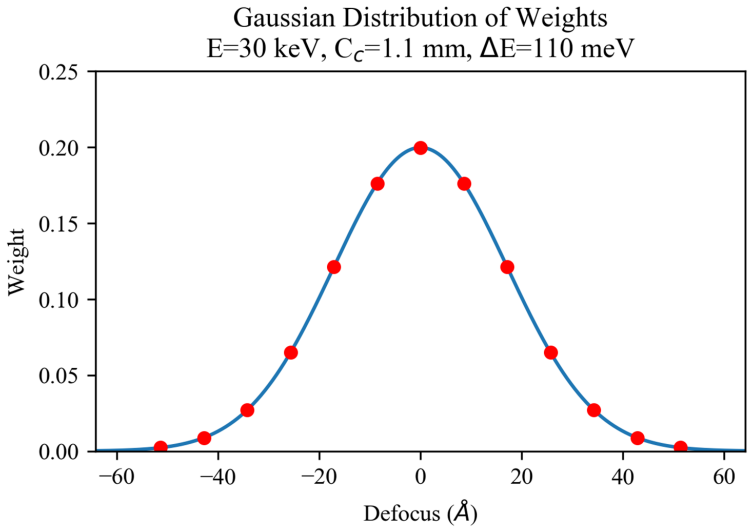

Figure A.1.: *Graph of the gaussian distribution of weights for the weighted summation of defocus planes. The range used was equally spaced defocus values spanning* $\pm 3\sigma$*. A Gaussian which has been normalised was then used to assign weights to each of these defoci.*

Appendix B.

Tableau of Simulated Images

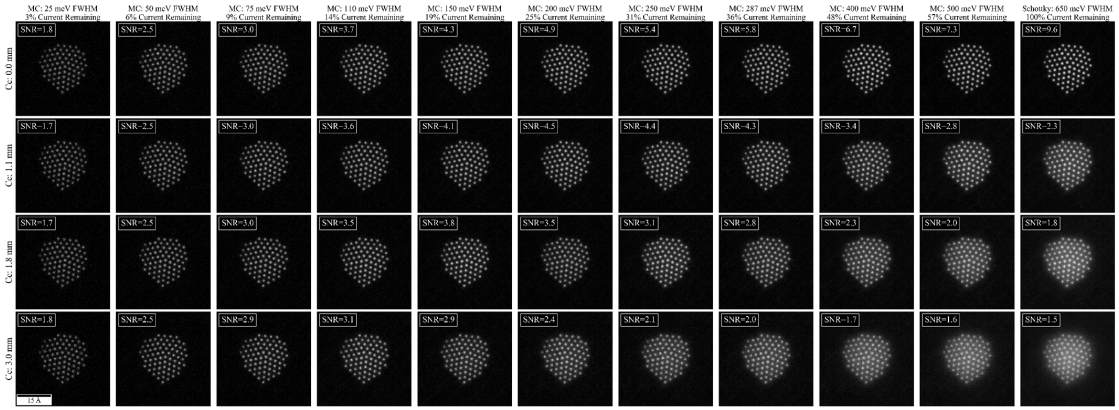

Figure B.1.: *Images of simulated Au nanoparticle at E = 60 keV with a Schottky field emission gun at various levels of monochromation. The Cc coefficient for each row is Cc = 0 mm, 1.1 mm, 1.8 mm, and 3.0 mm from top to bottom respectively. For each column ΔE = 25 meV, 50 meV, 75 meV, 110 meV, 150 meV, 200 meV, 250 meV, 287 meV, 400 meV, 500 meV, and 650 meV. The scale bar is 15 angstroms.*

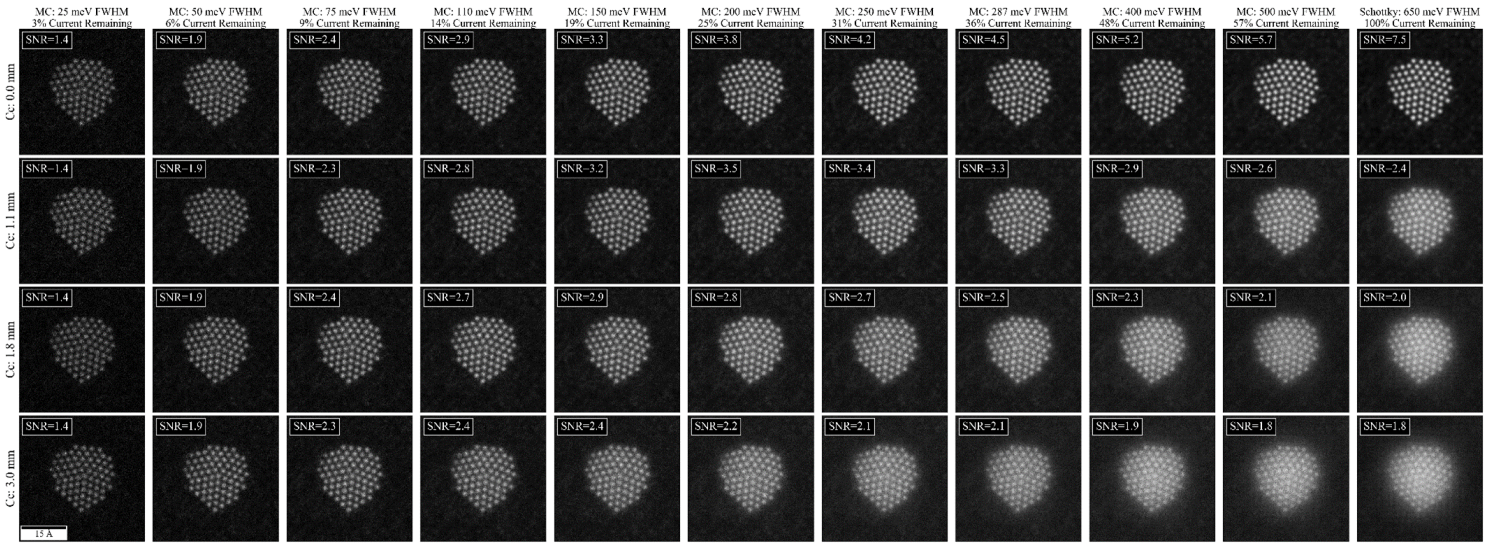

Figure B.2.: *Images of simulated Au nanoparticle at $E = 30$ keV with a Schottky field emission gun at various levels of monochromation. The Cc coefficient for each row is Cc = 0 mm, 1.1 mm, 1.8 mm, and 3.0 mm from top to bottom respectively. For each column $\Delta E = 25$ meV, 50 meV, 75 meV, 110 meV, 150 meV, 200 meV, 250 meV, 287 meV, 400 meV, 500 meV, and 650 meV. The scale bar is 15 angstroms.*

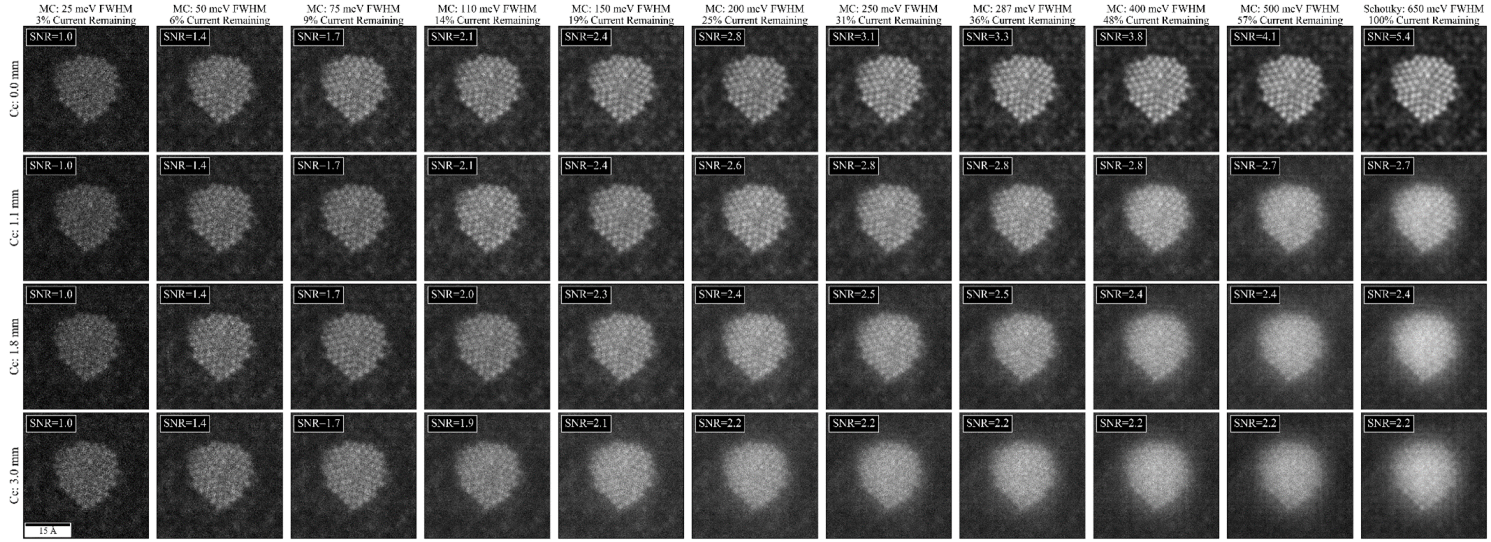

Figure B.3.: *Images of simulated Au nanoparticle at $E = 15$ keV with a Schottky field emission gun at various levels of monochromation. The Cc coefficient for each row is $Cc = 0$ mm, 1.1 mm, 1.8 mm, and 3.0 mm from top to bottom respectively. For each column $\Delta E = 25$ meV, 50 meV, 75 meV, 110 meV, 150 meV, 200 meV, 250 meV, 287 meV, 400 meV, 500 meV, and 650 meV. The scale bar is 15 angstroms.*

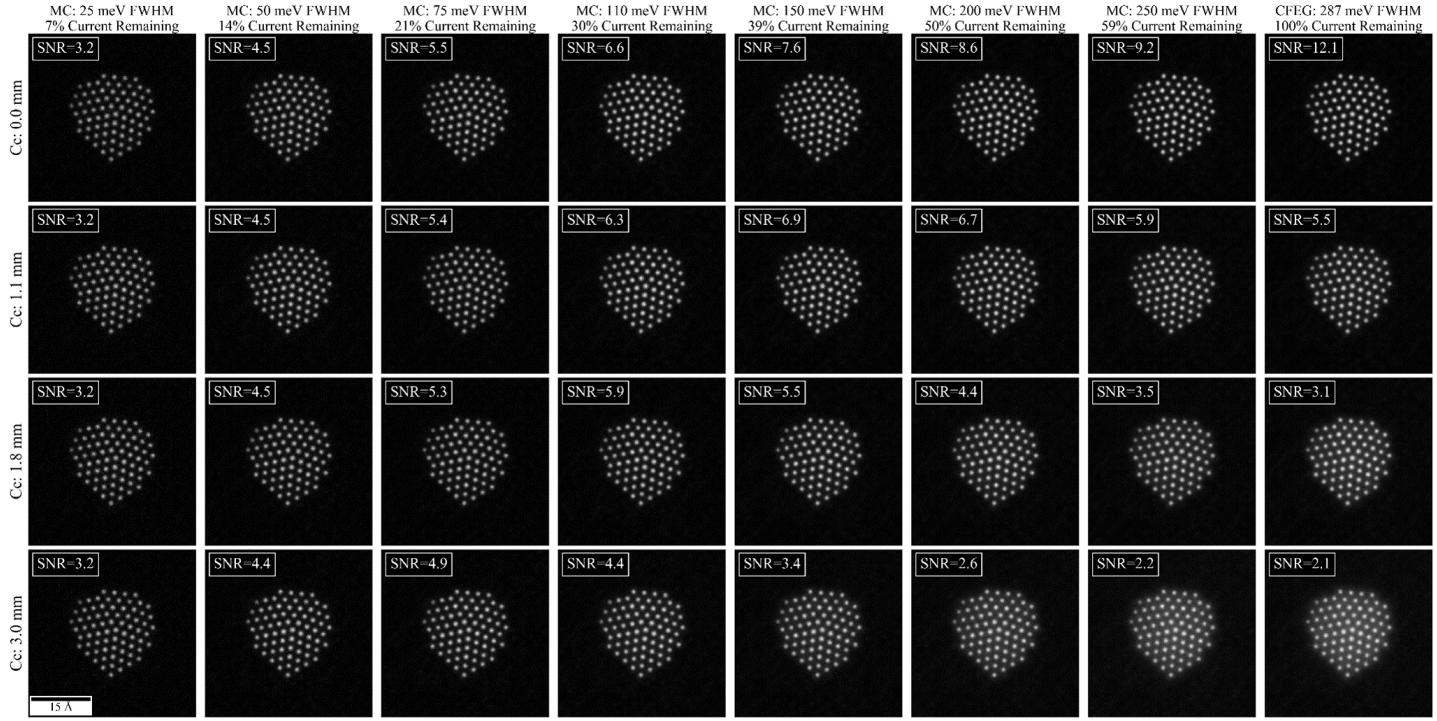

Figure B.4.: *Images of simulated Au nanoparticle at $E = 60$ keV with a cold field emission gun at various levels of monochromation. The Cc coefficient for each row is Cc = 0 mm, 1.1 mm, 1.8 mm, and 3.0 mm from top to bottom respectively. For each column $\Delta E = 25$ meV, 50 meV, 75 meV, 110 meV, 150 meV, 200 meV, 250 meV, 287 meV. The scale bar is 15 angstroms.*

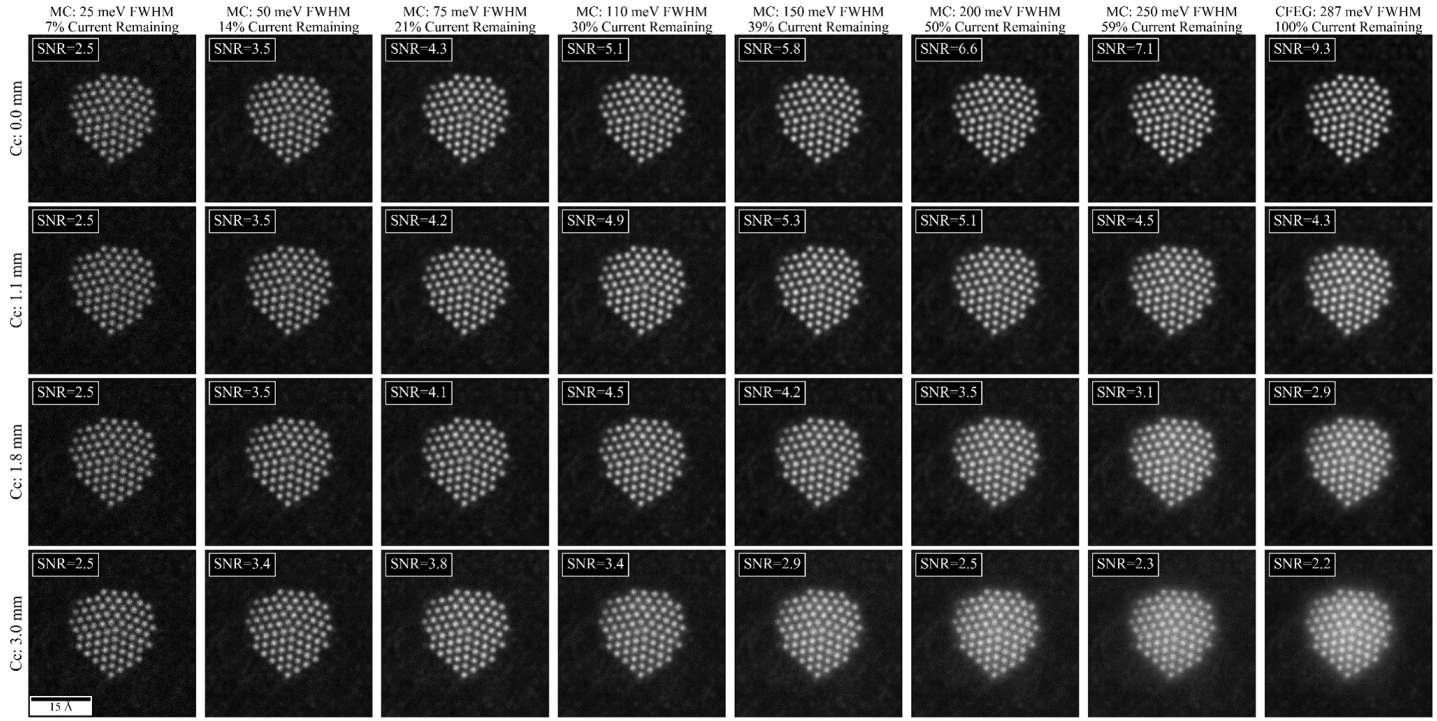

Figure B.5.: *Images of simulated Au nanoparticle at E = 30 keV with a cold field emission gun at various levels of monochromation. The Cc coefficient for each row is Cc = 0 mm, 1.1 mm, 1.8 mm, and 3.0 mm from top to bottom respectively. For each column ΔE = 25 meV, 50 meV, 75 meV, 110 meV, 150 meV, 200 meV, 250 meV, 287 meV. The scale bar is 15 angstroms.*

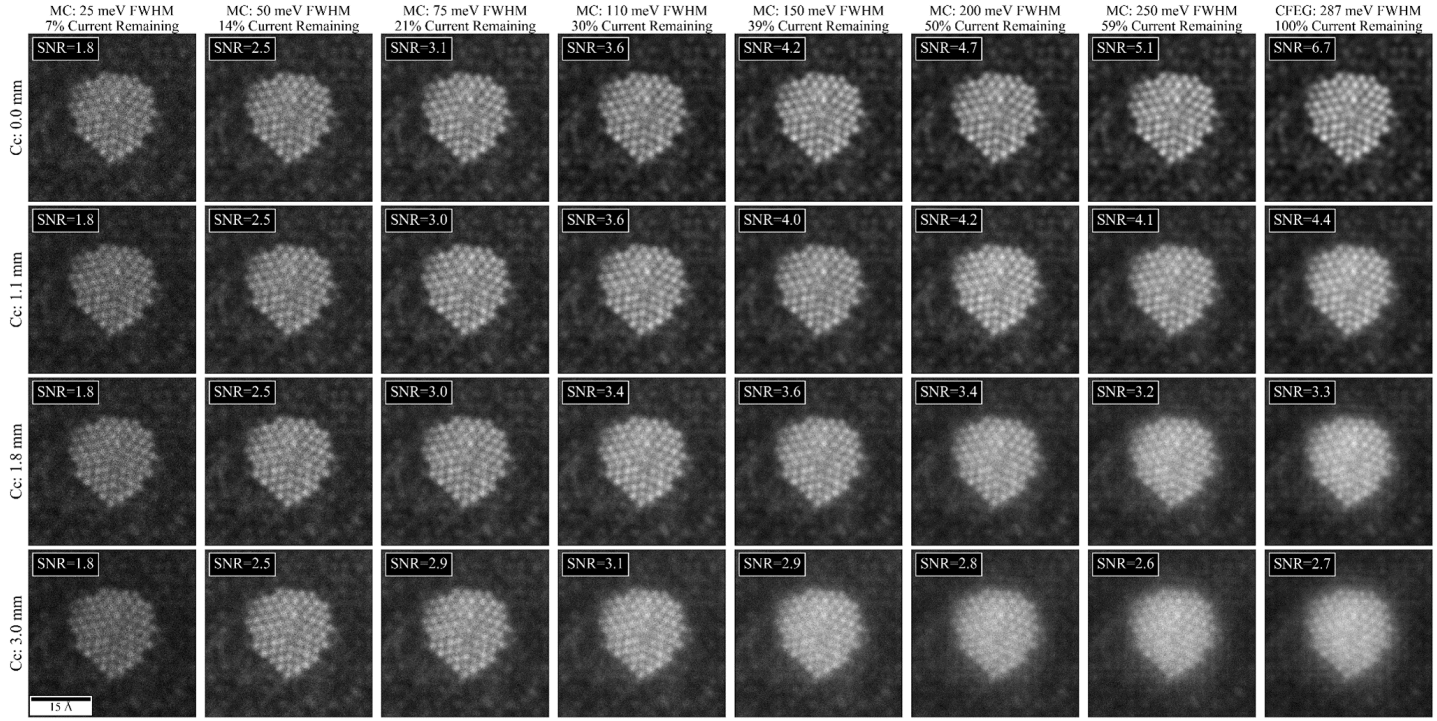

Figure B.6.: *Images of simulated Au nanoparticle at $E = 15$ keV with a cold field emission gun at various levels of monochromation. The Cc coefficient for each row is Cc = 0 mm, 1.1 mm, 1.8 mm, and 3.0 mm from top to bottom respectively. For each column $\Delta E = 25$ meV, 50 meV, 75 meV, 110 meV, 150 meV, 200 meV, 250 meV, 287 meV. The scale bar is 15 angstroms.*

Appendix C.

Quantum Efficiency Graph

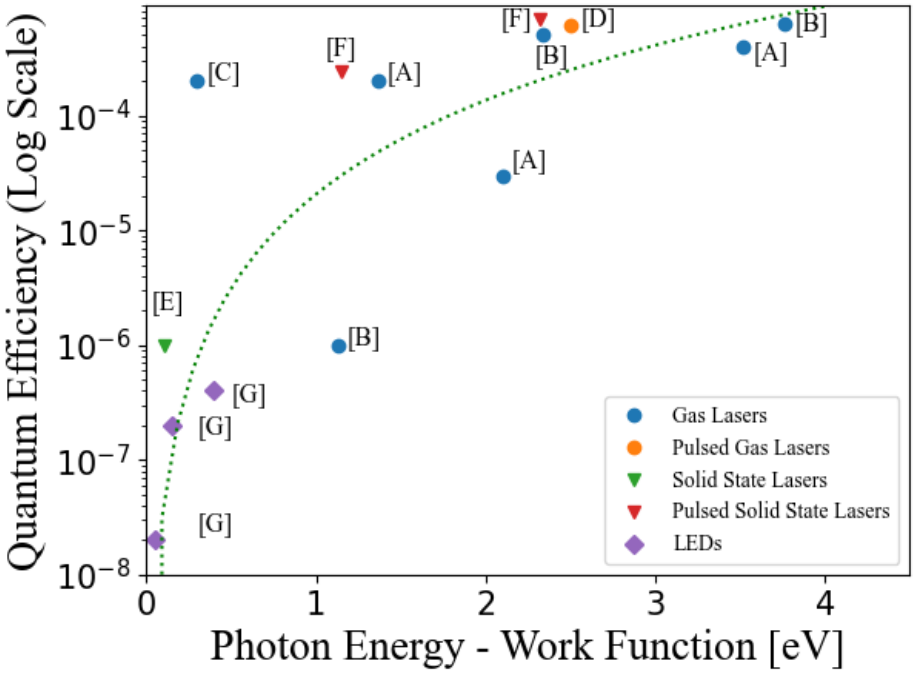

Figure C.1.: *Quantum efficiency versus photon energy minus the work function of lanthanum hexaboride for the literature values; [A] Oettinger et al. 1990 [50], [B] Lafferty et al., 1951 [46], [C] May et al., 1990 [47], [D] Qian et al., 1995 [49],[E] Sawa et al., 2017 [51],[F] Leblond et al., 1996 [75], [G] Konishi et al., 2012 [83]. A trend line in green has been fitted through the data points. This graph is reproduced from supplemental Figure 1 from Quigley et al. 2023 (Reference Number: [74]).*

Appendix D.

Electric Circuit Drawing of the Deconstructed Prototype

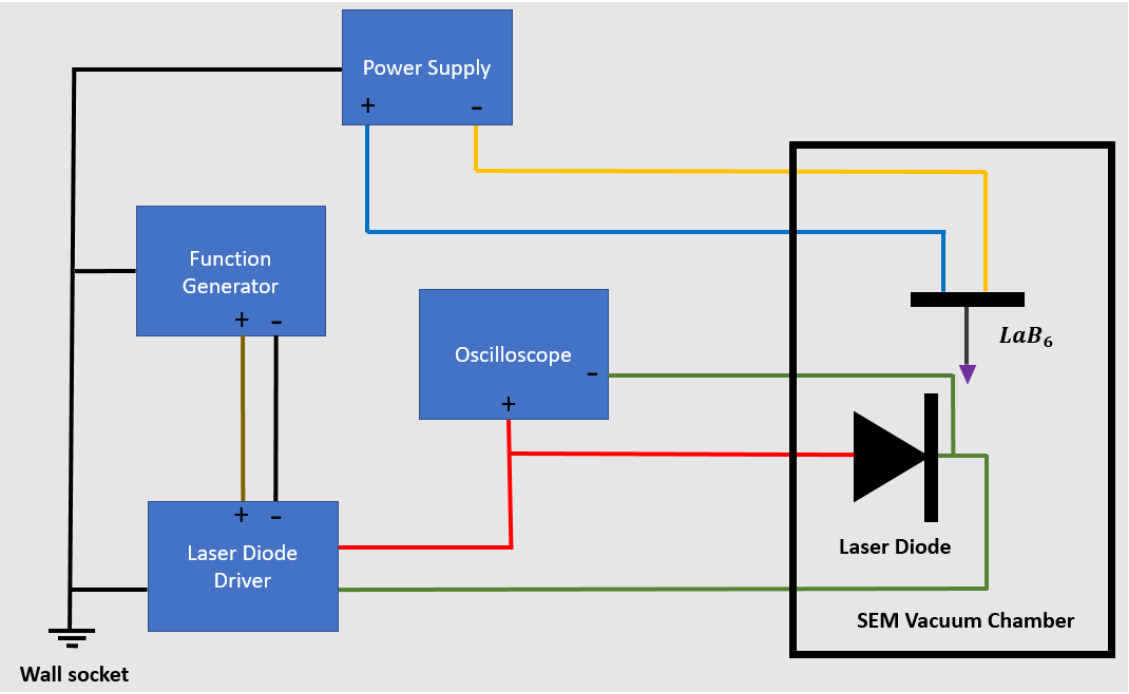

Figure D.1.: *Electric circuit drawing of deconstructed prototype experiment in the SEM as described in Section 4.2.2*

Appendix E.

Additional Experimental Data

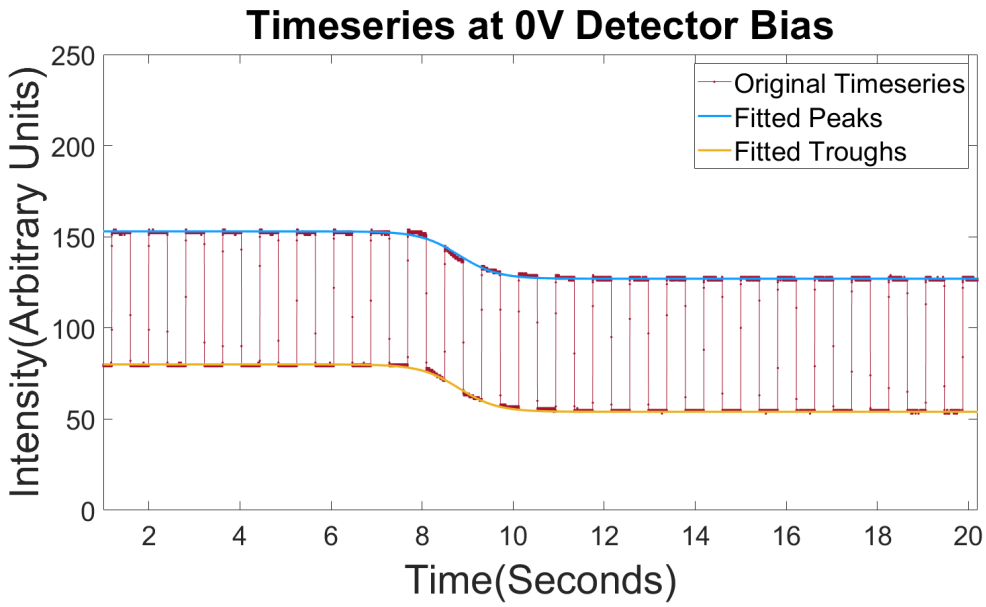

Figure E.1.: *The timeseries of pixel intensity versus time at a detector bias of 0V (red) and the average of the peaks (blue) and troughs (orange) of the timeseries.*

Appendix F.

COMSOL Simulation Graph

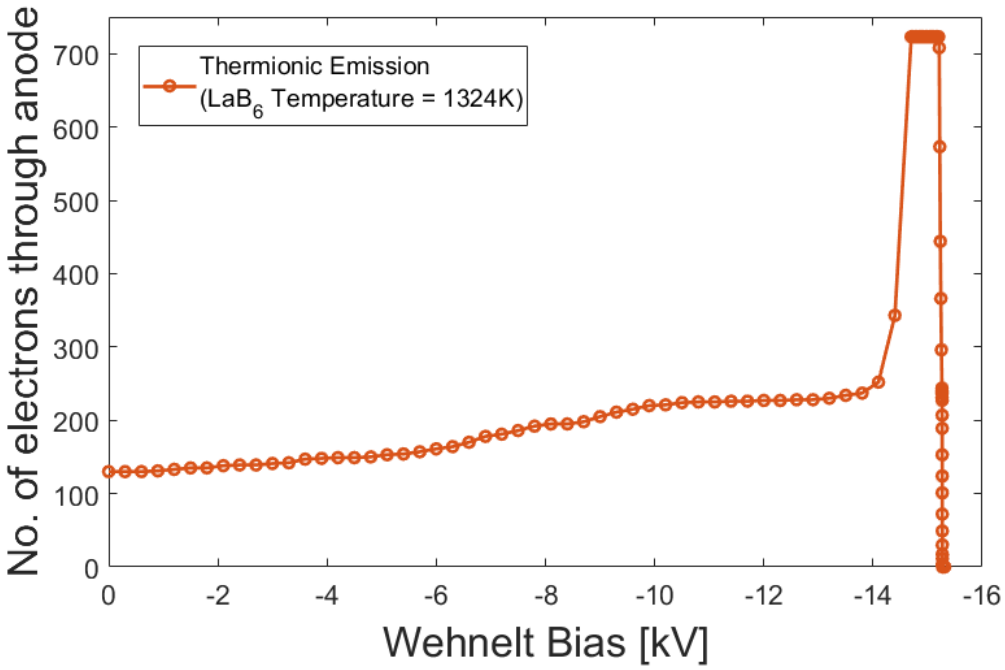

Figure F.1.: *Graph of number of electrons to get through the anode versus a change in Wehnelt bias for a cathode simulated at a temperature of 1234K.*